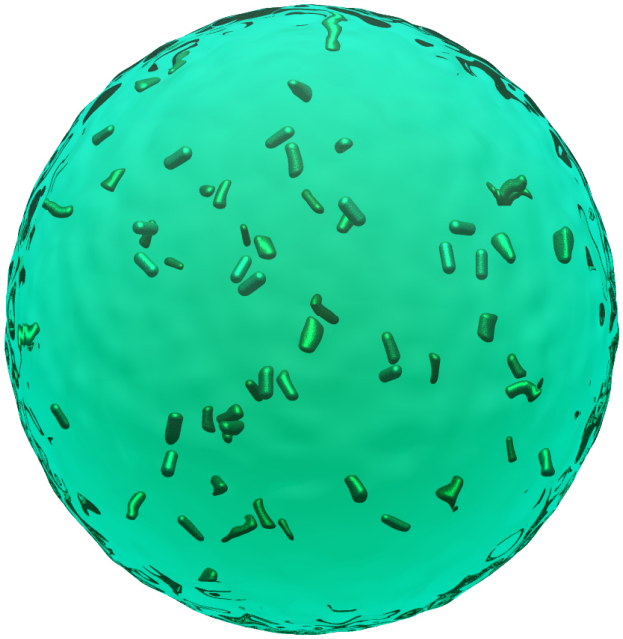

Development of New Methods for the Synthesis of Plasmonically-Active Precious Metal Rods and Shells

A thesis presented for the degree of Doctor of Philosophy

By

Jonathan A. Edgar

B. Sc. Hons. (Nanotechnology): University of Technology, Sydney

October 2011

Dedication

This thesis is dedicated to my family; past, present and future.

Certificate of Originality

I certify that the work in this thesis has not previously been submitted for a degree nor has it been submitted as part of requirements for a degree except as fully acknowledged within the text.

I also certify that the thesis has been written by me. Any help that I have received in my research work and the preparation of the thesis has been acknowledged. In addition, I certify that all information sources and literature used are indicated in the thesis.

Production Note:
Signature removed prior to publication.

Jonathan A. Edgar

10/10/2011

Acknowledgements

The first order of business is to express my gratitude to Prof. Michael B. Cortie for his role as principal supervisor for my research. His attitude and demeanour toward all of his students and colleagues encourages a comfortable yet challenging working environment, the daily 10 am coffee 'meeting' being a prime example. Thank you for the opportunity and the guidance that you have provided throughout my time at the University of Technology, Sydney (UTS). Also to my co-supervisor Dr Andrew McDonagh (who replaced Dr Hadi Zareie, whom I would also like to thank) I have always enjoyed our conversations and am grateful for all of your contributions to my research.

I would like to thank the Australian Research Council and AGR Matthey for providing financial support to this project and to me. To Mr Simon Gilbert and others at AGR Matthey, thank you for your hospitality and showing us around your facilities (also for assistance with arranging my wedding rings).

Assoc. Prof. Mike Ford and other key members of the Physics Department for their continued support both academic and social. A special mention to Dr Annette Dowd for useful discussions and TEM work.

Dr Brian Reedy and Dr Paul Thomas who both contributed greatly to my education and current field of interest. Also for numerous discussions which had no particular academic affiliation but were nonetheless just as thought provoking.

Thank you to all of the staff from the Microstructural Analysis Unit at UTS for all of their help and conversations.

Dr Tracey Hanley (Australian Nuclear Science and Technology Organisation, ANSTO), Dr Nigel Kirby (Australian Synchrotron) and Dr David Cookson (Australian Synchrotron) for their assistance with SAXS experiments. Also, Dr Catherine Kealley for her assistance with SAXS measurements and data analysis.

Dr Matthias Flöttenmeyer and the Australian Microscopy and Microanalysis Research Facility (AMMRF) for assistance with cryo-TEM experiments and funding, respectively.

Other post-graduates students, past and present, with whom I shared an office or worked with at some point thank you for your patience; Dr Burak Cankurtaran, Dr Nadine Harris, Dr Rainer Hoft, Dr Dakrong Pissuwan, Dr Nicholas Stokes, Vijay Bhatia, Tim Lucey, Jonathan Mak, Alex Porkovich, Dylan Riessen, Supitcha Supansomboon and Valerio Taraschi. A special mention for Dr Marty Blaber and David Bishop for many years of friendship and continuing the tradition of the Friday evening 'meeting'.

To my family, thank you for providing the support and encouragement that has gotten me to where and who I am today. Thank you to all of my friends, near and far, you know who you are and why you are special.

And last, but by no means least, my exquisite wife Allayna Edgar for her continuing support and tolerance for the duration of my PhD studies. Without her I would be lost.

Abstract

The ability to synthesise metal nanoparticles with various geometries has vastly improved in recent years. The plasmon resonance, the mechanism responsible for the optical response of metal nanoparticles, is highly sensitive to their geometry. This is the primary reason for the current interest in developing syntheses that produce a distinct geometry. In contrast, polydisperse samples of nanoparticles have relatively poorly defined plasmon resonances. Although nanospheres are still the most common geometry of metal nanoparticle synthesised, there is rapidly increasing interest in nanorods and nanoshells on account of their more flexible optical response. Therefore, developing a reliable synthesis for nanorods and nanoshells has been a target of much recent research. Gold is the most popular metal for the synthesis of plasmonically active nanoparticles.

In this thesis I present a development of synthesis methods for plasmonically active nanoparticles and a characterisation of the resulting products. In my work I have synthesised gold nanorods, a mixed dispersion of gold nanorings and hollow gold nanoparticles, silver nanorods and platinum nanospheres. To characterise these nanoparticles I have used a range of techniques including UV-Vis-NIR spectrometry, SEM, TEM, cryo-TEM, SAXS and electrodynamics simulations.

Early in my work I recognised that gold nanorods provided the best opportunities to achieve large scale applications. Some significant drawbacks in the existing methods of synthesis were identified, such as the inefficient reaction of gold. This realisation led me to focus the majority of my efforts on improving the understanding of the mechanisms involved in the synthesis of gold nanorods and, in particular, on the all-important transition from spherical seed particle to anisotropic rod. The nearest competitor to nanorods, with respect to applications, is nanoshells and so I have also compared these two geometries in the literature review.

From the exhaustive work presented in this thesis I present a set of optimum conditions for the synthesis of gold nanorods. Evidence for the disproportionation of gold (I) bromide as the mechanism of gold metal formation in the gold nanorod synthesis is presented. I also show that it is necessary to sacrifice control of the aspect ratio of the nanorods produced in order to improve the efficiency of the reaction. I use a co-reductant to show that the formation of nanorods is dependent on the effectiveness of the reductant that is present after the addition of the gold nanoparticle seeds. It is also apparent that it is possible to achieve a range of aspect ratios as well as particle dimensions by varying the amount of seed particles added to the growth solution.

I have used a range of experimental techniques including cryo-TEM, SEM, UV-Vis spectroscopy and small angle X-ray scattering to probe the physical dimensions and optical properties of gold nanorods at various stages of their growth and from this I have developed a new growth model. Simulations of the optical properties of the intermediate nanoparticle geometries observed support this new growth model.

Table of Contents

List of Publications

Portions of the work presented in this thesis have been published, contributed to or have been submitted for publication. The following is a list of the citations for these publications:

Jonathan A. Edgar, Hadi M. Zareie, Martin G. Blaber, Annette Dowd, Michael B. Cortie

"Synthesis of hollow gold nanoparticles and rings using silver templates"

2008 International Conference on Nanoscience and Nanotechnology **2008**, 36-39.

Jonathan A. Edgar, Michael B. Cortie

"Nanotechnological Applications of Gold Nanoparticles"

Gold: Science and applications. CRC Press: **2009**; p 369-397.

Andrey I. Denisyuk, Giorgio Adamo, Kevin F. MacDonald, Nikolay I. Zheludev, Matthew D. Arnold, **Jonathan A. Edgar**, Michael J. Ford, Viktor Myroshnychenko, Javier García de Abajo

"Transmitting hertzian optical nanoantenna with free-electron feed"

Nano Letters **2010,** 10, (9), 3250 – 3252

Nicholas L. Stokes, **Jonathan A. Edgar**, Andrew M. McDonagh, Michael B. Cortie

"Spectrally selective coatings of gold nanorods on architectural glass"

Journal of Nanoparticle Research **2010,** 12, (8), 2821 - 2830

Jonathan A. Edgar, Andrew M. McDonagh, Michael B. Cortie

"On the mechanism of formation of gold nanorods"

ACS Nano **2011** submitted

List of Abbreviations

^{1}H-NMR	nuclear magnetic resonance spectroscopy
A*	ascorbate radical
Ag or Ag^{o}	silver metal
Ag^{+}	silver ion
AgBr	silver bromide
$AgNO_3$	silver nitrate
AMMRF	Australian microscopy and microanalysis research facility
AR	aspect ratio
Au or Au^{o}	gold metal
Au_2S	gold sulphide
Au^{3+}	gold (III) ion
$AuBr_2^-$	gold (I) bromide
$AuBr_4^-$	gold (III) bromide
$AuCl_2^-$	gold (I) chloride
$AuCl_4^-$	gold (III) chloride
BDAC	hexadecyl-benzyldimethyl-ammonium chloride
BH_4^-	borohydride
Br^-	bromide
BSA	bovine serum albumin
BT	bow-tie
C_{16}TABr	hexadecyltrimethylammonium bromide
C_{16}TACl	hexadecyltrimethylammonium chloride
C_{16}TASBr	AgBr- C_{16}TABr complex
C_{16}TEABr	hexadecyl-triethylammonium bromide
CBT	conically-capped bow-tie
CC	conically-capped cylinder
CCG	complex conjugate gradient
CdSe-ZnS	cadmium selenide - zinc sulphide
CM	Clausius-Mossotti
CMC	critical micelle concentration
cryo-TEM	cryogenic transmission electron microscopy
DDA	discrete dipole approximation
DHA	dehydro-ascorbic acid
DNA	deoxyribonucleic acid
EM	electromagnetic
et alii	and others'
EXAFS	extended X-ray absorption fine structure
fastSPS	fast single-particle spectroscopy
FCC	face centred cubic
FE-SEM	field emission - scanning electron microscope
FFT	fast Fourier transform
FOM	figure of merit
FTIR	Fourier transform infrared spectroscopy

GM	Göppert-Mayer units
GS	growth solution
H_2A	ascorbic acid
H_2PtCl_6	hexachloroplatinic acid
HA^-	ascorbate anion
$HAuBr_4$	tetrabromoauric acid
$HAuCl_4$	tetrachloroauric acid
HCl	hydrochloric acid
HDT	hexadecanethiol
HNO_3	nitric acid
ICP-MS	inductively coupled plasma - mass spectrometry
IR	infrared
ITO	indium tin oxide
KBH_4	potassium borohydride
LDR	lattice dispersion relation
LSP	localised surface plasmon
MRI	magnetic resonance imaging
Na_2S	sodium sulphide
NaBr	sodium bromide
NaOH	sodium hydroxide
NaSal	sodium salicylate
NiPAAm	N-isopropylacrylamide
NIR	near infrared
NP	nanoparticle
OCT	optical coherence tomography
OH	hydroxide
PC	personal computer
PTFE	polytetrafluoroethylene
PVA	poly-vinyl alcohol
PVP	polyvinylpyrrolidone
QDs	quantum dots
RIU	refractive index unit
rpm	revolutions per minute
SALDI-MS	surface-assisted laser desorption/ionisation time-of-flight mass spectrometry
SAXS	small angle X-ray scattering
SC	spherically-capped cylinder
SEM	scanning electron microscopy
SERS	surface enhanced Raman scattering
SHE	standard hydrogen electrode
SiO_2	silicon dioxide
SPIO	super-paramagnetic iron oxide
SPP	surface plasmon polariton
$TC_{12}ABr$	tetradodecylammonium bromide

TC_8ABr	tetraoctylammonium bromide
TEM	transmission electron microscopy
TGA	thermogravimetric analysis
TPL	two-photon induced luminescence
UPD	underpotential deposition
UV	ultraviolet
Vis	visible
WAXS	wide angle X-ray scattering
XPS	X-ray photoelectron spectroscopy

List of Figures

1 Introduction

In recent years the advancement of the natural sciences has been significantly influenced by the ability to interact with and control systems at the nanoscale. These advancements have been generalised by designating these abilities as a distinct sub-field of research i.e. nanoscience.

Nanoscience and nanotechnology (the application of nanoscience) are considered by many as either the potential "cause of or solution to all of life's problems".[a] Opinions on this topic are, however, typically polarised to one or the other view. My belief is that the benefits of nanoscience are too great to suppress and that as long as suitable precautions are observed this will greatly reduce the chance of any negative consequences.

To write an account of the entire scope of nanoscience would perhaps require utilising one of the nanolithographic techniques that has emerged from the field. However, I feel that there are certain contributions that require attention to develop the impression of the scale of the systems that I will discuss in this thesis.

A major benefactor (and beneficiary) to advancements in nanoscience has been the conglomerate IBM. One of their primary contributions to nanoscience and nanotechnology is the scanning tunnelling microscope (STM).[1] This invention has allowed sub-nanometre imaging and also earned Gerd Binnig[b] and Heinrich Rohrer half the 1986 Nobel Prize for physics.[2] The other half was awarded to Ernst Ruska (not affiliated with IBM) for his contributions to the development of electron optics for electron microscopy, another vital contribution for the rapid progression of nanoscience.

The manipulation and construction of nanoscale features is also highly desirable. This is another area where IBM have offered significant advancement with their continual shrinking of features produced by optical lithography for processor chips. For example, their recent introduction of chemically-amplified photo-resists can produce features separated by only ~ 22 nm.[2] There are also other prominent lithographic techniques such as dip-probe, scanning electron and nano-imprint, to name a few.[3] The advantage of lithography is that there is a high level of control over the features produced. However, the limitation of lithography is that the features are constrained to two dimensions.

The preparation of nanosized features can be extended to three-dimensions by way of colloidal syntheses. A colloid is the discrete partitioning of one medium that is dispersed in another. Typically (at least one of) the dimensions of the dispersed medium are

[a] Paraphrased from The Simpsons episode 171: "Homer vs. the Eighteenth Amendment"

[b] In 1986 Binnig, in collaboration with Calvin Quate and Christoph Gerber, also introduced the atomic force microscope (AFM) another vital tool for nanoscience and nanotechnology.

between 1 nm – 1 μm.[4] Colloidal syntheses exist for a broad range of materials and provide a multitude of indispensible properties, but for the purposes of this thesis I will focus on colloids of precious metal nanoparticles and their syntheses.

The production and application of gold colloids extends back to around the 4th century A.D. shown by the famous Lycurgus Cup,[5] Figure 1-1. However, this does not signify the initiation of scientific study of these systems.

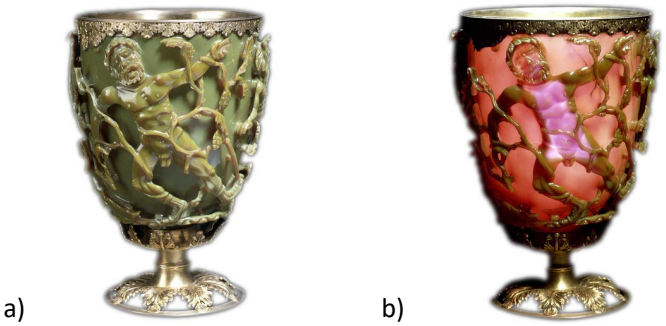

Figure 1-1 Roman 'Lycurgus Cup' from 4th century AD photographed in a) reflected light and b) transmitted light.

Images modified from reference [5]

The work of Michael Faraday is widely recognised as the initiation of modern research into aqueous gold colloids. In this work, Faraday correctly attributed the colour of the suspension that he synthesised to the size of the nanoparticles relative to the wavelength of incident light.[6] Work previous to Faraday typically referred to the gold in solutions or materials e.g. ruby glass, as either a compound or finely divided particles.[7] Another famous application of colloidal gold is the dye known as 'Purple of Cassius'. Although there appears to be some contention regarding the true originator of the technique behind the striking colours produced, Andreas Cassius was certainly a major contributor.[8]

Richard Zsigmondy is possibly the greatest recognised contributor to the advancement of gold colloids. He was awarded the 1925 Nobel Prize for his extensive characterisation and development of colloid chemistry.[2] Zsigmondy also played a major role in the development of the ultramicrosope in collaboration with Henry Siedentopf. This work manifests in modern research as dark-field microscopy or spectroscopy of single metal nanoparticles.

Zsigmondy also used a seeded growth procedure where he added a growth solution of ionic gold to a solution of gold nanoparticles in order to increase their volume such that they could be counted in a light microscope and thus the concentration of particles determined.[9, 10] This work is analogous to the syntheses that led to the introduction of the seed-mediated synthesis of gold nanorods.[11-13]

The Turkevich method for preparing gold colloids is another well known example.[14] This method was made famous by the publication of Turkevich *et al*. but was previously published 11 years earlier by Hauser and Lynn.[15] A significant contribution of Turkevich *et al*. was their analysis of the features of various syntheses of gold colloids using electron microscopy.[14]

Colloidal gold chemists appear to have had a slightly alcoholic inclination, with both Andreas Cassius in "De Operationibis Circa Aurum Chymicis" (some experiments in the alchemy of gold)[8] and Richard Zsigmondy noting that the colour of a colloidal suspension of gold is "like a good red wine".[7] Again, in the analysis of the well known citrate-reduction method, Turkevich *et al*. comment on the similarities of the colour to red wine.[14] However, the colour of gold nanospheres has much greater significance than as a simile to red wine. In fact, the optical response is what makes gold nanoparticles such a hot topic for modern research. The mechanism responsible for the unusual optical properties of metal nanoparticles is referred to as the 'localised surface plasmon resonance', or more simply as the 'plasmon resonance'. The primary influences on the plasmon resonance of metal nanoparticles will receive greater attention in Section 1.2 and a broad range of applications of these exotic properties is reviewed in Section 1.5.

Gold is the most popular option for the synthesis of plasmonically active nanoparticles. This is due to the vast array of methods for synthesising gold colloids as well as to their stability. The stability of the colloid is due in part to the nobility of the gold itself and the ability to preserve the integrity of the colloid through surface passivation. The optical response of gold is not the strongest or most efficient of the plasmonically active metals[16] but the ease of synthesis and manipulation are too attractive for most to ignore.

The colour of gold nanoparticles is not only limited to red wine. One of the most effective ways to control the optical properties of a gold colloid is by the preparation of gold nanorods. By varying the aspect ratio of the nanorod (length to width ratio) the peak extinction wavelength can be tuned from green wavelengths (~ 520 nm) into the NIR (> 700 nm). A similar effect can be achieved by preparing gold nanoshells and varying the shell thickness. If the optimum cases for each respective colloid are compared, then nanorods show a higher optical efficiency.[17, 18] Tuning the peak wavelength greatly expands the possible applications.

The wet chemical synthesis of gold nanorods has developed faster than the understanding of the mechanisms involved. A typical synthesis involves the overgrowth of gold nanoparticle seeds in a growth solution of ionic gold, stabilising surfactant (hexadecyltrimethylammonium bromide, $\mathrm{C_{16}TABr}$), slight excess of weak reducing agent (ascorbic acid, $\mathrm{H_2A}$) and a low concentration of ionic silver. Although numerous hypotheses have been presented there is, as of yet, no consensus for the formation mechanism of gold nanorods. Popular theories are based on a soft-template effect supplied by the surfactant micelles[19-22], passivation of the flanks of the nanorod by AgBr[13, 21, 23] or a AgBr complex[24], underpotential deposition of $\mathrm{Ag^0}$ on the flanks[25] and

an electric field driven process.[26] There is still no definitive explanation for the initiation of the nanorod geometry from seed to final product.

For publications that utilise gold nanorods it is common place to refer to a standard method of synthesis, usually that of Nikoobakht and El-Sayed.[21] The method in this paper is the earliest publication that represents the synthesis in its current form. The most notable modification to the original synthesis was the introduction of a $C_{16}TABr$ stabilised seed which improved the monodispersity of the product. The initial synthesis was reported by Jana *et al*.[13]

A major issue with the current gold nanorod synthesis is the fact that only $\sim 15\%$ of the initial gold concentration is used in the reaction.[27] This problem is typically addressed by removing the unreacted gold by centrifuging the nanoparticle dispersion and discarding the supernatant. If the unreacted gold is left in the solution then the nanorods will 'age' which results in a decrease of anisotropy i.e. the aspect ratio decreases. For a typical synthesis the total mass of gold used in the preparation of a solution of gold nanorods is ~ 1 mg and so the mass wasted is not large for a small number of samples. However, this percentage loss could be unacceptable when the synthesis is scaled up to the commercial quantities needed to realise large scale applications,

In the remainder of Chapter One I review the literature that is most relevant to the work that I have presented in this thesis. The majority of the review deals with gold nanorods but I have also included important points about gold nanoshells, which are the major competitors to nanorods. Following a discussion of the technical aspects of the properties and synthesis of each, I have reviewed the vast array of applications.

I have collated the various techniques and procedures that I have used throughout my work into Chapter Two. This includes a description of all the syntheses that I have presented. I also discuss calibrations for the determination of $AuBr_4^-$ concentration in solution, concentration of Au^0 in a gold nanoparticle solution and estimation of nanorod dimensions from UV-Vis-NIR spectra. I have also included a description of a 3D rendering script that I have developed to produce crystallographic representations of gold nanoparticles that are approximately to scale.

Chapter Three describes the work that I have done with precious metals other than gold, and on different shapes of nanoparticles. I have synthesised gold nanorings, hollow gold nanoparticles, silver nanorods and platinum nanospheres. I have used UV-Vis spectroscopy to characterise the optical properties of all the nanoparticles mentioned. DDA calculations and Mie theory were used to simulate the optical properties of gold nanorings and platinum nanospheres respectively. TEM and SEM were used to observe the dimensions of gold nanorings.

Chapter Four contains my optimisation of the gold nanorod synthesis. I use well-known solution conditions to validate the method that I use for the synthesis of gold nanorods. Evidence is provided for the disproportionation of $AuBr_2^-$ as the mechanism of Au^0

formation in the nanorod reaction. I also show the high dependence of the reaction on the concentration of excess weak reductant and how this is the result of the disproportionation mechanism. I also introduce the use of a co-reductant, sodium salicylate, which supports the disproportionation mechanism and highlights that there is a dependence on the efficacy of the excess weak reductant in the nanorod formation step.

In Chapter Five I present my new growth model for the silver-assisted, wet chemical gold nanorod synthesis. I had designed the experiments in this chapter to solve the mystery of the initiation of the nanorod geometry. Although I did not achieve this specific aim, I did develop a new perspective into the formation of gold nanorods. A descriptive model was developed by analysis of the kinetics of gold nanorod formation using multiple techniques including UV-Vis-NIR spectroscopy, SAXS, cryo-TEM and SEM. Briefly my new growth model involves a very rapid initial growth event followed by a gradual development of the particle features to approach the familiar hemispherically-capped cylinder. An important factor in the growth model is that not all seed particles experience the initial growth event simultaneously. This indicates that different particles can be at different stages of growth at a given point of the reaction.

1.1 Trends in Metal Nanoparticle Research

Metal nanoparticles, in particular those formed from precious metals, represent a significant contribution to the now-established field of nanoscience and nanotechnology. There is a generally good understanding of many of the basic aspects of synthesis, handling and application of metal nanoparticles, and much of current research pursues some specific and relatively narrow aspect of the field. The trends in metal nanoparticle research are illustrated in Figure 1-2, which shows an analysis of a literature search using the database Scifinder Scholar. Starting with the keywords “metal nanoparticles” and refining for reviews and duplicates, the total number of publications has been steadily increasing for the past 15 years.[c] The sub-divisions in Figure 1-2 correspond to refinements of the search data to establish the volume of the literature dealing with the keywords listed within the key.[d] These searches are heavily dependent on the keywords used so it should be noted that although metal nanoparticle research has been active for around 100 years the jargon used has changed over this period (e.g. sol generalised as colloid). Considering that the target here was to observe current trends, the popular term of ‘nanoparticle’ was selected.

[c] Data correct up to and including 20th January 2011.
[d] Boolean operator “AND” is used to separate reviews that contain both keywords.

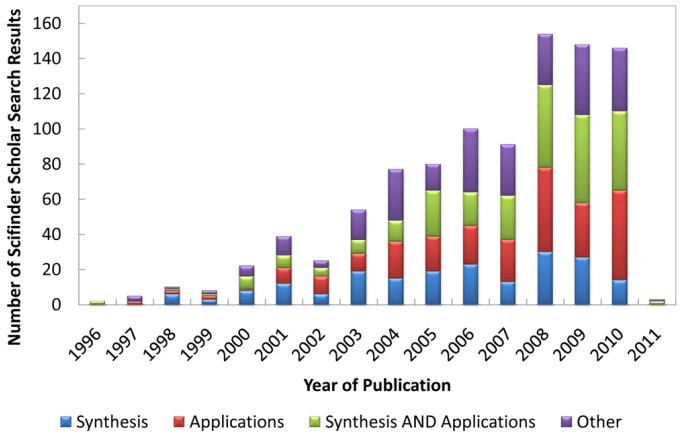

Figure 1-2 Scifinder Scholar analysis for reviews of "metal nanoparticles" subdivided by keyword

On closer analysis of the search data, the metal nanoparticle field has expanded so far that it is now commonplace to have focussed reviews dedicated to particular properties of these particles. This implies a significant depth in the literature where it has become necessary to collate with respect to each aspect as opposed to global basics.

Analysis of the search results for metal nanoparticles with respect to standard journal document types (e.g. letter, article etc.) and refining for gold, silver, copper, platinum and palladium shows that the bulk of the research has focussed on gold,[c] Figure 1-3. This may be due to the transferral of the inert properties of the bulk metal to the nanoscale, which leads to quite stable particles.

One of the primary developments in the research of gold nanoparticles is the deviation from the energetically favourable geometry of the solid nanosphere. This deviation brings with it a significant increase in the range of properties and hence applications for metal nanoparticles. Two simple geometric deviations are nanorods and nanoshells. There are other geometries that have been reported in the literature, such as nano-triangles, but nanorods and nanoshells are the two most prominent.

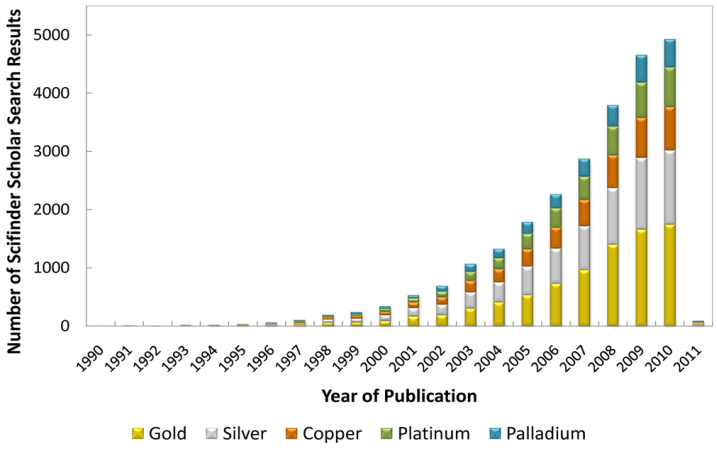

Figure 1-3 Scifinder Scholar analysis for metal nanoparticle research publications refined for precious metals

A database search for “gold nanorods” and “gold nanoshells” shows that nanorods are more prominent in the literature than nanoshells,[e] Figure 1-4. This is a reasonable indicator of the general preference of particle geometry, or possibly a reflection of relative ease of synthesis. This trend is supported by comparative properties of each that will be discussed in later sections.

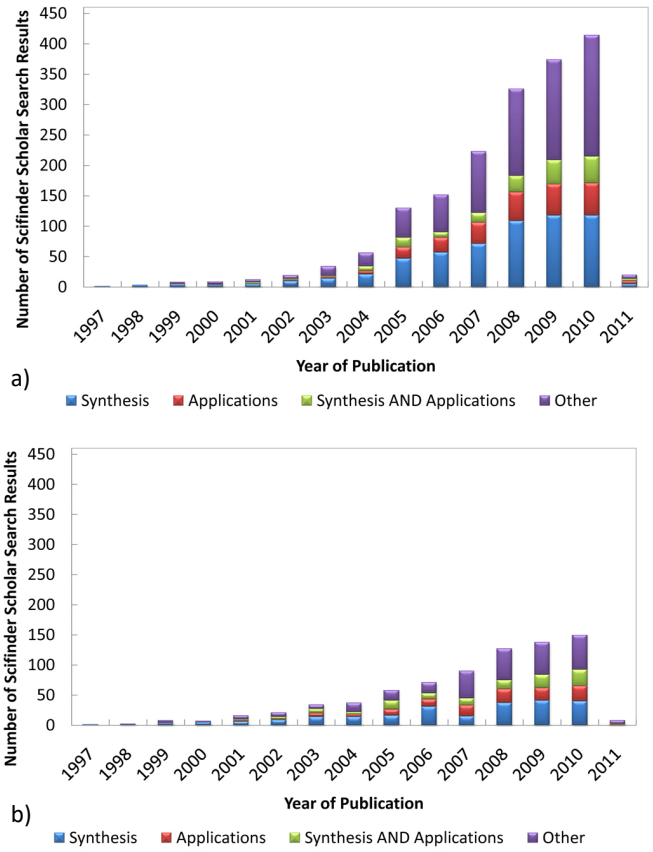

Figure 1-4 Scifinder Scholar analysis for a) “gold nanorod(s)” and b) “gold nanoshell(s)” research publications subdivided by keyword

[e] This search was performed using the additional keywords “hollow gold nanoparticles” and “gold core shell nanoparticles” due to varied terminology.

1.2 Optical Properties of Metal Nanoparticles

Optical response is the primary focus of the majority of research into plasmonically-active metals, which can manifest in the work as application of, characterisation by, or direct focus on. *Plasmons* arise from the interaction between incident electromagnetic (EM) radiation and the nanoparticle. The plasma or electrons (usually considered as conduction or 'free electrons'; see Section 1.2.1) oscillate in resonance with the incident electric field. If the oscillation is in the form of a standing wave on a discrete nanoparticle it is generally referred to as a localised surface plasmon (LSP), while if the oscillation is propagating along an interface it is more accurate to refer to this mechanism as a surface plasmon-polariton (SPP).[28] In either case the light is coupled to the plasma.[29] Figure 1-5 shows the response of the plasma to an incident EM wave (note: the EM wave and electron cloud are not to scale). The oscillation is sufficiently approximated as a dipole for the limit where the nanoparticles dimensions are small compared with the wavelength of the incident light.[29]

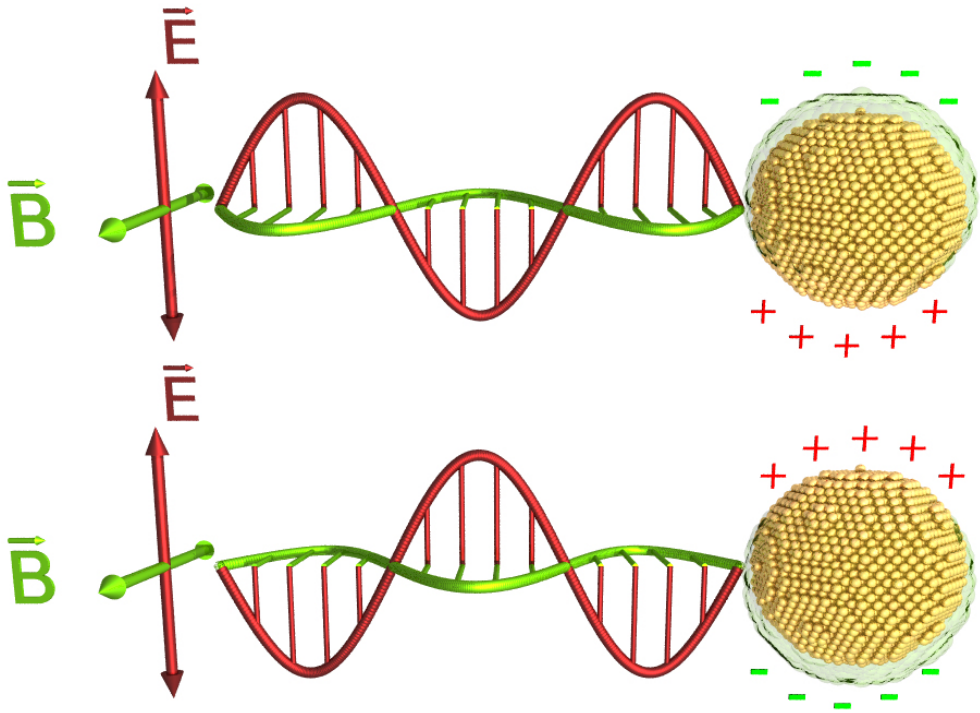

Figure 1-5 Schematic of a plasmon-polariton dipole resonance in a gold nanoparticle

The observation that the optical response of metal nanoparticles is due to their size is attributed to Michael Faraday who prepared and analysed various colloids of gold.[6] Faraday deduced that it was the very small dimensions of the gold particles that produced the macroscopic colour and scattering properties by studying aqueous and particulate films produced by chemical reduction and electric arc discharge respectively. Faraday also controlled the optical response of the colloid by varying the conditions under which the particles were prepared. Importantly, it was also determined that the particles were metallic gold, and not a compound.

The shape and relative size dependence of the optical properties of gold nanoparticles were also subject to Faraday's intuition;[6]

"I can see no reason to imagine any other variation than the existence of particles of intermediate sizes or proportions".

This comment was made in consideration of colour gradients in the preparation of gold particulate films and the gradual diffusion/settling of colloidal suspensions.

1.2.1 Optical Response of Metals

To model the optical response of metal nanoparticles the wavelength-dependent dielectric properties must be known. As the outermost electrons in metals tend to occupy the conduction band, transitions typically occur at relatively low energy. This allows for the electrons to be considered as 'free' and thus the optical response of a collection of 'free' electrons can be determined from the Lorentz harmonic oscillator model. This description is known as the Drude model and is expressed as follows:[29]

$$\epsilon(\omega) = 1 - \frac{\omega_p^2}{\omega^2 + i\gamma\omega} \qquad 1.1$$

The plasma frequency, ω_p, is given by:

$$\omega_p^2 = \frac{Ne^2}{m_e \varepsilon_0} \qquad 1.2$$

Where *N* is the density of free electrons, *e* is the charge on an electron, m_e is the effective mass of an electron, $\gamma = \frac{b}{m_e}$ *or* $\frac{1}{\tau}$, *b* is the damping constant, τ is the relaxation time and ε_0 is the vacuum permittivity.

Comparison of the Drude model with experimental data shows regions of significant departure from a pure 'free' electron model. This implies that there is an important contribution to the optical properties by interband transitions (due to bound electrons). Etchegoin *et al* have applied critical point transitions to the Drude model to obtain the following complex dielectric function for gold:[30]

$$\epsilon(\omega) = \epsilon_\infty - \frac{\omega_p^2}{\omega^2 + i\gamma_p\omega} + \sum_{i=1,2} A_i\,\omega_i \left[\frac{e^{i\phi_i}}{\omega_i - \omega - i\gamma_i} + \frac{e^{-i\phi_i}}{\omega_i + \omega + i\gamma_i}\right] \qquad 1.3$$

Equation 1.3 is presented in an analogous form to the Drude equation; where ϵ_∞ is the high-frequency limit dielectric constant.

Comparison of Equation 1.3 with two of the most commonly used dielectric tables, Johnson & Christy[31] and Weaver & Frederikse[32] shows a significant improvement to the

Drude function, Figure 1-6. The values applied to Equation 1.3 are specifically chosen to fit the data of Johnson & Christy and are found in Table 1-1.

Despite the improved accuracy of the function it is generally better to use the dielectric tables directly where possible, as even the modified Drude function can ignore the fine structure of the dielectric response.

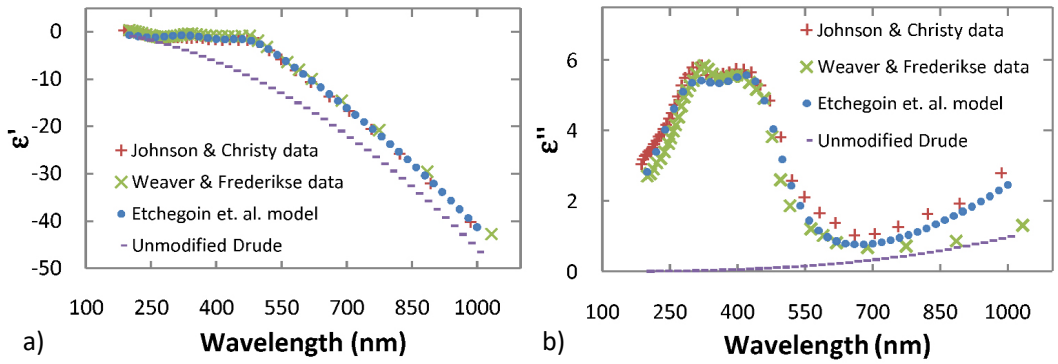

Figure 1-6 a) Real and b) imaginary parts of the dielectric function for gold from various sources

Table 1-1 Fit parameters for Etchegoin *et al*. complex dielectric function for gold

Parameter (units)	Value
ϵ_∞	1.530
ω_p (eV)	8.564
γ_p (eV)	0.073
A_1	0.940
ϕ_1 (rads)	$-\frac{\pi}{4}$
ω_1 (eV)	2.653
γ_1 (eV)	0.540
A_2	1.360
ϕ_2 (rads)	$-\frac{\pi}{4}$
ω_2 (eV)	3.752
γ_2 (eV)	1.321

For modelling the optical properties of nanoparticles that satisfy the quasistatic approximation i.e. r << λ, the strength of response to the incident EM field is specified by the polarisability, α:

$$\alpha(\omega) = AV\frac{\varepsilon_{NP}(\omega) - \varepsilon_m(\omega)}{\varepsilon_m(\omega) + L\left(\varepsilon_{NP}(\omega) - \varepsilon_m(\omega)\right)} \qquad 1.4$$

$\varepsilon_x(\omega)$ denotes the permittivity or dielectric function of the nanoparticle (NP) and surrounding medium (m) respectively. The inclusion of $\varepsilon_m(\omega)$ in the above term shows the dependence of the optical properties of the nanoparticle on the dielectric function

of the surrounding medium.[33] *A* is a strength factor and *L* is the depolarisation factor that affects the resonance position.[34] *V* is the volume of metal in the nanoparticle. In a vacuum *A* and *L* are independent of the metal but are geometry dependent.[29, 34] The volume of the nanoparticle also affects the resonance position but is not as significant as varying the geometry. The strength factor, *A*, can be omitted as it is a sum of the strengths in a multimode system.[35] In the quasistatic limit the dipole mode is dominant and often unaffected by adjacent modes.[34]

From the polarisability it becomes possible to determine the extinction, C_{ext}, and scattering, C_{sca}, cross-section of the nanoparticle:[29]

$$C_{ext} = k\, Im(\alpha) \tag{1.5}$$

$$C_{sca} = \frac{k}{6\pi}|\alpha|^2 \tag{1.6}$$

Where *k* is the wave vector of the incident EM radiation. These two results can be used to calculate the absorption cross-section, C_{abs}, as:[29]

$$C_{ext} = C_{abs} + C_{sca} \tag{1.7}$$

Typically the extinction cross-section is expressed as an efficiency which is commonly defined as follows:

$$Q_{ext} = \frac{C_{ext}}{A_{cross}} \tag{1.8}$$

Where A_{cross} is the cross-sectional area of the nanoparticle with the section taken perpendicular to the direction of propagation of the wave. However, it is more physically significant to express the optical cross-section with respect to the volume of the nanoparticle:[29]

$$Q_{ext} = \frac{C_{ext}}{V} \tag{1.9}$$

Surface effects are another important consideration for the calculation of the optical response of metal nanoparticles. As the nanoparticle gets smaller the dimensions approach the mean free path for the electrons. This can be accounted for in the damping constant where the interaction of electrons with the surface boundary can be assumed as diffusely reflected:[29]

$$\gamma = \gamma_{bulk} + \frac{v_F}{L} \tag{1.10}$$

v_F is the Fermi velocity and L is the effective mean free path for collisions with the boundaries of the particle. The main effect of surface scattering on the optical response of nanoparticles is to broaden and attenuate the surface plasmon absorption peak.[29]

1.2.2 Gold Nanorods and Gold Nanoshells

The optical extinction spectrum of gold nanorods is characterised by three significant features (Figure 1-7); a 'longitudinal' resonance peak that is due to plasma oscillations along the length of the nanorod; a 'transverse' resonance peak that is due to plasma oscillations across the width of the nanorod and which is at ~520 nm; and absorption between ~350 – 450 nm which is due to interband transitions and is independent of the geometry. The absorption at ~400 nm can be used to approximate the volume of metallic gold in a dispersion of nanoparticles.[22, 36]

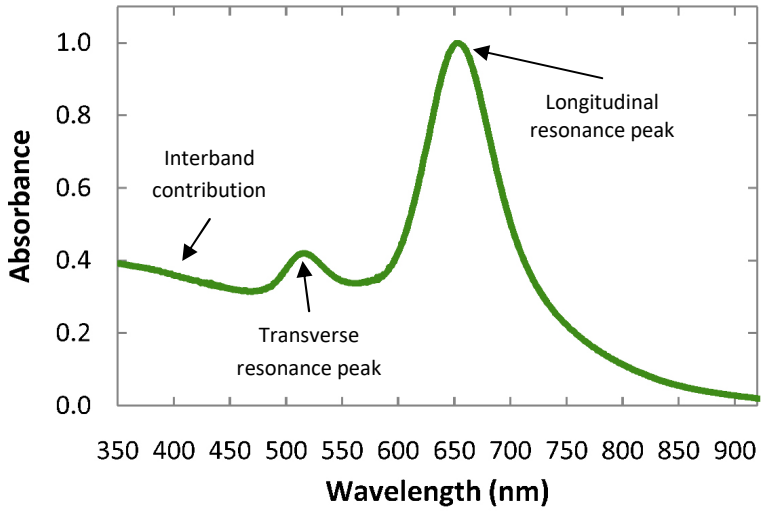

Figure 1-7 A typical gold nanorod absorption spectrum indicating primary features

As is evident from Figure 1-7, the longitudinal mode is the dominant feature in the optical response of a nanorod. The position of this resonance is controlled by changing the ratio of the length to the width, termed aspect ratio (AR):

$$\mathrm{AR} = \frac{\mathrm{Length}}{\mathrm{Diameter}} \qquad 1.11$$

Despite the oscillation being along the length of the nanorod, the resonance is primarily dependent on the aspect ratio i.e. nanorods with the same aspect ratio will have approximately the same longitudinal peak position (with larger volume causing a slight red-shift). Increasing the aspect ratio results in the longitudinal peak position being red-shifted, as $\mathrm{AR} \to 3$ the longitudinal peak position shifts from ~ 520 nm ($\mathrm{AR} = 1$, i.e. sphere) through the visible to the near-infrared, ~ 750 nm. For $\mathrm{AR} > 3$, the longitudinal resonance peak will continue to red-shift from the NIR to the infrared (IR) and as the

length begins to approach the wavelength of light the scattering cross-section begins to dominate the extinction spectrum.

Due to the anisotropic geometry the longitudinal and transverse plasmon resonances may be excited exclusively. If the polarisation of incident light is parallel to the longitudinal axis of the nanorod this will excite the longitudinal mode. When the nanorod is oriented perpendicular to the polarisation or the longitudinal axis is parallel to the direction of propagation of the EM wave then the transverse mode will be excited.

In a colloidal solution the nanorods will be randomly oriented with respect to any incident light. For a nanorod that has its longitudinal axis at any angle other than parallel or perpendicular, with respect to the polarisation of incident light, inefficient coupling to either resonance mode results in partial excitation of each (e.g. Figure 1-8d). The relative intensity of the resonance is determined by the angle of the longitudinal axis to the polarisation.

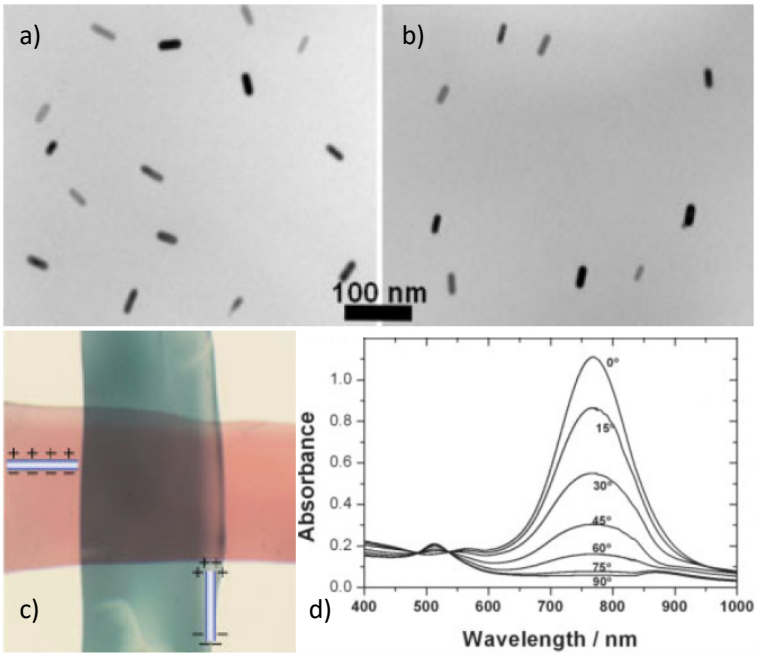

Figure 1-8 Gold nanorods in PVA film.

a) TEM of unaligned nanorods

b) TEM of aligned nanorods

c) Photograph of gold nanorods in a PVA film with longitudinal axis parallel (blue) and perpendicular (red) to polarisation of light

d) Absorbance spectrum of gold nanorod/PVA film with varied angle of polarisation with respect to longitudinal axis of gold nanorods

Images reproduced from reference [37]

The polarisation dependence of the optical response of gold nanorods can be extended to the macroscale. A nanorod film may be prepared by dispersing a nanorod colloid in a poly-vinyl alcohol (PVA) matrix and dehydrating the mixture.[37, 38] Upon stretching the film the nanorods align with the stretch direction, Figure 1-8b. By imaging (Figure 1-8c) or measuring (Figure 1-8d) the absorbance properties of these films with polarised light, it can be seen that the PVA-nanorod matrix displays polarisation-dependent optical properties.

It is known that particle plasmons can couple strongly for identical adjacent nanoparticles separated by less than their diameter. Coupling effects depend on the size, geometry and orientation of adjacent particles.[39] Calculations show that for axial[39-42](end-to-end) and lateral[39-41] (side-to-side) orientations of nanorods of equal aspect ratio a red and blue shift of the particle plasmon will be observed, respectively. In the latter case the intensity of the longitudinal peak is also attenuated.[40] The coupling effects of both arrangements can be closely approximated by the net structure approaching that of a single nanorod of double the original aspect ratio in the axial case or half the original aspect ratio in the lateral case. The origin of the resonances in adjacent nanorods has been discussed using plasmon hybridisation theory (see following discussion for gold nanoshells) with the effects of direct contact, various spacing's and relative angles having been considered.[43]

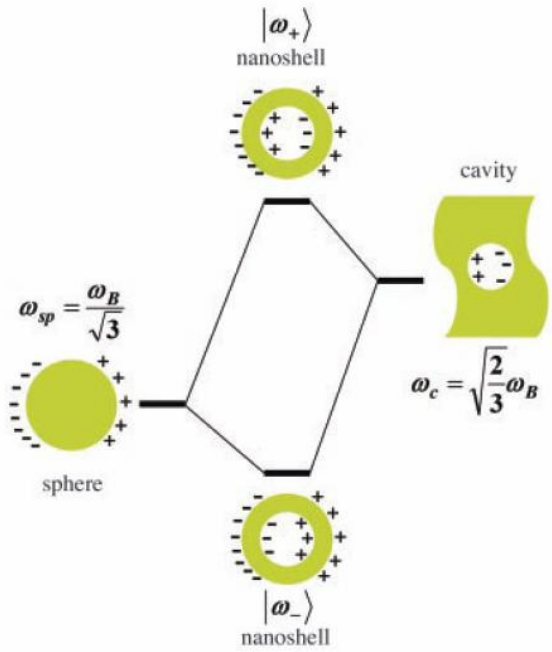

Figure 1-9 Hybridisation model for dipolar resonance modes of a metal nanoshell

Image reproduced from reference [46]

Gold nanoshells have an optical response that is also the result of a geometric restriction. There are two dipolar modes which are attributed to the coupling of resonance modes at the outer surface (interface between metal and surrounding

medium) and the inner surface (interface between metal and inner dielectric core) .[44, 45] The hybridised modes that result from the coupling have been described in an analogous manner to molecular orbital theory where the overlap of orbitals results in bonding and anti-bonding orbitals, termed symmetric and anti-symmetric modes respectively for metal nanoshells.[46] Figure 1-9 shows a diagram of the plasmon hybridisation model for the dipolar resonance modes of a metal nanoshell.[46] In Figure 1-9 ω_B corresponds to the plasma frequency (~ 8.55 eV for gold)[47, 48] in Equation 1.2, ω_{sp} and ω_c are the resonance frequency of the surface and cavity respectively.

Coupling efficiency of the inner and outer modes depends on the proximity of the surface and cavity, i.e. shell thickness.

As the nanoshell gets thinner i.e. $\text{aspect ratio} = \frac{r_i}{r_o} \rightarrow 1$ (where r_i is the inner radius and r_o is the outer radius) the resonance frequency of the symmetric mode red-shifts to lower energies/longer wavelengths.[49] This is a desired property of nanoshells, as synthesising nanoshells of varying thickness allows control of the optical response and hence broader application. The resonance frequency of the anti-symmetric mode is virtually fixed and is positioned near the bulk plasma frequency. As the position of the anti-symmetric resonance frequency is well outside the range of frequencies for which the most useful applications of nanoshells it will no longer be mentioned.

Figure 1-10a shows typical extinction spectra for large gold nanoshells. The dominant peak in each trace of the plot corresponds to the dipolar symmetric resonance mode and the shoulder peak corresponds to a higher order mode which is a result of the large size of the nanoshell.[50] Figure 1-10b shows typical extinction spectra for small nanoshells (within the quasistatic limit), specifically $Au_2S - Au$ (core – shell) nanoparticles.[51] Despite an improved absorption contribution, the tuneability of gold nanoshells in the quasistatic limit is greatly reduced due to a greater range of aspect ratios having dimensions less than the mean free path.[52] This qualification is important as during the synthesis a distinct population of solid nanospheres is also present in the dispersion (evidenced by the ~520 nm peak) (see Section 1.4.1). The resonance peaks at longer wavelengths (lower energies) correspond to the nanoshells in the dispersion.[51]

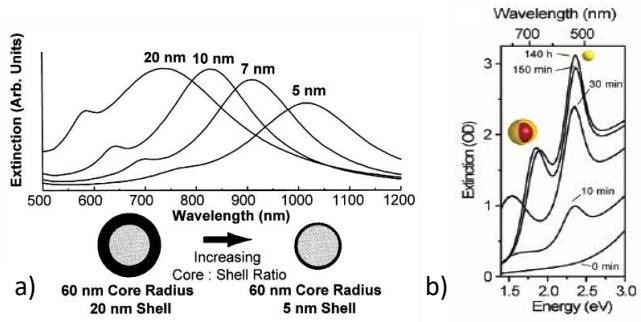

Figure 1-10 Typical spectra of a) large and b) small nanoshells

a) Image reproduced from reference [50]
b) Image reproduced from reference [51]

If the nanoshell thickness is decreased less than the mean free path of the electrons this will have the effect of broadening and attenuating the absorption peak.[17, 53, 54] This effect can be countered by increasing the total volume of the particle but this in turn has the effect of increasing the scattering component of the extinction as the nanoshell dimensions approach those of the wavelength of incident light.

Due to the core-shell structure the resonance position may be altered by varying either inner medium, outer medium or both.[44] However, the peak position is more sensitive to the outer medium[44, 55] as the symmetric mode frequency is primarily composed of the outer surface mode.[44]

For a spherically symmetric nanoshell, the optical response is independent of the polarisation of incident light.

Coupling effects in adjacent nanoshells have been determined, where strong red-shifts are observed for nanoshells in close contact.[56]

As with nanorods, when anisotropy is introduced to convert the nanoshells to nanocap or semishell particles,[57, 58] then a sensitivity to the polarization of the light occurs.

To directly compare the relative optical performance of gold nanorods and nanoshells it is important to fix the volume of metal in each as well as to restrict the dimensions of calculated targets to experimentally achievable ranges. With both considered it is generally accepted that in an ideal situation the optical response of gold nanorods gives a higher extinction cross-section with a lower scattering contribution.[17, 18] As noted by Cortie *et al*. the ideal situation is that the longitudinal resonance of the nanorod is being excited, as in a randomly oriented system the nanoshells may otherwise actually provide a stronger response per unit of gold used.[17]

1.2.3 Modelling Optical Response of User Defined Targets

Exact solutions to Maxwell's equations for the extinction cross-section of spherical and ellipsoidal gold nanoparticles have been determined by Mie[59] and Gans,[60] respectively. Gans' contribution was an extension of Mie's theory to include ellipsoids/spheroids. Aden & Kerker introduced an extension of the Mie theory for nanoshells[61]. Although ellipsoids give a good indication of the effects of anisotropy on the extinction properties of rod-like nanoparticles, to model the optical response of gold nanorods a true representation of the particle geometry is required as aspects such as the particle fine structure (e.g. end-cap geometry) have a pronounced effect on the resonance conditions.[62, 63] However, producing a more accurate geometric model for the nanoparticle results in a significant increase in the complexity which prevents an exact solution being found to Maxwell's equations. This pronounced variance calls for a method in which an optical response can be estimated for any desired geometry. A method that satisfies this requirement is the discrete dipole approximation (DDA).

The DDA is the discretisation of a target geometry by interacting dipoles, on a regular lattice and polarisable by incident EM radiation. The polarisability of each dipole is related to the Clausius-Mossotti (CM) polarisability:

$$\alpha_i(\omega) = \frac{3d^3}{4\pi}\left(\frac{\varepsilon_i(\omega) - 1}{\varepsilon_i(\omega) + 2}\right) \quad 1.12$$

With $\varepsilon_i(\omega)$ the frequency dependent complex dielectric function of each dipole and the lattice spacing of each dipole, $d = \left(\frac{V}{N}\right)^{\frac{1}{3}}$ where V is the total volume of the target and N is the number of dipoles.

Draine & Flatau have implemented DDA in an open source code known as DDSCAT.[64, 65] A correction to the DDA, known as the lattice dispersion relation (LDR), has been applied in order to extend the applicability of the CM polarisability to large particle sizes.[66]

The polarisation of each dipole $(i = 1, 2, 3, \ldots\ldots, \mathrm{N})$ is dependent on the polarisability, α_i, and electric field, E_i:

$$P_i = \alpha_i E_i \quad 1.13$$

Where E_i is due to the dipole's interaction with the incident EM wave, $E_{inc,i} = E_0 e^{i(k \cdot x - \omega t)}$, and the contribution from the other $N - 1$ dipoles:[64]

$$E_i = E_{inc,i} - \sum_{j \neq i} A_{ij} P_j \quad 1.14$$

$-A_{ij}P_j$ is the electric field contribution experienced at $\mathrm{x_i}$ that is due to the dipole polarisation, P_j, that is located at position $\mathrm{x_j}$, which includes retardation effects. The evaluation of the matrix element A is achieved by a combination of the iterative complex-conjugate gradient method (CCG) and fast, Fourier transform (FFT), which in most cases reduces computing time.[64] This iterative process allows for the definition of an acceptable tolerance value at which to terminate the calculations. The process is however very computation intensive.

Once the polarisation of each dipole is determined the extinction and absorption cross-sections may be determined by the following:

$$C_{ext} = \frac{4\pi k}{|E_0|^2} \sum_{i=1}^{N} Im\left(E_{inc,i}^* \cdot P_i\right) \quad 1.15$$

$$C_{abs} = \frac{4\pi k}{|E_0|^2} \sum_{i=1}^{N} \left\{ Im\left[P_i \cdot \left(\alpha_i^{-1}\right)^* P_i^*\right] - \frac{2}{3} k^3 |P_i|^2 \right\} \quad 1.16$$

E_0 is the amplitude of the incident EM wave and $k = \frac{\omega}{c}$. The scattering cross-section can be determined by rearranging Equation 1.7.

DDSCAT includes extinction, absorption and scattering efficiencies as part of the calculation output, e.g.:

$$Q_{ext} = \frac{C_{ext}}{A_{eff}} \quad 1.17$$

A_{eff} is the effective cross-sectional area of the target. This is calculated by converting the volume of the target to an equivalent sphere i.e. a sphere of equal volume to the target $\left(V = V_{eff} = \frac{4\pi}{3} r_{eff}^3\right)$, and using the radius of the sphere to evaluate the cross-section, $A_{eff} = \pi r_{eff}^2$. As discussed previously (Section 1.2.1) this efficiency rating conveys less physical information and so Q_{ext} should be adjusted to be with respect to volume. This is especially important for anisotropic geometries as the effective sphere does not necessarily have the same cross-sectional area as the target.

For analogous geometrical targets (e.g. sphere) DDSCAT gives results within a small error of Mie theory.[64, 67] This is used as second-hand validation of the method for geometries where the exact solution is too complex.

DDSCAT requires the input of a dielectric function or table to calculate the optical properties of the defined target. Greater accuracy is achieved if experimentally determined values are used because functions such as the Drude model (including any modifications) do not account for much of the fine structure of the dielectric function e.g. Figure 1-6. Choosing which dielectric data to use is quite contentious as there are numerous sources which do not necessarily correlate perfectly with respect to each other e.g. gold.[31, 32] There is also the issue of whether electron scattering should be taken into account or not. However, because the mean free path of an electron is less than the length of most gold nanorods, and because the effect of taking the scattering into account in the transverse direction of the rod is only to attenuate the relatively unimportant transverse resonance, this is very rarely done for nanorod calculations.

DDSCAT has been used to provide an empirical formula for gold nanorods in water correlating the aspect ratio (AR) with the longitudinal resonance peak (λ_{max}) :[68]

$$\lambda_{max} = 96AR + 418 \quad 1.18$$

From the calculated spectrum of the desired target it is possible to simulate the colour of either a dispersion or large array of the nanoparticles using the CIE $L^*a^*b^*$ coordinate system.[62, 69] L^* refers to the luminance of the colour, a^* is the green-red character and b^* is represents blue – yellow.[62] CIE $L^*a^*b^*$ was developed to approximate human vision a and so is a useful system to calculate colours. Standard tables have been prepared to convert spectra into CIE $L^*a^*b^*$ coordinates.[70]

1.3 Gold Nanorod Syntheses

Gold nanorods are typically synthesised by relatively complex processes, in which numerous factors affect the morphology of the product. There are four primary strategies in the literature to produce gold nanorods. One is non-chemical in nature and relies upon the physical evaporation of gold and its deposition into a template. The other common methods are chemical and they are differentiated by the method for converting ionic gold to metallic gold (listed in order of prevalence):

1) Wet chemistry
2) Photochemistry
3) Electrochemistry

Despite this distinction, however, there are multiple crossover points such that an innovation in each respective method has at some point advanced at least one of the other methods.

1.3.1 The Development of Gold Nanorod Syntheses

The primary method of nanorod synthesis in the current literature is the seed-mediated, Ag^+ – assisted, wet chemical synthesis pioneered by Jana *et al*.[13] This synthesis uses a growth solution of tetrachloro-auric acid, $HAuCl_4$, hexadecyl-trimethylammonium bromide, $C_{16}TABr$, ascorbic acid and silver nitrate (in most cases). The growth of the gold nanorods is initiated by adding a small amount of spherical gold nanoparticle seeds. It has also become possible in recent years to purchase gold nanorods made by these means, for example from Nanopartz Inc.[f]

Autocatalytic[g] seed-mediated growth of gold nanoparticles has been utilised since as early as 1906 where Richard Zsigmondy used the overgrowth of pre-synthesised particles to determine their concentration, by growing them until visible with an optical microscope.[9, 10]

In 1989 Wiesner and Wokaun varied the seed particle to gold salt ($HAuCl_4$) ratio to achieve varying degrees of anisometry in gold nanoparticles and discussed their resulting optical properties with respect to the geometry of particles present.[9] However, very few nanorods were produced.

[f] http://www.nanopartz.com/
[g] Autocatalysis refers to a reaction where a product of the reaction is also the catalyst.

The first monodisperse sample of gold nanorods was produced by an electrochemical method. By using a nanoporous alumina template, that may also be prepared by an electrochemical method,[71] gold can be deposited within the pores with the dimensions determined by the width of the pores and the deposition time.[72] This method also had the advantage that the nanorods were produced in a thin film in a regular array. The conductive substrate used to electro-deposit must be removed to isolate the optical properties of a single nanorod or ensemble effect of single nanorods.[73]

To produce an aqueous dispersion of gold nanorods from this method it is necessary to dissolve the template, coat the nanorods with a stabiliser, and then dissolve the sacrificial working electrode to disconnect the gold nanorods from the substrate.[74]

A major drawback to the electrochemical template method is the two-dimensional limit of the zone in which to grow the nanorods. This is highlighted by the fact that from an area of $\sim 200\ \mathrm{mm}^2$ the synthesis needs to be repeated 5 – 10 times to obtain 1 mL of solution with sufficient optical density.[74]

An important development for solution-based syntheses was the introduction of a long-chain, cationic surfactant hexadecyltrimethylammonium chloride $(\mathrm{C_{16}TACl})$, coupled with photochemical reduction of $(\mathrm{HAuCl_4})$ this introduced a distinct population of long gold nanowires (although the primary nanoparticle geometry was still spherical particles).[75] Previous photochemical methods only produced spheres.[76] In previous work by these authors, the formation of an insoluble complex between $\mathrm{AuCl_4^-} - \mathrm{C_{16}TA^+}$ was noted.[77] The insolubility is counteracted by increasing the concentration of free surfactant which results in the dispersion of the complex throughout the solution in the surfactant micelles. It was suggested that for the growth of nanowires the surfactant micelles acted as a soft template as for a high concentration of surfactant the micelles have a rod-like geometry. It is now known for syntheses that use $\mathrm{C_{16}TABr}$ that the complex is of the form $\mathrm{AuBr_4^-} - \mathrm{C_{16}TA^+}$, even if the initial gold salt is $\mathrm{HAuCl_4}$.[78-80]

One of the most important additives for the synthesis of low aspect ratio nanorods (AR 2 – 10) is ionic silver, $\mathrm{Ag^+}$. This was first introduced in the electrochemical synthesis of gold nanorods by Yu et al,[81] although not originally reported.[82] The introduction of silver was crucial for increasing the yield of nanorods to above 90%. Another important constituent used by Yu *et al*. was $\mathrm{C_{16}TABr}$ (Figure 1-11).

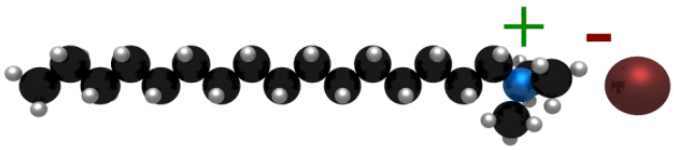

Figure 1-11 Structural representation of $C_{16}TABr$

Again emphasis was drawn to the presence of the high concentration of surfactant in the solution as well as the use of agents known to elongate the $\mathrm{C_{16}TABr}$ micelles, a co-surfactant, tetraoctylammonium bromide $\mathrm{TC_8ABr}$, and acetone as a facilitator to the co-

surfactant.[81] A similar co-surfactant ($TC_{12}ABr$) was later shown to provide no advantage in the photochemical synthesis.[83]

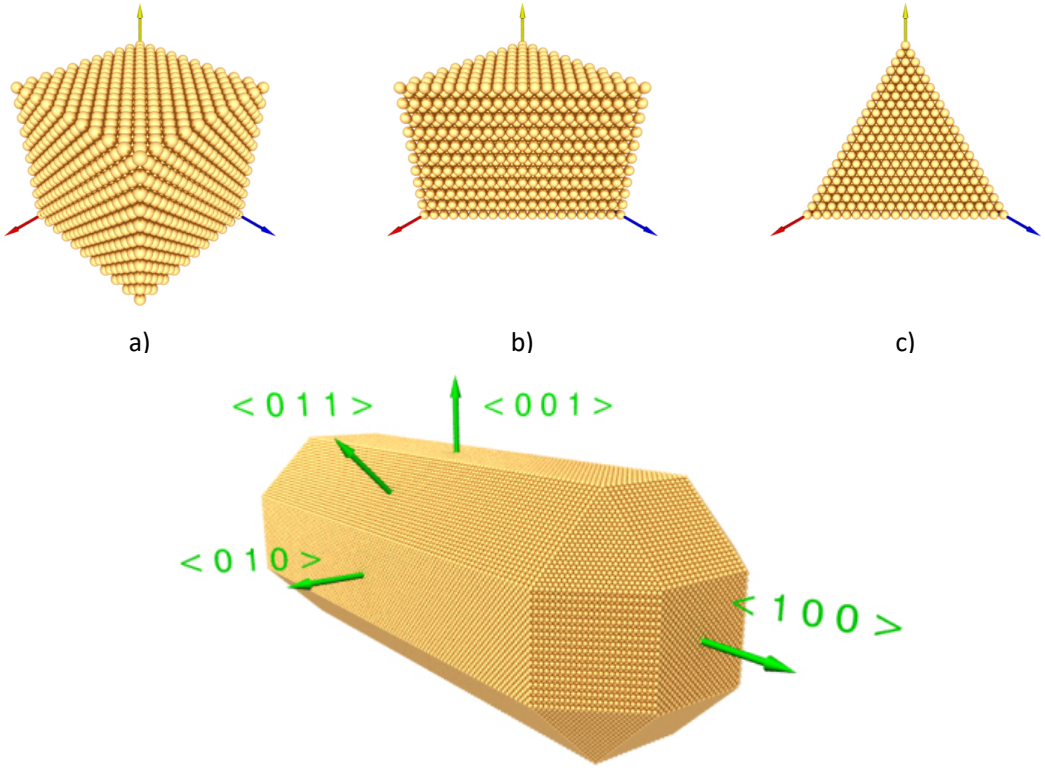

Figure 1-12 Face-centred cubic crystal bounded by the planes with normal vectors a) < 1 0 0 >, b) < 1 1 0 > and c) < 1 1 1 >. d) Previously proposed crystallographic structure of a single crystal gold nanorod.

Structural characteristics were subject to early investigation as determining the crystallography of the particles could provide insight into how anisotropy was achieved. High resolution TEM (transmission electron microscope) images indicated that the electrochemically produced nanorods were single crystals and expressed primarily the FCC (Face Centred Cubic) <100> and <110> crystal faces[84, 85] (Figure 1-12a and b respectively). The growth direction of the nanorods was along the <100> plane (Figure 1-12d). These parameters were also suggested for the nanorods synthesized by wet chemistry after the introduction of the $C_{16}TABr$ stabilised seed particles.[25] It was also reported that the <110> surfaces underwent partial reconstruction to introduce notches of the most stable FCC face, <111>. This would reduce the net surface energy of the <110> face.[86]

From this determination of the crystal structure it was suggested that the surfactant expressed a preferential attraction to the <110> facet and provided extra stability during and after growth.[86]

In a recent publication by the group of Liz-Marzán the structure for gold nanorods synthesised by the seed-mediated, silver-assisted method has been redefined.[87] It is now suggested that the flanks of the nanorod are dominated by {250} type facets, Figure 1-13.

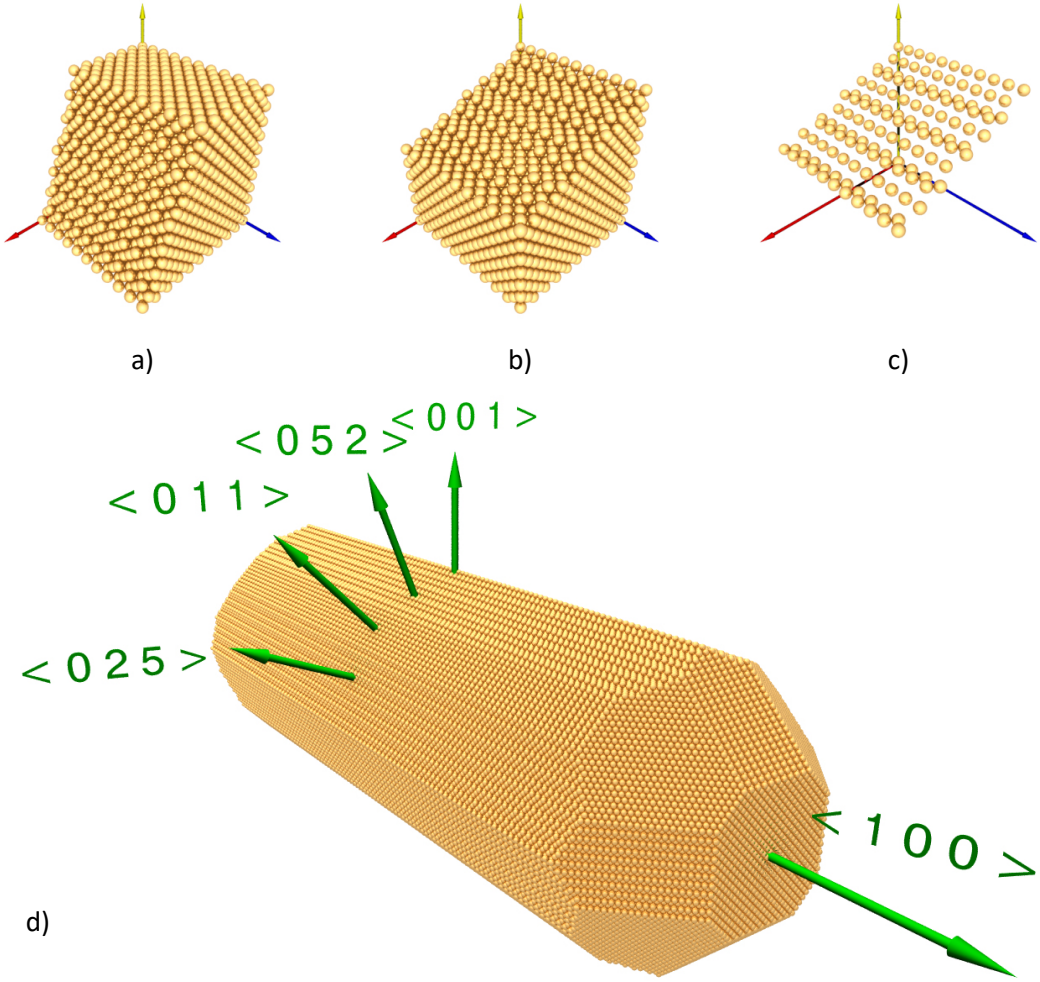

Figure 1-13 Face-centred cubic crystal (10 x 10 unit cells) bounded by the planes with normal vectors a) < 0 2 5 >, b) < 0 5 2 > where c) illustrates the surface atoms of b). d) Currently proposed crystallographic structure of a single crystal gold nanorod.

The cross-section of the nanorod in Figure 1-12 is octagonal (regular), which was deduced from dark-field TEM line profiles.[85] For the redefinition of the nanorod structure Liz-Marzán *et al*. assembled the nanorods so that their longitudinal axis was perpendicular to the substrate. This was achieved through the use of gemini surfactant[h] which they also used in place of $C_{16}TABr$ in the synthesis.[88] This assembly allowed visualisation of the cross-section of the rods and by measuring the angles between the

[h] A gemini surfactant has more than one hydrophobic tail and hydrophilic headgroup. The surfactant used in this work has two C_{12} hydrophobic sections with two dimethylammonium headgroups the two sections are linked by an ethylene oxide group in the equivalent position of the headgroup for the third methyl group of a trimethylammonium headgroup.

side facets in comparison with diffraction measurements the new structure was determined. The cross-section of the new structure, Figure 1-13d, is an irregular dodecagon where the flanks are dominated by the {250} facets. The point of intersection of the {250} facets is in the <011> direction, with respect to Figure 1-13d.

Nanorods prepared without the aid of Ag^+ have a pentafold twin structure but also have <110> crystal faces along their flanks, although they are terminated by five <111> faces.[89] This partial correlation gives support to the hypothesis that the growth mechanism relies upon the preferential binding of $C_{16}TABr$. The propagation of the twins is a likely contributor for the silver-less synthesis. Gold nanorods grown by the silver-less method and with the seeds tethered to a substrate have been shown to grow uni- or bi-directionally.[90]

In the work leading to the earliest form of the current wet chemistry synthesis, the use of Ag^+ in the overgrowth of seed particles was shown to reduce the production of nanorods.[11] However, it was highlighted that the counter-ion to the CTA^+ surfactant was Cl^- and not Br^-, an early indication of this crucial factor. Within this work the ascorbic acid was shown to be too weak to reduce $Au^{3+} \rightarrow Au^0$ and it was also noted that the reaction is autocatalytic.[12] The presence of nanorods/wires throughout some of these samples led to the implementation of the yield-enhancing factors from the electrochemical process, i.e. $C_{16}TABr$ and $AgNO_3$, resulting in much higher yields.[13, 91] The requirement for a high concentration of $C_{16}TABr$ was also emphasised, although it is possible to produce nanorods in a low concentration of $C_{16}TABr$ but in that case the concentration difference must be compensated for by additions of $NaBr$.[92] However, these nanoparticles are crystallographically different to the nanorods produced in the typical synthesis implying a change in growth process. Different aspect ratios were achieved by varying the amount of seed solution added to the growth solution and therefore the number of seed particles to gold salt ratio. For the syntheses that used Ag^+ it was noted that the reduction of gold metal was slower than without silver.[13]

The mechanism of involvement of Ag^+ was hypothesised to be adsorption of $AgBr$ at the gold surface to restrict growth, as ascorbic acid is too weak to reduce $Ag^+ \rightarrow Ag^0$,[13] although small gold clusters can be present in growth solution conditions prior to seeding.[93] The presence of $AgBr$ at the surface was shown to be possible from the surface enhanced Raman spectroscopy of gold nanorods,[94] though not originally stated.[21] It was noted that the Raman shifts for $AgBr$ and $AuBr$ overlap so no definitive assignment was possible.

The seed particles used in this early synthesis were tri-sodium citrate stabilised gold nanoparticles, although borohydride was used as the reductant resulting in a smaller particle size $(\sim 1.5 - 4\ nm)$[13, 25] than for typical citrate reduced particles. Despite using the same yield enhancing agents as the electrochemical method the geometry of the particles were not quite the same ("spheroidal and rod-like").[13]

Thermogravimetric analysis (TGA) of electrochemically produced nanorods (in the presence of $C_{16}TABr$) revealed that the surfactants were bound to the gold surface as a bilayer. FTIR (Fourier transform infrared spectroscopy) determined that the inner layer was oriented such that the polar head group was bound to the surface, and by deduction the outer layer with the head group facing outward.[95] The presence of the bilayer was used as support for a "zipping mechanism" proposed by Gao *et al*. in reference to the formation of high aspect ratio nanorods produced by silver-less synthesis. They showed that by decreasing the length, and therefore micellar (bilayer) stability, of the surfactant the yield of nanorods was also decreased.[96]

Following this success in improvement of the wet chemistry method Kim *et al*. introduced Ag^+ and $C_{16}TABr$ into the photochemical synthesis,[23] where increasing the concentration of Ag^+ also increased the aspect ratio. Similar improvements in the nanorod yield were observed, and the same crystal structure and growth direction were produced as for the non-photochemical method. Additional work into the mechanism of involvement of Ag^+ was also undertaken. In the absence of $AuCl_4^-$, $AgBr$ in the system was photochemically reduced to silver nanoparticles. When $AuCl_4^-$ was reintroduced to the solution the nanoparticles were readily oxidised to $AgBr$. It was also noted that when silver nanoparticles were pre-synthesised and added to the reaction mixture a similar gold nanorod product was achieved, with the same crystal structure. Due to the role of silver made apparent by this investigation emphasis was drawn to the silver (or $AgBr$) as the shape-determining factor. A controlled aggregation of gold clusters was suggested as the formation mechanism. A similar modification to the photochemical synthesis was made by Niidome *et al*. where they added ascorbic acid as well as Ag^+, which had the effect of increasing the rate of the reaction.[83] In this work samples taken at various times throughout the reaction were imaged with TEM showing intermediate particle geometries with flared ends.

The next aspect of the wet chemistry method to be improved was the gold nanoparticle seed. Instead of using the standard citrate-stabilised gold nanoparticles, Nikoobakht and El–Sayed used particles prepared by borohydride reduction but in the presence of $C_{16}TABr$.[21] Ag^+ concentration was also varied to control the aspect ratio. $C_{16}TABr$ – stabilised borohydride-produced seeds are $\sim 1-2$ nm[25] diameter. As mentioned above, this innovation produced nanorods of the same crystallographic structure as those produced by the electrochemical method.[25] This is likely due to the $C_{16}TABr$ – stabilised seed being single crystal and the citrate seeds having a five-fold twin.[25] It should be noted, however, that it has been shown that a single-crystal gold nanoparticle, ~ 2 nm in diameter, can undergo a transition to a twinned particle and back again under electron beam irradiation.[97]

Nikoobakht and El–Sayed also introduced hexadecyl-benzyldimethyl-ammonium chloride (BDAC) as a co-surfactant to $C_{16}TABr$.[21] This allowed the synthesis of nanorods with aspect ratios from 6 to 10 by adding further growth solution to the synthesised nanorods. It also reduced the average diameter of the rods from 12 nm to 6 nm.

Sau and Murphy investigated the effect of varying various constituents of the wet chemical gold nanorod synthesis.[22, 98] By holding all of the growth solution components constant and increasing the amount of seed solution added they determined that the aspect ratio also increased.[22] This was despite the length decreasing and was due to the fact the width decreased by a relatively greater amount. Increasing the concentration of ascorbic acid generally led to different nanoparticle geometries.[98] However, most of these samples were made with a large excess of ascorbic acid or decrease in $C_{16}TABr$ so the effect of small fluctuations was unconfirmed. In the photochemical method the effect of increasing the ascorbic acid concentration gradually (while holding other factors constant) was to initially red-shift the longitudinal peak.[20] After a threshold concentration was reached the longitudinal peak then blue-shifted. The primary effect on the nanorod product is the change in length, where the increase in ascorbic acid initially increases the length (and width), with a further increase the length decreases but width remains about the same.

In 2004, Pérez-Juste *et al*. introduced the 'electric-field-directed' mechanism for the growth of nanorods.[26] They pointed out that the points of highest curvature of a nanoparticle also have the greatest electric-field. This means that once a symmetry breaking event occurs for the spherical nanoparticle seed then the electric field contribution to the growth is self-catalysing as a higher aspect ratio nanorod has an even higher degree of curvature. Along with this new mechanism this specific paper is dedicated to optimising the silver-less synthesis, where re-confirmation of the detrimental effect of most co-surfactants, surfactant chain length, counter-ions and various seed-types are presented. Despite these parameters resulting in failure it is possible to replace $C_{16}TABr$ with $C_{16}TEABr$ (hexadecyl-triethylammonium bromide) which results in the slight elongation of the rods probably due to the increase in size of the head group destabilising the bilayer slightly.[99] In work that led to the redefinition of the crystal structure of gold nanorods mentioned earlier, Guerrero-Martínez *et al*. reported that using a gemini surfactant, two $C_{12}TABr$ molecules linked by an ethylene oxide between headgroups, resulted in a narrower distribution of aspect ratios produced by the synthesis i.e. longitudinal peak width decrease.[88] The $AuBr_2^- - C_{16}TA^+$complex[i] was also qualitatively shown to have a high-affinity for the $C_{16}TABr$ micelles. A mechanism for the reduction of $AuBr_2^- - C_{16}TA^+$ to Au^0 with respect to the gold nanorod synthesis was also discussed. There are two possible pathways for the conversion of $AuBr_2^- - C_{16}TA^+$ to Au^0:

$$3AuBr_2^- \rightleftharpoons AuBr_4^- + 2Au^0 + 2Br^- \qquad 1.19$$

or

$$AuBr_2^- + e^- \rightleftharpoons Au^0 + 2Br^- \qquad 1.20$$

[i] The gold – surfactant complex was reported as $AuCl_2^- - C_{16}TA^+$ but due to current knowledge this has been changed here to $AuBr_2^- - C_{16}TA^+$

Equation 1.19 is known as a disproportionation reaction where the reactant is both oxidised and reduced. $AuCl_2^-$ [100] and $AuBr_2^-$ [101] species have both been shown to undergo disproportionation reactions according to Equation 1.19. Also, this reaction is catalysed by a metallic gold surface such as a gold foil or perhaps a gold nanoparticle seed. The new atoms on the surface of the gold nanoparticle may provide a significant enough symmetry-breaking event for the postulated electric field growth mechanism to begin. Growth is unlikely to occur symmetrically due to the $C_{16}TABr$ layer. In the presence of a gold surface it is suggested that the disproportionation occurs exclusively at the solution/solid interface.[101]

However, for the nanorod synthesis Pérez-Juste *et al*. supported the mechanism in Equation 1.20, where $AuBr_2^-$ is reduced by electron transfer at the electron-rich seed surface. This was due to their previous work which indicated that Au^{3+} in the form $AuBr_4^- - C_{16}TA^+$ can oxidise metallic gold nanospheres and nanorods and thus would not allow the formation of nanorods.[26, 36] There has been recent support for this mechanism where the synthesis of a gold – ascorbic acid complex has provided a pathway for the reaction in Equation 1.20.[102] The Au^+ complex is said to undergo a one electron process to form Au^0 and an ascorbate radical that disproportionates to produce dehydroascorbic and ascorbic acid. This mechanism is further elaborated upon in Chapter 3. The disproportionation reaction in Equation 1.19 is still possible, however, as there is always the presence of excess ascorbic acid in the growth solution, usually $1.1 \leq Au^{3+}: \text{ascorbic acid} \leq 1.5$.[21, 22, 27] This excess ascorbic acid could consume the $AuBr_4^-$ formed by the disproportionation and thus drive the reaction forward. Despite this excess in reducing agent there is typically a significant proportion of unreacted gold left after the primary reaction.[27] This can lead to ageing effects where the nanorods will gradually fatten with time (hours, days, etc.).[103] Addition of excess ascorbic acid to the growth solution after the initial formation of gold nanorods usually results in different geometries, such as dog-bones, due to the presence of unreacted gold.[104-106] However, if the ascorbic acid is added slowly then the nanorod geometry is preserved.[107] An additional pathway to the consumption of the unreacted gold is to heat the solution which also results in the formation of dog-bone particles.[104] The heating-induced reduction is most likely due to the oxidation and subsequent hydrolysis products of ascorbic acid, dehydroascorbic acid and 2,3 – diketo – 1 – gulonic acid respectively. Both of these species have mild reducing abilities due to the presence of $-OH$ groups.[104]

In 2005, Liu and Guyot-Sionnest proposed a mechanism where Ag^+ may be reduced to Ag^0 preferentially on the <110> surface of gold nanoparticles.[25] It was noted early on that ascorbic acid is too weak a reducing agent to reduce Ag^+ in the nanorod growth solution.[13] However, as noted by Liu and Guyot-Sionnest, this is only necessarily applicable to bulk properties. From this observation they proposed that Ag^+ may be reduced by ascorbic acid at the surface of the gold nanoparticles in the growth solution as mono- or sub-monolayers by underpotential deposition (UPD). This mechanism will only work if the work function of the metal to be reduced is lower than that of the substrate; silver has a work function ~ 0.5 eV lower than gold.[25] Additionally, the

magnitude of the UPD shift generally increases with the decrease in stability of the crystal surface i.e. <111> < <100> < <110>. With respect to the new structure determined by Liz-Marzán *et al*., the possibility of the underpotential deposition of Ag^0 is expected to be aided by the dominant presence of higher index {250} type facets.[87] For gold nanorods this provides a mechanism in which the Ag^+ assists the development of the geometry by restricting the growth in the <250> and <520> crystal directions for a longitudinal growth direction of <001>. The presence of Ag^0 also supplies a reason why the diameter of the nanorods increases (aspect ratio decreases, longitudinal resonance peak blue shifts) as metallic silver will be replaced by ionic gold via galvanic replacement.[108, 109]

From a method previously formulated for the overgrowth of nanospheres[110] Jana introduced a mixture of strong (borohydride) and weak (ascorbic acid) reducing agents to streamline the synthesis of nanorods by removing the need for pre-synthesised seed solution.[19] The ratio of these two reductants is important as the strong reducing agent is only required to reduce a very small fraction of the gold in the growth solution, equivalent to the amount in the previously added seed solution. The emphasis on micellar involvement in the formation mechanism was again stressed. Zijlstra *et al*. used this pseudo-seeded method to prepare nanorods at temperatures up to $97℃$, where, although the aspect ratio is decreased, the reaction is complete in ~ 10 seconds.[111]

The vast majority of gold nanorod syntheses are batch processes. However, Boleininger *et al.* introduced an automated continuous flow synthesis that has live monitoring of the optical properties of the product solution.[112] This allows for in situ adjustment of the feed rates of the growth and seed solutions to achieve a target product and maintain those conditions automatically.

As mentioned previously, the species at the surface of the gold nanorods was potentially $AgBr$. This has since been confirmed by various methods such as $SALDI-MS$[113] (surface-assisted laser desorption/ionisation time-of-flight mass spectrometry), ^1H-NMR and XPS[24] (nuclear magnetic resonance spectroscopy and X-ray photoelectron spectroscopy respectively). In the work for the latter example the classification of the surface species was extended to a $AgBr$ and $C_{16}TABr$ complex, $C_{16}TASBr$.[24] This was supported by the use of the pre-synthesised complex in place of Ag^+ (using an equal silver content) in the gold nanorod synthesis. The nanorod product was identical to the conventional synthesis. This does not, however, prove that the UPD of silver does not occur at some point during the reaction.

Jiang *et al*. raised concerns over the gold nanorod synthesis as they presented results showing poor reproducibility for identical synthesis conditions.[114] This highlights the hypersensitivity of the reaction and requirement for tight control over the reaction parameters. It was also noted in a later publication that the age of the seed particle solution used to initiate the reaction plays an important role in the nanorod product.[115]

A major problem for the synthesis of gold nanorods was highlighted by Smith and Korgel in that the gold nanorod product was highly dependent on the supplier from which the $C_{16}TABr$ surfactant was obtained.[116] This was soon after assigned to the presence of trace impurities of iodide by Smith *et al*.[117] The iodide concentration in different batches and different suppliers of $C_{16}TABr$ can vary significantly.[117, 118] When used in conjunction with the silver-less synthesis the iodide impurities also give varied products but do not prevent nanorod formation.[119]

1.3.2 Kinetics of gold nanorod syntheses

Kinetic observations of the developing optical properties of growing nanorods have been reported since the earliest syntheses of these nanoparticles.[22] It was observed that the longitudinal plasmon peak first rapidly red-shifts which is then followed by a blue-shift. The red-shift coincides with the longitudinal axis growing very rapidly and reaching a maximum, with the following blue-shift a result of the diameter increasing.[22] TEM images were taken at various stages in the process but no discussion of the images or comment as to how the samples were prepared for imaging was made.[22]

In an attempt to prevent the ageing phenomenon (in which the end of the gold nanorods thicken) Zweifel and Wei added sodium sulphide, Na_2S to halt the growth reaction.[103] This successfully significantly reduced the ageing effect of gold nanorods by reacting sulphide with the unreacted gold in solution and stabilising the surface of the nanorods. They also added the sulphide solution to the nanorods during the growth process to probe the particle geometry at various stages. It was concluded that at times less than 15 minutes the nanorods underwent a very rapid growth in the longitudinal axis and for greater than 30 minutes a gradual development of the width, in between these times both length and width increased. The initial particles had flared ends with flat caps (dog-bone geometry) and the particles after 30 minutes developed straight flanks and rounded caps. No attempt was made to correlate particle dimensions to the optical data.

Gulati *et al*. used an extensive bank of calculated optical data to approximate the dimensions of the nanorods at different times throughout the reaction.[120] This involved approximating the nanorod structure as a prolate spheroid and calculating spectra using Gans' theory. Spectra were calculated for diameters from $3 - 40$ nm and lengths of $20 - 120$ nm, aspect ratios were limited to $1 - 5$. To extract the dimensions of the nanorods the experimentally determined extinction cross-sections and longitudinal resonance positions were compared to the calculated data. The region of intersection of these parameters gave a range of possible correlations and the dimensions were averaged. From the values for the average dimensions at different times they provided growth rates for the length of the nanorods which involved an initial rapid growth rate that decreased with time. The authors noted that an improvement in the results might be achieved if the geometry used for the optical calculations was more accurate.

Alekseeva *et al*. used a spherically-capped cylinder to fit their optical data and used these results to discuss the growth of gold nanorods.[121]

Becker *et al*. used a "fastSPS" (fast single-particle spectroscopy) method to monitor the overgrowth of immobilised gold nanorods.[122] FastSPS allows the simultaneous measurement of multiple nanoparticle scattering spectra. Two methods for determining the particle dimensions are used. First, the correlation to resonance energy and linewidth from a bijective[j] function interpolated from DDA and Mie theory calculations, second the input of resonance position into an empirically determined function for aspect ratio and the scattered light intensity at the maximum which can be expressed in terms of the volume and length parameter. It is noted that the growth is not necessarily directly comparable to that of 'free' nanorods but it is a useful model, and an impressive technique.

A model for the silver-less synthesis has been described by Takenaka and Kitahata,[123] however, assumptions made for this model include 100% yield of nanorods and all seed particles forming rods immediately. Any disagreement with the model is assigned primarily to these assumptions, the first of which is probably most significant for this synthesis. With respect to the photochemical synthesis, Miranda *et al*. have suggested that the growth process (nucleation and growth) of gold nanorods could be in parallel where each growth event is isolated to a micelle.[20] They also reaffirmed the importance of micellar dynamics to the reaction. It is also possible that the number of particles in the solution is dependent on the temperature.[111]

Small-angle X-ray scattering (SAXS) has also been paired with optical data to probe the growth kinetics of gold nanorods.[124, 125] SAXS provides information for the dimensions, geometry and volume fraction of particles within the system. Henkel *et al*. produced time dependent functions for the development of the length and width of the growing gold nanorods.[124] To fit their data they used a cylindrical model to extract data from the SAXS data. Comparison of the particle length determined from SAXS was compared with a function prepared for optical data to determine the aspect ratio using the spherically capped cylinder particle geometry[68] and width values obtained from SAXS. Morita *et al*. modified the SAXS results obtained by Henkel *et al*. by fitting the spherically capped cylinder model and use the same equation for optical determination of aspect ratio.[125] Both publications consider the effects of mixed particle dispersions (i.e. nanorods and spheres). Once again, the assumption is that the number of nanoparticles in the solution is constant.

Finally, an important clue to the formation of gold nanorods was recently published by Hubert *et al*.[126] They reported a bifurcation in the particle dimensions observed in the product of the synthesis for gold nanorods. Nanoparticles were observed with dimensions in between those with a similar size to the seed particles and that of larger

[j] Bijective infers one possible correlation of a resonance position and linewidth pair to a length and width pair.

spheres and nanorods. Above a critical value (~ 5 nm), the nanoparticles were either spherical or nanorod-shaped. The occurrence of this bifurcation suggests that for the nanorod geometry to be achieved the symmetry breaking event must occur when/by the time the seed particle reaches ~ 5 nm in diameter. The presence of nanoparticles of a size similar to that of the seed particles within this final product distribution is a strong indication that not all seed particles actually grew. From the data, a length growth rate:width growth rate ratio of 15 is suggested. The final shape obtained however appears to be limited by the availability of the reactants as the final aspect ratio achieved for this sample was 4.

1.4 Gold Nanoshell Syntheses

Gold nanoshells, like the nanorods, have tuneable optical properties achieved by a simple geometry. Gold nanoshells have enjoyed a relatively high profile existence due to the extensive work by one of the major contributors in the field, the research group of Naomi Halas at Rice University, Houston, Texas, USA. The work by Halas *et al* has ultimately culminated in the commercialisation and current clinical trials for photothermal ablation of tumours by use of gold nanoshells through a company called Nanospectra Biosciences Inc.[k]

The synthesis of gold nanoshell structures is achieved through diverse variations of the two main architectures; core-shell and hollow.

1.4.1 Core – Shell Structures

Core – shell nanoparticles consist of a dielectric core, which is commonly SiO_2,[50, 127-129] polymer[130, 131] or Au_2S [132] and a metallic gold coating or shell (Figure 1-14).

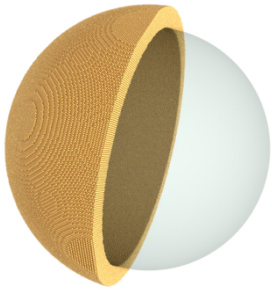

Figure 1-14 Cross-section of a gold nanoshell on a dielectric core

For SiO_2 and polymer core-shell particles the gold coating is grown by functionalising the surface and attaching pre-synthesised gold nanospheres. Additional gold is added, where the bound nanoparticles act as nucleation sites, until a continuous coating is obtained (Figure 1-15). SiO_2 and polymer core particles are limited for practical reasons to minimum diameters of ~ 100 nm. This causes them to exhibit large amounts of

[k] http://www.nanospectra.com/

scattering due to the relatively large volume of gold required to attain a continuous coating.

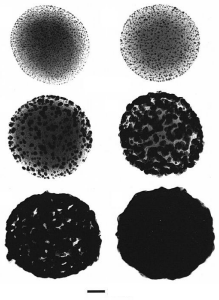

Figure 1-15 Silica – gold (core – shell) nanoshells with increased exposure to growth solution (left to right and top to bottom). Scale bar = 20 nm.

Image reproduced from reference [50]

Originally the $Au_2S - Au$ nanoshell growth conditions were considered to follow a diffusive reduction mechanism where Au_2S is reduced to Au.[132] This was followed by an adjusted two stage growth mechanism, supported by Mie theory calculations. The dielectric core, Au_2S, develops rapidly in the first stage and concurrent growth of spherical gold particles and nanoshell deposition upon the core particles completes the second stage.[133]

Due, however, to the nature of the synthesis for nanoshells, there has been some doubt concerning the source of the observed optical effects. For example, $Au_2S - Au$ syntheses form populations of nanoshells as well as nanospheres, as is evident from representative extinction spectra. This caused some debate as to whether the observed red-shifted peak was due to nanoshells or merely aggregates of nanospheres.[51, 134-136] However, evidence leans more towards nanoshells with two important examples. The first is sourced from characterisation of the growth kinetics of the reaction supported by Mie theory as presented by Averitt *et al*.[133] Within this study the development of two extinction peaks is monitored, one peak is characteristic of spherical gold nanoparticles, the other is attributed (by the authors) to the development of a nanoshell of gold. As a nanoshell thickens the extinction peak blue shifts and narrows for low size distributions. Mie theory was used to support this growth mechanism by calculating the combined extinction spectrum of spherical gold nanoparticles and a gradually thickening nanoshell. This model fits the measured growth kinetics extremely closely. Additional evidence for nanoshell geometry was provided by Raschke *et al*. where single particle spectra were measured by dark-field analysis.[51] This data provides good evidence for nanoshell geometry as the spectrum displayed a narrow linewidth and proved to be polarisation independent. It is unlikely that an aggregate will display spherical symmetry such as that observed in these experiments.

Anisotropic nanoshells termed semi-shells[137, 138] or nanocaps[58, 139] may be synthesised by shielding part of the core (semi-shells) or depositing metal at an oblique angle onto a monolayer of polymer spheres (nanocaps).

1.4.2 Hollow Gold Nanoshells

Hollow gold nanoshells are synthesised by galvanic replacement of a sacrificial metallic template such as silver[108, 140, 141] or cobalt.[142] It is possible to preserve the cobalt template to give bi-functional (optical and magnetic) nanoparticles.[143] The galvanic replacement takes place when $HAuCl_4$ solution is added gradually to a solution of template particles at an elevated temperature (with respect to room temperature). Gold metal is epitaxially deposited on the surface of the template particle, Figure 1-16. The final particle geometry is a hollow gold analogue of the template particle which means that the only limitation to this synthesis is the quality and shape of the template.[108, 141] In the case of silver template particles the resulting nanoshell is an alloy of gold and silver, where upon further addition of gold salt pin-holes will form in the shell and ultimately result in fragmentation.[140] This fragmentation can result in the formation of nanorings.[144] To prevent the formation of pin-holes in the final structure, $AuCl_2^-$ can be used in place of $AuCl_4^-$,[145] Figure 1-16. However, this results in less control over the shell thickness.

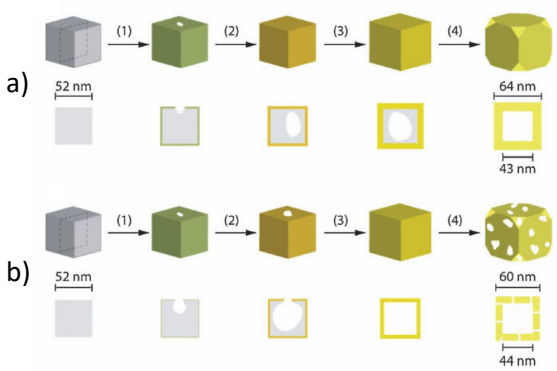

Figure 1-16 Galvanic replacement of silver nanocubes with a) $AuCl_2^-$ and b) $AuCl_4^-$

Image reproduced from reference [145]

1.5 Applications of Gold Nanorods and Nanoshells

1.5.1 Pigments and colorants

The use of gold nanoparticles to colour glass is now very well known.[5, 146] The colour is due to the plasmon resonance peak at about 520 nm, which absorbs the green portion of white light, and to interband transitions at 300 to 400 nm, which absorb the blue. What is left is red light, and this is what we see, Figure 1-1b. If the nanoparticles are big enough to also scatter some of the light (as they are for the famous Roman Lycurgus cup, Figure 1-1)[5] then the colour of the glass in reflection will be greenish (Figure 1-1a), corresponding to photons scattered by the particles by radiation damping of the plasmon resonance.

Gold nanoparticles have also occasionally been used to dye textiles, a practice that dates back to at least 1794[146] but which is occasionally still reported today in respect of silk,[147]

wool and cotton.[148] Reddish to purple colours are obtained. Stronger optical response and a unique range of colours make nanorods and nanoshells a possible choice for inks/colorants.[149]

1.5.2 Spectrally selective coatings

Spectrally selective coatings, as the description suggests, are intended to block or transmit a selected range of the electromagnetic spectrum. For example, coatings on the windows of buildings should ideally transmit the entire visible range but block all remaining wavelengths of the solar spectrum. Figure 1-17 shows the standard AM 1.5 solar spectrum and the photo-optic response of the human-eye (ASTM E971-88). However, regular window glass blocks the majority of the ultraviolet anyway so, predominantly, the role of any coating on it is to attenuate the near-infrared (NIR) and infrared (IR) wavelengths. There are other applications for spectrally selective coatings, such as the dichroic filters used in optics[40] but of course architectural windows represents by far the largest potential market.

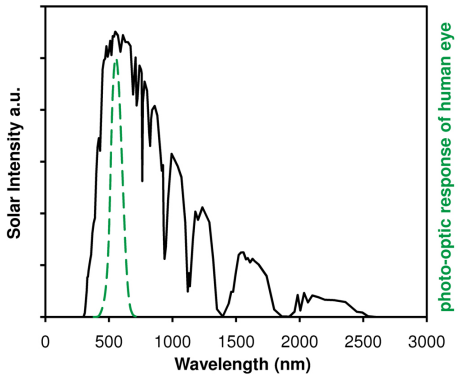

Figure 1-17 ASTM E971-88 standard solar spectrum and photo-optic response of the human eye

Currently, commercial exploitation of precious metals as spectrally selective coatings manifests in the form of continuous thin films. These films are used for their high reflectance of NIR and IR wavelengths, but in the case of Au films they also reflect some of the upper visible, giving them a reddish tinge in reflection and a green-blue colour in transmission. Some other issues with these films include the high cost of the vacuum systems required to produce them, while their high reflectance can cause intolerable quantities of glare in surrounding environments. The coatings are commonly characterised in terms of the ratio of transmitted visible light (weighted for ophthalmic response) to total solar radiation transmitted, a ratio designated as $\frac{T_{vis}}{T_{sol}}$. Under standardised conditions the maximum possible value for $\frac{T_{vis}}{T_{sol}}$ is 2.08 [150] whereby the entire visible spectrum is transmitted and all outlying wavelengths reflected or absorbed. The ratio possible for thin films of gold varies between 1.0 and 2.0 [151] but brightness in transmission is very low at the upper range of the ratio.

Coatings of hemispherical gold nanoparticles deposited in high density or as aggregated films have been also demonstrated as spectrally selective coatings[150, 152] but in this case the selectivity is achieved by selective absorption rather than reflection. Whereas isolated gold nanoparticles exhibit a distinct plasmonic absorption peak at about 520 nm, which is nearly in the middle of the visible range of the spectrum, high densities of hemispherical nanoparticles exhibit a broadened and red shifted absorption peak that extends from the upper visible into the NIR. This peak shift is due to the interaction of the neighbouring particle surface plasmons. This increases the ratio of $\frac{T_{vis}}{T_{sol}}$. So far, however, these films are not yet commercially competitive.[150]

Spectrally selective coatings consisting of gold nanorods or nanoshells could increase the optical efficiency of nanoparticulate gold films due to their enhanced optical response and the more precise control possible over peak absorption maxima. It has been determined that the ideal nanorod-based spectrally selective coating would consist of a mixture of nanorods with varying aspect ratios, $3 - 10$.[153] An analogous optimisation is possible with nanoshells.[154] A spectrally selective coating consisting of nanorods with aspect ratios of $3 - 10$ would give a maximum $\frac{T_{vis}}{T_{sol}}$ rating of 1.44 at a gold loading of $0.26\ \mathrm{g.m^{-2}}$. With gold prices currently about $\sim$US$\$1400$/troy ounce[l] this corresponds to a cost of about $US\$11.70\ .\mathrm{m^{-2}}$ for the coating without taking glass and production costs into account. This still presents a competitive option as commercially available coatings of similar ratings retail at a much greater price, commonly $\$50 - \$100.\mathrm{m^{-2}}$.

As discussed previously (Section 1.2.2), the plasmons of adjacent nanoparticles can couple and change the frequency of the resonance. This puts a restriction of the particle density in a film or coating. However, the plasmon resonances of nanorods of different aspect ratios (and therefore different frequencies) do not interact much.[40] Calculations of lateral arrangements of two nanorods of different aspect ratio, 2 and 4 (but equal volume), maintain distinct longitudinal peaks even at zero spacing i.e. touching. In the case of zero spacing between nanorods the intensity of the longitudinal resonance of the aspect ratio 2 nanorod is slightly enhanced whereas the intensity of the aspect ratio 4 nanorod is attenuated. In both instances, however, the position of the peak is red shifted noticeably. In addition to coupling effects the dielectric medium must be considered as the peak position will shift depending on the refractive index. For nanoparticles deposited on a substrate this problem is complicated by the fact that the particle is surrounded by at least two different media. An expression to adjust two distinct surrounding media into one effective medium is calculated and verified for gold nanorods on ITO (indium tin oxide) substrates in air by Vernon *et al*.[155]

Due to the dependence of the optical properties of nanorods on the polarisation of incident light, their orientation also needs be considered for optimal spectral selectivity. Nanorods lying flat on the surface of the glass will give minimum absorbance at NIR or IR wavelengths (depending on longitudinal peak position) for angles of incidence

[l] Correct as of April 2011

approaching $0°$. This means at times of maximum solar intensity (e.g. at midday) heat transfer due to $\mathrm{NIR/IR}$ transmittance will not be attenuated as much as at other times of the day (for a vertically oriented window). However, if the nanorods are oriented perpendicular to the plane of the window then the absorbance at times of high solar angle will be maximised.

Laminates or polymer coatings containing dispersed rods or nanoshells could provide a cheap and effective solution for application of spectrally selective coatings of nanoparticles to existing structures. A PVA coating on architectural glass functionalised by nanorods of an average aspect ratio of ~ 4 can provide a $\frac{T_{vis}}{T_{sol}}$ rating of ~ 1.03.[156] It has also been proposed that the $\mathrm{NIR/IR}$ extinction properties of nanoshells could be used for coatings on protective eyewear or contact lenses.[157]

In addition to spectral shielding applications, mixtures of nanorods and/or nanoshells [154] may be prepared that would absorb the vast majority of the solar spectrum. Such a coating would have utility in solar harvesting for photothermal applications.

Finally, due to the polarisation dependence of nanorods, colour change coatings could in principle be produced where nanorods are tethered to a substrate by a conformation switching molecule or polymer.[40, 158]

1.5.3 High density data storage

The ever-increasing requirement for storage of digital data has stimulated the introduction of a broad range of innovative technologies. Spectral encoding, i.e. the exploitation of optical rather than magnetic properties, is one of the modalities of data storage of interest. In this case, data is written and read by exploiting the optical properties of the data bit. Laser irradiation is used to induce a spectral change in the target region of the recording medium. Depending on the nature of the recording medium, the change may be folding of a protein or molecule, a phase change, or fragmentation or melting of a nanoparticle. In all cases the optical response of the 'written/recorded' region is altered.

Gold nanorods are an attractive option for optical data storage.[159, 160] This is because their optical properties are polarisation dependent and tuneable, they are thermally and chemically stable, and they do not bleach or age. Very high data densities are in principle possible due to the nanoscale dimensions of nanorods (typically the diameters are 10 to 20 nm, and lengths are in the range 30 to 100 nm). However, with conventional optics a dark-field spectroscope is required to detect data bits of single nanoparticles and without modification is only applicable to a two-dimensional system. While a two dimensional system can represent an exceedingly high data capacity, current technology now provides the option of detecting single nanoparticle information from multi-layer devices using confocal dark-field[161, 162] or two-photon luminescence spectroscopy,[160] Figure 1-18. Confocal microscopy only images focussed light and so can

access different depths of a vertical data storage column. Two-photon luminescence is discussed in Section 1.5.7.2.

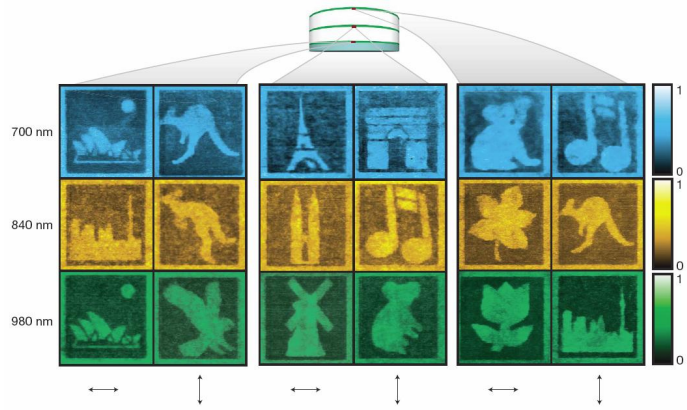

Figure 1-18 Demonstration of five dimensional data storage using gold nanorods with wavelength indicated on the left, two-photon luminescence intensity on the right and polarisation indicated below.

Image reproduced from reference [160]

Data storage devices based on gold nanorods are necessarily limited to the write-once/read-many paradigm as the structural change responsible for the spectral modification is irreversible.[163] However, these ideas can be extended to patterning and encryption applications.[164] Polymer films doped with nanorods could be patterned with characteristic or coded features to prevent counterfeiting of documents or currency.

Hollow gold nanoshells have also demonstrated utility as a high density data storage bit with the most important innovation being the use of deep-UV to write the data bits which increases the spatial resolution significantly.[165]

1.5.4 Catalysis

The fact that gold nanoparticles could, under some circumstances, be very effective catalysts was first noted independently in the 1980s by Haruta[166, 167] and Hutchings.[168] There has been a growing activity in this field since then, driven by both scientific curiosity and commercial interest.[169] Gold nanoparticle catalysts are interesting because they offer both the prospect of better yield or selectivity in some reactions, and because they appear to be effective at lower temperatures than many other catalysts. Gold can, for example, catalyse the oxidation of carbon monoxide at 217 K (-56°C)[170] – a remarkable attribute.

Gold nanorod catalysts are relatively unexplored but due to their geometry they offer stabilised forms of different crystallographic facets which may provide a catalytically active surface.[171, 172] Using dark field spectroscopy the injection of electrons into a single gold nanorod by ascorbic acid (and subsequently an inferred oxidation of ascorbic acid) can be monitored which provides excellent proof of concept for surface chemistry at the

surface of nanorods.[173] The scattering peak shift observed is due to a change in the electron density. Electrochemical charging produces a similar effect.[174]

Alternatively the surface of the nanoparticle may be modified with a catalytically active agent e.g. palladium, and the surface enhanced Raman scattering (SERS) signal can be monitored, a process demonstrated with gold nanoshells.[175]

1.5.5 Sensors

Spherical metallic nanoparticles, generally as a proof of concept, have demonstrated utility as substrates for sensor applications,[176-178] however gold nanorods and nanoshells could be even better[51, 179, 180] due to their more tuneable optical properties.

The optical properties of gold nanorods can be exploited in at least three ways for sensing applications: polarisation dependence, where the orientation of a tethered nanorod is probed;[181] local refractive index change resulting from surface environment properties changing with binding events of an analyte;[179, 182-185] and aggregation induced by cross-linking of nanorods due to analyte/detecting molecule binding.[186]

Gold nanoshells have also demonstrated three possibilities for sensing architectures. These are SERS detection of adsorbed analytes;[129, 187, 188] dependence of scattering spectra on local refractive index;[51, 180] and aggregation by cross-linking nanoshells resulting in extinction peak broadening and attenuation.[189]

In order to achieve high sensitivity, a simple detection method capable of probing the optical response of single nanoparticles is required. Dark-field optical microscopy has been used to measure the spectrum of a single particle using conventional optics.[51, 181, 190-192] An alternative method to obtain scattering spectra of single particles is total internal reflection microscopy.[193]

The polarisation dependence of the optical properties of gold nanorods affords the possibility of orientation based sensors.[181, 194] A change in chemical environment (e.g. pH) or in a tether species (e.g. oxidation or specific binding) would trigger a conformational response in the tether. This switch of conformation directly affects the orientation of the bound nanorod and the optical properties in polarised incident light. Dark-field microscopy can be used to detect the orientation change of single gold nanorods by probing the polarised optical response of the sensing substrate and analysing the signal of individual particles. Polarisation-sensitive photothermal imaging may also be used.[195]

As noted (Section 1.2.1), plasmonic response not only depends on polarisation and shape but also on the local refractive index of the surrounding medium. A change in local refractive index can be induced by varying the bulk medium in which the nanorod or nanoshell is dispersed, or by an increase or displacement of adsorbates at the interface of the nanoparticle and bulk medium. This effect can be exploited to construct

trace chemical or biosensors, where binding events in proximity to the nanoparticles trigger a shift in local refractive index and thus optical response.

As an example, a nanorod sensor based on refractive index change has been suggested for the biotin – streptavidin couple.[179, 183] In the case of detection of streptavidin, which has a very high affinity for the thiolated biotin molecule, an absorbance peak shift of 366 nm/refractive index unit (RIU) was observed.[179] This corresponded to a limit of detection of 0.42 nM (25 ng/mL). This is superior to the results reported for a similar scheme based on gold nanospheres in which a shift of only 76.4 nm/RIU was achieved, corresponding to a limit of detection of 16 nM (~ 950 ng/mL) .[196] Yu and Irudayaraj report even higher sensitivities and, importantly, that local refractive index sensitivity of gold nanorods increases with aspect ratio.[185] Nanorods with aspect ratios with aspect ratios $2.8 - 7$ gave sensitivities from $445 - 1100$ nm/RIU. It has been claimed that nano-bipyramids are even better than parallel-sided nanorods for this type of sensor.[197] For nano-bipyramids single molecule detection has been demonstrated.[198]

A more sophisticated type of system uses an array of gold nanoparticles attached to a substrate. Each nanoparticle could in principle be conjugated to detect a different analyte. This increases the efficiency of any potential assay by allowing multiple simultaneous analyses from one sample. Arrays such as these would be particularly useful in providing indicative results in emergency rooms or for field analysis in forensics or environmental sampling.

Sensitivity to local refractive index of hollow gold nanoshells has also been reported by Sun *et al*. A maximum response of 408.8 nm/RIU was obtained by immersing nanoshells attached to a glass substrate in varying solvents and measuring extinction spectra.[180] However, the source of this value is uncertain as a calculated peak shift of 306.6 nm/RIU was determined for nanoshell dimensions approximated as representative. This discrepancy has been suggested as being due to polydispersity of the sample[180] supported by broad peak widths of ~ 325 nm (906 meV) as displayed by the spectrum. SEM and TEM images provided 'typical' particle dimensions of 50 nm total diameter and 4.5 nm shell thickness, dimensions that were utilised in the calculated value.

Dark-field single-particle spectroscopy of gold nanoshells with an Au_2S dielectric core has provided somewhat different results than those for hollow gold nanoshells.[51] A measured value of 123.6 nm/RIU is reported in contrast to a calculated value of 162 nm/RIU. In any case, an increased response to local refractive index variations is evident for nanoshell geometries with respect to spherical gold nanoparticles. Dependence of the plasmon peak position on the chain length of an alkanethiolate adsorbate on a nanoshell has been reported with a shift of ~ 2.94 nm/methylene unit.[180] From this value the limit of detection for hexadecanethiol (HDT) was estimated to be ~ 27 nM.

A figure of merit (FOM) for gold nanorod based refractometric sensors has been developed by the group of Sönnichsen by considering numerous aspects of the particle spectrum i.e. peak shift and linewidth, of gold nanorods.[199] Consideration of the various

factors indicates that the optimum aspect ratio for gold nanorods for sensing applications is $\sim 3-4$ (width 20 nm).[199] Despite the specific use of nanorods in the development of the FOM it is suggested by the authors that it should be just as applicable to other geometries and creates a point of direct comparison in relative performance.

Assigning a peak shift to the binding event of an analyte could be subject to interference by subtle changes of the refractive index of the bulk medium, particularly at trace levels. Such interferences could be a result of temperature fluctuations, surface charge or turbulence. This problem could be circumvented by the inclusion of unconjugated nanoparticles of distinct extinction peak to that of the conjugated particles. The presence of these particles would provide a reference peak to which the variations due to the medium could be assigned and removed from the detecting peak of the conjugated nanoparticles, leaving the shift due to adsorbed/bound species. In addition to providing a reference peak, a mixture of particles with distinct aspect ratios would allow multiplexing for the detection of multiple species simultaneously.[185, 200] Alternatively the single particle spectra could be monitored pre- and post addition of the sample using dark-field analysis where a "large" area can be monitored with detection achieved through digital analysis of the optical signal from the particles.

1.5.6 Surface Enhanced Raman spectroscopy

Analytical techniques that exploit non-linear optical properties have the capacity to gain from the intense near-field enhancement observed in the vicinity of gold nanostructures. This implies that previous detection limits may be surpassed up to the point of single molecule detection.[201]

Raman scattering spectroscopy is one such technique for exploiting near-field enhancements: detection of a single DNA base molecule has been demonstrated using clusters of colloidal silver nanoparticles.[202] Clusters of nanoparticles exhibit strong plasmon coupling, with near-field enhancements generally located at the points of contact between particles. Raman spectroscopy probes the inelastic scattering of photons by vibrational modes of chemical bonds (e.g. C – C). Different vibrational modes will give rise to characteristic shifts in the incident radiation. Signal intensity depends on the number of bond species present and Raman scattering events. Unfortunately only a small fraction of incident photons are Raman scattered with the majority undergoing elastic or Rayleigh scattering. Surface Enhanced Raman Scattering (SERS) was first observed in 1974 on a silver electrode roughened by cycled redox reactions.[203] Originally the enhancement of the Raman signal was assigned to an increase in the surface area and thus an increase in adsorbed analyte, however, subsequent work has shown that the Raman effect is mostly amplified by the near-field enhancement of the electric field at the metal surface.

Following a suggestion by Moskovits, Creighton *et al*. demonstrated SERS from adsorbates on silver and gold sols.[204] Within this work, supporting evidence for the near-

field enhancement mechanism was presented as the maximum enhancement coincided with the plasmon resonance of the metallic nanosphere. It should be noted that, following addition of the analyte to the sol, the absorbance spectrum developed a shifted peak most likely due to coagulation. This would have resulted in coupling of the particle plasmons potentially giving slightly inaccurate but elevated enhancements.

An additional order of magnitude enhancement (with respect to spherical nanoparticles) was predicted for substrates comprised of prolate spheroids of silver and gold.[205] Following recent progress in the syntheses of nanorods, these predictions have been demonstrated experimentally.[94] Analogous to the problems of agglomeration experienced in the case of nanospheres, replacing the shape-directing/capping surfactant on nanorods can be difficult. However, SERS has been recorded for the surfactant itself[94] and some foreign analytes[206, 207] in solution giving enhancements of approximately five orders of magnitude for plasmon resonant excitations.

SERS on nanoshell substrates also shows large enhancements[208] and is once again correlated with plasmon resonance.[208, 209] A single Au nanoshell, with a rough surface, has a calculated SERS enhancement of $\sim 4 \times 10^4$ whereas an Au nanoshell dimer gives a polarisation-dependent enhancement of $\sim 5 \times 10^7$.[210] Arrays of Au or Ag semi-shells seem to offer considerable potential as a reproducible SERS substrate.[211]

Off-resonance Raman enhancement has also been demonstrated for isolated nanorods,[94] but no such effect seems to have been observed for isolated nanospheres or nanoshells. SERS from the capping agent of the nanorods was probed resulting in an enhancement of 10^4 to 10^5. This presented an additional one to two orders of magnitude enhancement over the Wang and Kerker model at the same excitation wavelength. Discrepancy with the model in the off-resonance condition is attributed to the increase in the polarisability of the molecule adsorbed to less stable facets of gold nanorods[94] i.e. (110) or (100). Another consideration for discrepancies between experimental results and early theoretical models is the exclusion of the effects of radiation damping which has a negative effect on the SERS enhancement.[212]

Electric field calculations of isolated Au nanoshells and nanoshell dimers illustrate the regions of greatest enhancements (the 'hot spots'). For a dimer configuration the strongest field enhancement is in the region of nearest separation of the nanoshells.[210, 213] It is also apparent that for dimer pairs of equal aspect ratio but varied volume the enhancement is slightly higher again.[213] Calculations of surface roughened nanoshells indicate that they should cause greater enhancements than smooth nanoshells[210].

Films of aggregated nanospheres and nanorods have also been compared.[214] SERS of analytes on aggregated nanorods are expected to give extremely large enhancements.

Overall, there is considerable commercial interest in SERS and this creates the requirement that factory-made substrates should be stable for extended times, a factor that could favour the use of gold over silver. Shifting of the wavelength of the plasmon

resonance to the near-infrared by use of Au (rather than Ag) is also possibly useful since it allows the SERS measurement to be taken, in principle, through the 'tissue window'[215] in live patients.

As a final example of a SERS-based sensor, we note the "all-optical nanoscale pH meter" utilising a pH sensitive adsorbate on $SiO_2 - Au$ (core-shell) nanoshells.[187] In this case, the value of the pH is determined by analysing the SERS signal of 1,4-mercaptobenzoic acid (para-MBA) which is in a protonated, partially protonated or deprotonated state at low, intermediate or high pH respectively (in the range pH 5.80 to 7.60). An analogous functionality could be anticipated in respect of para-MBA conjugated nanorods.

1.5.7 Use of gold in medical diagnostics

1.5.7.1 General

Gold nanoparticles have been the basis of diverse cell or protein-specific staining techniques for a few decades, a capability that was evidently pioneered by Faulk in 1971.[216] Being a heavy element, Au nanoparticles in tissue sections are particularly visible in an electron microscope.[217] This fact is used in combination with the ability of gold nanoparticles to bind to selective antibodies to produce highly selective stains for biological tissue. Actually, since the gold nanoparticles also scatter visible light, such selective binding can often also be detected in an ordinary optical microscope, possibly using the dark-field techniques described earlier. Many of the relevant principles and procedures are summarised in an authoritative text on the subject.[218] There has been continuing development of the technology, with the enhanced scattering properties of large gold nanoshells[219] and nanorods[220] having been recently exploited for the early diagnosis of cancer.

Biomedical imaging techniques, in particular, multiphoton luminescence microscopy,[221, 222] optical coherence tomography[223] and photoacoustic imaging[224-226] have utilised gold nanorods as contrast enhancing agents. SERS has been demonstrated as a complimentary feature to diagnostic applications of conjugated nanorods whereby analysis of the Raman signal allows for distinction between benign and cancer cell lines[207]. Nanoshells have also demonstrated contrast enhancement for photoacoustic imaging,[227] two-photon luminescence microscopy[228] and contrast enhancement for optical coherence tomography.[229] These enhancements of existing medical diagnostic techniques have implications for improved procedures which could lead to improvement in treatment due to early detection. Each will be discussed in turn below.

1.5.7.2 Two-photon luminescence

Two-photon induced luminescence (TPL) is a multiphoton process whereby absorption of two photons causes an electron to transit from ground to excited state by way of an intermediate virtual state.[230] Relaxation results in the recombination of the electron-hole pair and emission of a photon. Probability of two-photon absorption is very low, so high intensity irradiation is required for a measurable effect. Although this seems like a disadvantage it signifies that TPL will only be produced within a localised volume around

the focal point.[230] This means that by scanning through x, y and z a detailed three-dimensional image may be formed with boundaries on resolution being primarily limited to the spot size of the laser. Diagnostically, imaged data presented in two-dimensional slices is highly useful since it provides cross-sectional information of irregularities or areas of interest. Rendering the cross-sectional information into three dimensional reconstructions provides additional information, which can guide surgical procedures.

Plasmon enhanced TPL of roughened metal substrates was characterised in 1986 by Boyd *et al*.[231] Gold nanorods[222] and nanoshells[228] exhibit a plasmon enhanced TPL signal where the intense near-field present under resonant conditions enhances the relatively weak luminescence. A single gold nanorod produces a TPL signal ~ 60 times brighter than the two photon fluorescence from a single rhodamine 6G molecule, a common contrast agent (2320 GM and 40 GM for gold nanorod and rhodamine 6G respectively) .[222] (Two photon emission intensities are quantified in terms of an action cross-section given in Göppert-Mayer (GM) units.[230]) Of course, semiconducting $\mathrm{CdSe} - \mathrm{ZnS}$ quantum dots (QDs) have demonstrated TPL intensities of $2000 - 47000$ GM [232] which is far greater than for gold nanorods. However, such QDs are highly toxic and although *in vivo* experiments have been performed,[232] the protective layer coating the QDs could breakdown prior to excretion resulting in heavy metal (Cd) poisoning. Gold nanoparticles are generally considered as bio-inert.[233, 234]

In vivo demonstrations of TPL with gold nanorods have been published utilising live mouse models. In this case unmodified nanorods were injected intravenously upon which single nanorod TPL signals were observed within the vasculature.[222] Targeted TPL microscopy is also possible where conjugated nanorods are injected for specific location of, for example, tumour cells.[221] Once located, the laser excitation can be focussed on the tumour cells to induce localised plasmonic heating and hence cell death (see the section on Medical Therapeutics to follow). Targeted TPL with gold nanoshells has also been shown by *in vitro* trials.[228]

1.5.7.3 Magnetic resonance imaging

Due to their geometry, incorporation of super-paramagnetic iron oxide nanoparticles (SPIO) into the core of metallic nanoshells allows for contrast enhancement for magnetic resonance imaging (MRI) and subsequent photothermal treatment.[235] Super-paramagnetic properties can also be imposed on gold nanorods by coating with iron oxide nanoparticles.[236] MRI is a broadly applied diagnostic tool for discerning abnormal tissue deposits or for studying body mechanics at a fine scale. SPIO nanoparticles have been shown to provide strong contrast in MRI for numerous systems (e.g. bowel, liver, lymph nodes etc.).[237] Super-paramagnetism refers to the absence of a net magnetic moment without an externally applied magnetic field. This property of the nanoparticles prevents them from self-aggregating due to magnetic attraction and protective coatings allow for separation after termination of the external magnetic field.

Gold nanoshells with an inner SPIO nanoparticle core have demonstrated high contrast efficiency for MRI.[235, 238] In addition, the metallic shell can be conjugated with antibodies raised against a particular cellular trait (e.g. tumour cells), and upon NIR irradiation photothermal treatment may be administered and subsequently tracked using MRI.[235, 238]

1.5.7.4 Photoacoustic microscopy

Photoacoustic microscopy is a sensitive diagnostic tool for detecting abnormalities in soft tissues such as skin and vasculature. This technique is non-invasive and, unlike X-ray imaging, non-ionising so there is no undue damage caused by the imaging process. A photoacoustic signal is induced by irradiating the target region with pulses from a laser. Body tissue within this region will absorb the incident radiation and undergo rapid thermal expansion. This rapid expansion induces an acoustic signal which is detected by an ultrasonic transducer.

Formation of the image is analogous to conventional ultrasound. Two-[239] and three- [240] dimensional images can be formed using photoacoustic microscopy, with the three dimensional images being reconstructed from two-dimensional slices of incremental depth, a process known as tomography. As mentioned previously, wavelengths in the red-NIR range ($650 - 900$ nm) must be used to increase the penetration of the laser.[215] However, as the strength of the photoacoustic signal is proportional to the absorption coefficient and the absorption by unmodified soft tissue is minimal at these wavelengths, formation of acoustic images is difficult. Gold nanorods[224-226, 241] or nanoshells[227] tuned to express maximum absorption within the soft tissue window can be used to increase the absorption dramatically and thus increase the acoustic signal through plasmonic heating effects. Specific cell line targeting can be achieved by conjugating the surface of the nanoparticles with antibodies. This process can be used for diagnostics or observation of retaliatory systemic processes, such as nanorod enhanced imaging of early inflammatory response.[225] Finally, systemic imaging can be performed such as, for example, improved contrast in brain images as provided by intravenous injections of nanoshells.[227] This could result in early detection, and thus prevention, of life threatening conditions.

1.5.7.5 Optical coherence tomography

Optical coherence tomography (OCT) was first modified for biological systems by Huang *et al* in 1991.[242] OCT provides high resolution, *in vivo* images of biological systems rapidly and non-invasively. The principal of operation is analogous to ultrasonic imaging but using NIR light in place of sound waves. A two dimensional cross-section is formed by analysing differential scattering signals using low-coherence interferometry. Time-of-flight information is determined by use of a Michelson interferometer where the low-coherence light source is split into two paths. One path reflects off a reference mirror the other is incident on the tissue sample. The amplitudes and delays from the sample reflections are quantified by scanning the reference mirror position. OCT has proven to

be a useful diagnostic tool and has made significant advancements for ophthalmic diagnoses,[243] for such conditions as glaucoma and macular degeneration.

Nanoshells tuned to exhibit high extinction in the soft tissue and OCT illumination window have been shown to provide high contrast enhancement for healthy tissue and tumourous tissue.[229] These nanoshells were synthesised to exhibit both high absorption and scattering cross-sections. High scattering properties are essential for providing contrast in the OCT image.

1.5.8 Therapeutic possibilities for nanoscale gold

For medical applications gold nanoparticles are synthesised to express peak absorbance within the aforementioned 'soft tissue window', $\sim 650 - 900$ nm.[215] Within this range haemoglobin and water, primary absorbers of visible and infrared (IR) wavelengths respectively, exhibit their lowest absorption coefficient, allowing penetration of light up to 10 cm.[215] Implementation of gold nanoparticles into *in vivo* medical applications relies on characterisation of their effect on biological systems. In general, studies utilising gold nanoparticles have revealed that any cytotoxicity that they might have is due to species, usually surfactants or capping ligands, adsorbed onto their surface. There is broad (but not complete) agreement in the field that the gold itself is inert. For example, in the case of gold nanorods, the shape directing surfactant ($C_{16}TABr$) is a known cell lysing agent.[244] Therefore, pre-treatment of the nanorods to remove excess $C_{16}TABr$ in the surrounding medium is required.[245] In contrast, $C_{16}TABr$ coated nanorods themselves show low cytotoxicity[246-249] but by using various layer-by-layer polymer coating architectures the toxicity can be further reduced and the surface properties engineered to produce a tuneable cell uptake.[246] Another option is to replace the $C_{16}TABr$ with a polymerisable analogue.[250] Nanoshells are also reported as showing low toxicity for a range of cell lines.[251, 252] Broader biological effects of environmental release of nanorods also show minimal detrimental effect. Using model estuarine mesocosms a sample of nanorods was determined by mass of gold to be widely distributed throughout biofilms, sediment, plants, animals and sea water.[253] Despite being exposed to the gold nanoparticles there was no sign of adverse health effects for the species involved over the time frame of the experiment.

The rational therapeutic use of gold nanoparticles[254] is based on one of three modalities. The particles can be used (1) to deliver either a localised heating effect, or (2) as a platform onto which to attach cytotoxic or other organic molecules, or (3) as radioactive sources. Combined therapeutic and diagnostic applications of gold nanorods[186, 222, 225, 247, 248, 255-258]and gold nanoshells [227, 229, 235, 259-267]have been published. Particles with such dual functionality are sometimes described as 'theranostic'.[268]

The application of nanorods and nanoshells in the photothermal mode can be both primary and secondary. Both utilise the localised heating of nanoparticles induced under plasmon resonant conditions[269] but they differ in terms of the effect sought from this heating. The heating effect for nanorods[270] and nanoshells[271] has been modelled for

aqueous systems. Primary nanoparticle treatment involves two main stages; first, nanoparticles are conjugated with antibodies for specific cell line targeting, upon injection the conjugated particles will bind to cells expressing targeted characteristics. Induction of cell death, stage two, is achieved by localised plasmonic heating at nanoparticle binding sites i.e. tumour site (target cells), using laser irradiation. This localised heating causes thermal stress resulting in cell death.

Primary nanoshell applications mainly utilise photothermal tumour ablation in demonstrating the efficacy of nanoshells as therapeutic agents[272, 273] and were pioneered by the group of N. Halas.[219, 260, 262] Targeting excessive or inappropriate neovasculature, which is commonly a function of tumour development, is a suggested demonstration of hyperthermic nanoshell treatment.[274] Examples of nanoshell photothermal therapy tend to utilise laser intensities of $\sim 4 \times 10^4\ \mathrm{W.m^{-2}}$, [229, 260, 262]which are comparatively high. Post-surgical treatment has also seen improvement from plasmonic heating properties of nanoshells. Near-infrared laser tissue welding exploits a "bio-solder" to improve healing of surgical incisions.[259] The "bio-solder" consists of a moderate concentration of nanoshells in a BSA (bovine serum albumen) solution. Near-infrared wavelengths are used to minimise damage to surrounding areas and increase penetration which ultimately results in a stronger, faster healing weld.

In the case of gold nanorods, laser intensities as low as $\sim 5 \times 10^2\ \mathrm{W.m^{-2}}$ have been used to induce cell death where dependence on total laser fluence rather than flux is emphasised (a minimum fluence of $30\ \mathrm{J.cm^{-2}}$ seems required).[247] At such low power less than 1% of healthy cells were killed whereas 81% of the target cells (to which the gold nanorod had been conjugated) were terminated. Several applications of primary nanorod therapeutics have been demonstrated ranging from targeted destruction of immune cells or macrophages[247] to destruction of tumour cells,[256] bacteria[275] and even of protozoan parasites.[248] Although the destruction of macrophage cells may seem counterintuitive in some cases it may prove beneficial[276] assuming antibodies can be raised to differentiate between healthy and infected macrophages.

Secondary nanoparticle therapeutic applications also utilise plasmonic heating properties. Nanorods[277] or nanoshells[278, 279] are embedded in a thermoresponsive polymer matrix doped with a therapeutic agent. The thermoresponsive polymer, commonly NiPAAm (N-isopropylacrylamide), could be injected as a colloidal solution of micrometre scaled beads or implanted as a pellet.[263, 280, 281] Alternatively the core of the nanoshell could constitute the thermoresponsive polymer/therapeutic agent for diffusive release upon plasmonic heating.[282] Sequestering the composite within the nanoshell leaves the surface for adsorption of antibodies etc. for targeting particular regions or species in the body to maximise therapeutic efficacy. Once inserted, NIR laser irradiation excites the plasmon of the nanoparticles whereby the surrounding medium is heated. This causes a conformational change of the polymer molecules leading to a decrease in volume of the composite. This decrease is accompanied by release of the therapeutic agent into the surrounding environment e.g. bloodstream. By controlling

the laser intensity or exposure of the polymer composite the rate of drug release could be controlled to achieve prolonged, constant administration to maximise therapeutic efficacy.

Another, somewhat unrelated mode of therapy is to use the gold nanoparticles simply as platforms with which to transport a drug[283] or genetic material[284] into a cell. In this case there is no plasmonic heating required and the property of the gold that is being exploited is its surface chemistry.

A major issue with the application of nanoparticles to medical applications is the relatively unknown effect that the particles themselves have over long periods. The broadest view is that they are excreted as waste in an unspectacular manner and are generally non-toxic.[245] Dynamic light scattering has been demonstrated as a quantitative method for monitoring the concentration of nanoshells remaining in the bloodstream prior to administration and exhaustion of their therapeutic role.[285] This method could also be applied to monitoring concentrations of nanorods, although interpretation of the results requires additional consideration due to the rod geometry.[286] The uptake of gold nanoparticles into live cells seems to depend on their size, shape and the nature of any capping ligands present.[233]

Finally, I note in passing that it has been claimed that gold nanoparticles can serve as an active adjuvant[m].[287]

1.6 Motivation

In this introduction I have discussed the vast amount of research in characterisation and application of gold nanorods and nanoshells. From this review it is my opinion that when all factors, e.g. synthesis and optical performance, are considered gold nanorods show greater utility than nanoshells for a broad range of applications. For this reason I primarily focus on the synthesis of gold nanorods in this thesis.

However, I have also drawn attention to the limitations in the understanding and implementation of the gold nanorod synthesis. A major consideration for the gold nanorod synthesis is the inefficient conversion of ionic to metallic gold. This problem is highlighted in the literature but it is not quantified. The concentration of gold that remains unreacted is significant, in most cases $\sim 80\ \%$. It is my aim to address this issue and provide a set of conditions whereby the synthesis is optimised. Additionally, altering the reductant conditions will provide deeper insight into the mechanisms involved in the reaction. Efficiency is a particularly relevant point for the aims of this research when considering the collaboration with the industrial partner.

It is also my aim to simplify the gold nanorod synthesis by exploring and quantifying the parameter space of aspect ratio and particle sizes that is achievable for a constant gold nanorod growth solution where only the amount of seed added to initiate the reaction is varied.

[m] A substance that increases the efficacy of a vaccine

Another major hole in the current literature is a precise mechanism of formation for gold nanorods. The most significant factor is the mechanism of the transition from spherical seed to nanorod. I have designed experiments using multiple techniques to characterise the various stages of the gold nanorod reaction, in particular the early stages.

The work in this thesis is designed to increase the awareness of the utility of plasmonically active precious metal nanoparticles as well as aid the development of new applications by simplifying synthetic procedures.

2 Experimental Methods and Materials

This chapter describes the various experimental procedures that I have used for the wet chemical synthesis of gold nanorods as well as for selected other precious metals and particle geometries. Where variable concentrations of reagents were used, I have simplified the description here to indicate nominal amounts and/or ranges used. The specific concentrations actually used for each sample are noted with respect to the presentation of the data in later chapters.

I prepared all aqueous solutions using ultrapure water from a Sartorius Arium 611 VF purification system with $18.2\ \mathrm{M\Omega.cm}$ resistivity. I washed all glassware with either lab-grade detergent or aqua regia and thoroughly rinsed with ultrapure water.

2.1 Synthesis of $HAuCl_4$

Gold metal (99.99% purity) was obtained from AGR Matthey Australia. Hydrochloric acid (AnalaR) and Nitric acid (AnalaR) were obtained from BDH Chemicals.

I synthesised $\mathrm{HAuCl_4.xH_2O}$ by dissolving pure gold metal in aqua regia ($\mathrm{HCl:HNO_3}$ $3:1$ v/v). The method may be found in the literature.[288] Briefly, 4.9131 g pure gold was dissolved in excess aqua regia (~ 80 mL). The solvent was then evaporated under aspirator vacuum. To remove the $\mathrm{HNO_3}$ the solution was strongly heated with concentrated HCl, twice. The resulting solution was then diluted to 100 mL to obtain an ~ 0.25 M $\mathrm{HAuCl_4}$ stock solution.

It should be noted that some gold precipitated from the solution and so the actual concentration was verified by ICP-MS as follows. I prepared a series of 5 mL $\mathrm{Au^{3+}}$ calibration solutions from a 1 ppm standard solution (Choice Analytical) through dilution by mass. The $\mathrm{Au^{3+}}$ concentration of the solutions were 10, 50, 100, 150, 400, 750 and 100 ppb. I diluted the ~ 0.25 M $\mathrm{HAuCl_4}$ stock solution assuming no loss of gold by a factor of $491.31\times$ to achieve an approximate concentration of 100 ppb. The ICP-MS analysis[n] returned a $\mathrm{Au^{3+}}$ concentration of 0.2306 M, this was diluted accurately to produce a stock solution of 0.1 M.

2.2 Precious Metal Nanoparticles

All other chemicals were purchased from respective suppliers with $\geq 95\%$ purity and were used as-received. $\mathrm{HAuBr_4}$ – Sigma Aldrich, $\mathrm{C_{16}TABr}$ – Nanjing Robiot and Alfa Aesar, $\mathrm{AgNO_3}$ – Sigma Aldrich, sodium salicylate – Ajax Finechem and Alfa Aesar, $\mathrm{KBH_4}$ – Sigma Aldrich, ascorbic acid – Sigma Aldrich and Alfa Aesar.

2.2.1 Gold Nanoparticle Seed Solution

I prepared the growth solution for the gold nanoparticle seed according to one of two procedures, slightly modified from the procedure of Nikoobakht and El-Sayed: [21]

[n] ICP-MS analysis was performed at the University of Technology, Sydney by David Bishop using an Agilent Technologies 7700 series ICP-MS.

Seed A: 10 mL of u mM $HAuCl_4$ -25 mM $C_{16}TABr$, where u was typically of the order of 0.1 mM. Briefly, 0.091 g $C_{16}TABr$ was dissolved in ultrapure water with some gentle heating ($\sim$45°C) and agitation. Next, an aliquot of 0.1 M $HAuCl_4$ was added to achieve the desired concentration (specific values noted later). Finally the solution was made up to 10 mL with ultrapure water.

Seed B: 10 mL of 0.1 mM $HAuCl_4$ $-$ 25 mM $C_{16}TABr$ stock solution. A one litre 0.1 mM $HAuCl_4$ – 25.0 mM $C_{16}TABr$ stock solution was prepared by dissolving 9.1118 g $C_{16}TABr$ in $\sim$800 mL ultrapure water by gentle heating ($\sim$45°C), stirring and ultrasonic agitation. Then, 1.0 mL of 0.1 M $HAuCl_4$ was dispersed through the $C_{16}TABr$ solution by gentle heating ($\sim$45°C), stirring and ultrasonic agitation. The solution was then made up to one litre with ultrapure water.

To form the gold nanoparticle seeds, 10 mL of seed growth solution was heated for 10 minutes at 45°C, after which 0.5 mL of an ice cold, freshly prepared 0.01 M KBH_4 solution (26.97 mg KBH_4 made up to 50 mL with ultrapure water) was added with stirring. The seed was left to stand for one hour at 30°C in a water bath before adding an aliquot to the nanorod growth solution.

2.2.2 Gold Nanorod Growth Solution

For the synthesis of gold nanorods I prepared growth solutions (GS) according to one of the two following procedures, both of which are based on the literature procedure by Jana *et al*:[13]

GS method A: I prepared fresh 10 mL of growth solution for each sample, each contained 0.1 M $C_{16}TABr$, 0.5 mM $HAuCl_4$, v mM H_2A and w µM $AgNO_3$. Briefly, 0.3645 g $C_{16}TABr$ was dissolved in $\sim$8 mL of ultrapure water with aid of gentle heating and ultrasonic agitation. Then, 50 µL of 0.1 M $HAuCl_4$ stock solution was added and dispersed through the $C_{16}TABr$ solution by gentle heating, stirring and ultrasonic agitation. An aliquot of 0.1 M H_2A (final concentrations noted later) was added, with stirring, to reduce Au^{3+} to Au^{+}. I prepared H_2A solutions fresh for each experiment. $AgNO_3$ was then added as an aliquot of a 0.01 M stock solution (again final concentrations are noted later). Finally, this combination was made up to 10 mL with ultrapure water.

GS method B: For this procedure I prepared a range of stock solutions to construct the nanorod growth solution with 8 mL 0.625 mM $HAuCl_4$ $-$ 0.125 M $C_{16}TABr$ stock solution, 1 mL x mM H_2A, 1 mL 0.7 mM $AgNO_3$ stock solution. One litre of 0.625 mM $HAuCl_4$ $-$ 0.125 M $C_{16}TABr$ stock solution was prepared by dissolving 45.557 g $C_{16}TABr$ in $\sim$800 mL ultrapure water by gentle heating, stirring and ultrasonic agitation. This was then followed by addition of 6.25 mL of 0.1 M $HAuCl_4$ stock solution and was dispersed through the $C_{16}TABr$ solution by gentle heating, stirring and ultrasonic agitation. This solution was then made up to one litre with ultrapure water and stored it in an ambient, dark place wrapped in aluminium foil. One litre of 0.7 mM

$AgNO_3$ stock solution was prepared by dissolving 0.119 g $AgNO_3$ in ultrapure water and making this up to one litre. I prepared H_2A solutions fresh for each experiment at a millimolar concentration to add to the other solutions to result in a 10 mL total sample volume.

The growth of the gold nanorods was initiated by the addition of an aliquot of seed solution, as prepared above, with the amount and method noted accordingly in Chapter 4 and 5.

All nanorod samples were thermostatted at $30℃$ using a water bath for the duration of the reaction.

2.2.3 Gold Nanorings/Hollow Nanoparticles

I synthesised silver nanoparticles according to one of two procedures for use as template nanoparticles in the galvanic replacement reaction with $AuCl_4^-$. Chemicals were used as received. Tri-sodium citrate – Sigma Aldrich, $AgNO_3$ and $C_{16}TABr$ were sourced from the suppliers mentioned previously. A solution of 1 mM $HAuCl_4$ was prepared by diluting a 100 µL aliquot of the 0.1 M stock solution mentioned above (Section 2.1).

Template 1: I prepared a 412 mL stock solution of $C_{16}TABr$ stabilised silver template nanoparticles. Briefly, 36.5 mg $C_{16}TABr$ was dissolved in ultrapure water with some gentle heating and agitation. To this, 17 mg $AgNO_3$ was added and stirred until it was dissolved. This solution was then made up to 400 mL with ultrapure water. Under constant stirring 12 mL of a freshly prepared 0.01 M KBH_4 solution (26.97 mg KBH_4 made up to 50 mL with ultrapure water) was added to reduce the Ag^+ to form silver nanoparticles.

Template 2: A ~ 20 mL sample of silver template nanoparticles stabilised with tri-sodium citrate was prepared. Briefly, ~ 1.84 mg of tri-sodium citrate was dissolved in ultrapure water. Then, 0.625 mL of 0.01 M $AgNO_3$ was added and the solution made up to ~ 20 mL with ultrapure water.

Galvanic Replacement Reaction: A y mL aliquot of template solution was refluxed at $\sim 75℃$ for 15 minutes. Following this step z mL of 1 mM $HAuCl_4$ (100 µL of 0.1 M stock diluted to 10 mL) was added drop-wise. Specific volumes and template solutions are noted with respect to data in Section 3.1.1. The solution was refluxed for a further 20 minutes or until the colour of the solution was stable.

2.2.4 Ag Nanorods

I prepared silver nanorods according to a modification of a procedure originally published by Jana *et al*.[289] Stock solutions of 100 mL 0.08 M $C_{16}TABr$, 10 mL 0.01 M $AgNO_3$, 100 mL 0.1 M H_2A and 10 mL 1 M $NaOH$ were prepared. The $C_{16}TABr$ solution was prepared by dissolving 2.9158 g of $C_{16}TABr$ and making up to 100 mL; the $AgNO_3$

solution was prepared by dissolving 16.99 mg and making up to 10 mL; the H_2A solution was prepared by dissolving 1.7612 g and making up to 100 mL; the $NaOH$ was prepared by dissolving 0.4 g and making up to 10 mL; all solutions were prepared with ultrapure water.

Silver nanoparticle seed: A 20 mL 0.25 mM $AgNO_3$ and 0.25 mM $C_{16}TABr$ growth solution was prepared by adding 0.5 mL of 0.01 M $AgNO_3$ stock solution and 62.5 µL of 0.08 M $C_{16}TABr$ stock solution, this was then made up to 20 mL with ultrapure water.

To this solution 0.6 mL of ice cold 0.01 M KBH_4 (26.97 mg KBH_4 made up to 50 mL with ultrapure water) was added, with stirring, to form the silver nanoparticle seeds. This solution was left to stand at 30°C for one hour before adding to the nanorod growth solution.

Silver nanorod growth solution: Five growth solutions were prepared all containing 0.25 mL of 0.01 M $AgNO_3$ stock solution, 0.5 mL of 0.1 M H_2A stock solution and 10 mL of 0.08 M $C_{16}TABr$ stock solution.

To these growth solutions 2.00, 1.00, 0.50, 0.25 and 0.06 mL of seed was added respectively. The growth of the silver nanorods was initiated by adding a 0.1 mL aliquot of the 1 M $NaOH$ stock solution.

2.2.5 Platinum Nanoparticles

Hexachloroplatinic acid, $H_2PtCl_6.xH_2O$, was synthesised[o] according to a similar procedure to the preparation of $HAuCl_4.xH_2O$. Briefly, ~ 0.293 g of platinum metal was dissolved in an excess of aqua regia ($HCl: HNO_3$ $3:1$ v/v). The solvent was then evaporated under aspirator vacuum. To remove the HNO_3 the solution is strongly heated with concentrated HCl, twice, in the same manner. The resulting solution was diluted to 25 mL accurately to obtain an ~ 0.06 M $H_2PtCl_6.xH_2O$ stock solution. PVP (polyvinylpyrrolidone, 10000 MW), TC_8ABr (tetraoctylammonium bromide) and nonylamine – Sigma-Aldrich ($\geq 95\%$), toluene – BDH (AnalaR grade) were used as received.

Aqueous synthesis: A growth solution was prepared with 10 mL of 0.06 M H_2PtCl_6 stock solution and 0.1 g PVP which was then made up to 100 mL with ultrapure water. The formation of platinum nanoparticles was initiated by adding 10 mL of ice cold 0.1 M KBH_4(53.94 mg KBH_4 made up to 10 mL with ultrapure water). Upon addition of the KBH_4 solution I noticed that a black precipitate formed in parallel to the pale brown colour of the solution. This was filtered before characterisation by UV-Vis spectrometry.

Organic synthesis: I prepared platinum nanoparticles in an organic solvent using the Brust-Schiffrin method.[290] Briefly, 1.5 g of $TOABr$ and 0.2865 g of nonylamine were dissolved in 50 mL of toluene. This was stirred with 10 mL of 0.06 M H_2PtCl_6 stock

[o] $H_2PtCl_6$was synthesised by Linda Xiao at the University of Technology, Sydney.

solution until the colour transferred into the organic layer. The formation of platinum nanoparticles was initiated by stirring the organic layer, vigorously, with 10 mL of ice cold 0.1 M KBH_4(53.94 mg KBH_4 made up to 10 mL with ultrapure water). I also noticed that a small amount of precipitate was formed in this method.

2.3 Characterisation and Calibration

2.3.1 Characterisation of Au(III) species

$HAuBr_4$, $HAuCl_4$ and $C_{16}TABr$ were obtained from suppliers as mentioned above, while $C_{16}TACl$ was sourced from Nanjing Robiot. All were used as-received. I prepared 10 mL solutions of all permutations, with respect to halide counter-ions, with 0.5 mM Au^{3+} and 0.1 M $C_{16}TA^+$ concentrations.

I also calculated the extinction coefficient for the $AuBr_4^- - C_{16}TA^+$ complex. Figure 2-1 shows the UV-Vis spectra of the concentrations with respect to Au^{3+} listed in the Figure. All solutions were prepared by dilution from a stock 0.5 mM Au^{3+} – 0.1 M $C_{16}TABr$ solution.

$$\varepsilon_{395} = \sim 4776\ \mathrm{L.mol^{-1}.cm^{-1}} \qquad 2.1$$

$$[AuBr_4^- - C_{16}TA^+](\mathrm{M}) = \frac{A_{395}}{4776} \qquad 2.2$$

where, ε_{395} and A_{395} are the molar extinction coefficient and absorbance at 395 nm respectively.

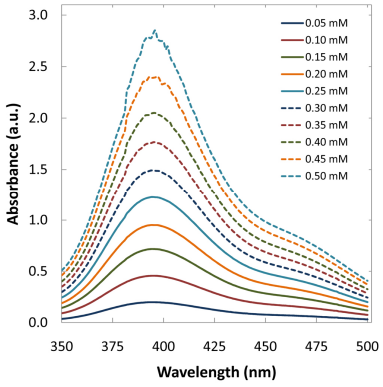

Figure 2-1 Calibration of $AuBr_4^-$ extinction in aqueous $C_{16}TABr$ solution

I used the lowest concentrations to calculate the extinction coefficient due to the upper range of data approaching the detection limit for the spectrophotometer.

2.3.2 Calibration of Au^0 Concentration in Aqueous Solution

I used a similar procedure to the synthesis of gold nanoparticle seed A where 0.5 mM $HAuCl_4$ was reduced in the presence of 25 mM $C_{16}TABr$ by an excess of KBH_4. I prepared two independent solutions to validate the measurement. The size of the initial nanoparticles is expected to be $\sim 2-3$ nm in diameter. The solutions were allowed to age under ambient conditions until the plasmon resonance developed, signifying the Ostwald ripening of the fine particles to larger particles. Figure 2-2 shows the absorbance spectra for the as prepared and aged gold nanoparticle solutions.

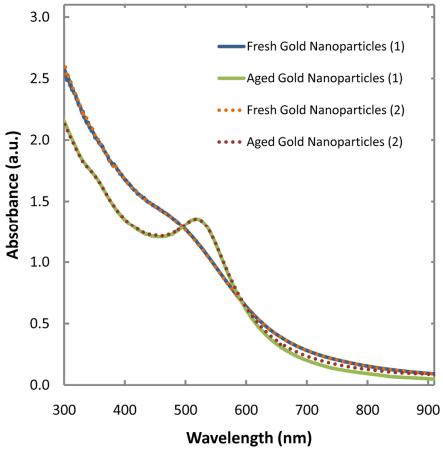

Figure 2-2 Calibration for Au^0 in solution

As can be seen from Figure 2-2, the fresh particles suffer a size dependent contribution to the interband transition region which interferes with the amount of gold that is in the solution.

The factor for calculating the Au^0 concentration (mM) from the aged samples of gold nanoparticles was determined using the Beer-Lambert law from the above data and is given by the equation:

$$[Au^0] = 0.3551 \times A_{390} \qquad 2.3$$

I have compared my calibration factor to data published by Orendorff *et al.*[27] In this publication they determine the gold concentration in nanorod samples via ICP-MS. I used the optical data from the publication to calculate the Au^0 concentration. The values determined by each method are listed in Table 2-1.

Table 2-1 Comparison of my optical determination factor with published ICP-MS results for [Au^0]

Aspect Ratio	[Au^0] ICP-MS (μM)	[Au^0] Optical (μM)
2.0	71.0	76.0
2.9	75.0	91.5
3.5	71.0	84.7
4.5	73.0	83.3

The values determined by my optical factor are within 20% of those determined from the Orendorff data, which may be an acceptable deviation for the purposes of a crude estimation of the Au^0content of a colloid. In any case, for the ICP-MS results a discrepancy of ~ 20 μM between initial and recovered metal is evident anyway (as reported). The values determined by my optical factor are well within this and possibly closer to the true value if loss of gold is considered through the sample preparation for the ICP-MS study. My calculation factor was calibrated using an Agilent Technologies 8453E photodiode array UV-Vis-NIR spectrophotometer so some discrepancy could be due to the use of different equipment as well.

2.3.3 UV-Vis-NIR Spectroscopy

The UV-Vis-NIR spectra I present in this thesis are measured using either a Shimadzu UVmini 1240 UV-Vis-NIR spectrophotometer or an Agilent Technologies 8453E photodiode array UV-Vis-NIR spectrophotometer. Samples were diluted as required with the final spectrum adjusted to reflect the original concentration or normalised within a sample set for clarity. UV-Vis-NIR spectra have been measured using polymer, optical glass or quartz cuvettes throughout my work.

With respect to my experiments for measuring the kinetics of a gold nanorod solution during the growth process, the initial optical density is not great enough to provide a measureable spectrum when using a cuvette of 1 cm path length. Therefore, the earliest stages of the growth were monitored using a 10 cm path length, water-jacketed, quartz cuvette sourced from Starna. For later times a 1 cm quartz cuvette was placed in the spectrophotometer which contained an unmodified aliquot of the same growth solution. The temperature of the solution was maintained at $30℃$ for the duration of the reaction. This was achieved for the 10 cm path length cuvette by circulating thermostatted water through the water jacket by use of a water bath and tubing. Continuous flow of the solution was achieved by using a Gilson minipuls 3 peristaltic pump. The spectrophotometer has a thermostatted 1 cm cuvette holder.

I have labelled the UV-Vis-NIR spectra for the nanoparticle samples presented herein as absorbance as this is the primary contribution to the extinction properties. Any contributions likely due to scattering are noted where relevant.

2.3.4 SEM

Samples were prepared for SEM imaging by a drop cast/desiccation method. First a 1.5 mL aliquot of nanoparticle sample was taken and centrifuged at a minimum of $10{,}000$ rpm, at least twice. Following each intermediate centrifugation the supernatant was decanted and discarded, the pellet was redispersed with ~ 1.5 mL ultrapure water. After the final centrifugation ~ 0.1 mL of ultrapure water was added to redisperse the nanoparticles. Using a drop cast method a $2-3$ μL aliquot of the concentrated pellet was deposited onto a small piece of silicon wafer that was fixed to an aluminium stub with an adhesive carbon tab. Conductive silver paint was used to ensure a good

electrical connection between the silicon and SEM stub. I then placed the sample in a desiccator for a minimum of 24 hours. I measured SEM images using a Zeiss Supra 55VP FE-SEM under high vacuum, $\sim 10^{-5}$ torr, at $5 - 20$ keV accelerating voltage.

SEM images have been selected throughout this thesis to reflect the population of nanorods present. Not all samples have a high proportion of nanorods but this is indicated by the absorbance spectrum for each respective sample. It is extremely difficult to obtain a quantitative particle distribution from the SEM images of these samples as different nanoparticle geometries can accumulate in different regions of the substrate.

Nanoparticle measurements from SEM images were performed manually using the image analysis software ImageJ[p]. An algorithm for extracting length and width data for rod shaped objects from digital images has been written by Dougherty[q]. However, this was not used for the bulk of my analysis for the reasons discussed in Appendix A.

I have also performed a kinetic observation of growing gold nanorods using the SEM. A growth solution with 0.60 mM H_2A was prepared according to GS method B and the growth was initiated with 10 µL of freshly prepared gold nanoparticle seed B. This concentration of H_2A was selected to reduce the rate of the reaction. At numerous times throughout the reaction ($1, 5, 10, 15, 20, 30, 40, 50$ and 60 minutes) a 1 mL aliquot of the solution was removed and centrifuged at $13{,}000$ rpm for 2 minutes. The supernatant was decanted and discarded then the pellet was redispersed with ultrapure water. At this point the vast majority of the unreacted $AuBr_2^-$ should have been removed from the solution. The aliquot was then centrifuged for a further 5 minutes at $13{,}000$ rpm. Upon removal of the supernatant the pellet was redispersed in 100 µL of ultrapure water. A $2 - 3$ µL aliquot of this was deposited onto a small piece of silicon wafer and placed into a desiccator. The $1, 5, 10$ and 30 minute samples were imaged in the SEM. No nanoparticles were observed at 1 minute or less.

2.3.5 Cryo-TEM

Cryo-TEM experiments[r] were performed to probe the early stages of development of gold nanorods. Images were taken using an FEI TECNAI F30 G2 TEM at 300 keV using a liquid nitrogen cooled sample stage under high vacuum. Images were captured with a Direct Electron™ lens coupled CCD camera.

For the cryo-TEM experiments I prepared two nanorod growth solutions according to procedure GS method B with 0.60 mM H_2A and 0.65 mM H_2A respectively. The nanorod growth was initiated by adding 10 µL of freshly prepared seed B.

[p] http://rsb.info.nih.gov/ij/

[q] Dougherty (http://www.optinav.com/Measure-Roi.htm)

[r] Operation of the cryo-TEM and cryo-sample preparation was performed by Dr Matthias Flöttenmeyer at the University of Queensland. This work was performed with funding provided by the AMMRF travel and access program; grant number #9052

TEM samples were prepared with the aid of an FEI Vitrobot system to ensure reproducible sample conditions. $2-3$ μL of sample was taken and placed on a TEM grid. The TEM grid was held in a controlled environment at 30℃ and 100% relative humidity. A blotting time of 8 s was used to achieve an ice thickness of $\sim 50-100$ nm. After blotting, the TEM grid was plunged into a bath of liquid ethane to form a layer of vitreous ice. Multiple grids were prepared and subsequently stored in liquid nitrogen. A limiting factor in this procedure is the requirement to re-liquefy the ethane after ~ 10 minutes. For the sample preparation no chemical changes were made to the standard growth solution as well as maintaining the reaction conditions for the samples observed with UV-Vis-NIR spectroscopy. Aliquots of the seeded growth solution were prepared at various time points to monitor the variation of the nanoparticle dimensions with respect to time.

2.3.6 TEM

Images of gold nanorings were collected[s] using a Phillips CM 120 Biofilter TEM. An accelerating voltage of 50 – 370 keV was used. Sample grids were prepared by a drop cast/drying method.

2.3.7 Estimation of nanorod dimensions from a UV-Vis-NIR spectrum

I have written a Mathematica script to calculate the average dimensions of a gold nanorod suspension from the UV-Vis-NIR spectrum and concentrations used for the synthesis. An example of the script is provided as Appendix A.

Briefly, the number of nanorods in the solution is estimated by dividing the number of Au^0 atoms in the added seed solution (determined from the concentration) with the number of Au^0 atoms in an ~ 2 nm diameter seed. There are some spheres produced in the reaction as by-products, however, as there is no way to separate an accurate diameter for the spheres i.e. an accurate volume, I assume that they have the same volume as the nanorods.[t] The volume of each nanorod is then determined using the number of particles in the solution and the concentration of gold as estimated from the absorbance at ~ 390 nm. The aspect ratio, AR, is calculated from the longitudinal peak position, λ_L, using the following equation:[u]

$$\mathrm{AR} = (0.0084 \times \lambda_{\mathrm{L}}) + 3.1081 \qquad 2.4$$

[s] Operation of the TEM was performed by Dr Annette Dowd at the University of Sydney.

[t] For a nanorod of 8000 nm^3 this corresponds to a sphere with a diameter of ~ 25 nm, not unrealistic.

[u] This equation was determined from an extensive set of DDA calculations for gold nanorods approximated by a hemi-spherically capped cylinder.

A hemi-spherically capped cylinder has been used as the model geometry for the nanorod and $AR = \frac{\mathrm{L}}{2\times\mathrm{r}}$ to produce an equation for the volume of a gold nanorod, V_{GNR}, where the only unknown variable is the radius:

$$\mathrm{V_{GNR}} = 2\pi r^3 \left(\mathrm{AR} - \frac{1}{3}\right) \qquad 2.5$$

This rearranges to give:

$$\mathrm{r} = \sqrt[3]{\frac{\mathrm{V_{GNR}}}{2\pi\left(\mathrm{AR} - \frac{1}{3}\right)}} \qquad 2.6$$

The length is calculated using the aspect ratio equation.

As with the calibration of Au^0 described previously, I have compared the particle dimensions calculated with my Mathematica script to the published values of Orendorff *et al*. The values for aspect ratio and seed diameter (3 nm) have been taken from their published data. The concentration of Au^0 has been calculated from their optical data using my factor to determine the volume of each nanorod. Table 2-2 compares the results produced by my Mathematica script with the published values for the nanorod dimensions as measured by TEM. The agreement for all but the shortest rods is very good. The deviation in the case of the shortest rods may be due to their shapes not complying with the hemispherically-capped right cylindrical model or that the population of nanorods is much lower for this sample (as indicated by the absorbance spectrum).

Table 2-2 Nanorod dimensions calculated using my Mathematica script compared to TEM measurements

Aspect Ratio	Mathematica		TEM	
	D (nm)	L (nm)	D (nm)	L (nm)
2.0	14.9	29.7	18.2	36.0
2.9	13.7	39.7	14.3	41.1
3.5	12.4	43.6	12.3	42.0
4.5	11.3	50.8	11.8	52.5

2.3.8 Small-Angle X-Ray Scattering

Small-angle x-ray scattering measurements[v] have been performed on a growing gold nanorod solution as well on the various liquid components of the synthesis.

[v] SAXS data was recorded at the SAXS/WAXS beamline of the Australian Synchrotron using an X-ray wavelength of 1.1985 nm by Dr Nigel Kirby with assistance provided by Dr David Cookson and Dr Catherine Kealley.

All SAXS measurements were recorded at constant temperature. To achieve this I constructed flow cells from a combination of Kapton (polyimide, inner diameter 1.46 mm) and Tygon (PTFE, inner diameter 1.6 mm) tubing – John Morris Scientific. Briefly, two lengths of Tygon tubing were glued to either end of a section of Kapton tubing, $\sim 3-4$ cm. The other end of each length of Tygon tubing was then inserted into the reaction/storage vessel. The temperature of the reaction vessel was controlled by placing it in a water bath at $30℃$. Continuous flow of the solution was achieved by using a Gilson minipuls 3 peristaltic pump. The total volume of the flow cell did not exceed ~ 5 mL. The volume of each sample measured was 10 mL.

For measurement of the samples the Kapton tubing section was placed in the beam path.

Data was recorded at two camera lengths, 1 m and 8 m, on all samples to increase the range of data collected to cover the size ranges that I had predicted for the system.

The raw synchrotron data (2D scattering image) was reduced using Wavemetrics data analysis software IGOR Pro 6.0 and the analysis package Irena.[291] Two methods have been used to determine the radius of gyration, $\mathrm{R_g}$. I manually constructed Guinier plots with values directly from the ASCII data file from the output of the data reduction. Also, I used the small-angle scattering analysis software PRIMUS.[292] Primus is a component of the software suite ATSAS developed by Svergun *et al*.[293] PRIMUS was also used to determine the Porod volume.

SAXS data was also obtained using a smaller, lab-based setup,[w] the results of which are not presented in this thesis. In these lab experiments it was noted that there was some interaction of the X-ray beam with the sample indicated by a coloured spot on the wall of the quartz capillary with the dimensions of the incident beam. This problem was addressed by using a polymer capillary, polyimide, and flushing the capillary with $\mathrm{C_{16}TABr}$ solution for the synchrotron experiments to prevent nanoparticle adsorption.

2.4 Simulation of Optical Properties

2.4.1 DDSCAT

I have used an implementation of the discrete dipole approximation, DDSCAT,[64, 294] to simulate the optical properties of gold nanorods and gold nanorings. This method has been used to validate my new growth model by simulating the proposed intermediate particle geometries observed in cryo-TEM experiments. The results of these calculations have been compared directly to experimentally measured data.

The extinction spectra I have calculated have been for gold nanoparticles in water. For these simulations the gold dielectric table provided by Weaver and Frederikse[295] has been used. As these values are determined for gold in a vacuum they must be adjusted

[w] Lab SAXS data was recorded at ANSTO by Dr Tracey Hanley and Dr Catherine Kealley.

by complex number division with the dielectric table for water. The complex dielectric table for this modification was obtained from the software application MiePlot and represent the optical properties of water at a temperature of $20°C$.

The wavelengths for the calculation must be modified for the refractive index shift from air to water for input into DDSCAT. This is achieved by using the equation:[x]

$$\lambda_{water} = \frac{(\lambda_{air} - 0.0143)}{1.2995} \qquad 2.7$$

The units for wavelength in Equation 2.4 and for the input into DDSCAT are micrometres, µm. For the conversion of the output, Equation 2.4 is rearranged to solve for λ_{air}.

I used an evaluation version of CurveExpert[y] to interpolate the calculated data within the upper and lower bounding wavelengths at an interval of 1 nm. A cubic spline was used for the interpolation. The interpolated data was used to simplify the combination of the spectra to approximate the mixed dispersions of intermediate geometries and to smooth the curve.

I used desktop PCs[z] with Microsoft Windows XP or 7 as the operating system to run the DDSCAT calculations.

2.4.1.1 Gold Nanorods and Intermediate Geometries for Growth Model

The program CryoRods has been used to generate the target geometries for input into DDSCAT. This program was authored by Prof. Michael B. Cortie and was written to create DDSCAT shape files for the geometries that were observed in the cryo-TEM experiments.

A wavelength range of $350 - 800$ nm (with an interval of 12.5 nm) has been used for all the calculations of the extinction properties of the intermediate and nanorod geometries in my new growth model (Section 5.1.5). The results were evaluated to locate the longitudinal peak position for each particle and selected wavelengths around this position in smaller intervals to improve the definition of the peak. The calculated data was extended to 900 nm, with a maximum of $3 - 4$ wavelengths, for each particle to match the UV-Vis-NIR spectra. All the intermediate and nanorod geometries have been calculated at three orientations and the contribution from each has been averaged to approximate a randomly oriented dispersion of nanoparticles.

The intermediate nanoparticle geometries have been designated as bow-tie (BT), conically-capped bow-tie (CBT), conically-capped cylinder (CC) and spherically-capped

[x] This correlation was determined by Prof. Michael B. Cortie.
[y] http://www.curveexpert.net/
[z] I ran some of the calculations using the personal computer of Aiden Ichsan. Also some calculations were run by Prof. Michael B. Cortie.

cylinder (SC). A schematic of the cross-sections of each nanoparticle with their defining parameters are illustrated in Figure 2-3.

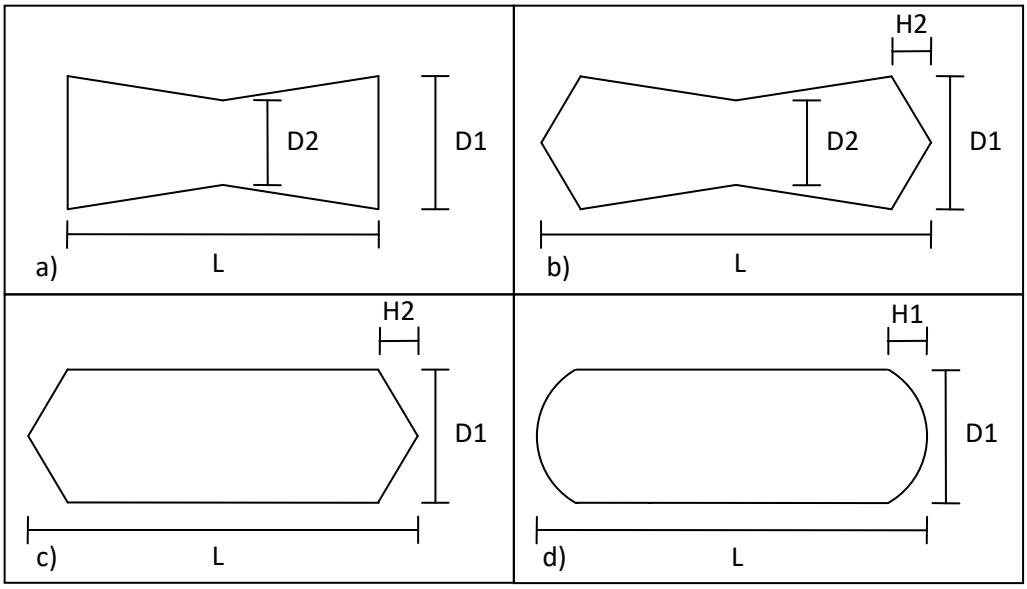

Figure 2-3 Nanoparticle cross-sections of the geometries calculated for my new growth model indicating the parameters used to define the structure. a) Bow-tie (BT), b) conically-capped bow-tie (CBT), c) conically-capped cylinder and d) spherically-capped cylinder.

I initially calculated the intermediate geometries where the BT was the most basic and then conical end-caps were added to this for CBT, this was followed by filling in of the waist of the nanorod, CC, and finally a spherically-capped cylinder, SC, Figure 2-4. The parameters that were used for the calculations in Figure 2-4 can be found in Table 2-3.

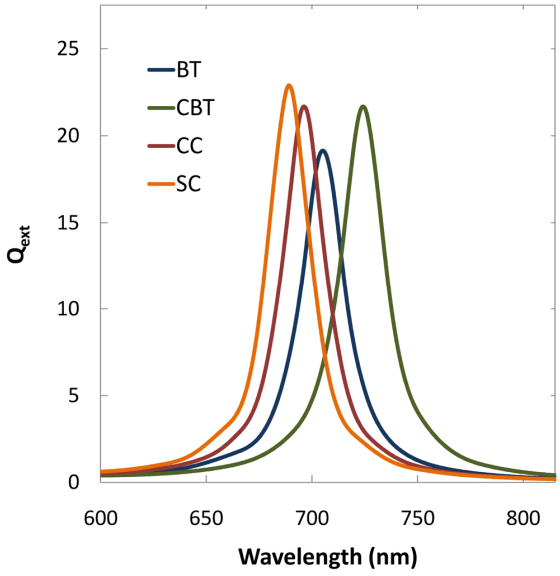

Figure 2-4 Extinction spectra for the intermediate nanoparticle geometries calculated using DDSCAT.

Table 2-3 Nanoparticle parameters used for the test calculation of the intermediate geometries

Particle	Length, L (nm)	Diameter, D1 (nm)	Diameter, D2 (nm)	Spherical Cap, H1 (nm)	Conical Cap, H2 (nm)
BT	33.1	15.5	14.0	-	0.0
CBT	46.1	15.5	14.0	-	6.5
CC	46.1	15.5	-	-	6.5
SC	46.1	15.5	-	6.5	-

From this test calculation I noticed that this particle progression provided the same trend observed in the UV-Vis kinetics of the nanorod reaction i.e. red shift followed by sustained blue shift. The wavelength shift, however, was significantly lower than observed for experiments and so this was accounted for by adjusting the particle volumes and relative aspect ratios to increase the shift and mimic the experimental data. The nanoparticle dimensions used for the model geometries are presented in Table 2-4.

To fit the simulated data to the experimental data I applied several rules that were defined from observations of the experimental measurements. These rules are presented with the discussion of the analysis in Section 5.1.5.

Table 2-4 Nanoparticle dimensions used for the DDSCAT calculations.

Particle	Length, L (nm)	Diameter, D1 (nm)	Diameter, D2 (nm)	Spherical Cap, H1 (nm)	Conical Cap, H2 (nm)
BT	30.0	12.0	10.5	-	0.0
CBT1	38.3	13. 5	11.8	-	2.2
CBT2	46.7	14.6	12.8	-	4.3
CBT3	55.0	15.5	14.0	-	6.5
CBT4	54.9	15.8	14.8	-	6.5
CBT5	54.7	16.2	15.7	-	6.5
CC1	54. 6	16.5	-	-	6.5
SC1	49.3	16.8	-	6.5	-
SC2	47.7	17.2	-	6.5	-
SC3	46.1	17.5	-	6.5	-
SC4	44.6	17.8	-	6.5	-
SC5	43.1	18.2	-	6.5	-
SC6	41.6	18.6	-	6.5	-

2.4.1.2 Gold Nanorings

DDSCAT has also been used to simulate the optical extinction properties of an aqueous dispersion of gold nanorings of different aspect ratios.

The Cartesian equation for a torus was used to build the shape[aa] for the input file for DDSCAT calculations of gold nanorings:

$$\left(R - \sqrt{x^2 + y^2}\right)^2 + z^2 = r^2 \qquad 2.8$$

r is equal to half the thickness of the nanoring, i.e. $r = \frac{t}{2}$, and R is equal to the outer diameter minus r i.e. $R = OD - r$. x, y and z are the familiar algebraic stand-ins for coordinates on a Cartesian axis.

To ensure all modes were investigated I used two orientations. Subsequently, two polarisations for each orientation were calculated. The orientation was altered in the shape file prior to input into DDSCAT whereas the polarisation was set in the parameter file. The results from each polarisation and orientation were averaged to approximate a random dispersion of nanorings.

The aspect ratio, inner and outer diameters of the nanorings that have been calculated are presented in Table 2-5.

Table 2-5 Size Parameters for Gold Nanoring Simulations

Aspect Ratio	Outer Diameter (nm)	Inner Diameter (nm)
3	30	10
4	40	20
5	50	30

2.4.2 MiePlot

MiePlot is an implementation of Mie theory, an analytical solution to Maxwell's equations for the interaction of electromagnetic waves with spherical particles of a desired diameter (nm to µm). MiePlot provides a convenient platform for determining the optical properties of metallic nanospheres. I have used MiePlot to calculate the optical properties of platinum nanospheres to compare with experimentally obtained spectra.

For the simulation of the extinction properties of platinum nanospheres in an aqueous solution I have used the built-in complex dielectric function for water at $25℃$ and $n = 1.4961$ for calculations in toluene.[295]

2.5 POV-Ray Diagrams of Gold Nanoparticles

POV-Ray is an abbreviation of Persistence Of Vision – Raytracer. It is an open source program which allows the three dimensional construction and observation of user-defined structures. POV-Ray has an extensive array of built-in features for constructing

[aa] I generated the shape file using an Excel spreadsheet and macro authored by Dr Martin G. Blaber.

shapes as well as directives for applying a multitude of textures, finishes and other media properties. There are also directives such as loops and functions for construction of periodic features.

For some of the diagrams of gold nanoparticles throughout this thesis I have used a POV-Ray scene that I created to illustrate their crystallographic structure. The POV-Ray code for my gold nanoparticle generator is presented as Appendix .

The FCC structure of gold has been replicated using nested while loops to place 'atoms' in the correct lattice positions for a pre-defined set of boundaries. In the simplest form of the scene these boundaries are simply the number of unit cells to draw in the x, y and z axes. I have set the lattice parameter equal to one to reduce any issue with rounding errors in the placement of atoms and so any dimensions in the scene must be converted from nanometres accordingly with a factor of ~ 2.45, i.e. 1 nm $= \sim 2.45$ units.

To achieve a simple geometry of nanoparticle e.g. a sphere, an #IF statement can be inserted into the innermost while loop which contains the Cartesian equation for the desired geometry. The condition for the #IF statement is that IF the coordinates satisfy the equation then an atom is drawn, else, it moves to the next set of coordinates etc. In this case the dimensions of the particle are inserted into the Cartesian equation e.g. for a sphere the equation is equal to the radius squared. For structures with particular crystallographic facets an #IF statement can be included for each crystal face. This increases the computation time by a factor of about five for particles with approximately the same number of atoms. The time taken for the simple case is ~ 1 minute and the crystal facet case ~ 5 minutes. This includes parsing and rendering time. In its current form the POV-Ray scene generates the crystallographic structure published by the group of Luis Liz-Marzán (Figure 2-5).[87]

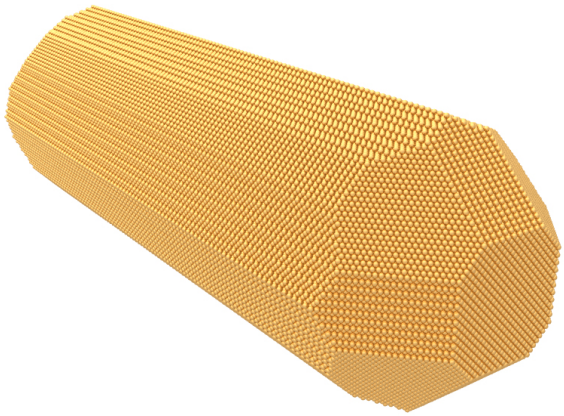

Figure 2-5 Gold nanorod with <052>, <025> and <011> side facets,<110> and <111> end-caps and the growth direction <100>

3 Other Precious Metal Colloids

The bulk of this thesis focuses on the formation and characterisation of gold nanorods. However, the initial brief of the project was to investigate a wide range of precious metal nanoparticles with a view to selecting types that would be most interesting for possible commercial development. Therefore, during the course of my work I also prepared colloids of gold nanorings and nanocages, silver nanorods and platinum nanospheres.

As discussed previously (Section 1.2.1), the optical properties of metal nanoparticles are heavily dependent on the composition and geometry of the nanoparticle in question. Using metals other than gold and/or changing the geometry of the nanoparticle, with respect to nanorods, allows access to different resonance wavelengths and/or geometric properties. For example, silver nanospheres have a resonance position, in vacuum, at 361 nm for a radius of 23 nm which provides the optimum absorption efficiency, Q_{abs}.[296] For silver nanospheres in an aqueous environment this resonance will shift to ~ 400 nm. This implies that for silver nanorods (or nanoshells) the entire visible spectrum is accessible as the longitudinal resonance position may be red-shifted from the transverse resonance position by the aforementioned modifications to the geometry (Section 1.2.1). However, silver metal is much more chemically reactive than gold and so the nanoparticles may require extra treatment to maintain the desired optical properties.

Platinum nanoparticles exhibit the weakest plasmonic response of the noble metals.[16] Therefore, despite having high nobility, the use of platinum as a plasmonically active metal is unusual. However, the catalytic properties of platinum are extremely potent.[297, 298] Also, due to platinum's high conductivity it would also be possible to employ platinum nanoparticles as sinterable inks for microelectronic applications.[299-301]

In this chapter I present methods for preparing gold nanorings and nanocages, silver nanorods, and platinum nanospheres. Simulations are used in part to help characterise the optical properties of nanorings and platinum nanospheres. The optical absorbance spectra of silver nanorods are compared with those from literature. Issues that arose during the course of preparation are also mentioned.

3.1 Gold Nanorings

Hollow gold nanoparticle analogues can be formed for any geometry of silver nanoparticles[108, 302, 303] This is achieved by using a galvanic replacement reaction popularised by Xia *et al*.[108, 140] The replacement takes place according to the following reaction:[108]

$$3\mathrm{Ag}^0 + \mathrm{AuCl}_4^- \rightarrow \mathrm{Au}^0 + 3\mathrm{Ag}^+ + 4\mathrm{Cl}^- \qquad 3.1$$

This synthesis allows for the preparation of nanoshells, effectively, with the geometry limited only by the template nanoparticle. The nanoshell formed is not a pure gold shell as there is some silver remaining which forms an alloy with the gold. This fact is highlighted in the dealloying of the nanoshells by further addition of gold salt which forms pinholes in the shell.[140]. The pinhole formation can be prevented by using $AuCl_2^-$ in place of $AuCl_4^-$, which results in a $1:1$ stoichiometry ($Ag:Au$) and subsequently causes less reconstruction in the developing nanoshell. [145] However, using $AuCl_2^-$ results in a broader range of shell thicknesses as the pinholes give more evenly distributed access to the remaining silver.

Figure 3-1 shows a schematic for the galvanic replacement reaction. Steps 5 and 6 illustrate the effect of adding $HAuCl_4$ after the formation of the continuous Au/Ag alloy shell.

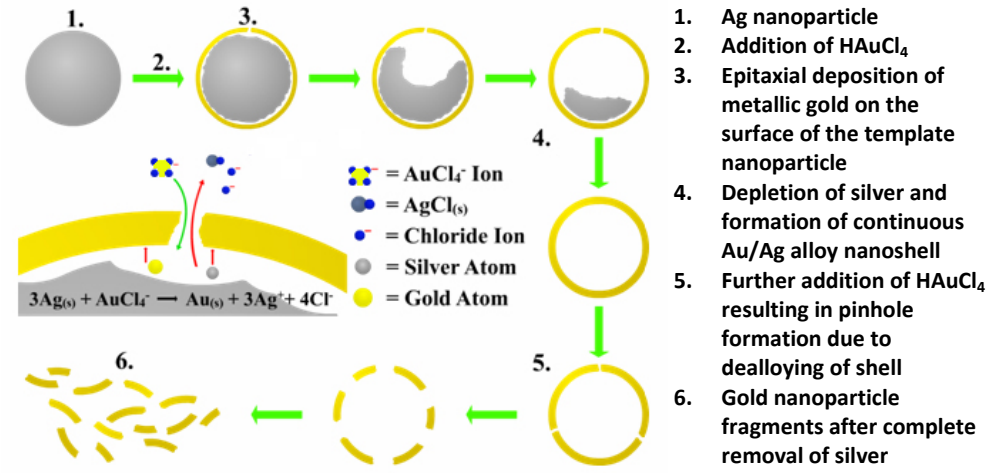

Figure 3-1 Schematic for the formation of a hollow Au/Ag nanoparticle by the galvanic replacement of a silver nanoparticle template. Modified from [142]

During the dealloying process it is possible that the pinholes are positioned such that a gold nanoring is eventually formed.[144, 145] For template particles such as spheres and cubes this nanoring formation appears to be predominantly fortuitous. However, if a plate-like template particle is used then the gold will epitaxially deposit on the perimeter, forming a ring.[302, 303] Gold nanorings have also been prepared by colloidal sphere lithography,[304-306] imprint lithography[307] and electron beam lithography.[308, 309]

The optical properties of gold nanorings arise from the hybridisation of dipolar modes at the inner and outer surfaces of the nanoring.[304] Analogous to nanoshells, the plasmon resonance is dependent on the ratio between the outer diameter and thickness (i.e. difference between inner and outer radius).

Gold nanorings also exhibit a strong near-field enhancement and have been shown to provide a strong SERS enhancement.[304, 306]

3.1.1 Results and Discussion

Template nanoparticles used for the galvanic replacement in aqueous solutions typically have dimensions of ~ 25 nm (cobalt template),[142] ~ 20 nm,[310] ~ 50 nm,[108] ~ 75 nm[140] and ~ 100 nm.[141, 145]

I prepared particles by a method analogous to that used in the preparation of gold nanoparticle seeds for the synthesis of gold nanorods in an attempt to reduce the size of the silver template (synthesis details can be found in Section 2.2.3). I did not characterise the diameter of the silver template nanoparticles directly, however, the inner diameter of the resulting gold nanoparticles is a close indicator of the original diameter as the initial gold coating is deposited epitaxially.[141] The silver template particles do not have a long lifetime at ambient conditions in a high halide solution and therefore no further characterisation was performed e.g. SEM.

Figure 3-2 shows the UV-Vis spectra for silver template nanoparticles (pre$-\mathrm{Au}^{3+}$ addition) and the resulting Au-Ag alloy particles (post$-\mathrm{Au}^{3+}$ addition). I prepared the gold nanoparticles according to the procedure in Section 2.2.3 with 50 mL of "Template 1" and 2.5 mL of 1 mM $\mathrm{HAuCl_4}$ solution.

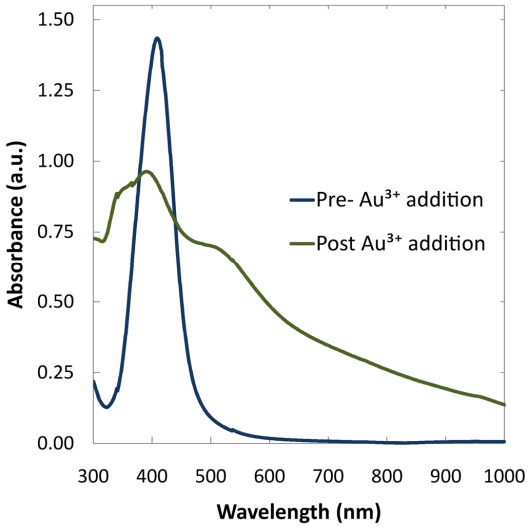

Figure 3-2 Spectra for nanoparticles pre- and post addition of $\mathrm{HAuCl_4}$

To prepare the post$-\mathrm{Au}^{3+}$ sample in Figure 3-2 I purposely added less than a stoichiometrically equivalent amount of gold ($\sim 5:1, \mathrm{Ag:Au}$) in an attempt to produce a distribution of Au/Ag hollow nanoshells. By adding this amount of gold there would inevitably be unreacted silver present somewhere in the solution. From the nanoparticle spectra it would seem that there are silver nanoparticles remaining in solution (or nanoparticles with significant silver content) due to the peak contributions around 400 nm.

Figure 3-3 and Figure 3-4 show TEM and SEM images, respectively, of the nanoparticles after the reaction with $\mathrm{AuCl_4^-}$.

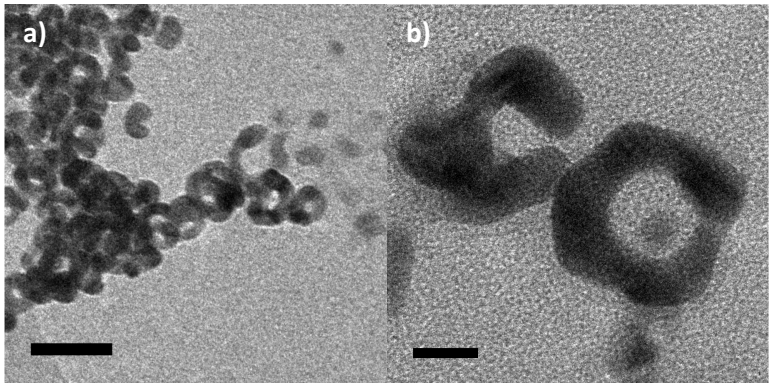

Figure 3-3 a) Low and b) high resolution TEM images of gold nanorings. Scale bars 50 nm and 10 nm for a) and b) respectively. Images courtesy of Dr A. Dowd.

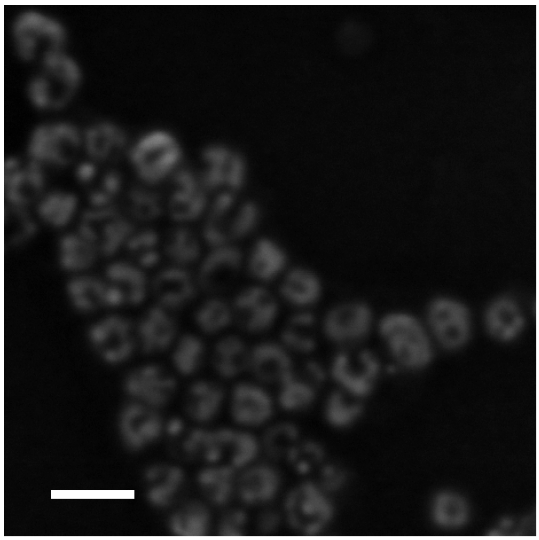

Figure 3-4 SEM image of gold nanorings and cages. Scale bar = 50 nm.

It is clear from these images that there is a mixed population of nanoparticles with nanorings, nanocages and fragmented particles representative of the distribution. This would signify, considering the mechanism of formation (Figure 3-1), that some template particles have reacted completely, due to the presence of fragmented and pin-hole nanoparticles (Figure 3-3 and Figure 3-4), and some not at all. A potential contributor to this effect is the high concentration of bromide in the reaction solution which may also cause the dealloying of silver from the nanoshell resulting in fragmentation.

I also prepared silver nanoparticle templates in the presence of $C_{16}TABr$ and tri-sodium citrate to investigate the effects of the stabilising surfactant on the geometry of the gold nanoparticles formed by the galvanic replacement reaction. I prepared the $C_{16}TABr$ stabilised silver template nanoparticles according to the method “Template 1” and the tri-sodium citrate silver nanoparticles according to “Template 2”, Section 2.2.3. For the galvanic replacement reaction I added 1 mL of 1 mM $HAuCl_4$ to ~ 20 mL of each template nanoparticle solution. Figure 3-5 displays the absorbance spectra for the gold

nanoparticles prepared by galvanic replacement of silver nanoparticles stabilised with $C_{16}TABr$ and tri-sodium citrate, respectively.

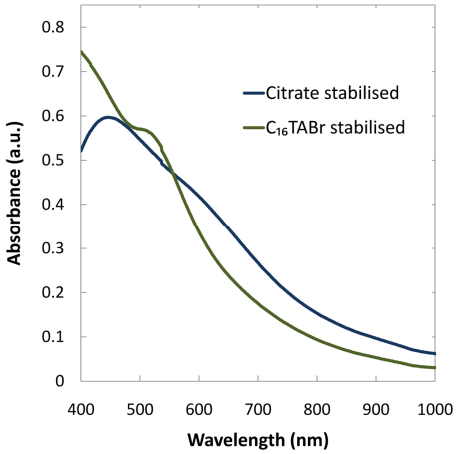

Figure 3-5 Gold nanoparticles prepared by galvanic replacement of silver nanoparticles stabilised with citrate and C_{16}TABr molecules respectively

The absorbance spectrum for the gold nanoparticles prepared in the presence of tri-sodium citrate show a peak absorbance at ~ 440 nm with a shoulder at ~ 590 nm. The position of these two peaks indicates that there are Au/Ag alloy nanoparticles/nanoshells and gold nanocages or nanorings. SEM images of this sample show that there is a mixture of disc-like nanoparticles and nanorings, Figure 3-6a.

The absorbance spectrum for the gold nanoparticles prepared in the presence of $C_{16}TABr$ produces a shoulder peak at ~ 520 nm (data for these samples was not measured below 400 nm as the main aim was to compare the effect on gold nanoparticle formation). This peak could be due to Au/Ag alloy nanoshells but is probably more likely due to fragmented particles which should express a plasmon peak similar to spherical particles. The SEM images of this sample also show the presence of some nanorings with fragmented nanoparticles (Figure 3-6), as for the sample presented in Figure 3-3 and Figure 3-4.

The absence of fragmented nanoparticles for the galvanic replacement reaction in the presence of tri-sodium citrate indicates that bromide could be affecting the silver present in the alloyed nanoparticles.

Following the observation of the nanorings in the above samples, I used DDSCAT to approximate the extinction properties of randomly oriented, aqueous dispersions of nanorings with varied aspect ratios (Figure 3-7). The dimensions used for the calculations can be found in Section 2.4.1.2.

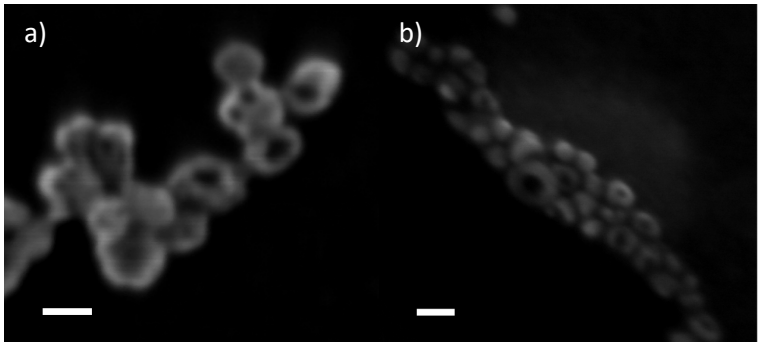

Figure 3-6 SEM images of nanorings prepared from a) citrate stabilised and b) C_{16}TABr stabilised silver nanoparticles. Scale bars = 20 nm

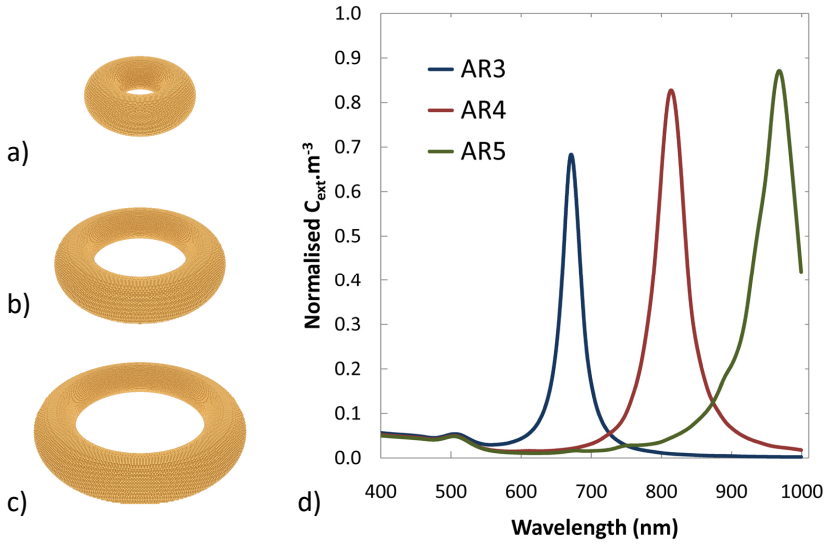

Figure 3-7 Diagrams of gold nanorings with aspect ratios equal to a) 3, b) 4 and c) 5 respectively. d) Corresponding extinction spectra for dispersions of gold nanorings of different aspect ratios calculated with DDSCAT

In the present work the aspect ratio of a nanoring, $\mathrm{AR_{ring}}$, was defined as the ratio of the outer diameter, *OD*, to the ring thickness, *t*:

$$\mathrm{AR_{ring}} = \frac{OD}{t} \qquad 3.2$$

From Figure 3-7 it can be seen that nanorings exhibit two plasmon modes. The low intensity peak at ~ 510 nm corresponds to oscillations across the plane of the nanoring and is independent of aspect ratio. The dominant peak of the extinction spectrum is attributed to oscillations within the plane of the nanoring and is proportional to the aspect ratio.

Figure 3-8 shows a schematic for the calculation of the extinction properties of a gold nanoring. The nanoring is oriented in the *YZ* plane with the wave propagating in the *+X* direction and polarised in the Z axis.

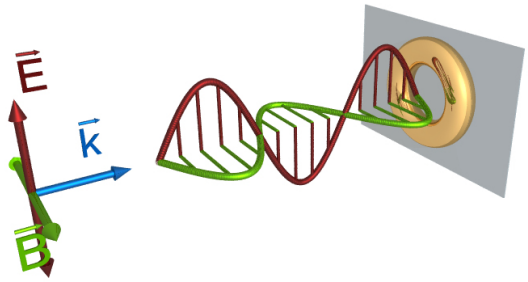

Figure 3-8 Gold nanoring oriented in the *YZ* plane (grey area) with incident EM wave travelling in the *+X* direction and polarised in the Z axis

The extinction spectra for all the calculated orientation and polarisation combinations are illustrated in Figure 3-9. This plot indicates that nanorings are polarisation independent when oriented perpendicular to the angle of incidence of the propagating EM wave (as in Figure 3-8) and polarisation dependent if oriented parallel.

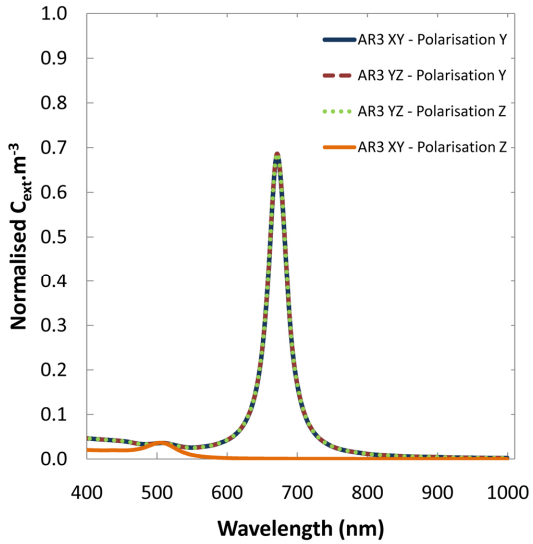

Figure 3-9 Plasmon resonance peaks for an aspect ratio 3 gold nanoring in various orientations. The traces are labelled for the respective plane of orientation and incident polarisation of incident light for a wave propagating in the x direction

Intensities in the calculated extinction spectra are more than likely overestimated due to the small size of the nanorings and the exclusion of surface scattering effects in the DDSCAT calculations. The mean free path of electrons for bulk gold and silver are of the order of 40 – 50 nm.[269] Oscillating electrons in nanoparticles smaller than this distance will suffer plasmon damping due to surface scattering events which reduces the intensity of the absorption and increases the peak width. Despite the thickness of each ring being 10 nm, the effective mean free path, l_{eff} (for surface interactions), is slightly greater and can be approximated using an expression determined for nanoshells by Granqvist and Hunderi[311] (as cited by Mulvaney).[312]

$$l_{eff} = \frac{\sqrt[3]{(d_{shell} - d_{core})(d_{shell}^2 - d_{core}^2)}}{2} \qquad 3.3$$

The effective mean free path, as estimated using Equation 3.3, for the nanorings calculated here are 12.6, 14.4 and 15.9 nm for aspect ratio 3, 4 and 5 nanorings respectively.

3.1.2 Summary

With some refinement, the wet chemical synthesis I have presented here could provide a route to producing large quantities of gold nanorings with well-defined dimensions. When compared to nanorings prepared by lithographic techniques, the nanorings produced here will have a significantly smaller scattering contribution as they are well within the quasistatic limit. However, lithography has the advantage of being able to prepare 'identical' nanorings in ordered arrays, in principal, over large areas.

Nanorings can show a well-developed plasmon resonance that can be either dependent or independent of polarisation depending on their orientation with respect to incident light. Nanorings dispersed on a two dimensional substrate oriented with their plane parallel to the substrate (i.e. flat) will be independent of the polarisation of incident light (for an angle of incidence of 90^o). However, for rings oriented perpendicular to the substrate the transverse and planar plasmon modes may be excited selectively by changing the polarisation. From this characteristic the optical properties of gold nanorings can be considered a hybrid of gold nanorods and nanoshells.

The efficacy of the optical properties of gold nanorings has been proven for applications such as SERS,[304] however, due to their tuneable nature they could also be used in the same applications as nanorods and nanoshells (see Section 1.5.6).

3.2 Silver Nanorods

Silver nanorods were synthesised with a wet chemical, seed-mediated growth procedure, originally published by the same group (Murphy *et al*.[289]) that had pioneered the currently used synthesis for gold nanorods. A key difference to the gold nanorod synthesis (Chapter 4) is the requirement for the synthesis to be performed at high pH. This is due to the inability of ascorbic acid to reduce Ag^+ at low pH. The reduction potential of ascorbic acid increases with increasing pH[313, 314] (as does the degree of dissociation). Also, in contrast to gold nanorods, the aspect ratio of the silver nanorods is increased with decreasing volume of seed solution. This implies a radically different formation mechanism.

The optical properties of silver are well known to provide a significantly enhanced plasmonic performance with respect to gold and many other plasmonic metals.[16, 315, 316] This is due, in part, to the diminished effect of interband transitions as indicated by smaller values in the imaginary part of the dielectric function, ϵ'', (Figure 3-10).[31, 316]

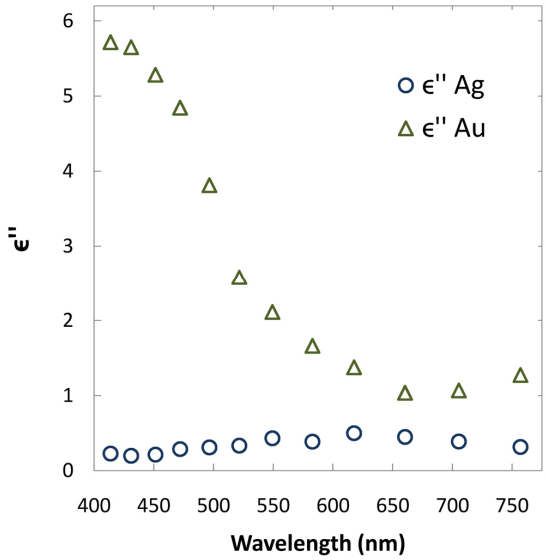

Figure 3-10 Comparison of the imaginary part of the complex dielectric functions for silver and gold. Data from reference [295]

This feature of the dielectric function of silver implies that it should have a high performance in proposed optical applications such as superlenses (which could provide sub-wavelength features for optical lithography[317]) and metamaterials.[315] It also causes a decreased peak width[33] for silver nanoparticles with respect to other metals.

Although silver outperforms gold optically, use of silver nanoparticles in medical applications is not common, despite very good bactericidal properties[318], as they show size dependent toxicity where gold nanoparticles do not.[319]

3.2.1 Results and Discussion

The experimental procedure used for the original silver nanorod synthesis was identical to that of the original gold nanorod synthesis, where an aliquot of a tri-sodium citrate-stabilised seed ($\sim 3-4$ nm diameter) solution is added to a growth solution. The seed solution was modified in a later publication to utilise Au/Ag seed particles of ~ 1.5 nm diameter, although, the stabiliser was not mentioned.[19] The effect of this seed particle on the range of aspect ratios was not published.

I decided to use C_{16}TABr-stabilised seeds in place of tri-sodium citrate or Au/Ag seeds to see if this provided a similar enhancement to the silver nanorod synthesis analogous to the effect observed for the gold nanorod synthesis.[21] Synthesis conditions for the silver nanoparticle seed may be found in Section 2.2.4.

Figure 3-11 shows a comparison for the UV-Vis spectra of tri-sodium citrate and C_{16}TABr-stabilised silver nanoparticles respectively. Both spectra exhibit a peak position at the expected resonance wavelength of ~ 400 nm, however, the citrate stabilised nanoparticles have a sustained contribution across the entire visible spectrum into the near-infrared. This implies a mixture of particle shapes with varied geometries which have a red-shifted plasmon resonance with respect to spheres, e.g. disc-shaped nanoparticles.[320] The peak position for the C_{16}TABr-stabilised particles appears to be slightly red shifted also but this could be due to the slightly more hydrophobic environment provided by the surfactant which is most likely bound to the particles in a bi-layer.

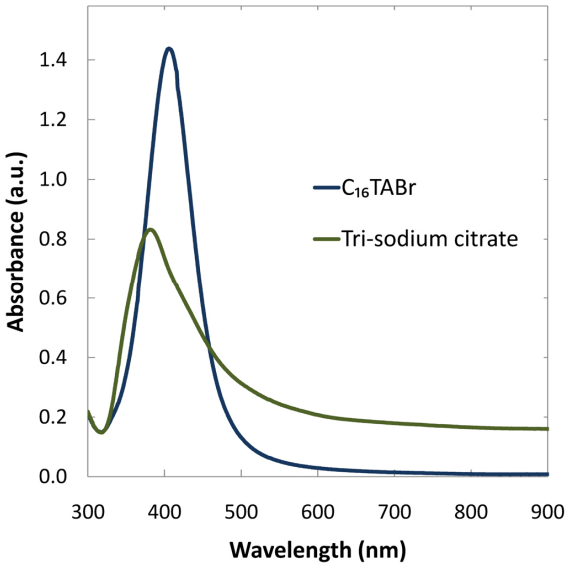

Figure 3-11 UV-Vis spectra of C_{16}TABr and tri-sodium citrate-stabilised silver seed particles

Figure 3-12a shows the UV-Vis spectra for the silver nanorod samples. It can be seen that the longitudinal peak position does not shift over the same range when compared to the silver nanorods that were prepared from tri-sodium citrate stabilised seed

particles from the literature (Figure 3-12b). However, the peak width is narrower for the nanorods prepared from C_{16}TABr-stabilised seeds implying a tighter distribution of aspect ratios for each respective sample. From the ratio of the intensities of the transverse and longitudinal resonance peaks/shoulders it is also clear that there are fewer spherical particles in the samples prepared from the C_{16}TABr-stabilised seeds.

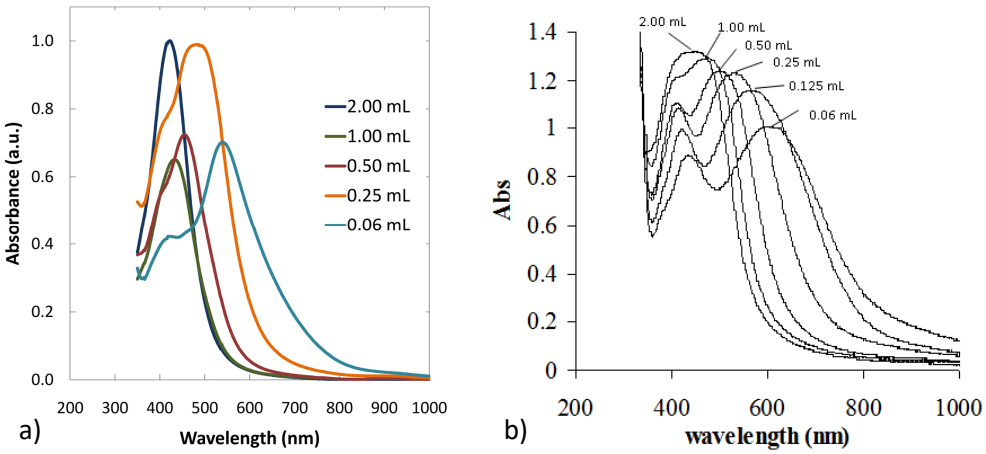

Figure 3-12 Absorbance spectra for silver nanorods a) synthesised in the current work using different volumes of CTAB stabilised silver seed particles and b) literature procedure using citrate stabilised seed particles.

Image in b) modified from reference [289]

Although the peak shift for the nanorods prepared from the C_{16}TABr-stabilised seed particles is not as significant, there is enough evidence from the absorbance spectra to indicate that there is an improvement in the product relative to that produced using citrate-stabilised seed as shown in Figure 5.12(b).

I left the silver nanorod samples under ambient conditions for a few days which resulted in their discolouration. This indicated the oxidation of the silver which could be due to ambient oxygen or high halide concentration in the reaction solution. Due to the instability of the nanoparticles I did not obtain any electron microscopy images and I decided to focus on the preparation of gold nanorods instead. A potential solution to the oxidation problem would be to coat the silver particles with a layer of SiO_2.[321]

3.2.2 Summary

In this section I have shown that the preparation of silver nanorods with a range of aspect ratios is possible. I used some modifications to the literature procedure to reflect similar efforts made in the synthesis of gold nanorods. These modifications appear to have improved the synthesis for silver nanorods because the resulting peaks due to plasmon resonance were sharper and better defined. Nevertheless, a further analysis of the modifications that were made to the synthesis technique for silver nanorods is required to fully evaluate their effect.

Unfortunately, the lifetime of the nanoparticles is particularly short in the absence of some post-treatment of the silver to prevent oxidation. This has negative implications for the long term application of silver nanorods despite an improvement in optical performance.

3.3 Platinum Nanoparticles

Platinum does not have a dielectric function suitable for a strong localised plasmon resonance; Figure 3-13 shows the comparison of the imaginary part of the complex dielectric functions for platinum and gold. As already discussed, the interband transitions in the optical response of gold are a major contributor to the losses associated with the plasmonic response. An indicator to the strength of these losses is the magnitude of the imaginary part of the complex dielectric function. As evident from Figure 3-13, platinum would suffer significant optical losses.[16] For this reason application of platinum in plasmonic applications is not usually considered. However, it has been shown that platinum nanodisks can provide an increasingly red shifted optical response with increasing anisotropy.[322]

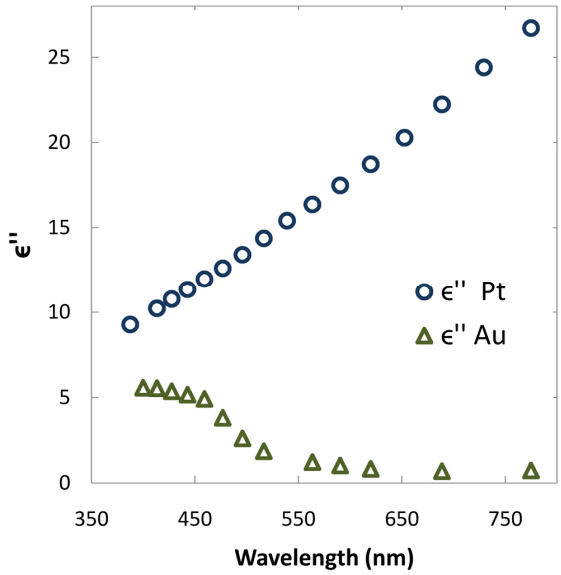

Figure 3-13 Comparison of the imaginary part of the complex dielectric functions for platinum and gold.

Much more attention is directed toward the catalytic properties of platinum nanoparticles. In particular, control of the geometry of platinum nanoparticles is sought as this allows for the provision of specific crystal facets that provide an enhanced efficiency for catalytic activity.[298, 323, 324]

The electrical conductivity of platinum is quite high, accompanied with a very low reactivity, which suggests application for electronics. However, as platinum is very expensive it would be advantageous to have a method that results in very little waste. The development of nanoparticle inks for use in consumer inkjet printers could be one such application.[301] This was the idea that was explored here.

3.3.1 Results and Discussion

I have prepared colloids of platinum nanospheres in an aqueous environment and an organic solvent to demonstrate the efficacy of the synthesis for potential use as nanoparticle inks.

Figure 3-14 shows the absorbance spectrum of platinum nanoparticles prepared in the presence of PVP (poly-vinylpyrrolidone), solid trace. Synthesis conditions may be found in the Section 2.2.5. This spectrum is compared to calculations performed using MiePlot, dashed traces in Figure 3-14. I noticed that during the synthesis a black precipitate formed in parallel to the pale brown colour of the solution. It is likely that the black precipitate is aggregated platinum particles. Before measuring the UV-Vis spectrum for this sample I filtered the solution to remove the precipitate.

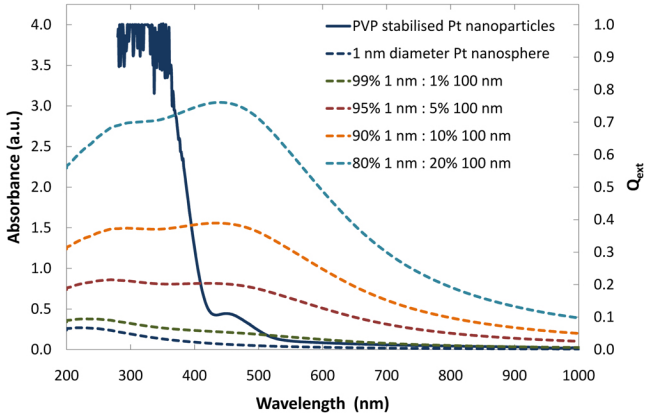

Figure 3-14 Measured extinction spectrum of platinum nanoparticles synthesised in water compared with the MiePlot result for a 1 nm diameter platinum nanosphere and various mixtures of 1 nm and 100 nm diameter spheres, also in water

From the measured absorbance spectrum for the PVP stabilised platinum nanoparticles it can be seen that there is a peak at ~ 460 nm. This is not expected for a solution of ~ 10 nm diameter platinum nanoparticles, which is typical for the conditions used[325] (as cited by Sastry *et al*.[326]). From this observation I investigated the possibility of a larger spherical contaminant in the filtered solution by simulating a range of platinum nanospheres with increasing diameters. I determined that the extinction spectrum of a 100 nm diameter platinum sphere exhibited a peak in the same position, Figure 3-14, (which is primarily due to scattering at this particle size). However, the extinction peak for the 100 nm diameter sphere is very broad and so for this solution this contaminant is potentially also due to some other contributor e.g. degraded polymer.

To implement a platinum nanoparticle solution as a nanoparticle ink it would be required that the particles be dispersed in a volatile solvent. For an aqueous solution, such as that prepared above, this can be achieved by a phase transfer method where a molecule with high affinity for platinum, e.g. thiol or amine, is dissolved in an organic solvent, e.g. toluene, and the two solutions are stirred vigorously. This process is usually

aided by an ionic surfactant, e.g. tetraoctylammonium bromide, with sufficient hydrophobicity to form reverse micelles and facilitate the transition.

Alternatively, the nanoparticles may be synthesised in the organic phase by the Brust-Schiffrin method, originally published as a method for the preparation of fine gold nanoparticles.[290] Due to the partial formation of precipitate in the aqueous synthesis I decided to attempt to directly synthesise the platinum nanoparticles in an organic phase with the Brust-Schiffrin method, see Section 2.2.5 for details.

Figure 3-15 shows the absorbance spectrum for the platinum nanoparticles prepared in toluene, by the Brust-Schiffrin method, in the presence of nonylamine as a stabilising agent. Once again there was the presence of a black precipitate but not as significant as for the aqueous synthesis. This spectrum is compared with the MiePlot result for a 1 nm diameter platinum sphere in toluene. A normalised extinction spectrum for a 1 nm diameter sphere was used as the shape of the spectrum does not change for nanospheres of platinum until the scattering contribution becomes noticeable i.e. large particle sizes. Also, this method typically produces nanoparticles of the order of 1 – 3 nm in diameter.[290, 327]

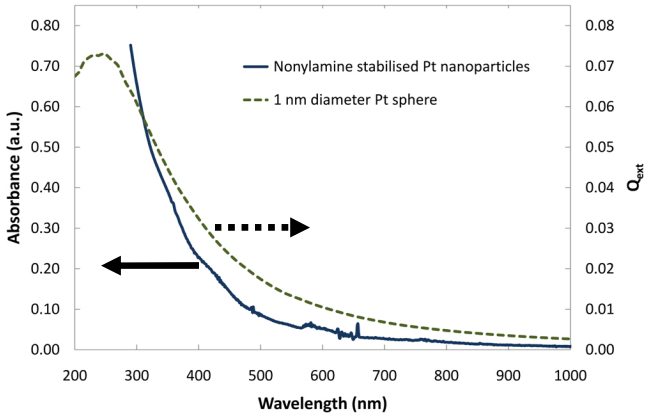

Figure 3-15 Measured extinction spectrum of platinum nanoparticles synthesised in toluene compared with the MiePlot result for a 1 nm diameter platinum nanosphere also in toluene

The sintering properties of the nanoparticles prepared above have not been determined. However, published TGA results for octadecylamine stabilised platinum nanoparticles indicated a ligand desorption temperature of $\sim 230°C$.[328] It is expected that desorption of the nonylamine stabilising agent could be achieved at a heating temperature below $\sim 200°C$ due to the desorption/sintering temperature decreasing with the length of the alkyl chain.[299]

3.3.2 Summary

Platinum nanoparticles were synthesised in an aqueous solution and an organic solvent and the colloidal suspensions characterised with UV-Vis and optical simulations. Some issues were encountered with the aggregation and subsequent precipitation of some of

the platinum particles for each synthesis. Synthesising the platinum nanoparticles in an organic solvent with stronger stabilising agents appeared to reduce the problem of aggregation.

Characterisation of the sintering properties were not performed in the present work. Nevertheless, implementation of platinum nanoparticles as sinterable inks is an attractive option particularly for microelectronic applications as fine structures can be deposited using, for example, inkjet printing. This provides a bottom up approach without significant waste, a major concern for such an expensive material.

4 Optimisation of the synthesis of gold nanorods

The wet chemical synthesis of gold nanorods has developed greatly within the last ten years. Details of this development are described in the literature review, see Section 1.3.1. There are, however, many procedures where a more detailed understanding of the reaction mechanisms may lead to significant improvements in yields and/or control over the products. For example, the presence of unreacted gold in the reaction solution, which results in a slow change in shape of the product during subsequent storage and a short 'shelf life', is a direct result of the amount of ascorbic acid used in the reaction solution. For a typical gold synthesis the concentration of ascorbic acid used in the reaction is usually below the stoichiometrically required amount to reduce all Au^{3+} to Au^{0}. With many syntheses producing only $\sim 15-20\%$ gold metal in the nanorod product,[27] with respect to initial Au^{3+} concentration, this provides an avenue to explore and provide an improvement on the methods of synthesis reported in the literature.

All of the components in the nanorod synthesis can be considered variables i.e. changing the concentration of any component will result in alteration of the product. For example, it is well known that changing the silver concentration will result in different aspect ratios of nanorods. In this case it is hypothesised that the silver preferentially adsorbs[13] or is reduced[25] at different crystal faces of the developing nanorod.

Another method for changing the aspect ratio is the volume of seed solution added to the growth solution. The concentration of the solution used to grow the gold seed particles is usually 0.25 mM and 0.1 M, for Au^{3+} and $\mathrm{C}_{16}\mathrm{TABr}$ respectively.[21, 22, 25, 104, 116] Use of a 0.5 mM Au^{3+} concentration seed has also been reported.[124] In general, addition of greater volumes of seed leads to an increase in aspect ratio.[98] Alternatively the seed can be formed *in situ* by reducing a small fraction of the nanorod growth solution by adding an equivalent aliquot of strong reductant, BH_4^-.

In the following chapter, a systematic approach has been applied to the role of the weak reducing agent by introducing a co-reductant which reacts with Au^{3+} in the same way but at a different rate. A broad range of seed parameters, with respect to Au^{3+} and $\mathrm{C}_{16}\mathrm{TABr}$ concentrations are also studied and discussed with respect to phenomena reported in the literature.

Variation of Ag^{+} and $\mathrm{C}_{16}\mathrm{TABr}$ concentration are also explored as a validation of the procedure.

4.1 Results and Discussion

4.1.1 Ag^+ concentration

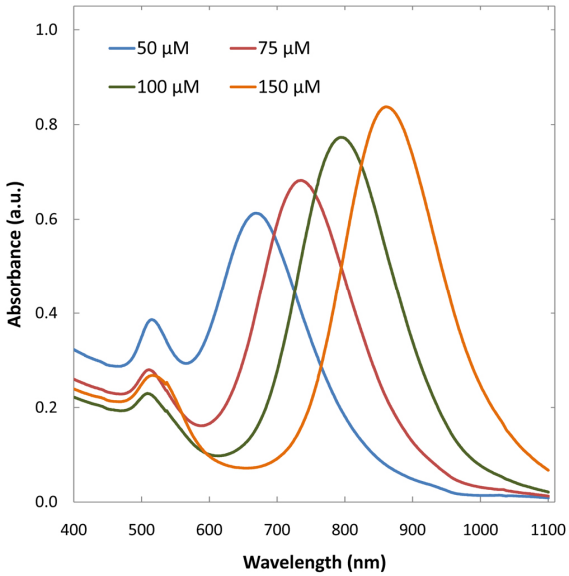

Figure 4-1 Increasing the silver nitrate concentration in the gold nanorod growth solution produces a proportional shift of the longitudinal plasmon peak.

The mechanism by which silver enhances the wet chemical synthesis of gold nanorods still holds some mystery but there is no question that it is vital to achieve product yields approaching 100%. 'Yield' here is the proportion of Au nanorods compared to nanospheres. Actually, as mentioned, only a small proportion of the gold in solution is typically reduced so 'yield' in the context of usage of gold is always rather low. It is hypothesised that the silver is reduced at the developing $< 110 >$ crystal faces of the gold nanorod by some of the H_2A.[25] Typically H_2A cannot reduce Ag^+ but at the surface of another metal, e.g. gold, underpotential deposition can occur. This involves the formation of a sub-monolayer of silver on the gold surface. The silver will not remain metallic for very long as under these conditions any Au^{3+} remaining will undergo a galvanic replacement reaction to form Au^0.[108] Figure 4-1 shows an example of the effect of varying the concentration of $AgNO_3$ in the nanorod growth solution while holding all other components constant. All samples were prepared according to GS method A, with 0.55 mM H_2A and growth was initiated with10 µL of 0.1 mM $HAuCl_4$ seed A solution. It is obvious from Figure 4-1 that slight variations in concentration of $AgNO_3$ can produce a broad range of aspect ratios. In Figure 4-1 there is an increase in the absorbance at 400 nm for the sample with 50 µM Ag^+, with respect to the other samples (Au^0 as estimated by absorbance at 400 nm). The spectra for these samples were measured approximately two days after initiation of the reaction. There will be significant quantities of unreacted gold present in these samples due to the concentration of ascorbic acid used, see Section 4.1.4. This may indicate that the ageing process is faster in samples with a low concentration of Ag^+.

4.1.2 C_{16}TABr concentration

From the initial use of surfactants in the synthesis of gold nanorods it has been hypothesised that surfactant micelles play an important role in the structural development of the nanoparticles. A typical nanorod synthesis will use a concentration that is ~100 times the first critical micelle concentration (CMC) of C_{16}TABr. The first CMC for C_{16}TABr is ~0.9 mM and the second CMC is ~20 mM,[329] however these values drop significantly as the concentration of other electrolytes increases.[330] The second CMC is an indication of the micelles taking on a more complex structure, e.g. rod-shaped. Another reason for maintaining the concentration of C_{16}TABr at a high concentration is to solubilise the $AuBr_4^- - C_{16}TA^+$ complex which, as mentioned, is insoluble.

Figure 4-2 shows the effect of varying the concentration of C_{16}TABr from 0.03 – 0.1 M. A minimum value of 0.03 M was selected as this is the approximate value for the concentration of $AuCl_4^-$ used where complete solubilisation of the complex is achieved.[26] Each sample was prepared according to GS method A with 0.1093 – 0.3645 g C_{16}TABr for 0.03 – 0.1 M respectively, 70 µM $AgNO_3$ and 0.65 mM H_2A. Growth was initiated with15 µL of 0.1 mM $HAuCl_4$ seed A solution.

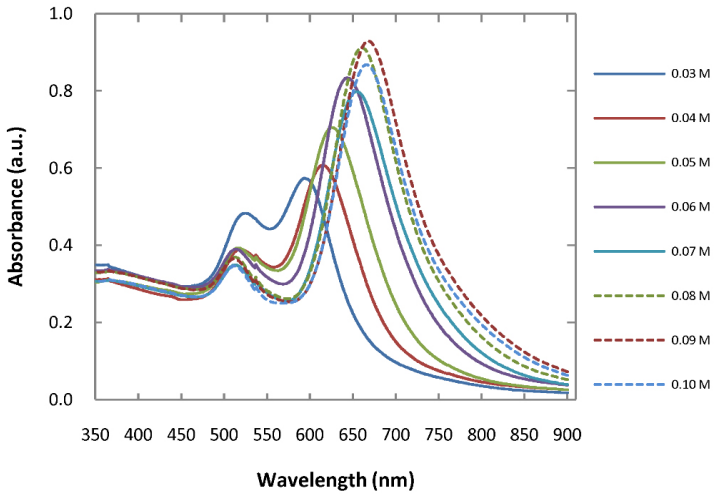

Figure 4-2 Varying the C_{16}TABr concentration of the gold nanorod growth solution shows a dependence of the sample quality on the elevated concentration.

The optimum range for the C_{16}TABr concentration is between 0.08 and 0.1 M. This shows that there is a high reliance on the dynamics of the surfactant at concentrations well above the CMC. Micelle shape is presumably not a controlling factor as all of the concentrations used here are above the second CMC (which may be quite low considering the number of ionic species used). Concentrations of C_{16}TABr higher than the optimum are not deleterious. The proportion of nanorods relative to nanospheres also increases as the surfactant concentration increases. This is indicated by the relative intensities of the transverse and longitudinal peaks. The relative intensity of the peaks

can be due to an increase in aspect ratio (and fixed volume) but this happens over a broader wavelength range than observed in Figure 4-2.

4.1.3 Gold Source

It is well known that halide ions other than bromide interfere with the formation of gold nanorods,[11, 26, 117, 118] yet no attempt has been made to confirm that the chloride ions released from the ionic gold source, $HAuCl_4$, during the reaction do not have a negative effect. By comparison with previously reported results,[331, 332] or by consideration of cyclic voltammetry[78] or EXAFS (extended X-ray absorption fine structure) measurements,[80] it has been concluded in the literature[78-80] that the chloride ions are replaced by bromide upon addition to a concentrated solution of $C_{16}TABr$. This indicates that the chloride is released early and could interfere with nanorod formation.

To quantify the extent to which the chloride ions are replaced by bromide, I prepared solutions of analogous concentration to the nanorod synthesis, i.e. 0.5 mM Au^{3+} and 0.1 M $C_{16}TA^+$, with all permutations of counter-ions with respect to Au^{3+} and $C_{16}TA^+$. These solutions were then diluted by 2 and 10 times to bring the absorbance intensity to an acceptable range for the spectrophotometer.

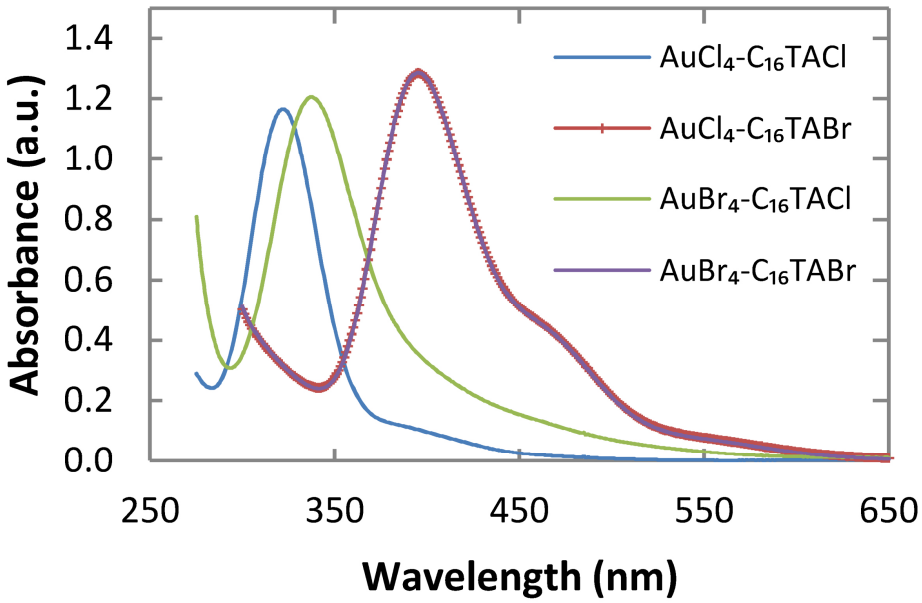

Figure 4-3 UV-Vis absorbance spectra of Au (III) – $C_{16}TA^+$ solutions indicating that the gold species present in the gold nanorod growth solution is $AuBr_4^-$-CTA^+.

Figure 4-3 shows normalised absorbance spectra for each of these combinations with the trace labels referring to the original source of each respective component. As mentioned in a previous chapter (Section 1.3.1) the gold halide species are complexed to the $C_{16}TA^+$ surfactant molecule. From Figure 4-3 it can be seen that regardless of the origin of the Au^{3+} the species present in a $C_{16}TABr$ solution is $AuBr_4^-$, i.e. the species present in the growth solution for the nanorod synthesis. The extinction coefficient for

the $AuBr_4^- - C_{16}TA^+$ complex is $\varepsilon_{395} = \sim 4776\ \mathrm{L.mol^{-1}.cm^{-1}}$, calculated using the Beer-Lambert law in Section 2.3.1.

Following this confirmation, gold nanorod samples were prepared using identical seed and growth solution conditions with the exception of the gold compound used as the source of gold. The seed solutions were prepared using seed method A with the final concentration of Au^{3+} being 0.1 mM. Growth solutions were prepared according to GS method A. Figure 4-4 shows representative absorbance spectra of the as-prepared products of this reaction.

From Figure 4-4 it is clear that synthesis using either $AuBr_4^-$ or $AuCl_4^-$ will produce nanorods of good quality.

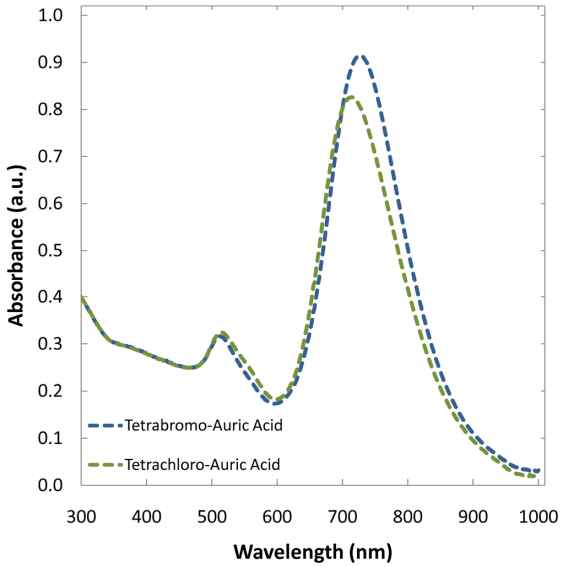

Figure 4-4 Absorbance spectra of nanorods prepared with $HAuBr_4$ and $HAuCl_4$

Attenuation of the longitudinal peak and a slight increase in the transverse peak indicates an increase in the relative nanosphere population as the absorbance at ~400 nm is fixed (absorbance at 400 nm provides shape independent indication of metallic gold in solution). Despite this, the use of $HAuCl_4$ does not suffer any significant disadvantage despite the presence of some free Cl^-.

4.1.4 Mechanism of Reduction

An important component of the nanorod synthesis is the use of the weak reductant ascorbic acid (H_2A). H_2A has been used since the infancy of the wet chemistry nanorod synthesis to reduce $AuBr_4^-$ to $AuBr_2^-$. The concentration of H_2A in the synthesis of nanorods is in slight excess of the concentration of $AuBr_4^-$, typically $1:1.1 - 1.6$.[21, 22, 27, 124] This range is suggested to maintain the nanorod geometry with larger concentrations resulting in dog-bone shapes[104, 107, 333] while a further large increase forms spiked nanoparticles.[98]

It has been reported that H_2A can reduce $AuBr_4^-$ to Au^0 which results in the formation of Au_{13} clusters.[93] These gold clusters are then hypothesised to aggregate on the surface of seed particles to form nanorods. TEM shows that these particles can appear in the preparation of the growth solution after addition of ascorbic acid to $AuBr_4 - C_{16}TA^+$ (Figure 4-5b). However, by adding insufficient concentrations of ascorbic acid to the Au^{3+} solution it can also be seen that the Au^{3+} is reduced in an almost $1:1$ ratio (Figure 4-5a). If all the ascorbic acid was reducing the Au^{3+} to Au^0 then there should be $\sim\frac{1}{3}$ of the Au^{3+} remaining for a $1:1$ ascorbic acid to gold ratio; this is not observed. Due to the slight deviation from $1:1$ reduction it is possible that some Au^0 is formed but any clusters formed will be present in a very small amount.

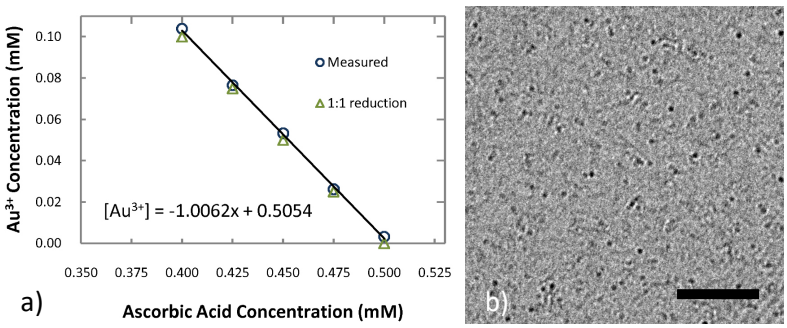

Figure 4-5 a) Concentration of Au^{3+} measured by UV-Vis spectrometry for solutions with ascorbic acid approaching 1:1 with respect to initial Au^{3+} concentration b) Cryo-TEM image of solution of Au^{3+}-C_{16}TABr and ascorbic acid, scale bar = 50 nm

The degree of dissociation of ascorbic acid in a $C_{16}TABr$ solution is greater than in water alone and implies an interaction with the surfactant monomers or micelles,[334] furthermore the oxidation potential of ascorbic acid is lower in micellar environments.[102] Figure 4-6 shows the dissociation, oxidation and degradation pathway for ascorbic acid. 2,3 – diketogulonic acid was chosen as the degradation product for the diagram as there is a specific reference in the literature to the potential involvement of this species in the ageing of untreated gold nanorod samples.[104]

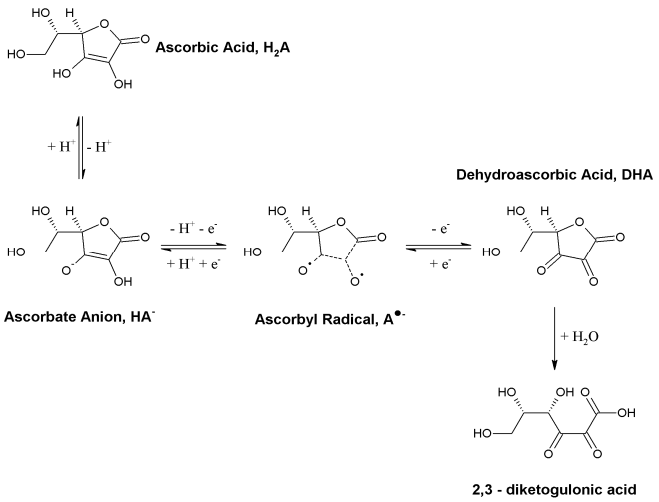

Figure 4-6 Oxidation and degradation pathways for ascorbic acid

With respect to the gold nanorod synthesis Pérez-Juste *et al*. introduced a mechanism for the reduction of gold based on a one-electron process that relied on the introduction of seed particles to the growth solution:[26]

$$\mathrm{AuCl_2^-} + \mathrm{e^-} \rightleftharpoons \mathrm{Au^0} + 2\mathrm{Cl^-} \qquad 4.1$$

Zümreoglu-Karan has synthesized a gold-ascorbate complex (Figure 4-7) that implies a pathway for the above mechanism, Equation 4.1.[102]

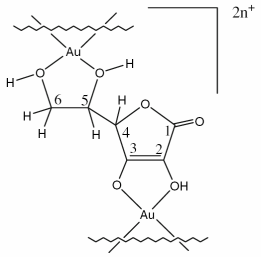

Figure 4-7 Au^{3+} - ascorbate complex

Image reproduced from reference [102]

In the following mechanisms $\mathrm{HA^-}$ is the ascorbate anion and DHA is the oxidation product of ascorbic acid, dehydro-ascorbic acid. Reduction of $\mathrm{Au^{3+}}$ by $\mathrm{HA^-}$ is achieved by an inner-sphere mechanism,[bb] which in the context of a typical gold nanorod synthesis is as follows:

$$\mathrm{AuBr_4^-} + (1+n)\mathrm{HA^-} \rightarrow \{\mathrm{Au(HA)}\}^{2+} + n\mathrm{HA^-} + 4\mathrm{Br^-} \qquad 4.2$$

$$\{\mathrm{Au(HA)}\}^{2+} + n\mathrm{HA^-} + (2-\mathrm{n})\mathrm{Br^-} \rightarrow n[\mathrm{Au(HA)Br}]^- + (1-n)\mathrm{AuBr_2^-} + \mathrm{DHA} + \mathrm{H^+} \qquad 4.3$$

Equation 4.3 represents the reduction of $\mathrm{Au^{3+}}$ to $\mathrm{Au^+}$ by the complexed $\mathrm{HA^-}$ which is released into the solution as DHA and replaced by the excess $\mathrm{HA^-}$ and $\mathrm{Br^-}$ from solution.

The inclusion of the $\mathrm{AuBr_2^-}$ in the second mechanism only applies for the condition $0 < n < 1$, i.e. a maximum initial gold to ascorbic acid ratio of $1:2$. If $1 < n < 2$ then there is no need for the uncomplexed $\mathrm{AuBr_2^-}$ term as there is sufficient $\mathrm{HA^-}$ for complete complexation. It should be noted that although the $\mathrm{AuBr_2^-}$ is not complexed to $\mathrm{HA^-}$ it is still complexed to $\mathrm{C_{16}TA^+}$. It is then hypothesized that the reduction of $\mathrm{Au^+}$ to $\mathrm{Au^0}$ takes place via another inner-sphere mechanism which produces $\mathrm{Au^0}$ and an ascorbate radical, $\mathrm{A^*}$ (Figure 4-6), while the ascorbate radical disproportionates[335] to DHA and $\mathrm{HA^-}$:

[bb] Inner-sphere implies the redox species are bound to one another

$$2n[\mathrm{Au(HA)Br}]^- \xrightarrow{A^*} 2n\mathrm{Au}^0 + n\mathrm{DHA} + n\mathrm{HA}^- + 2n\mathrm{Br}^- \qquad 4.4$$

The algebraic quantity n represents the excess of $\mathrm{H_2A}$ required for the reaction and shows the dependence on this value of the amount of metallic gold in the final product. For values of $0 < n < 1$ the formation of HA^- from the disproportionation of the ascorbate radical could result in the further complexation of remaining $\mathrm{AuBr_2^-}$ from Equation 4.3. The reaction would then proceed as a converging series with half the initial excess of HA^- feeding the subsequent steps. The point of convergence is the complete reaction of initial Au^{3+} concentration. From Equation 4.4 it can be seen that the disproportionation of ascorbate radical results in half of the concentration of HA^- that preceded it. This suggests a possible mechanism for the gradual ageing process. It is also possible for the oxidation products of ascorbic acid, dehydroascorbic and 2,3 – diketogulonic acids to reduce Au^+ or Au^{3+} ions.[104] However, it is typically required that the solution is at high temperature, approaching 100°C, before this reduction is evident on a short time scale. It should be noted that the ascorbate complex mechanism does not account for the requirement to add nanoparticle seed.

In the gold nanorod synthesis there is typically unreacted gold remaining in solution and so would indicate that the reaction is being limited by some factor. As noted by Henkel *et al*. the amount of ionic gold in the solution is the result of "a depletion of ascorbic acid".[124] As discussed previously Pérez-Juste *et al*. proposed that the reduction of Au^+ with respect to the gold nanorod synthesis was occurring via a one-electron process as per Equation 4.1. This was suggested in favour of a disproportionation mechanism as the disproportionation of $\mathrm{AuBr_2^-}$ results in the formation of $\mathrm{AuBr_4^-}$, Equation 4.5. The presence of $\mathrm{AuBr_4^-}$ and $\mathrm{C_{16}TABr}$ oxidises gold nanoparticles.[26, 36] However, any Au^{3+} reformed by disproportionation would be consumed by the excess $\mathrm{H_2A}$ which, as mentioned, is a requirement for nanorod formation.

$\mathrm{AuCl_2^-}$[100] and $\mathrm{AuBr_2^-}$[101] species in solution can disproportionate to form Au^0 and Au^{III} species:

$$3\mathrm{AuBr_2^-} \rightleftharpoons 2\mathrm{Au}^0 + \mathrm{AuBr_4^-} + 2\mathrm{Br}^- \quad \mathrm{K} = 2.112 \times 10^5 \qquad 4.5$$

The equilibrium constant for Equation 4.5 is estimated from the combination of the reaction Gibbs' energies of the standard half equations at 25°C:[295]

$$\mathrm{AuBr_2^-} + \mathrm{e}^- \rightleftharpoons \mathrm{Au}^0 + 2\mathrm{Br}^- \qquad \mathrm{E}^0 = +0.959\ \mathrm{V} \qquad 4.6$$

$$\mathrm{AuBr_4^-} + 3\mathrm{e}^- \rightleftharpoons \mathrm{Au}^0 + 4\mathrm{Br}^- \qquad \mathrm{E}^0 = +0.854\ \mathrm{V} \qquad 4.7$$

The reaction Gibbs' energy is related to the standard reduction potential by:

$$\Delta_\mathrm{r}\mathrm{G} = -\mathrm{vFE}^0 \qquad 4.8$$

Where, v is the stoichiometric coefficient of the electrons transferred, F is Faraday's constant and E^0 is the standard potential of the reduction half equation with respect to the standard hydrogen electrode, S.H.E. The equilibrium constant in Equation 4.5 is then estimated from the Gibbs' energy of reaction by:

$$K = e^{-\frac{\Delta_r G}{RT}} \qquad 4.9$$

An important factor in the disproportionation of gold species is that the reaction is catalysed by metallic gold.[100, 101] This factor correlates with the reaction being initiated by the nanoparticle seed and is shown schematically in Figure 4-8.

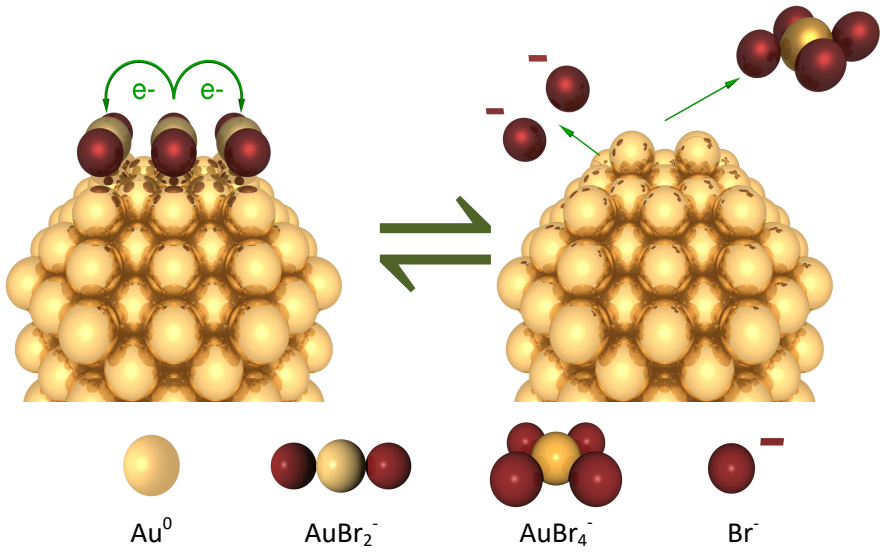

Figure 4-8 Schematic of the disproportionation mechanism of $AuBr_2^-$ at the surface of a gold nanoparticle

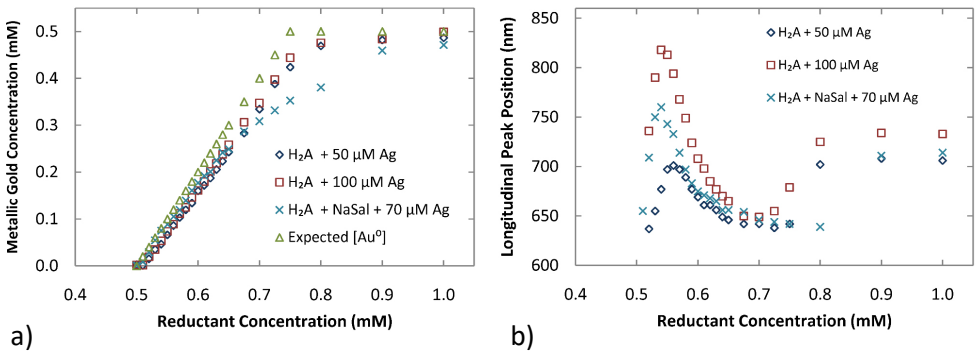

Figure 4-9 a) Proportional increase of metallic gold concentration to excess reductant concentration in gold nanorod samples and b) corresponding longitudinal peak positions

For disproportionation to be the driving mechanism in the formation of gold nanorods, the concentration of metallic gold expressed in the product of the reaction should display a proportional relationship to the excess concentration of reductant added to the growth solution. As a reminder, the excess reductant is hypothesised to be consuming the Au^{3+} from the disproportionation reaction. From Equation 4.5 it can be

seen that for any given ratio of excess ascorbic acid to initial Au^{3+} the expected concentration of metallic gold in the nanorods will be twice the excess concentration of ascorbic acid. This correlation is closely represented in Figure 4-9a. (The concentration of Au^0 is approximated from optical properties as detailed in the experimental procedures, Section 2.3.2).

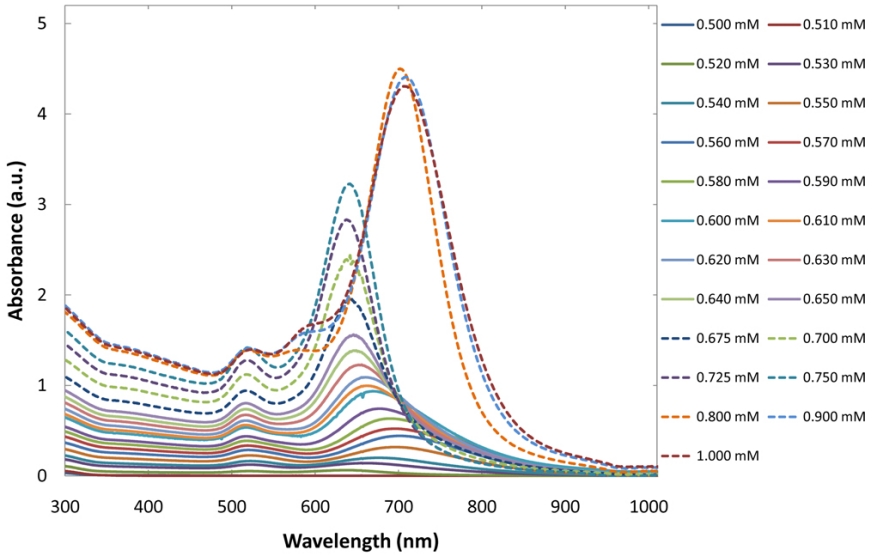

Figure 4-10 Nanoparticle spectra for samples in Figure 4-9 where growth solutions contain 50 µM Ag^+ and ascorbic acid as the sole excess reductant

Expected $[Au^0]$ in Figure 4-9a refers to the stoichiometrically expected concentration from the disproportionation mechanism with respect to the excess concentration of reductant used in each sample. With the exception of the 'Expected $[Au^0]$' trace, each data point in Figure 4-9a corresponds to a distinct sample prepared from identical growth solutions according to GS method B[cc]. Nanoparticle growth was initiated with 10 µL of seed B. Corresponding nanoparticle spectra for samples in Figure 4-9 can be seen in Figure 4-10 and Figure 4-11 for samples with 50 µM and 100 µM $AgNO_3$ respectively.

The complexation pathway proposed by Zümreoglu-Karan is certainly possible, but it is likely that for this process to progress quickly enough the ascorbic acid must be in an excess of $1:2$ (gold:ascorbic acid) or more so that the cascade of reproduction of ascorbic acid can feed the formation of the nanoparticles. Also, the rate of disproportionation of ascorbate radical and its re-complexation needs to be rapid to be able to supply the amount of gold evident in Figure 4-9a.

Although it has been reported that the concentration of Ag^+ in the growth solution controls the aspect ratio (Figure 4-1) of the nanorod product, it is clear from Figure 4-9b, Figure 4-10 and Figure 4-11 that the concentration of reductant displays a much more potent control over the aspect ratio with the longitudinal peak position reaching an equilibrium position for all Ag^+ concentrations before the onset of the development of dog-bone geometries occurs at elevated reductant concentrations. The presence of a

[cc] With respect to GS method B the highest concentration of ascorbic acid was added as a 1 mL aliquot of 10 mM stock solution. The other samples were made with appropriate aliquots of the 10 mM stock and made up to the same total volume with ultrapure water.

third plasmon peak in the absorbance spectra is an indication of dog-bone particles[333] (Figure 4-18). At the equilibrium point $\sim 70\%$ of the initial Au^{3+} concentration is present in the nanorod product. Therefore, to achieve a reasonable spread of aspect ratios through variation of Ag^{+} concentration, a trade-off of limiting the amount of total gold reacted to $< 70\%$ is necessary.

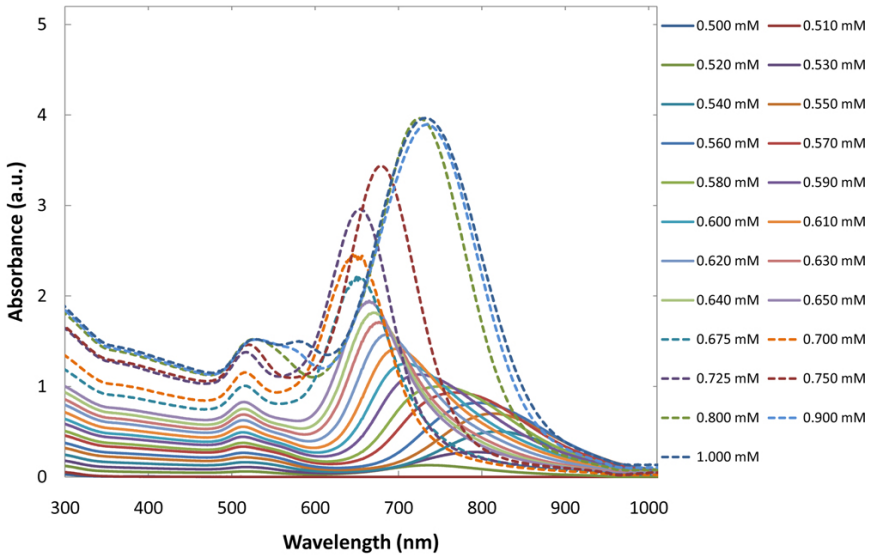

Figure 4-11 Nanoparticle spectra for samples in Figure 4-9 where growth solutions contain 100 µM Ag^{+} and ascorbic acid as the sole excess reductant

4.1.5 Sodium Salicylate as a Co-reductant

Sodium salicylate (NaSal) was included in the nanorod synthesis to examine its influence based upon its strong interaction with C_{16}TABr. Upon addition of NaSal to a C_{16}TABr solution, where the concentration is above the critical micelle concentration, the salicylate anion passivates the charged head-group of the surfactant by inserting into the micelle. As $[\mathrm{NaSal}] \rightarrow [C_{16}\mathrm{TABr}]$ the micelles elongate and at high concentrations the solution becomes extremely viscous.[336, 337]

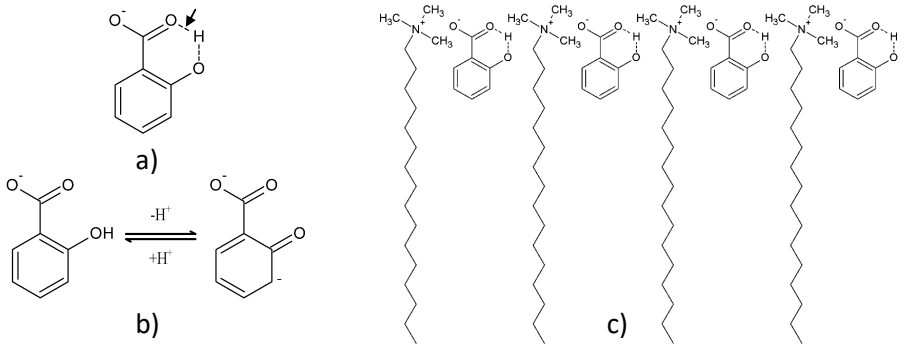

Figure 4-12 a) Structure of the salicylate anion with intramolecular hydrogen bond indicated, b) probable structure of the salicylate di-anion and c) insertion of the salicylate anion into a C_{16}TABr micelle

I hypothesised that this interaction with the $C_{16}TABr$ micelles would result in the formation of larger aspect ratios based on the growth model of the 'soft templating' effect. However, upon addition of $NaSal$ to a $AuBr_4^- - C_{16}TABr$ solution, a gradual decrease in the familiar colour of the $AuBr_4^- - C_{16}TA^+$ complex was observed. This is attributed to $NaSal$ acting as a weak reducing agent. Figure 4-12 shows the salicylate anion (a), di-anion (b) and insertion into $C_{16}TABr$ micelles (c). To date, there have been no reports of implementation of different weak reducing agents in the gold nanorod synthesis.

Figure 4-13 shows the time dependent interaction of $NaSal$ with $AuBr_4^- - C_{16}TABr$ in a $1:1$ stoichiometric ratio. As time increases the spectrum approaches that of the growth solution for the nanorod synthesis, post H_2A addition (Figure 4-14a). The traces from Figure 4-14a $NaSal + (Au^+$ and $Au^{3+})$ are from the sum of each respective spectrum and not from mixed solutions of those components. The concentration of Au^{3+} was determined from the extinction coefficient determined in Section 2.3.1. The time taken for complete reduction of $AuBr_4^-$ by salicylate is significantly longer than for ascorbate, which is very rapid.

In the presence of $AuBr_4^- - C_{16}TABr$ the salicylate peak shifts from ~ 297 nm to ~ 306 nm during the reaction. This could indicate complexation of the salicylate with Au^{3+} or Au^+. Complexation of salicylate with Al^{3+} results in a red shift of the salicylate peak but also a significant increase in the shoulder of the peak.[338] Figure 4-14b shows the attenuation of the shoulder of the salicylate peak due to increasing water concentration in an acetonitrile solution.[339] The lack of a significant shoulder to the salicylate peak in Figure 4-13 could indicate that the salicylate is not complexing with the gold ions or that the solvent effect from water is reducing the strength of the peak.

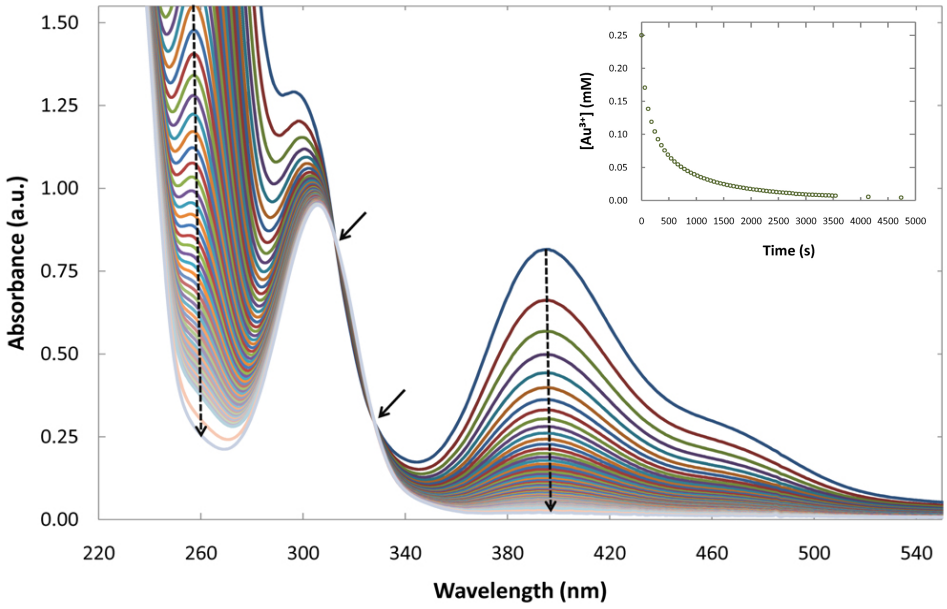

Figure 4-13 UV-Vis kinetics data for the interaction of sodium salicylate with $AuBr_4$ – $C_{16}TABr$ at 30°C , dashed arrows indicate increasing time, solid arrows indicate isosbestic points. Inset shows decrease of Au^{3+} concentration with time

The red shift of the salicylate peak in this instance could also be due to the location of salicylate in the micelles. This shift would be due to the insertion of salicylate into the hydrophobic environment of the micelle, analogous to a solvatochromic effect. Isosbestic points indicated in Figure 4-13 show that no intermediates are resolvable for this experiment.

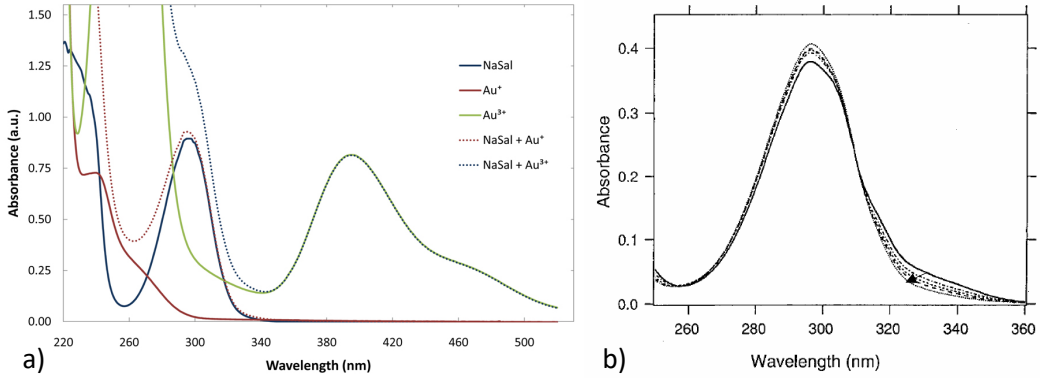

Figure 4-14 a) Combinations of NaSal and Au^{+}- and Au^{3+}-C_{16}TABr spectra and b) effect of water on the spectrum of salicylate anion in acetonitrile (arrow indicates increasing concentration of water)

Image b) reproduced from reference [339]

The reduction of Au^{3+} requires a two electron process in the conditions of the nanorod growth solution. From the inset of Figure 4-13 and considering the initial half life (see below), it is probable that the two electrons come from the one salicylate anion in one process. This is supported by the rapid decrease beyond half the initial concentration without an inflection in the kinetics for this stage of the reaction. An inflection may indicate dissociation of the counter ions of the salicylate anion.

From standard plots[340] for determining the rates of first and second order chemical reactions there are three stages apparent in the reaction of salicylate with $AuBr_4^- - C_{16}TABr$, Figure 4-15. In the first stage the reaction follows second order kinetics while there are two stages that follow first order kinetics in the later two stages of the reaction.

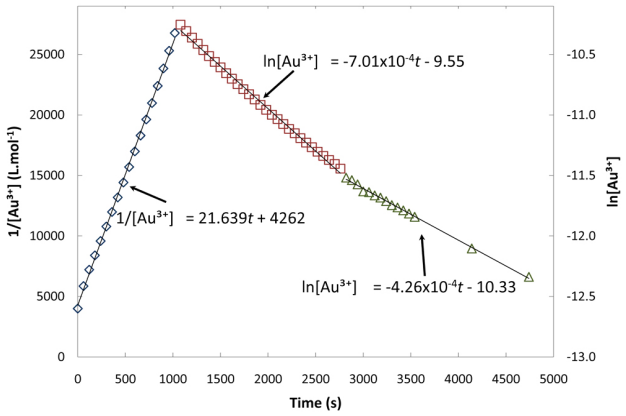

Figure 4-15 Integrated rate law plots for kinetics of the reaction of NaSal and Au^{3+}

Integrated rate law for a first order chemical reaction:

$$\ln[\mathrm{Au}^{3+}] = -k\mathrm{t} + \ln[\mathrm{Au}^{3+}]_0 \qquad 4.10$$

Integrated rate law for a second order chemical reaction:

$$\frac{1}{[\mathrm{Au}^{3+}]} = k\mathrm{t} + \frac{1}{[\mathrm{Au}^{3+}]_0} \qquad 4.11$$

For Equations 4.10 and 4.11, $[\mathrm{Au}^{3+}]$ is the concentration of Au^{3+} at any given time, t, $[\mathrm{Au}^{3+}]_0$ is the concentration of Au^{3+} at $t = 0$ and k is the rate constant for the reaction.

It can be seen that for a first order reaction a plot of $\ln[\mathrm{Au}^{3+}]$ vs t will yield a linear plot with a slope of $-k$. Similarly, for second order reactions a plot of $\frac{1}{[\mathrm{Au}^{3+}]}$ vs t will yield a linear plot with a slope of k.

The half-life of a first order chemical reaction:[340]

$$\mathrm{t}_{\frac{1}{2}} = \frac{\ln 2}{k} \qquad 4.12$$

The half-life of a second order chemical reaction:[340]

$$\mathrm{t}_{\frac{1}{2}} = \frac{1}{\mathrm{k}[\mathrm{Au}^{3+}]_0} \qquad 4.13$$

Rate constants and half-lives determined for each stage of the reaction can be found in Table 4-1.

Table 4-1 Reaction rates and constants of the kinetics of the reaction of NaSal and Au^{3+}

Time (s)	Reaction Order	Rate Constant, k	Half Life, $t_{\frac{1}{2}}$ (s)
$0 - 1020$	2^{nd}	$21.64\ \mathrm{L.mol^{-1}.s^{-1}}$	185
$1080 - 2760$	1^{st}	$7.01 \times 10^{-4}\mathrm{s^{-1}}$	989
$2820 - 4740$	1^{st}	$4.26 \times 10^{-4}\mathrm{s^{-1}}$	1627

The first stage of the reaction is most likely due to the reaction of free salicylate with Au^{3+} at the surface of the micelle or immediate reaction upon inter-micelle exchange of molecules. The following two stages are related processes but differ slightly as they are associated with distinct rate constants. These stages could be determined by intra-micelle reorganisation where the Au^{3+} and NaSal are not initially adjacent within the micelle.

From the qualitative observation alone, it is clear that salicylate is much slower at reducing Au^{3+} than ascorbate. This observation is reflected in the values for the first and second log scale dissociation constants, pK_a, where $pK_{a1} = 2.98$ and $pK_{a2} = 13.6$ for salicylic acid and $pK_{a1} = 4.10$ and $pK_{a2} = 11.7$ for ascorbic acid.[295] It should be noted that the value for the first pK_a for salicylic acid does not apply here as the proton is replaced by a sodium ion. Also the second pK_a may vary due to the variation in the ionic strength, but not significantly. The greater magnitude of the second pK_a with respect to salicylate indicates that the second de-protonation occurs less readily than for ascorbate. The conditions in the surrounding solution also require consideration. For instance the first pK_a of ascorbic acid will be reduced if in the presence of $C_{16}TABr$.[334] A similar effect is expected for the salicylate as it is known that the salicylate anion has a high affinity for $C_{16}TABr$ micelles.

To investigate the use of $NaSal$ as a reductant in the synthesis of nanorods I prepared a growth solution with $NaSal$ in place of H_2A. In these samples, for concentrations of $NaSal$ equivalent to H_2A concentration in a typical nanorod synthesis, no nanoparticles were formed. However, when $NaSal$ is used as a co-reductant to H_2A the synthesis is equally as effective. The co-reductant effect of $NaSal$ can be seen in Figure 4-9a. Each sample was prepared from identical growth solutions according to GS method B.[dd] Nanoparticle growth was initiated by addition of 10 µL of seed B. Some deviation from the expected trend is observed but this is probably due to the $NaSal$ not having sufficient time to react with Au^{3+} before the seed was added. This effect is discussed with respect to Figure 4-17.

For each of these samples the concentration of H_2A was maintained at 0.5 mM, i.e. in a $1:1$ ratio with the gold concentration. Figure 4-16 shows the corresponding nanoparticle spectra prepared with $NaSal$ for the data points in Figure 4-9a. It is clear from the first data point in these samples that a $1:1$ ratio of reductant to gold is not sufficient to grow gold nanorods, Figure 4-9a, Figure 4-10, Figure 4-11 and Figure 4-16.

[dd] With respect to GS method B the highest concentration of sodium salicylate was added as a 0.5 mL aliquot of 10 mM stock solution, the other samples were made with appropriate aliquots of the 10 mM stock and made up to the same total volume with ultrapure water.

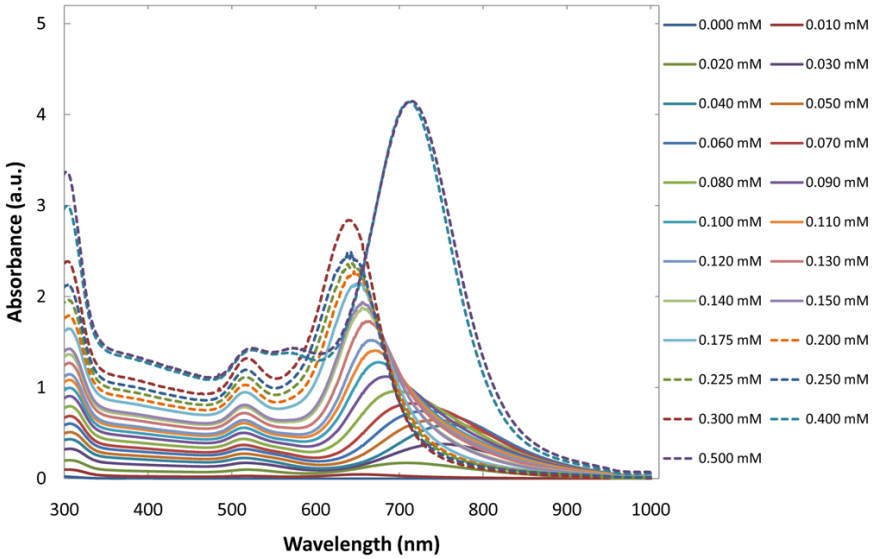

Figure 4-16 Nanoparticle spectra for samples in Figure 4-9 where growth solutions contain 70 µM Ag^+ and sodium salicylate as the excess reductant, traces are labelled according to NaSal concentration

Further evidence for the strong dependence of nanorod synthesis on the nature and concentration of reductant may be found by observing the effect of varying the order in which they are added. It is critical that NaSal is added before $\mathrm{H_2A}$ in the preparation of the growth solution. Figure 4-17 shows the effect of changing the order of addition of the reactants to the growth solution.

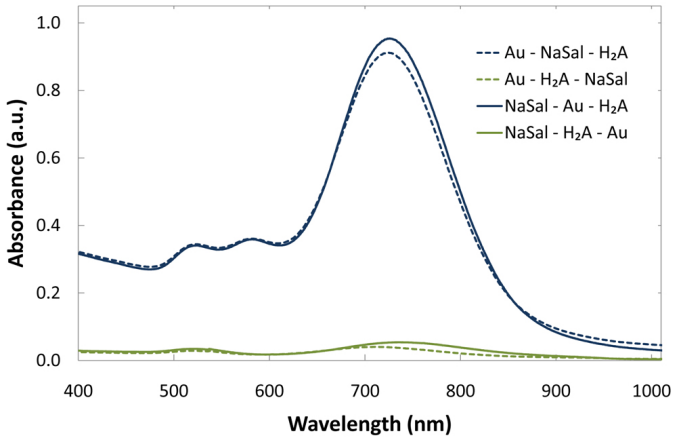

Figure 4-17 By varying the of order of addition of reactants for nanorod growth solutions containing H_2A and NaSal as reductants a dependence of ascorbate as the excess reductant is evident

The samples in Figure 4-17 all contain identical concentrations of each constituent. The growth solutions were prepared according to GS method A with 0.55 mM $\mathrm{H_2A}$, 0.5 mM NaSal and 75 µM $\mathrm{AgNO_3}$. Nanoparticle growth was initiated with 15 µL of 0.1 mM $\mathrm{HAuCl_4}$ seed A. The order of addition (post-$\mathrm{C_{16}TABr}$ and pre-$\mathrm{AgNO_3}$) is indicated in the legend of Figure 4-17 with the left-most component added first. After each addition the solution was mixed thoroughly.

From this result it can be deduced that the chief role of NaSal is to reduce the Au^{3+} to Au^{+}. This is implied by the samples where NaSal and Au^{3+} are allowed to react before the addition of H_2A. This also has the implication that the rate-limiting factor in the formation of nanorods is the efficacy of the reductant present in excess of the Au^{3+} concentration. This supports the disproportionation mechanism because the consumption of Au^{3+}drives the equilibrium toward the formation of metallic gold and the reduction by ascorbate is much quicker than by salicylate. This also implies that the nanorod formation step is very rapid.

As with H_2A, increasing the concentration of NaSal to great excess has a pronounced effect on the geometry of the nanoparticles produced, and in particular increases the proportion of 'dog-bone' shaped nanoparticles, Figure 4-18 and Figure 4-19.

The growth solutions for each sample represented in Figure 4-18 and Figure 4-19 were prepared according to GS method A with 0.55 mM H_2A and 75 µM $AgNO_3$ constant for all samples. The concentration of NaSal used was in the range of $0.25 - 500$ mM and for each sample is indicated with respect to the data in Figure 4-18 and Figure 4-19. For samples with $0.25 - 2.00$ mM NaSal, growth was initiated with 15 µL of 0.1 mM seed A. Samples with $5.00 - 100$ mM NaSal did not require any nanoparticle seed with the growth initiated upon addition of H_2A. Samples with NaSal concentrations 250 and 500 mM did not require H_2A or seed to initiate growth.

Figure 4-18 displays the effect of a low-range increase in the concentration of NaSal, $0.25 - 2.00$ mM. As established above, H_2A will be the reductant present in excess at the point of initiation of the reaction (seed addition) and so it is no surprise that the trend in nanoparticle geometry follows that observed for H_2A. Figure 4-18a and Figure 4-18b represent nanoparticles from the same sample which show distinct populations of nanorods and dog-bones. The growth solution for this sample has a concentration of reductant at the threshold of formation of dog-bones, 0.80 mM, Figure 4-9a and Figure 4-16. When the NaSal is added to the C_{16}TABr solution it can be seen by eye that micellar aggregates are formed, indicated by the presence of a gelatinous mass. With thorough mixing this mass is dispersed until it is no longer visible. However, from this observation, and the consideration of the mixed dispersion of nanorods and dog-bones in Figure 4-18a and Figure 4-18b, it would seem that NaSal is not entirely evenly dispersed through the solution and, therefore, in regions of higher reductant dog-bones form. For higher concentrations of NaSal this effect is not observed i.e. there is sufficient reductant to form dog-bones only.

No appreciable difference is apparent in the nanoparticle dimensions in the SEM images in Figure 4-18 that show dog-bones. However, if the absorbance spectra for these samples are normalised to fix the amount of gold in the solution (by adjusting the absorbance at 400 nm), Figure 4-18f, then the effect on the nanoparticles becomes more obvious. The third peak in the spectrum indicates that the nanoparticles have an

additional growth phase in the transverse axis that is more pronounced with increasing reductant.

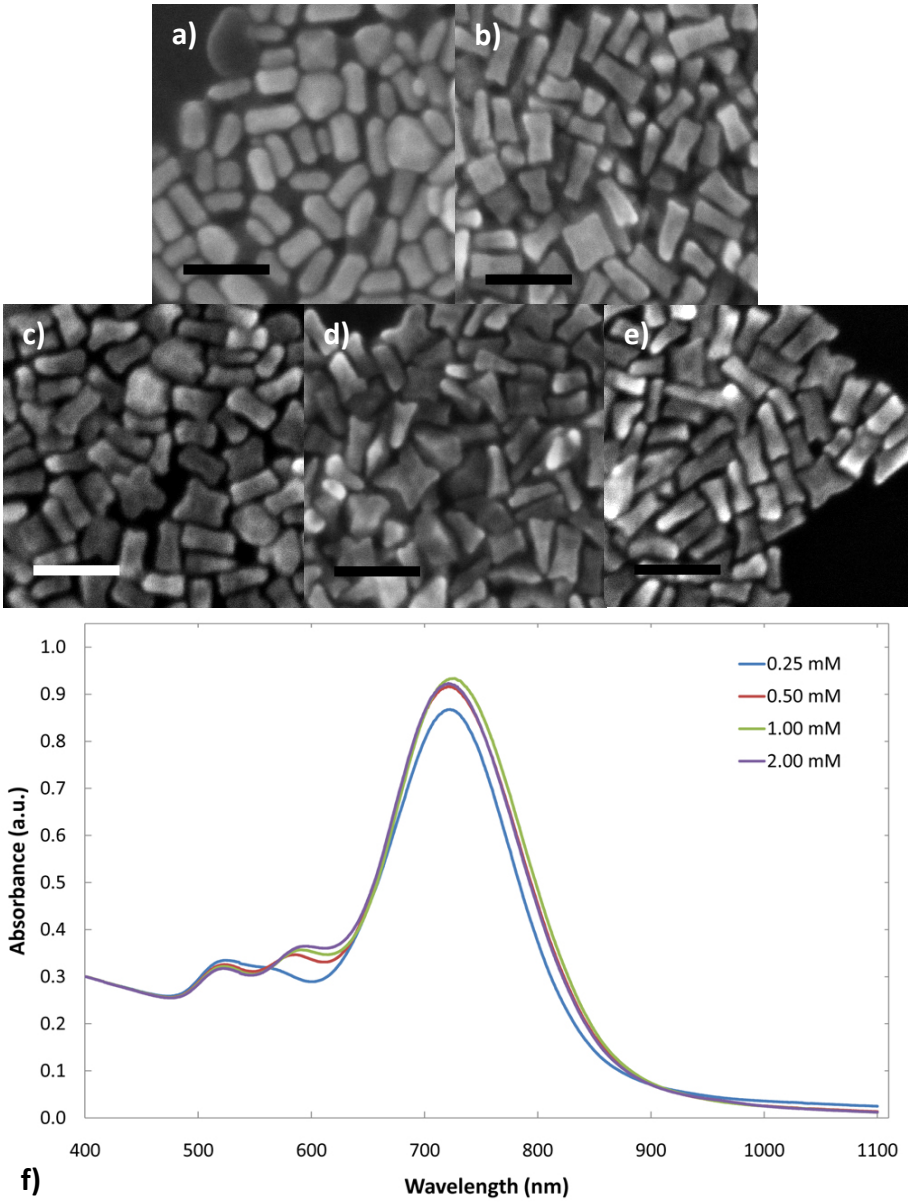

Figure 4-18 a) – e) SEM images of nanoparticles formed with a) and b) 0.25 mM, c) 0.50 mM, d) 1.00 mM and e) 2.00 mM NaSal in their respective growth solutions (all scale bars are 100 nm). f) Corresponding normalised absorbance spectra for samples a) – e)

The longitudinal peak appears to be relatively invariant for samples with a reductant concentration above the threshold for forming dog-bones. Examples of this can be seen in Figure 4-9b, Figure 4-10, Figure 4-11, Figure 4-16 and Figure 4-18. Variation of the concentration of Ag^+ is also less effective at shifting the longitudinal peak position under these conditions.

In the case that a seed particle initiator is not required, i.e. $[\mathrm{NaSal}] = 5.00 - 100$ mM, spiky or dendritic nanoparticles are formed, Figure 4-19a – e, rather than nanorods. It is

likely that the micellar conditions for these samples are more complex than normal. The viscosity in this range of concentrations is noticeably higher and suggests that the micelles are increasingly elongated and entangled. Actually, spiked particles prepared with ascorbic acid and without the addition of seed particles have been reported at a concentration of ascorbic acid that is only double the Au^{3+} concentration.[341] However, that observation is puzzling because others who have investigated similar conditions (i.e. growth solutions with the same ascorbic acid concentration) found indefinite stability[26] i.e. no nanoparticle formation.

The formation of the spiked features on the nanoparticles implies a multi-directional growth burst. Although the soft micelles may ultimately not provide any geometrical confinement of crystal growth, the distribution of reductant through the reaction solution may provide pathways for the reduction of gold to form nanoparticles with geometry proportional to the complexity of the micelles in the solution. The distribution of reductant in the seeded synthesis may also play a role in the formation of nanoparticles. However, for seeded samples the state of the seed during the early stages of growth may provide an equally limiting factor for nanoparticle growth, this will be discussed further in Section 4.1.6.

Above the concentration of NaSal where the onset of spiked nanoparticles is observed a decrease in average particle size and the production of less anisotropic particles occurs, Figure 4-19a - e. If it is assumed that the number of particles in the solution is fixed then the decrease in size from the initial growth burst will leave unreacted $AuBr_2^-$ which will lead to gradual ageing of the spikes to a lower energy structure. Alternatively the increase in reductant and stability of the micelle network could result in formation of finer, filament-like spikes that restructure with time or during the sample preparation process for imaging.

When a great excess of NaSal is used, for example 250 and 500 mM (Figure 4-19f and Figure 4-19g respectively) the particle geometry reverts to a mixed distribution mostly represented by spheres and disc shaped nanoparticles.

Figure 4-19h shows the absorbance spectra for samples with a concentration of NaSal in the range $5.00 - 500.00$ mM. It can be seen from the SEM images and spectra that the proportion of spiked particles is very high. The lack of a significant peak at ~ 520 nm is also associated with the high yield of anisotropic nanoparticles. Although the extinction for these particles appears quite broad, the range of wavelengths where the strongest extinction occurs could still find use in some spectral shielding applications.[156] Alternatively, the sharp points found on these nanoparticles have strong implications for application in SERS.[342, 343]

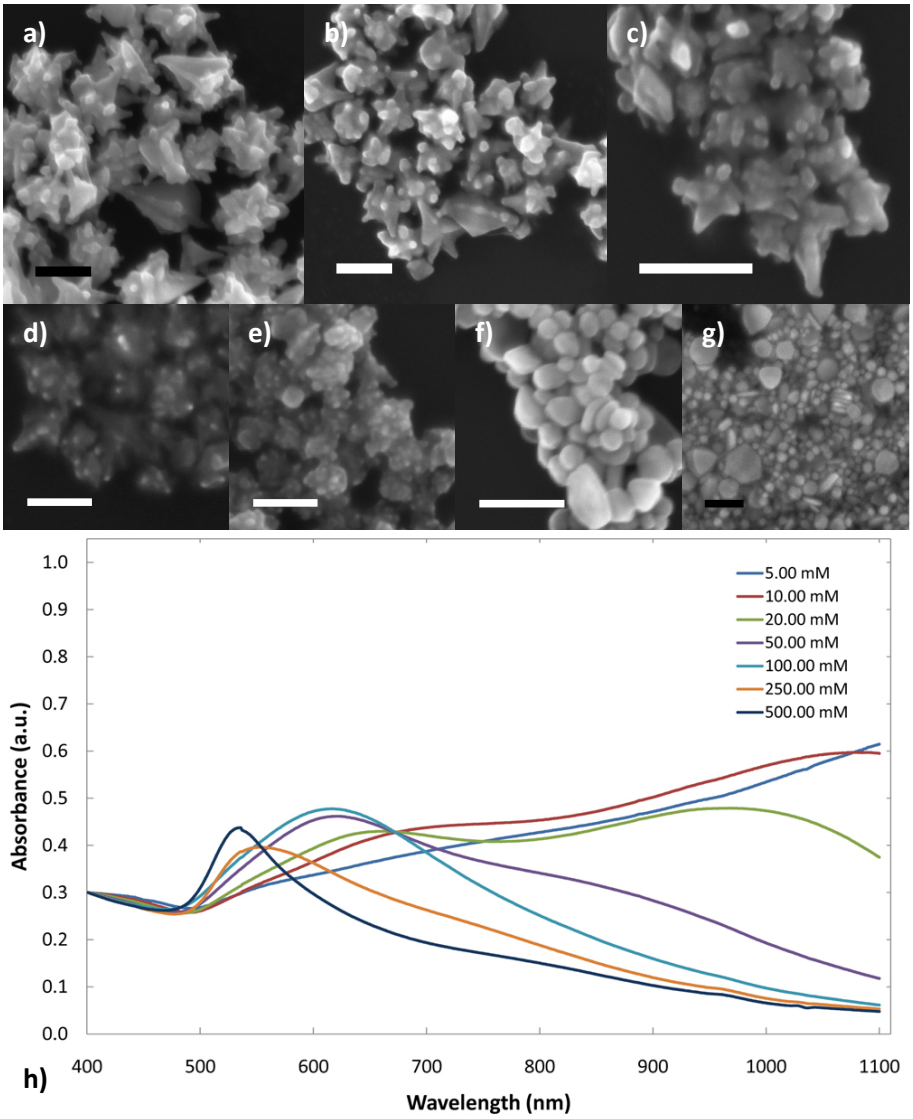

Figure 4-19 a) – g) SEM images of nanoparticles formed with a) 5.00 mM, b) 10.00 mM, c) 20.00 mM, d) 50.00 mM, e) 100.00 mM, f) 250.00 mM and g) 500.00 mM NaSal in their respective growth solutions. h) corresponding normalised absorbance spectra for samples a) – g). Scale bars a) – c), f) and g) are 200 nm, d) and e) are 100 nm

Further validation of the NaSal co-reductant synthesis is provided in Appendix D. The seed volume added to the reaction was varied resulting in a red-shift of the longitudinal peak position. Also, the reliance on $AgNO_3$ is confirmed. In particular, low aspect ratio nanorods are not formed in the absence of Ag^+. Samples prepared with an H_2A concentration less than $1:1$ with respect to Au^{3+} but high in NaSal still form nanorods.

4.1.6 Gold Nanoparticle Seed

The volume of seed solution used to initiate the growth is yet another factor that can be used as a variable to control the aspect ratio of gold nanorods. With respect to the Ag^+ – assisted synthesis, increasing the seed concentration also increases the aspect ratio[22]. When the number of seed particles increases the amount of ionic gold per

particle decreases. The primary effect of this is to reduce the width of the nanorods. I will show in Chapter 7 (Mechanism of Formation) that the width of the nanorod is strongly influenced by a secondary growth phase.

To investigate the effect of the preparation conditions on the seed particles and subsequently the nanorod synthesis, I prepared the range of seed solutions represented in Figure 4-20. All seed solutions were prepared according to seed method A with appropriate amounts of $C_{16}TABr$ and Au^{3+} added to achieve the concentrations listed.

For concentrations of $[C_{16}TABr] < 50 \times [Au^{3+}]$ there appears to be a mixture of nanoparticle sizes formed, Figure 4-20. This is signified by the presence of the plasmon peak and an increase in the extinction at higher wavelengths which could be the result of an increased scattering contribution. This effect is attributed to a non-ideal distribution of the $AuBr_4^- - C_{16}TA^+$ complex; the solution appears cloudy which suggests fine crystals of the complex may be present. For the 10 mM $C_{16}TABr - 0.5$ mM Au^{3+} seed solution there is also a distinct population of nanoparticles with diameters less than ~ 5 nm. This is indicated by the shoulder at ~ 350 nm, which is present for samples that reproducibly form sub-5 nm diameter nanoparticles, e.g. 100 mM $C_{16}TABr - 0.1$ mM $HAuCl_4$. This is a commonly used seed and the particle size has been verified by TEM.[25]

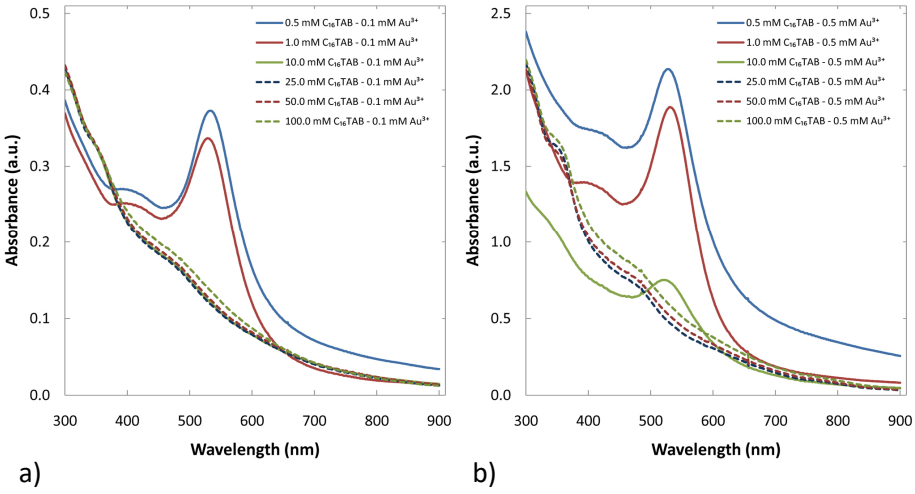

Figure 4-20 Absorbance spectra for seed solutions with a) 0.1 mM and b) 0.5 mM $HAuCl_4$ and a range of concentrations of $C_{16}TABr$

A good seed solution for a reliable nanorod product should have a size less than ~ 5 nm in diameter. The size/quality of the seed solution can therefore be inferred from the lack of a plasmon resonance peak at ~ 520 nm. With this consideration, an optimum range of concentrations is evident for 0.1 and 0.5 mM Au^{3+}. For 0.1 mM Au^{3+} this optimum occurs at concentrations of $C_{16}TABr$ between 10.0 and 50.0 mM. Although the shape of the curve for the 100 mM $C_{16}TABr$ is similar there appears to be a deviation from the tight distribution present for samples with $10 - 25$ mM $C_{16}TABr$ and so it has not been included in the ideal range. The optimum for 0.5 mM Au^{3+} also occurs around this range

with the exception of the 10 mM $C_{16}TABr$ sample as it is below the optimum ratio of Au^{3+}:$C_{16}TABr$. The slight variation in the seed solution for 100 mM $C_{16}TABr$ is reflected in the samples with 0.5 mM Au^{3+} and so would be an effect imposed by the concentration of $C_{16}TABr$.

Synthesising seed particles at various Au^{3+} concentrations allows for a wide variation in the number of seed particles per unit volume, assuming of course that there is no variation in the product size. Figure 4-21 displays the absorbance spectra of seed solutions with a range of gold concentrations at the optimum concentration of $C_{16}TABr$ (25 mM). From Figure 4-21 it is clear that there is no significant difference in the optical characteristics over this range of Au^{3+} concentrations. These solutions were prepared according to seed method A.

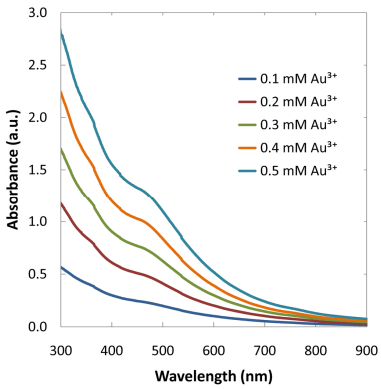

Figure 4-21 UV-Vis absorbance spectra of gold nanoparticle seed solutions prepared at different Au^{3+} concentrations

Figure 4-22 shows SEM and optical data for gold nanorods prepared from the seed solutions in Figure 4-20a. All growth solutions for these samples are identical and were prepared according to GS method B with 0.6 mM H_2A and 70 µM $AgNO_3$. Growth was initiated with a 10 µL aliquot of 0.1 mM Au^{3+} seed with the $C_{16}TABr$ concentration as indicated.

Particle dimensions for nanorods formed from seeds in the optimum range of $C_{16}TABr$ concentration and for 100 mM $C_{16}TABr$ are clustered together, Figure 4-22h. However, broadening of the transverse peak for the 100 mM $C_{16}TABr$ indicates either the formation of dog-bones or the presence of large spherical particles. From the SEM image it is clear that the rod-like portion of the ensemble have the typical nanorod geometry. Therefore, there is an increase in the proportion of spherical particles.

The proportion of nanorods is still reasonably high for samples prepared from seed solutions with a sub-optimum $C_{16}TABr$ concentration. Despite the aspect ratio being as expected, the overall nanorod dimensions are increased quite significantly with respect to those produced under typical conditions. This indicates that nanorods can form from seed particles with a diameter of ≥ 5 nm. This will be discussed below with respect to the literature and further experimental data.

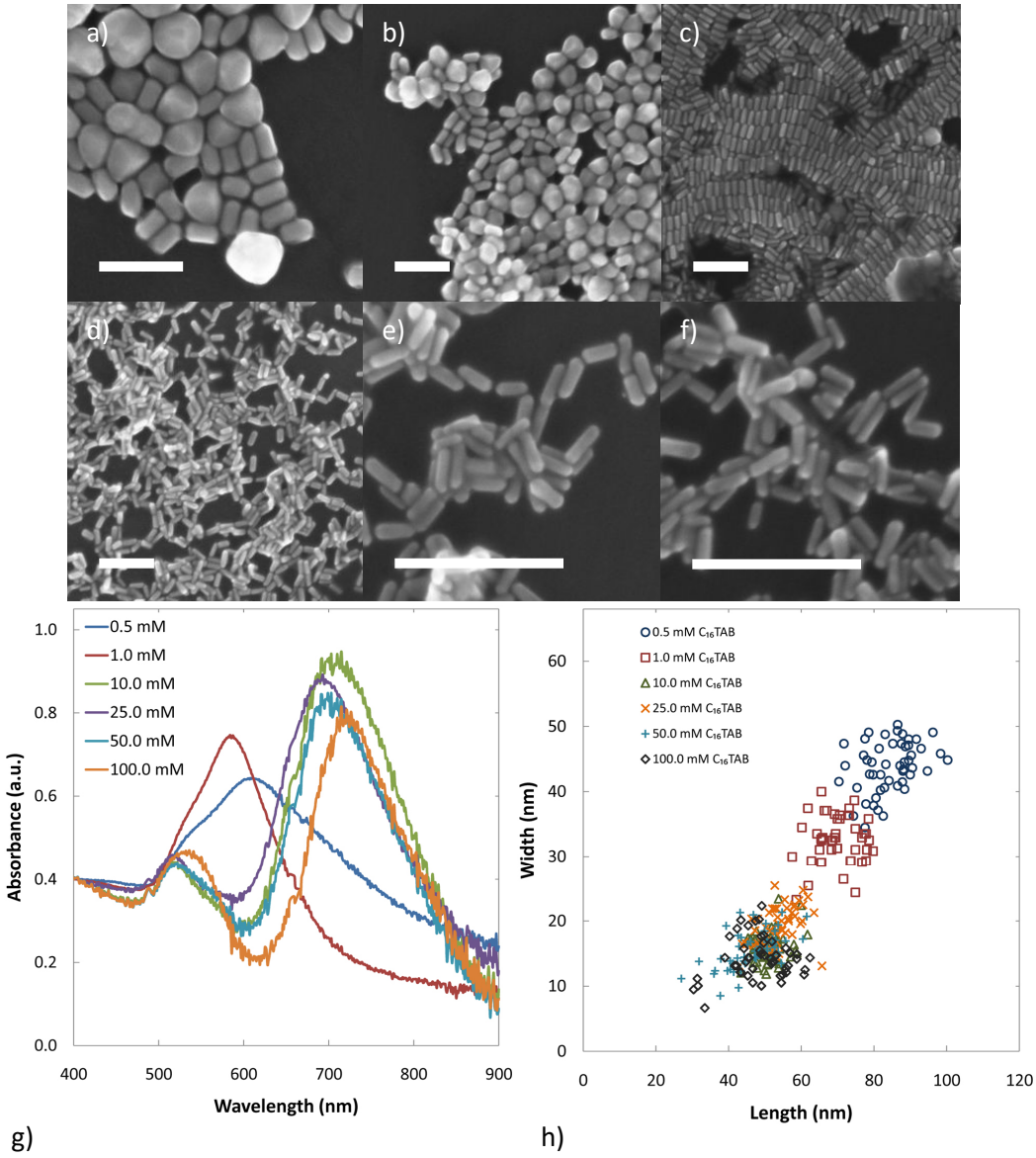

Figure 4-22 a) – f) SEM images for samples prepared using seed solutions with 0.1 mM $HAuCl_4$ and a) 0.5 mM, b) 1.0 mM, c) 10.0 mM, d) 25.0 mM, e) 50 mM and f) 100.0 mM C_{16}TABr respectively. g) Corresponding normalised absorbance spectra for a) – f). h) Nanorod dimensions for a) – f). Scale bars = 200 nm

Figure 4-23 shows SEM and optical data for gold nanorods prepared from the seed solutions in Figure 4-20b. All growth solutions for these samples are identical and were prepared according to GS method B with 0.6 mM H_2A and 70 µM $AgNO_3$. Growth was initiated with a 10 µL aliquot of 0.5 mM Au^{3+} seed with the $C_{16}TABr$ concentration as indicated. Despite forming suitable seed particles within the optimum range with respect to the 0.5 mM Au^{3+} concentration, the proportion of nanorods formed from these solutions is much lower. Those nanorods formed express particle dimensions within a similar range, Figure 4-23h. Again, the proportion of nanorods with respect to nanospheres drops for seeds formed in 100 mM $C_{16}TABr$.

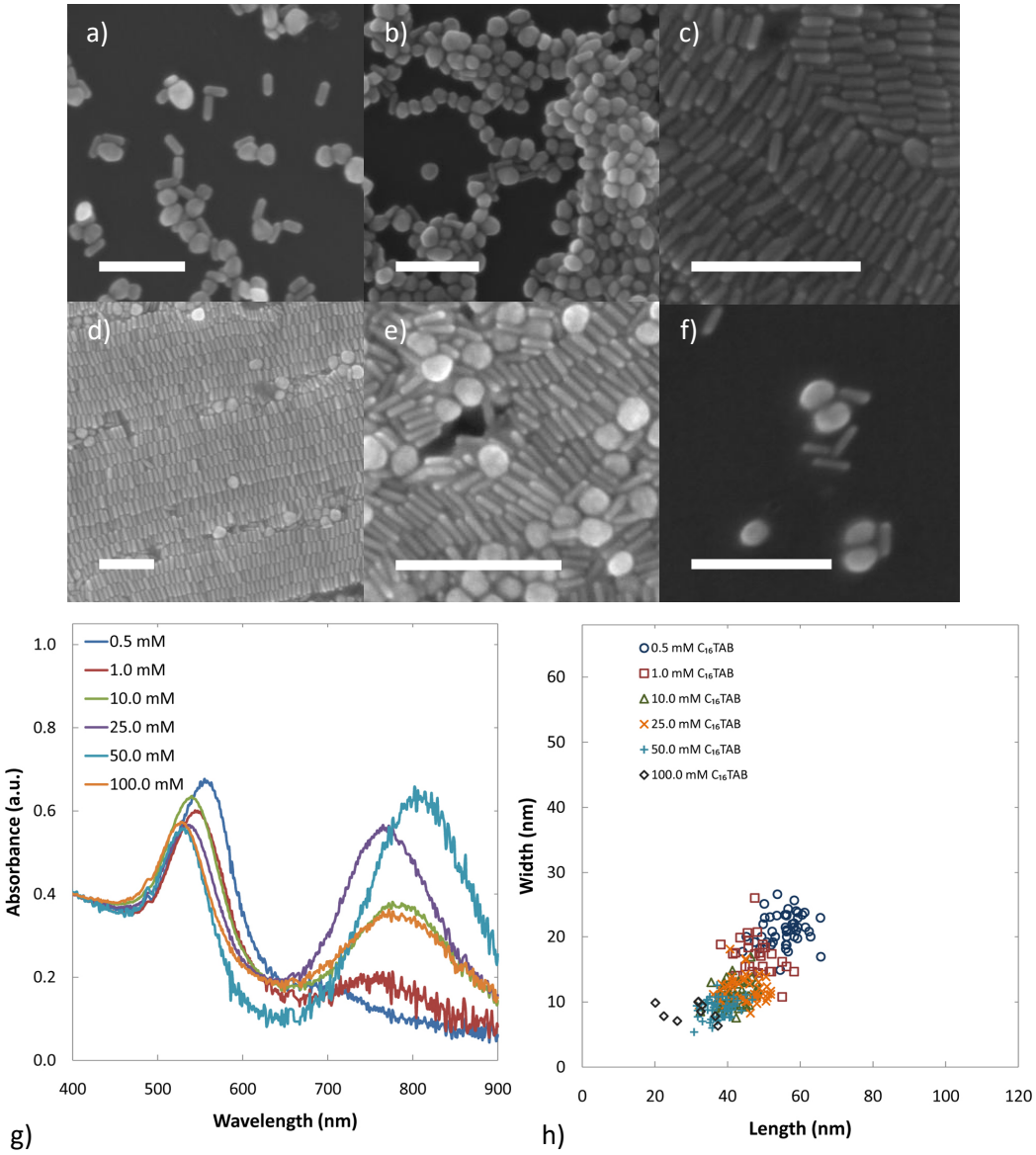

Figure 4-23 a) – f) SEM images for samples prepared using seed solutions with 0.5 mM $HAuCl_4$ and a) 0.5 mM, b) 1.0 mM, c) 10.0 mM, d) 25.0 mM, e) 50 mM and f) 100.0 mM C_{16}TABr respectively. g) Corresponding normalised absorbance spectra for a) – f). h) Nanorod dimensions for a) – f). Scale bars = 200 nm

Hubert *et al*. have reported a bifurcation in the particle dimensions observed for the nanospheres and nanorods produced in the nanorod synthesis.[126] This bifurcation is assigned to a critical condition for the seed particles to either initiate the process of rod growth or to simply coarsen as a sphere. The bifurcation point was reported to be at ~ 5 nm and was determined by plotting length *vs.* width (where these two dimensions are the same for spheres). Below the bifurcation point the only geometry of nanoparticles is nanospheres. Above the bifurcation point there are two branches in the data that represent the proportion of nanospheres and nanorods respectively. In this publication they use the modified synthesis method of Jana[19] where BH_4^- is added to the growth solution in a concentration equivalent to the $Au^{3+}(GS):Au^0(seed)$ mole ratio, where

$Au^0(seed)$ is the moles of gold in the added seed solution. This is a pseudo-seeded process as the seed particles are formed in the growth solution. For a typical synthesis this would require a $[BH_4^-]$ of ~ 75 nM (with respect to a $[Au^{3+}]$ of 0.5 mM and total sample volume of 10 mL). This low concentration could result in significant error in the final product as it is difficult to achieve reliable reproduction of such a low concentration and any variation would affect the amount of seed present. This was accounted for by Hubert *et al* by scaling the concentrations of the growth solution components to ~ 4 mM $HAuCl_4$, ~ 4.8 mM H_2A, ~ 1 mM $AgNO_3$ and 0.2 M $C_{16}TABr$. Although this method produces rods in high yield it is as yet not known whether the linear scaling of the components results in a proportional scaling of the nanorod product. The pseudo-seeded process was initially introduced due to problems producing seed particles at higher concentrations.[19] Also, from the samples in Figure 4-22 and Figure 4-23 it appears that the seeds form differently at the higher concentrations of $C_{16}TABr$ i.e. similar or equal to the concentration of $C_{16}TABr$ in the growth solution.

The following samples were prepared over a range of seed concentrations and volumes in an effort to optimise the seeding process. Particle dimensions of the nanorods produced are also considered with respect to the bifurcation mechanism reported by Hubert *et al*. The spherical particles in these samples are acknowledged but not measured. These samples cover a significantly greater range of $Au^{3+}(GS):Au^0(seed)$ mole ratios than reported by Hubert *et al*. This ratio is explored from $150{,}000:1$ to $50:1$ for samples A1 – E5 respectively. The range covered by Hubert *et al*. only spans $\sim 1{,}500:1$ to $\sim 30:1$. It is worth noting that at either end of their ratio range the population of nanorods was quite low. For the samples presented here the proportion of nanorods is significant for the majority of the samples as indicated by the UV-Vis and SEM data. This highlights a potential difference between the seeded and pseudo-seeded methods.

All samples have identical growth solutions prepared according to GS method A with 0.6 mM H_2A and 70 µM $AgNO_3$. This concentration of $AgNO_3$ is approximately half the proportional concentration with respect to Hubert *et al*. An increase in Ag^+ would have decreased the width of the nanoparticles produced.[27]

Table 4-2 Seed parameters for samples A1 – E5

	Seed Volume (µL)				
Seed $[HAuCl_4]$ (mM)	**10**	**25**	**50**	**100**	**150**
0.005	A1	B1	C1	D1	E1
0.010	A2	B2	C2	D2	E2
0.100	A3	B3	C3	D3	E3
0.500	A4	B4	C4	D4	E4
1.000	A5	B5	C5	D5	E5

For the samples represented in Figure 4-24, Figure 4-25, Figure 4-26, Figure 4-27 and Figure 4-28 the concentration of $HAuCl_4$[ee] in the preparation of the seed particle and the volume added to initiate the growth are represented by the information in Table 4-2 and are hereafter referred to with respect to their grid position in the table.

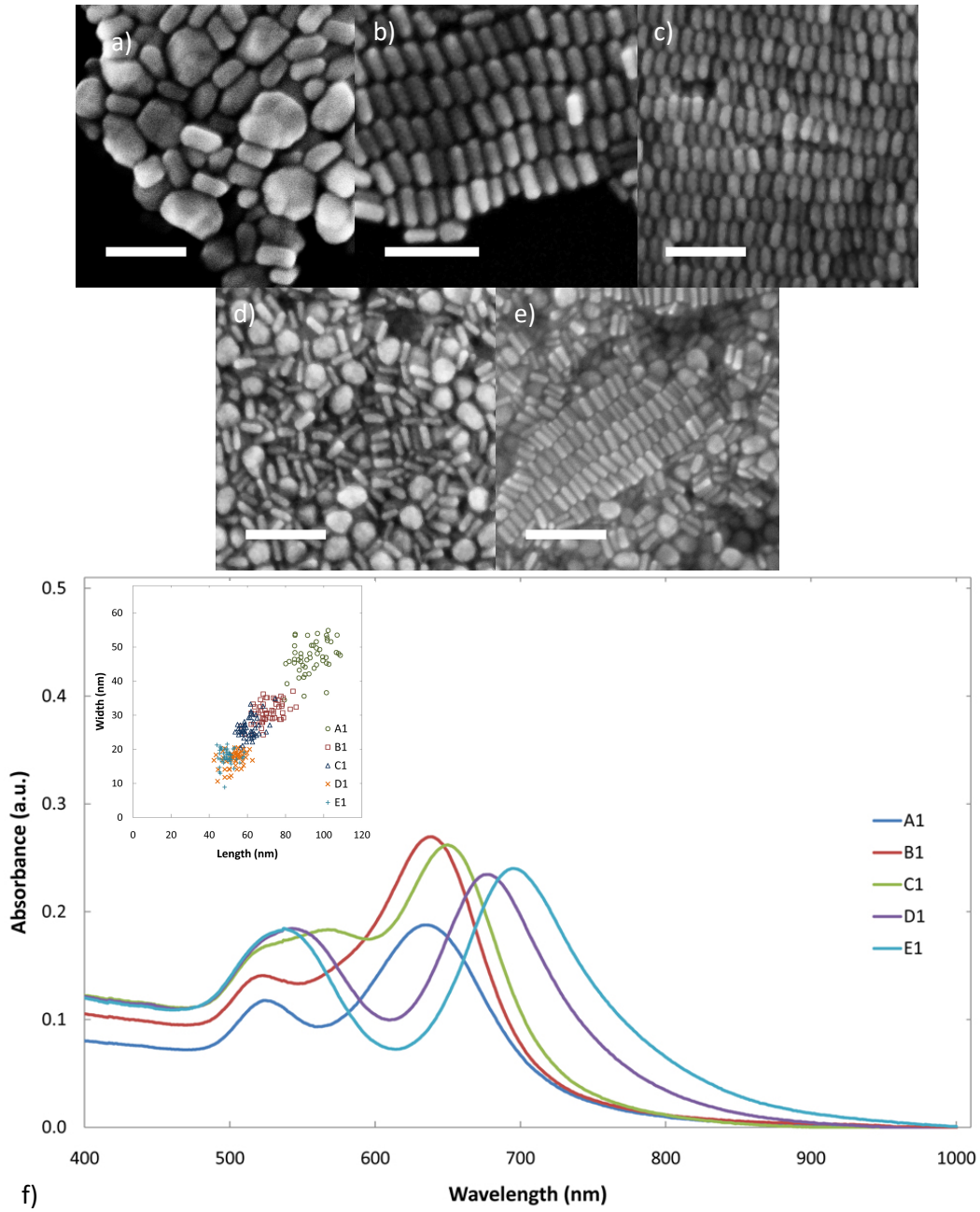

Figure 4-24 a) – e) SEM images for samples a) A1, b) B1, c) C1, d) D1 and e) E1. f) Corresponding absorbance spectra for samples A1 – E1. The inset of f) shows the nanorod dimensions measured from the SEM images. Scale bars = 200 nm

[ee] This concentration refers to the 10 mL growth solution for each respective seed solution. After the addition of BH_4^- all seed solutions were made up to 15 mL as 5 mL was the greatest aliquot required for the reduction of the highest concentration of Au^{3+}. Any calculations based on the added concentration of gold to the growth solution for nanorods have been adjusted accordingly.

Figure 4-24 shows the SEM and optical data for the range of samples A1 – E1. As expected, the aspect ratio increases with an increase in the volume of seed added. As mentioned previously the increase in aspect ratio is attributed to a decrease in nanorod width, however, in this case both length and width decrease significantly and in approximate proportion as the number of added seeds is increased.

For samples C1 – E1 the onset of a significant population of large spheres is implied by the broadening of the transverse peak. This implication is supported by the SEM images. The diameter of these spherical particles follows the same trend as the nanorod dimensions for this range of samples i.e. decreasing with increasing seed volume. The by-product nanoparticles in C1 could also be slightly more anisotropic than for samples D1 and E1.

Figure 4-25 shows the SEM and optical data for the range of samples A2 – E2. As with samples A1 – E1, the aspect ratio increases gradually with increasing seed volume. The particle dimensions also decrease to achieve this effect. The particle dimensions for A2 – E2 are spread over a narrower range with respect to A1 – E1 but produce similar aspect ratios. However, a major difference between A1 – E1 and A2 – E2 is the reduction in the presence of spherical by-products in the A2 – E2 sample range.

If it is assumed that the size of the seed particles prepared at each concentration of $\mathrm{Au}^{3+}$is the same then the effect of changing the concentration or volume is only to change the number of seed particles. I have shown that this assumption seems to be true for Au^{3+} concentrations between $0.1 - 0.5$ mM at an optimum $\mathrm{C}_{16}\mathrm{TABr}$ concentration, Figure 4-21. The pairs of samples C1 & B2 and D1 & C2 have equal $\mathrm{Au}^{3+}(\mathrm{GS}):\mathrm{Au}^{0}(\mathrm{seed})$ mole ratios, $30{,}000:1$ and $15{,}000:1$ respectively. Therefore, the aliquot of seed solution being added to the respective pair of samples should contain the same number of seed particles. The nanorod dimensions produced for each pair are reasonably similar. However, the samples in the first row of the table have a much higher proportion of spherical by-products. This indicates that the density of seed particles in the added solution is an important factor to control by-products as although there is the same number of moles of Au^{0} in the seed solutions for each pair, the volume is halved for the samples in the second row of the table.

The longitudinal peaks for samples D2 and E2 appear to have an asymmetry about the peak position. This asymmetry appears to favour the red-shifted side of the peak which would indicate either that there is a broad range of aspect ratios present above the peak distribution or that there is a significant distribution of equal aspect ratios but with increasing volume. The SEM data shows that the length and width of the nanorods in each of these samples varies by ~ 10 nm. The fact that the width varies by an equal amount to the length indicates that the aspect ratio is more significantly affected than the volume. This asymmetry in the longitudinal peak is also observed when monitoring the growth kinetics of a developing gold nanorod solution by UV-Vis-NIR spectroscopy, see Section 5.1.1.

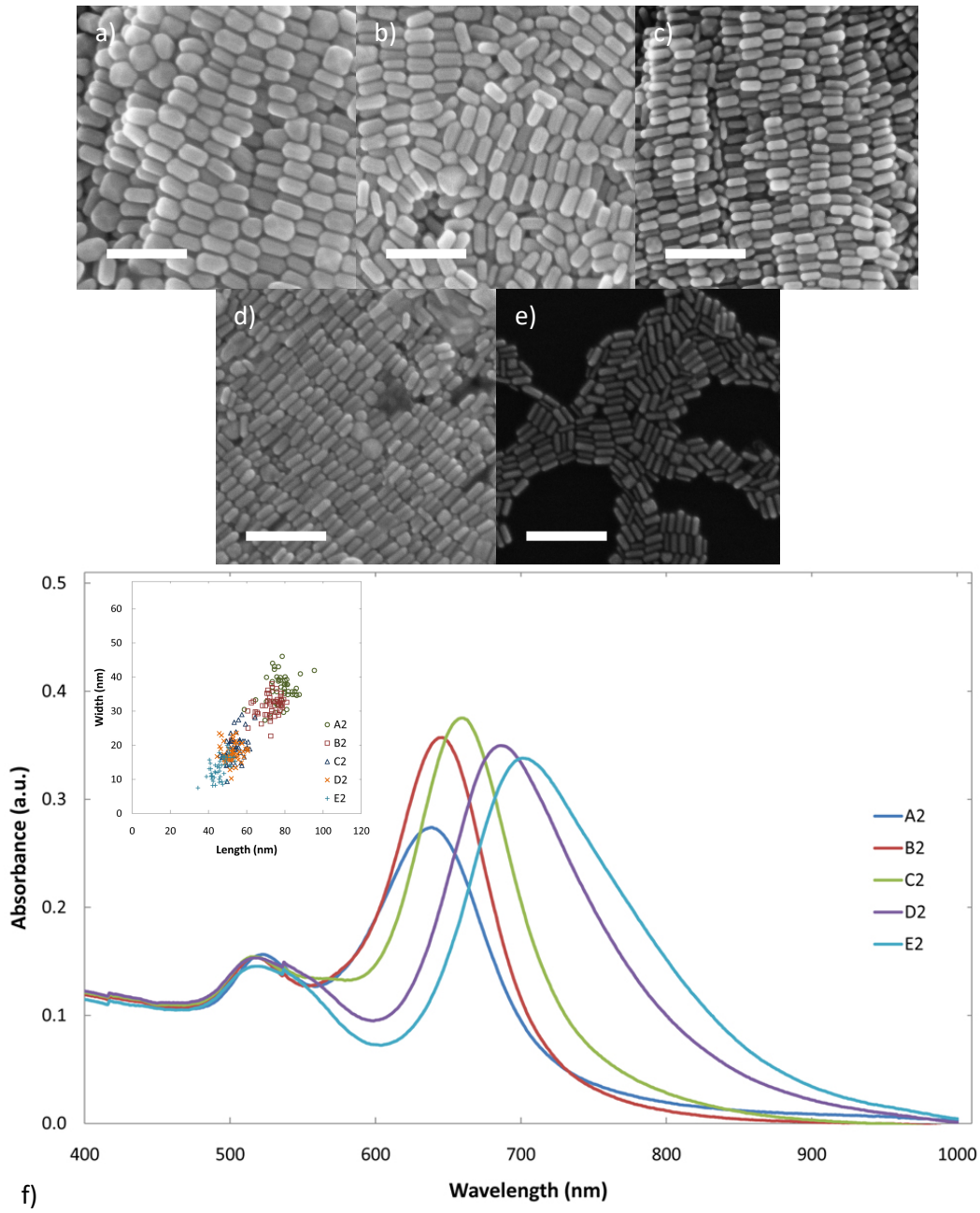

Figure 4-25 a) – e) SEM images for samples a) A2, b) B2, c) C2, d) D2 and e) E2. f) Corresponding absorbance spectra for samples A2 – E2. The inset of f) shows the nanorod dimensions measured from the SEM images. Scale bars = 200 nm

Figure 4-26 shows the SEM and optical data for the range of samples A3 – E3. These samples produce the greatest shift in aspect ratio and the highest proportion of nanorods. Although the shift in aspect ratio is quite large, the nanorod dimensions for this range are within a reasonably tight distribution. For this reason samples A3 – E3 represent very fine control over the nanorod product and so are examples of optimum seed parameters for these growth solution conditions.

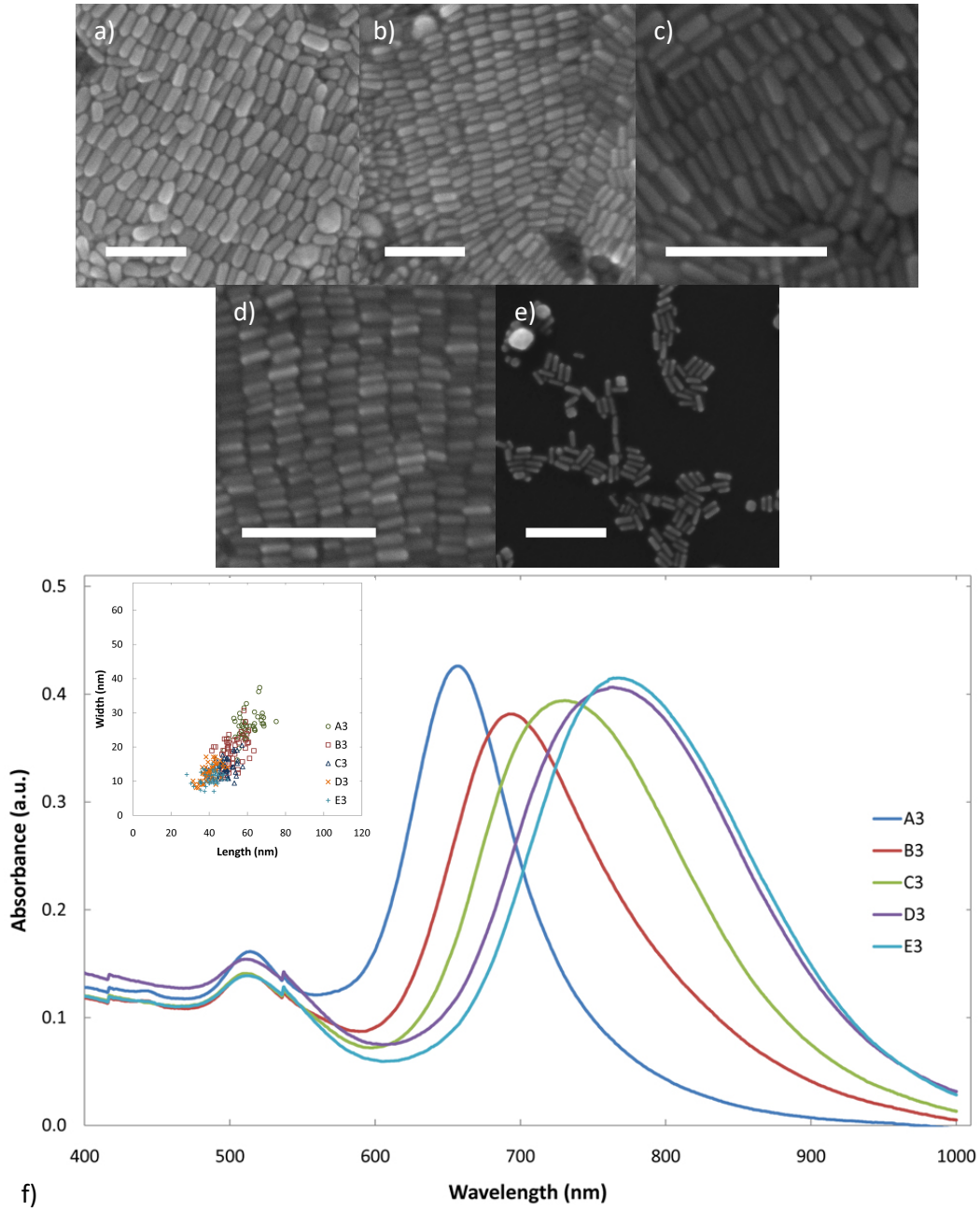

Figure 4-26 a) – e) SEM images for samples a) A3, b) B3, c) C3, d) D3 and e) E3. f) Corresponding absorbance spectra for samples A3 – E3. The inset of f) shows the nanorod dimensions measured from the SEM images. Scale bars = 200 nm

Sample D3 is the closest correlation of the $\mathrm{Au}^{3+}(\mathrm{GS}):\mathrm{Au}^{0}(\mathrm{seed})$ mole ratio to the optimum conditions reported by Hubert *et al*. The range of nanorod dimensions for D3 is shifted by $+5$ nm and $+10$ nm for the width and length with respect to those measured for the equivalent sample of Hubert *et al*. Considering the difference in relative $\mathrm{AgNO_3}$ concentration between the growth solutions this correlation is surprisingly close. Therefore, within an optimum range, the seeded and pseudo-seeded methods can produce similar products.

The longitudinal peak width broadens quite significantly as the aspect ratio increases for samples A3 – E3. This peak broadening corresponds to a broader range of aspect ratios as is observed in the SEM data and is evidently due to the increase in seed used.

Figure 4-27 shows the SEM and optical data for the range of samples A4 – E4. For samples A4 – D4 the aspect ratio initially increases with increasing volume of seed added. However, this trend ends and reverses by sample E4. Nanorods for sample E4 could not be found in the SEM and so no particle dimensions are supplied.

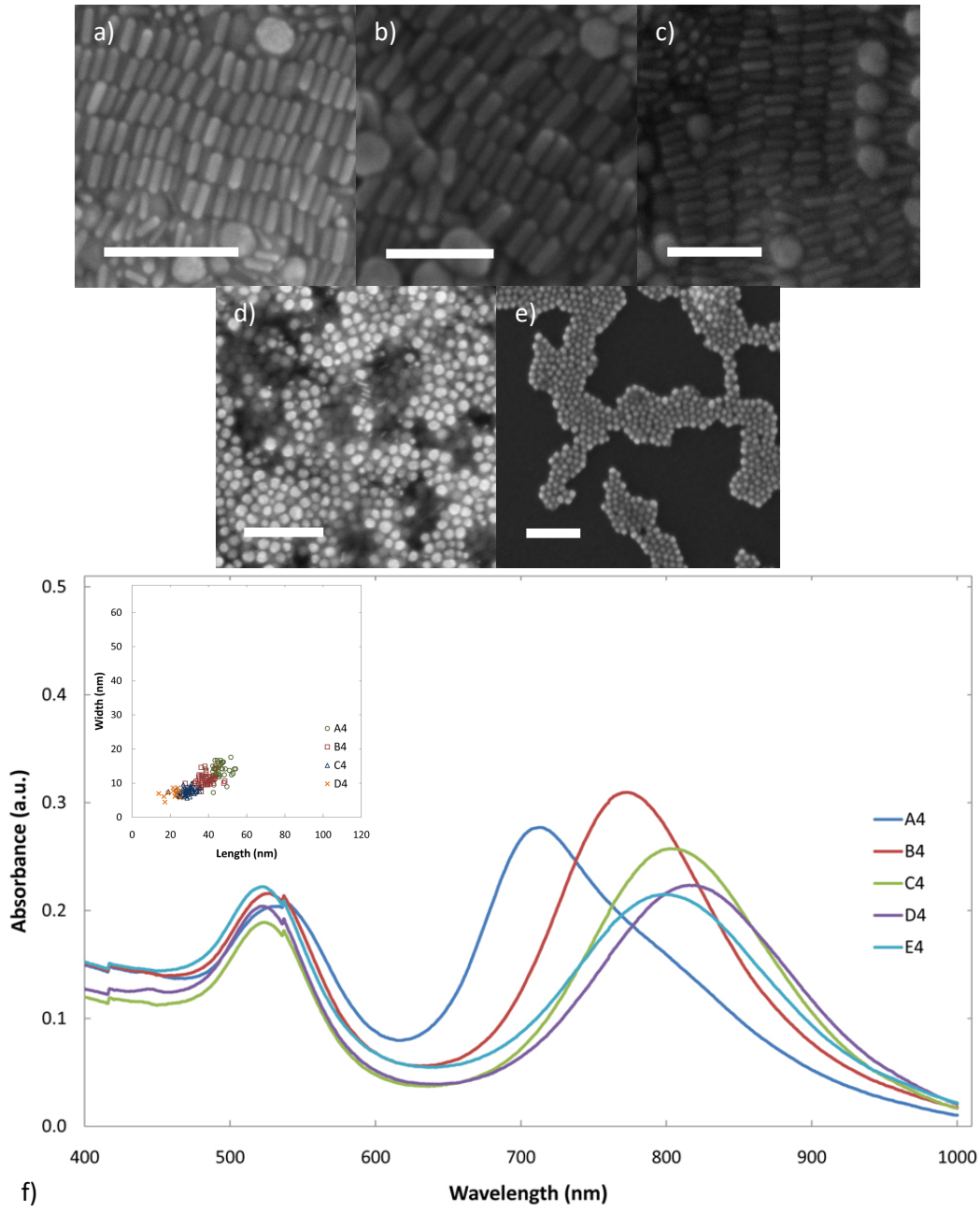

Figure 4-27 a) – e) SEM images for samples a) A4, b) B4, c) C4, d) D4 and e) E4. f) Corresponding absorbance spectra for samples A4 – E4. The inset of f) shows the nanorod dimensions measured from the SEM images. Scale bars a), d) and e) are 200 nm, b) and c) are 100 nm

Due to the trends in nanorod geometry, the dimensions of nanorods formed in E4 are expected to be of the order of $\sim 15\ \mathrm{nm} \times 5\ \mathrm{nm}$. For this range of samples the onset of a significant proportion of spherical by-products is evident. Sample A4 has the same $\mathrm{Au}^{3+}(\mathrm{GS}):\mathrm{Au}^{0}(\mathrm{seed})$ mole ratio as sample C3. Once again the nanorod dimensions produced for these samples are closely related. However, this time the increase in seed particle density (again assuming identical seed properties) increases the by-product formation. This is most likely because the density of added seed has departed from the optimum range.

Figure 4-28 shows the SEM and optical data for the range of samples A5 – E5. The conditions under which this range of samples was grown are well outside of the optimum. Some nanorods were observed in SEM for A5. It may be deduced from the absorbance spectra for samples B5 – E5 that there are nanorods present but any particles formed are likely to be of very small dimensions. A5 shares the same $\mathrm{Au}^{3+}(\mathrm{GS}):\mathrm{Au}^{0}(\mathrm{seed})$ mole ratio as sample D3. This is further evidence for the importance of keeping the volume of seed added within the optimum conditions.

The bifurcation mechanism reported by Hubert *et al*. suggests that there is a critical condition for the seed particle to achieve before it will form a nanorod. According to their data this critical condition must occur at or by the point where the seed particle has a diameter of ~ 5 nm. The same approach applied to the data above does not provide a reliable linear fit, possibly due to insufficient data points.

The particle dimensions for samples A1 and A2 are in the same range as nanorods formed from the larger seed particles in the low Au^{3+} and low $\mathrm{C}_{16}\mathrm{TABr}$ concentration (i.e. 0.1 mM Au^{3+}, 0.5 and 1.0 mM $\mathrm{C}_{16}\mathrm{TABr}$) range , Figure 4-22h. This could indicate that the seed particles produced in these solutions are at ~ 5 nm and the bifurcation of nanoparticles occurs at 5 nm. Alternatively it could indicate that the bifurcation point can be shifted to greater diameters. Another possibility is that the critical condition for nanorod growth can be achieved in the seed solution before addition to the growth solution. This could be possible as the seed solution used in this method is allowed to age for one hour before addition to the growth solution.

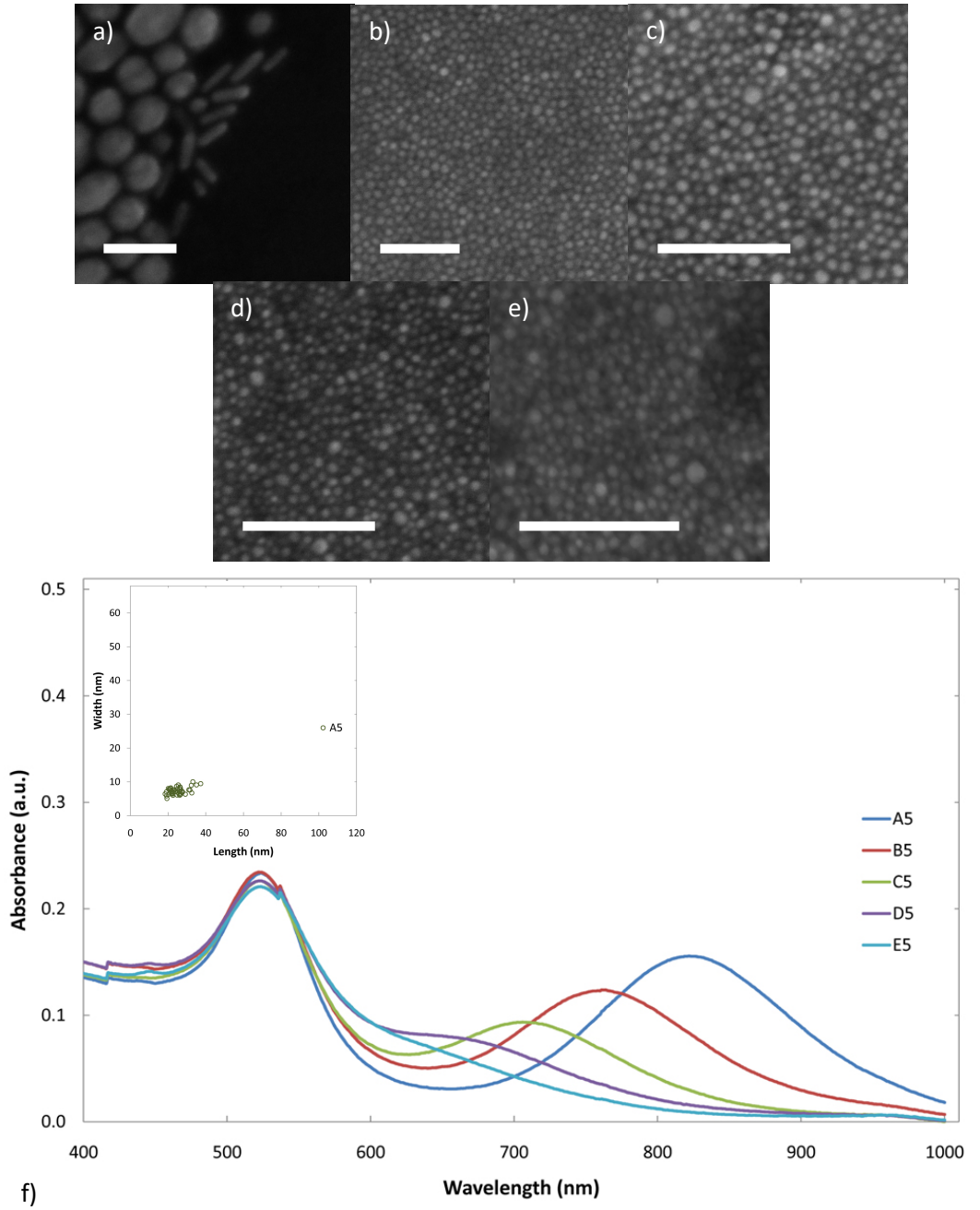

Figure 4-28 a) – e) SEM images for samples a) A5, b) B5, c) C5, d) D5 and e) E5. f) Corresponding absorbance spectra for samples A5 – E5. The inset of f) shows the nanorod dimensions measured from the SEM images. Scale bar for a) is 50 nm, scale bars for b) – e) are 200 nm

If the particle dimensions from all of the above samples (which were prepared from different seed solutions) are plotted together then a general relationship for the length and width of nanorods develops. It appears that the width of the nanorods produced in these conditions follows a quartic relationship with respect to the length, Figure 4-29. The line of best fit applied to the data has a point of intersection with the $1:1$ line (i.e. spherical particle dimensions) of ~ 6 nm. This intersection provides a reasonable

correlation to the bifurcation point reported by Hubert *et al*. but implies a relationship that transcends an individual sample.

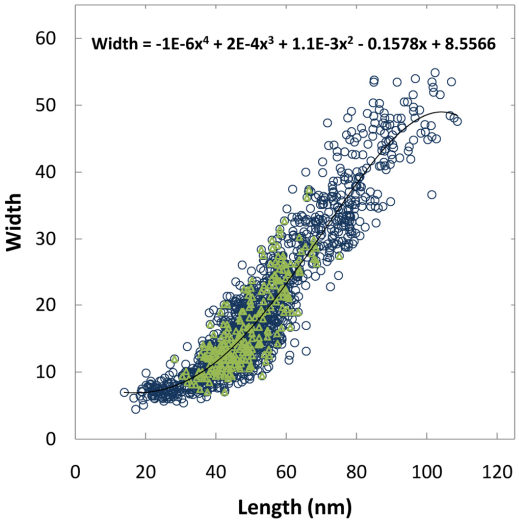

Figure 4-29 Apparent quartic relationship for nanorod dimensions prepared from varied seed solutions. Green triangles indicate optimum range A3 – E3

Figure 4-30 shows the aspect ratios and longitudinal peak positions measured from the SEM and optical data (blue circles), respectively, for all the samples prepared from the numerous seed solutions. The red squares and green triangles in Figure 4-30 correspond to predictions of the aspect ratio based on the measured longitudinal peak position. These predictions are based on simulations for a range of aspect ratios of gold nanorods with various volumes calculated by Cortie (red squares) and Brioude *et al*. (green triangles). The data of Cortie was calculated to simulate a distribution of aspect ratios to assess nanorods as spectrally selective coatings for architectural glass.[156]

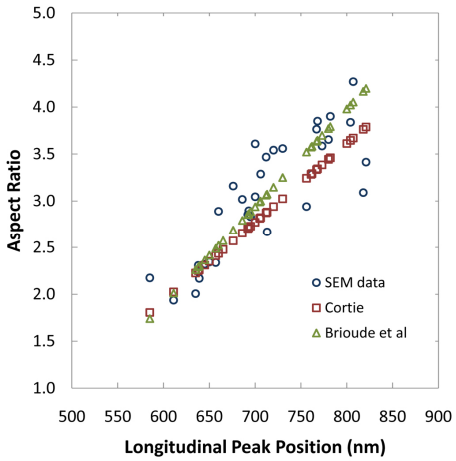

Figure 4-30 Comparison of optically and physically (from SEM data) determined gold nanorod aspect ratios

Despite DDA being utilised in the determination of the results for both sets of data, there appears to be some discrepancy. One source of the discrepancy could be the use

of different dielectric data for the simulations; another could be in the precise details of the rod shape assumed. Figure 4-31 shows some deviation in the real and imaginary parts of the dielectric data used for the simulations by Cortie, CRC (Weaver),[295] and Brioude *et al*., Palik,[344] respectively.

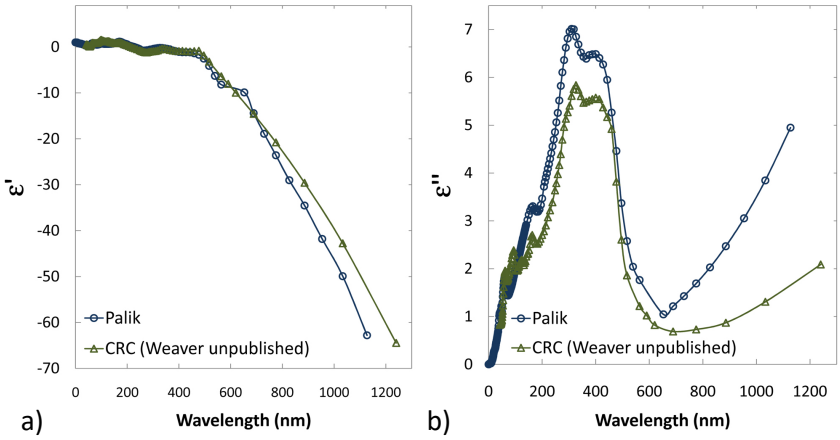

Figure 4-31 a) Real and b) imaginary parts of the dielectric data for gold from Palik and CRC Handbook of Chemistry and Physics

As far as target shape is concerned, Cortie used a hemi-spherically capped cylinder which is commonly used throughout the literature. Brioude *et al*. note that they use the 'real shape' for their calculations but do not describe explicitly the target they use.

4.1.7 Summary

This chapter has investigated some important aspects of the wet chemical synthesis of gold nanorods. To validate the methods used to prepare the samples I used the well-known effects of varying Ag^+ and $C_{16}TABr$ concentration to correlate my results with those of other researchers.

Previous reports have noted that the gold species formed in the growth solution is $AuBr_4^-$. This implies that the chloride ions from the original compound, $AuCl_4^-$, are released into the reaction solution. Although it is well known that a large excess of chloride ions has a poisoning effect on nanorod synthesis, I have shown here that the release of these ions from the gold salt does not have a significant effect on the nanorod product. This was achieved by comparing the standard method with one in which $HAuBr_4$ replaces $HAuCl_4$.

I have also shown that a significant shift in the aspect ratio can be achieved by slight variations in the amount of the reductant added to the growth solution. If this is used in conjunction with a varied Ag^+ concentration, the achievable aspect ratios converge as the reductant concentration is increased. Although the increase in reductant allows for better efficiency with respect to the amount of gold used in the reaction, a trade-off may be required to produce the desired aspect ratio.

The gradual increase in reductant concentration also provides evidence for the disproportionation of $AuBr_2^-$ as the mechanism by which Au^0 is formed. This is supported by replacing the excess concentration of H_2A in the growth solution with $NaSal$. By changing the order of addition of reactants, it was shown that the formation of a significant quantity of nanorods requires an efficient reductant.

Using a broad range of seeding conditions, an optimised process has also been determined for the growth solution conditions. The particle dimensions of the nanorods prepared from these samples also provided an insight into the process required for the seed particle to form a nanorod.

From the experiments described here, I conclude that the seeded process offers a number of advantages over the pseudo-seeded process. First, BH_4^- solutions decompose quite rapidly and are difficult to control, and second, measuring the low concentration and low volume required for the pseudo-seeded process is prone to introduce errors.

5 On the Formation of Gold Nanorods

Regardless of the precise mechanism of nanorod formation it is a necessity for the growth process to favour the longitudinal direction at some point in the reaction.

There have been only a few studies in which the growth rates of nanorods have been specifically determined.[111, 120, 124, 125] In these studies it has been concluded that the radial and longitudinal growth rates are comparatively rapid to start with, and then decline asymptotically to zero. A coupled pair of empirical growth models for Au nanorods has been proposed.[124]

All of the methods used to determine a model for the growth of gold nanorods have combined their optical absorption properties with measured or inferred physical dimensions. (Inferred physical dimensions were invoked by Gulati *et al*. where they correlated the measured extinction cross-section to a large array of calculations performed using Gans' theory for ellipsoids.) Although this method rapidly provides the exact solution for the extinction of the nanoparticle calculated it has the drawback that the non-ellipsoidal shape of real nanoparticles will result in significant differences with respect to features of the spectrum.[63, 333] On the other hand, using a more accurate model for the nanorod geometry results in a significant increase in the computation time for the simulation.

The physical dimensions of nanorods during growth have been probed using TEM[22, 103] and SAXS[124, 125]. For TEM studies it is essentially a requirement that excess surfactant and ionic species are removed from the solution in order to prevent interference in the imaging process. Zweifel and Wei have shown that the centrifugation process affects the nanorod geometry, typically shortening it, and therefore detailed analysis of the fine structure of the nanorods during the growth process using this method is compromised.[103] However, by using a chemical agent to arrest the growth (confirmed by observation of the absorbance spectrum) they were able to show that the nanorods undergo a rapid initial growth phase (less than 15 minutes) followed by a subsequent slow phase in which they get wider. However, there is also no guarantee that the chemical agent does not affect the fine structure of the nanorod.

SAXS can provide the physical dimensions of a colloidal solution without significant effect on the sample. It is then possible to analyse the intensities and shape of the scattering profile to extract parameters such as particle volume, shape and dimensions.[345] However, in order to gain this information some prior knowledge of the particles must be available in order to apply the appropriate analysis functions. Analogous to the geometry effect on the optical absorption properties, approximate geometries, e.g. a cylinder[124], may be used to roughly fit the SAXS data for nanorods, however, use of a more accurate model i.e. sphero-cylinder[346, 347] improves the value of the parameters that are extracted[125, 348]. It should also be noted that the presence of particles with similar volumes but radically different geometries i.e. by-products, significantly affect the structural characterisation of the nanorods.[348] Nevertheless, the nanorod dimensions obtained by SAXS studies fit into the range expected from representative TEM images. This includes the aspect ratio, which correlates reasonably well with the aspect ratio calculated from the longitudinal peak position using the equation of Brioude *et al*.[68]

In this chapter I investigate how data from various techniques can be combined to provide insight on the physical properties of gold nanorods during their growth process. The methods I have used to analyse the growth kinetics include UV-Vis-NIR spectroscopy, SAXS and cryo-TEM and SEM. I will show that if the results from these methods are considered individually then the implications from each are shown to be somewhat contradictory in context of globally accepted assumptions.

A critical assumption in previous studies is that that all seed particles grow to rods simultaneously. Instead, I propose a new growth model, in which nuclei transform into rods at random times. This model satisfies all the observations made in the various experiments and is also supported by DDA simulations. This new model casts doubt on the globally assumed growth mechanism.

5.1 Results and Discussion

5.1.1 UV-Vis-NIR Spectroscopy

The optical extinction properties of gold nanorods are experimentally readily accessible and can be monitored during a time-dependent study of their growth. I have performed experiments to probe the optical properties of developing nanorod solutions with 0.60 mM (Figure 5-1a and Figure 5-1c) and 0.65 mM H_2A (Figure 5-1b and Figure 5-1d), respectively. I prepared the growth solutions for each sample according to GS method A to contain 0.50 mM $HAuCl_4$, 0.1 M $C_{16}TABr$, 0.60 mM or 0.65 mM H_2A and 70 µM $AgNO_3$. Growth of the gold nanorods was initiated by adding 10 µL of freshly prepared seed A solution which had $HAuCl_4$ concentration of 0.1 mM.

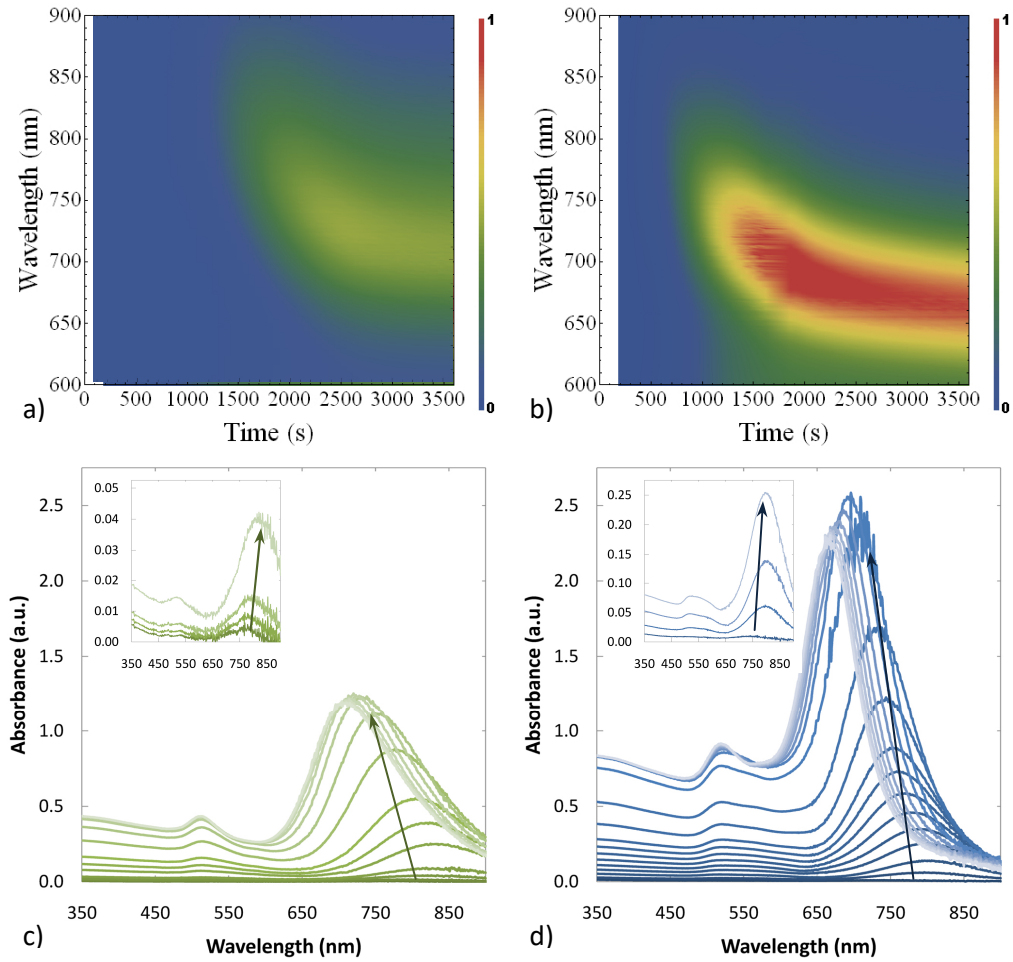

Figure 5-1 UV-Vis-NIR spectroscopy of the reaction kinetics of gold nanorods. Density plots for gold nanorods with a) 0.60 mM and b) 0.65 mM H_2A in the growth solution respectively. The scale of these plots has been normalised to the maximum absorbance of the 0.65 mM dataset. Time-dependent, two-dimensional absorbance plots indicating the transition of the longitudinal resonance peak for gold nanorods with c) 0.60 mM and d) 0.65 mM H_2A in the growth solution respectively. The insets in c) and d) are an enlargement of the earliest traces for each respective dataset. The arrows indicate increasing time.

Figure 5-1a and Figure 5-1b display density plots for the kinetic observation of gold nanorod growth up until one hour, where the absorbance intensity (represented by colour) is normalised to the maximum absorbance for the 0.65 mM H_2A sample. I decided to stop measuring at this point in the reaction as the longitudinal peak position and the concentration of Au^0 (as indicated by the absorbance at 400 nm) appeared to have stopped changing significantly. This was confirmed by measuring the spectrum of the 0.60 mM H_2A sample at ~ 24 hours, which revealed that there was a slight increase in the volume of gold and intensity of the transverse peak but no change in the position of the longitudinal peak. This could indicate that there is a slight increase in the particle dimensions (not significant enough to shift the longitudinal peak) or, in consideration of the absorbance intensity of the transverse peak, an increase in the population of spherical particles.

Figure 5-1c and Figure 5-1d show two dimensional plots that provide a clear indication of the movement of the longitudinal peak position; the insets show the earliest recorded data for each respective dataset. I measured spectra at earlier times, however, there was some fluctuation in the intensity due to the low signal to noise ratio and so I have not included this data in any quantitative observations.

The absorbance intensity of the kinetics data for the 0.65 mM H_2A sample approached the limit for the spectrophotometer during the reaction (1620 s) so the sample was diluted for the remainder of the reaction. The Au^0 concentration for the 0.65 mM H_2A sample follows the same curve shape (Figure 5-2) as the 0.60 mM H_2A sample and so diluting the sample does not appear to have affected the reaction.
In both samples the first spectrum shows that the position of the longitudinal peak is significantly red-shifted with respect to the transverse peak. This represents very rapid growth in the longitudinal axis, which happened well before the nanorods achieved a high optical density. Also, the longitudinal peak position reaches its maximum wavelength in the early stages of the reaction. If it is assumed that all of the seed particles form nanorods concurrently then this indicates that the longitudinal growth rate has reached its maximum before (or approximately at) the first measurable spectrum. The possibility of seeds forming nanorods in sporadic growth events i.e. at different times will be discussed below in Sections 5.1.4 and 5.1.5.

The longitudinal resonance position gradually blue-shifts for the remainder of the reaction after the initial, rapid red-shift. Again, if it is assumed that all seed particles are reacting concurrently, then this indicates that the relative growth rates should be approximately equal or that the length growth phase is complete. The latter is unlikely because the concentration of Au^0 in the reaction is a very small fraction of the final concentration at this point in the reaction (Figure 5-2).

During the blue-shift phase of the change in longitudinal peak position, the shape of the peak is asymmetric. Toward the end of the reaction this asymmetry reduces and the peak width narrows. This is difficult to account for in a concurrent seed growth model as it implies that the distribution of aspect ratios is biased towards higher values. If all of the nanorods are developing simultaneously then there should be no bias. This

asymmetry fits easily into a growth model that does not assume concurrent growth of seed particles and is discussed further in Section 5.1.5.

In the final stages of the reaction the concentration of Au^0 reaches its maximum value *before* the longitudinal resonance peak becomes fixed, Figure 5-2. This indicates that the aspect ratio is still decreasing even though no further gold is being reduced. Therefore, at this point the length must decrease and the width increase, in order to simultaneously maintain the net concentration of Au^0 and a blue-shifting peak.

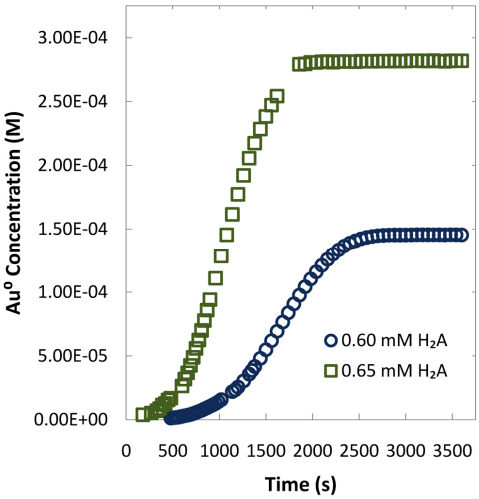

Figure 5-2 Au^0 concentration as a function of time for growing gold nanorod solutions with 0.60 mM and 0.65 mM H_2A in the growth solution respectively.

As mentioned previously, the formation of gold nanorods is an autocatalytic process where the gold nanoparticle seed initiates the reaction and is a part of the final product. As further gold is deposited on the surface of the seed particles, the rate of the reaction will increase rapidly due to the increase in the amount of catalyst. From Figure 5-2 it is clear that the rate of Au^0 formation rapidly increases in the first half of the reaction and then decreases steadily until it reaches the endpoint. The disproportionation mechanism can be approximated by a second order autocatalytic reaction of the form $A + P \rightarrow 2P$, where P is present on the left hand side of the mechanism in some concentration to initiate the reaction, has the rate equation:[349]

$$\frac{\mathrm{d[P]}}{\mathrm{dt}} = k[\mathrm{A}][\mathrm{P}]_0 \qquad 5.1$$

Where, $[\mathrm{A}]$ is the reactant concentration, $[\mathrm{P}]_0$ is the initial catalyst concentration, $\frac{\mathrm{d[P]}}{\mathrm{dt}}$ is the rate of formation of P and k is the rate constant. The integrated rate law for this reaction is defined by the equation:[349]

$$k\mathrm{t} = \frac{1}{[\mathrm{A}]_0 + [\mathrm{P}]_0} \ln\left(\frac{[\mathrm{A}]_0([\mathrm{P}]_0 + [\mathrm{P}])}{([\mathrm{A}]_0 - [\mathrm{P}])[\mathrm{P}]_0}\right) \qquad 5.2$$

This relation can be expressed with the concentration of product, $[\mathrm{P}]$, as the subject:[350]

$$[\mathrm{P}] = \frac{([\mathrm{A}]_0 + [\mathrm{P}]_0)}{1 + \left(\frac{[\mathrm{A}]_0}{[\mathrm{P}]_0}\right) \mathrm{e}^{-([\mathrm{A}]_0 + [\mathrm{P}]_0)kt}} \qquad 5.3$$

In consideration of the disproportionation mechanism provided in Section 4.1.4, if it is assumed that the $\mathrm{H_2A}$ consumes the $\mathrm{AuBr_4^-}$ without any delay and the reaction progresses at first order with respect to $\mathrm{AuBr_2^-}$ and $\mathrm{Au^0}$ then Equation 5.3 can be used to approximate the reaction kinetics for the formation of gold nanorods. The equation then takes the form:

$$[\mathrm{P}] = \frac{\left([\mathrm{AuBr_2^-}]_0 + \left[\mathrm{Au^0_{seeds}}\right]_0\right)}{1 + \left(\frac{[\mathrm{AuBr_2^-}]_0}{\left[\mathrm{Au^0_{seeds}}\right]_0}\right) \mathrm{e}^{-\left([\mathrm{AuBr_2^-}]_0 + \left[\mathrm{Au^0_{seeds}}\right]_0\right)kt}} \qquad 5.4$$

The rate constant for any given reaction is independent of the concentration of the species involved but highly dependent on the temperature.[349, 350] As the reaction mechanism is the same and the temperature is constant for the two data sets this indicates that the rate constant is fixed.

Figure 5-3 shows the application of Equation 5.4 to approximate the reaction kinetics of the formation of gold nanorods with 0.60 mM and 0.65 mM $\mathrm{H_2A}$ in the growth solution respectively. The value of $[\mathrm{AuBr_2^-}]$ used for the fit is indicated with respect to the corresponding trace in Figure 5-3. These values are selected to correspond with the initial gold concentration (i.e. absolute maximum for the product) of the growth solution, 0.50 mM, and the final values measured for each sample, 0.145 mM and 0.282 mM for 0.60 mM and 0.65 mM $\mathrm{H_2A}$ respectively. These measured values are close to the expected $\mathrm{Au^0}$ concentrations predicted by the ascorbic acid driven disproportionation mechanism presented in Section 4.1.4. The value applied for the rate constant is $= 22.5\ \mathrm{L.mol^{-1}.s^{-1}}$.

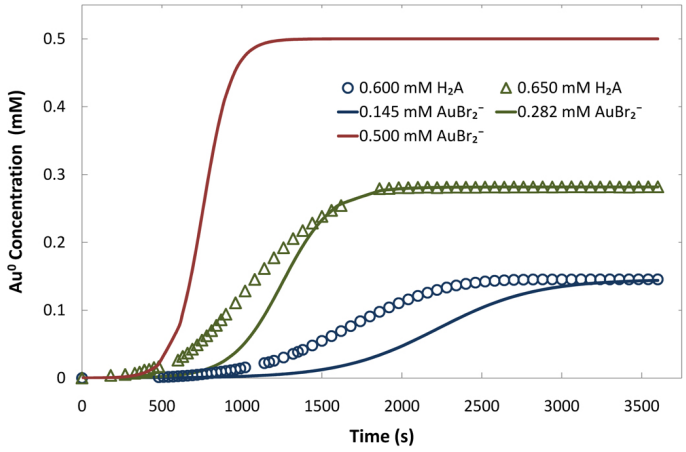

Figure 5-3 Second order autocatalytic growth model applied to the measured optical absorbance data for the growth of gold nanorods.

It is clear from Figure 5-3 that the fit for the second order autocatalytic rate described by Equation 5.4 is poor for this reaction. One reason for the poor quality of the fit is the exclusion of the concentration of $\mathrm{H_2A}$ in the description of the reaction rate as this determines the final concentration of $\mathrm{Au^0}$ present in the nanorods. However, in the initial stages of the 0.65 mM $\mathrm{H_2A}$ the data correlates with the total gold concentration approximation and as the reaction progresses approaches that of the final measured value (which is closely predicted by the concentration of $\mathrm{H_2A}$ used). In consideration of the disproportionation mechanism this indicates that the rate limiting step in the reaction is the reduction of $\mathrm{AuBr_4^-} \rightarrow \mathrm{AuBr_2^-}$ by $\mathrm{H_2A}$. It also appears that the primary effect of $\mathrm{H_2A}$ on the progression of the reaction is to approach the rate for the limited concentration.

A closer fit for the 0.60 mM H_2A data can be achieved with a higher value of k, but the same value applied to the 0.65 mM H_2A data gives an unsatisfactory fit with the rate overestimated as the end of the reaction is approached.

5.1.2 Estimation of nanorod dimensions from a UV-Vis-NIR spectrum

The optical response of a colloidal solution of gold nanorods is dependent upon the average aspect ratio and number of particles with volume, V.

By using these facts, and some assumptions, I have written a Mathematica script to provide an estimation of the physical dimensions of gold nanorods from the UV-Vis-NIR spectrum of a sample (details of which are provided in Section 2.3.7 and Appendix B.

Figure 5-4 shows the change in nanorod volume over time using parameters obtained from the optical data presented in the previous Section 5.1.1. For this calculation I used a seed diameter of 1.8 nm as this produced a particle volume that correlates with data I have produced by SAXS on the 0.65 mM $\mathrm{H_2A}$ growth reaction, Section 5.1.3. Also, I have assumed here that all seed particles grow concurrently.

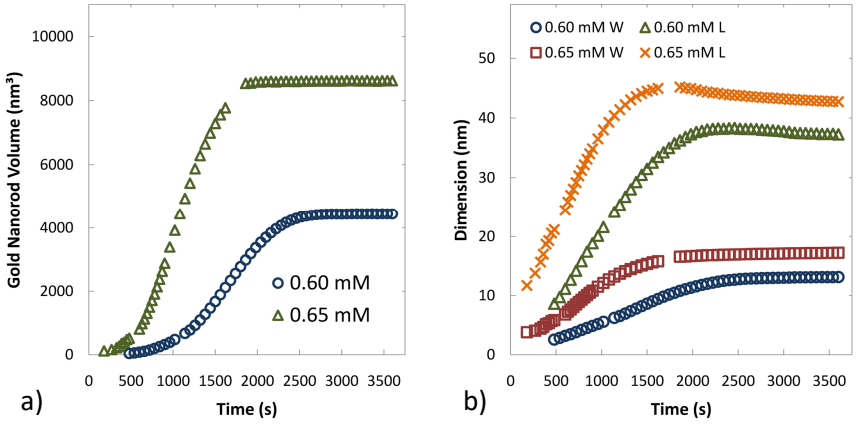

Figure 5-4 Physical properties of growing gold nanorods interpreted from UV-Vis spectra a) volume and b) length (L) and width (W).

Figure 5-5 shows the effect of changing the diameter of the seed particle used for the calculation of the number of particles in the solution. As there is the same amount of gold in the measured solution, changing the number of particles used in the calculation will result in a variation of particle dimensions produced. A 3 nm seed diameter provides a better match to the range of values measured using SEM for these reaction conditions, sample A3 Section 4.1.6 (length $\approx 50-70$, width $\approx 25-30$).

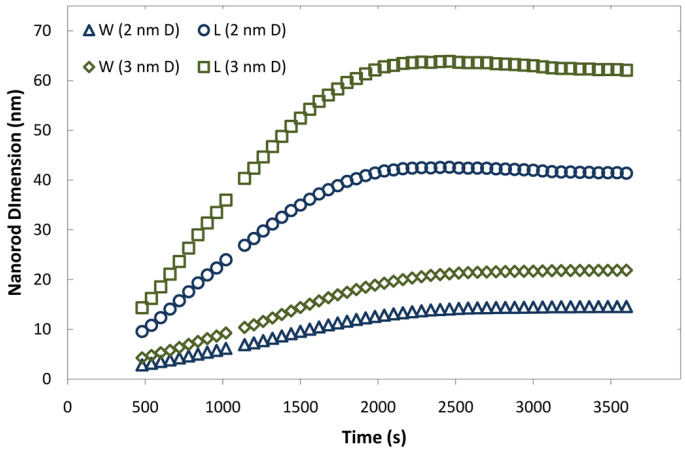

Figure 5-5 Particle dimensions estimated from optical data for the growth of gold nanorods with 0.60 mM H_2A in the growth solution using a 2 nm (2 nm D) or 3 nm (3 nm D) diameter nanoparticle seed.

The shape of the optical extinction spectrum of a dispersion of gold nanorods is quite characteristic. However, there can be features of the spectrum that can be a contribution of a by-product of the reaction or an indication that the reaction has progressed to form a new geometry, e.g. dog-bones,[333] Section 4.1.4. The extraction of particle dimensions using this set of equations (for the hemi-spherically capped cylinder) for nanoparticle distributions with geometries such as dog-bones would be inaccurate, as the longitudinal peak position in that case will be affected by the extent of the dog-bone structure and not just the aspect ratio.[333]

5.1.3 Small-Angle X-ray Scattering

Small-angle X-ray scattering is a technique that measures inhomogeneities of colloidal size. An inhomogeneity is considered to be a distinct change in electron density i.e. a distinct boundary between scatterer and medium. The scattered intensity is proportional to the square of the difference in the electron density between the scatterer and the surrounding medium.[345] The scattering angle is inversely proportional to the size of the scattering object. Therefore the small-angle scattering profile may be analysed to provide dimensions of these colloidal features.

I have used SAXS to probe the particle dimensions of gold nanorods during the growth process. I prepared the growth solution for the gold nanorods according to GS method A with 0.65 mM or 0.675 mM H_2A and 70 µM $AgNO_3$. Nanorod growth was initiated with 10 µL of freshly prepared seed with a 0.1 mM $HAuCl_4$ concentration.

I also prepared solutions containing 0.1 M $C_{16}TABr$, 0.1 M $C_{16}TABr - 0.5$ mM $HAuCl_4$, 0.1 M $C_{16}TABr - 0.5$ mM $HAuCl_4 - 0.65$ mM H_2A and 0.1 M $C_{16}TABr - 0.5$ mM $HAuCl_4 - 0.65$ mM $H_2A - 70$ µM $AgNO_3$ with the intention of investigating the effect of the different growth solution components on the structure of the CTAB micelles. However, on observation of the scattering curves there did not appear to be any difference in the scattering profiles produced and so I did not complete any further analysis. SAXS data was also recorded for the kinetics of an ageing gold nanoparticle seed sample. Unfortunately a suitable background was not measured for all samples. In the majority of cases this resulted in negative intensity values. No suitable background was obtained for the short camera length data and therefore I have not used any of this data in my analysis.

In this section I only present the analysis of one of the gold nanorod kinetics measurements (0.65 mM H_2A) as the background for all other samples produced questionable or no results. Figure 5-6 shows SAXS data recorded at various times during the growth process of a gold nanorod solution. This data corresponds to the same growth solution and synthesis conditions as the 0.65 mM H_2A used in Section 5.1.1. GS in Figure 5-6a refers to 'growth solution'. This measurement was performed on a complete growth solution prior to seeding and I used this profile as the background for the growth profiles. I used a fresh growth solution for the measurement of the nanorod growth process.

The peak at $q \approx 0.05$ Å^{-1} is the correlation peak for a concentrated solution of $C_{16}TABr$ micelles where the position indicates the average separation distance of the micelles.[351] This distance is calculated by:

$$d = \frac{2\pi}{10q} \qquad 5.5$$

The factor of 10 accounts for the conversion of angstroms to nanometres. Using Equation 5.5 the average separation of $C_{16}TABr$ micelles in the nanorod growth solution is ~ 12.6 nm. It is clear that the effect of this peak is much more significant in the earlier data when there are few or no nanoparticles present.

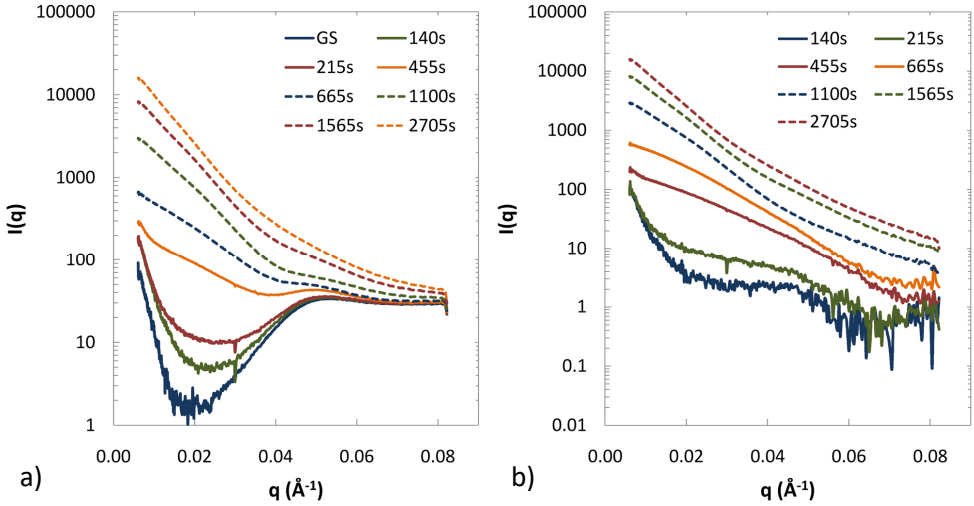

Figure 5-6 a) Raw SAXS data of a typical gold nanorod growth solution (GS) and during nanorod growth at various times. b) SAXS profiles of the kinetics data using the GS profile as a background signal.

One of the simplest and more fundamental values obtained from SAXS is the radius of gyration, R_g. The radius of gyration is defined as the 'mean square distance from the centre of gravity'. The radius of gyration can be determined using the Guinier approximation/law: [345]

$$I_1(q) = I(0)e^{-\frac{q^2R_g^2}{3}} \qquad 5.6$$

By taking the logarithm of both sides this becomes:

$$\ln I_1(q) = -\frac{q^2R_g^2}{3} + \ln I(0) \qquad 5.7$$

Therefore, a plot of $\ln I(q)$ vs q^2 will yield a straight line with a slope of $-\frac{R_g^2}{3}$. This is known as a Guinier plot and is valid in the limit $2\theta \to 0$, therefore it is applied to the 'innermost' range of the scattering curve i.e. lowest values of q. Figure 5-7 shows the Guinier plots for the various traces measured during the growth of gold nanorods.

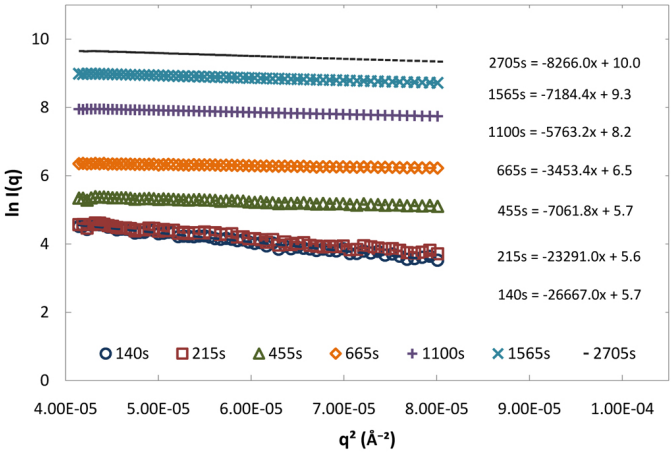

Figure 5-7 Guinier plots for SAXS data of a growing gold nanorod solution where the profile for the growth solution has been used as a background.

Table 5-1 shows the R_g values calculated from the background subtracted SAXS kinetic data for a growing gold nanorod solution using Equation 5.7.

Table 5-1 Radius of gyration values extracted from SAXS kinetics data for growing gold nanorods (column 2 obtained by fitting only low *q* data, column 3 obtained by fitting over a higher range of *q*).

Time (s)	Rg (nm)	Rg* (nm)
140	28.00	2.03
215	22.70	3.60
455	14.50	5.76
665	14.00	8.00
1100	12.50	12.50
1565	14.20	14.20
2705	15.40	15.40

The values calculated for the times 140s, 215s and 455s are unlikely to be true values. For instance if an R_g is calculated (using Equation 5.8 below) for a hemi-spherically capped cylinder with a radius of 2.0 nm (the approximate radius for an elongated $C_{16}TABr$ micelle at this concentration)[352] then the length needs to be ~ 95 nm to achieve an R_g value of 28 nm. The high value for R_g in Table 5-1 is most likely due to a poor background subtraction for the low q region. The effect of which is most significant for the earlier data. If the Guinier fit is applied to a higher q range then this gives values that are closer to what is expected but not necessarily reliable. These values are displayed in the R_g^* column in Table 5-1.

The R_g of a spherically capped cylinder (where the centre of the end-cap sphere may be positioned inside, outside or equal with the end of the cylinder) can be calculated using the equation derived by Kaya *et al*.:[347]

$$R_g^2 = \left[\frac{12}{5}R^5 + R^4\left(6h + \frac{3}{2}L\right) + R^3(4h^2 + L^2 + 4Lh) + R^2\left(3Lh^2 + \frac{3}{2}L^2h\right) + \frac{2}{5}h^5 - \frac{1}{2}Lh^4 - \frac{1}{2}L^2h^3 + \frac{1}{4}L^3r^2 + \frac{3}{2}Lr^4\right](4R^3 + 6R^2h - 2h^3 + 3r^2L)^{-1} \quad 5.8$$

Where R is the radius of the end-cap, h is the location of the centre of the spherical end –cap (this value can be positive or negative) and L is the length of the cylinder.

If Equation 5.8 is used to calculate the R_g for the nanorod parameters estimated from the optical data at 45 minutes ($\sim$2705 s) (Figure 5-4) a value of $\sim$13.1 nm is obtained. This is a good match with the R_g estimated from the SAXS data.

The average particle volume of a sample may be determined from the SAXS curve by using the equation:

$$V = \frac{2\pi^2 \cdot I_1(0)}{\int_0^\infty q^2\, dq \cdot I_1(q)} \quad 5.9$$

The intensity at zero angle, $I(0)$, is equal to the square of the total number of electrons in the irradiated volume.[345] This quantity cannot be directly measured and is determined by extrapolation of the $I(q)$ vs q curve.[345] The integral in the denominator of Equation 5.9 is known as the invariant and indicates that the entire scattering curve is used in the evaluation. In order to use this method it must be determined that the scattering intensity, $I(q)$, shows a dependence to q^{-4} at the higher values of q.[345, 353] This is known as Porod's law and is confirmed by observation of the Porod plateau within a plot of $I(q)q^4$ vs q. Figure 5-8 shows the Porod analysis for my SAXS data with the Porod plateau highlighted by the green shaded area.

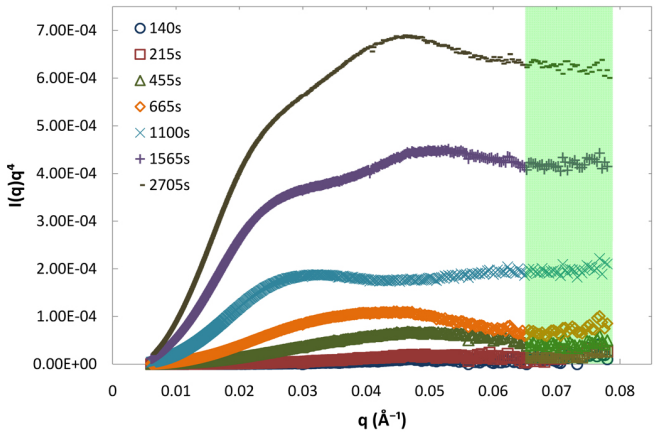

Figure 5-8 Analysis of SAXS data using $I(q)q^4$ vs q plot indicating Porod plateau (green shaded region).

The evaluation of the scattering curve using this method provides a weighted average volume and assuming the particles are homogeneous and the number of particles is fixed, the mean volume.[124, 345] With respect to using this method for the kinetic analysis of gold nanorods, this indicates that the particle volume will only be correct if all the seed particles grow concurrently.

Table 5-2 shows the mean particle volume from my SAXS data which I obtained using the application PRIMUS[292] (from the ATSAS[293] software suite).

Table 5-2 Particle volumes extracted from SAXS data

Time (s)	Volume (nm^3)
140	-
215	-
455	-
665	-
1100	4755
1565	6169
2705	8159

I was not able to determine the volume for the early data as this required removing too many data points to match the radius of gyration i.e. the Guinier law could not be guaranteed. The PRIMUS software automatically refuses a result if too many data points are excluded.

The distance distribution function, $P(r)$, can be used to determine the largest particle dimension assuming a homogeneous dispersion of particles:[345]

$$P(r) = \frac{1}{2\pi^2}\int_0^\infty I(q)\cdot qr\cdot \sin qr\cdot dq \qquad 5.10$$

Analysis of my data using the application GNOM[354] (from the ATSAS[293] software suite) gave unsatisfactory results (as indicated by quality factors within the software) and so further analysis was not completed.

The subscript of the intensity in the above equations for calculating the radius of gyration and volume denotes the assumption that no interparticle effects contribute to the scattering profile. This assumption should be valid for the analysis where the nanorods dominate the scattering as they are present in an approximately nanomolar concentration. However, an interparticle contribution could be the reason for the unusual values calculated for R_g at the earlier times.

5.1.4 Cryo-TEM and SEM

Cryo-TEM is the combination of advanced sample preparation with a familiar imaging tool. By a process called 'rapid vitrification' the solvated species is suspended in an

amorphous film of the solvent. The sample is applied to a regular holey-carbon TEM grid upon which the excess solution is blotted away. The grid is then plunged into a bath of liquid coolant which is usually ethane or propane as both have better thermal conductivity than liquid nitrogen.[295] The purpose of the rapid freezing process is to prevent solidification and thus crystallisation of the solvent which interferes with the imaging process. The primary advantage of cryo-sample preparation is that the structure of solvated species is maintained.[355] This is most significant for the imaging of soft matter structures such as micelles,[356, 357] liposomes[358] and cells.[359] Also, due to the low temperatures used for the process any reactions will be essentially stopped. The growth of Au/Ag nanowires has also been observed with cryo-TEM.[360] This technique is therefore ideal for monitoring the shape transition of the wet chemical synthesis for gold nanorods, as by taking aliquots at various times a snapshot of the reaction at that time step will be obtained.

For the cryo-TEM experiments I prepared two nanorod growth solutions according to procedure GS method B with 0.60 mM HA and 0.65 mM H_2A respectively. I initiated the nanorod growth by adding 10 μL of freshly prepared seed B. I chose cryo-TEM as it allowed me to image the nanorod sample without making any chemical changes.

It was my aim to use cryo-TEM images to confirm the growth trajectory inferred from my UV-Vis-NIR data and Mathematica analysis. (See earlier. In summary, this was that the length of the nanorod appeared to increase relatively rapidly in the initial stages with a concurrent slight increase in aspect ratio. This was then followed by the gradual ageing process where the aspect ratio decreased at first due to the nanorod fattening but in the later stages by some actual shortening.) I was also expecting to see the stage of the reaction where the initiation of the nanorod geometry occurred. However, this did not eventuate.

Figure 5-9 shows the images obtained from the cryo-TEM experiments for a) 2.5 minutes, b) 15 minutes, c) 25 minutes and d) 24 hours. The sample at 24 hours was treated by centrifugation/redispersion prior to cryo-preparation. The surprising finding was that although the end profile of the rods found varied from flat-ended, through conical to hemispherical, as time progressed, the size did not change a lot. Even at 2.5 minutes into the growth sequence there were already rods of nearly full size. The images in Figure 5-9 correspond to the 0.65 mM H_2A sample. Images were also measured for the 0.60 mM H_2A sample which shows similar results. The earliest observed nanorods for this sample were at 13.5 minutes, Figure 5-10. Importantly though, the nanorods observed at this time show particle dimensions that are a significant percentage of the final volume of nanorods synthesised in these conditions.

It should be noted that at typical synthesis concentrations and the observed particle dimensions the nanorod concentration is on the order of nanomolar. This leads to the issue of locating nanoparticles in the TEM and thus obtaining a representative sample. However, the present work was sufficiently exhaustive that it can be safely concluded

that rods of a size intermediate between those shown and the starting seed must be exceedingly rare.

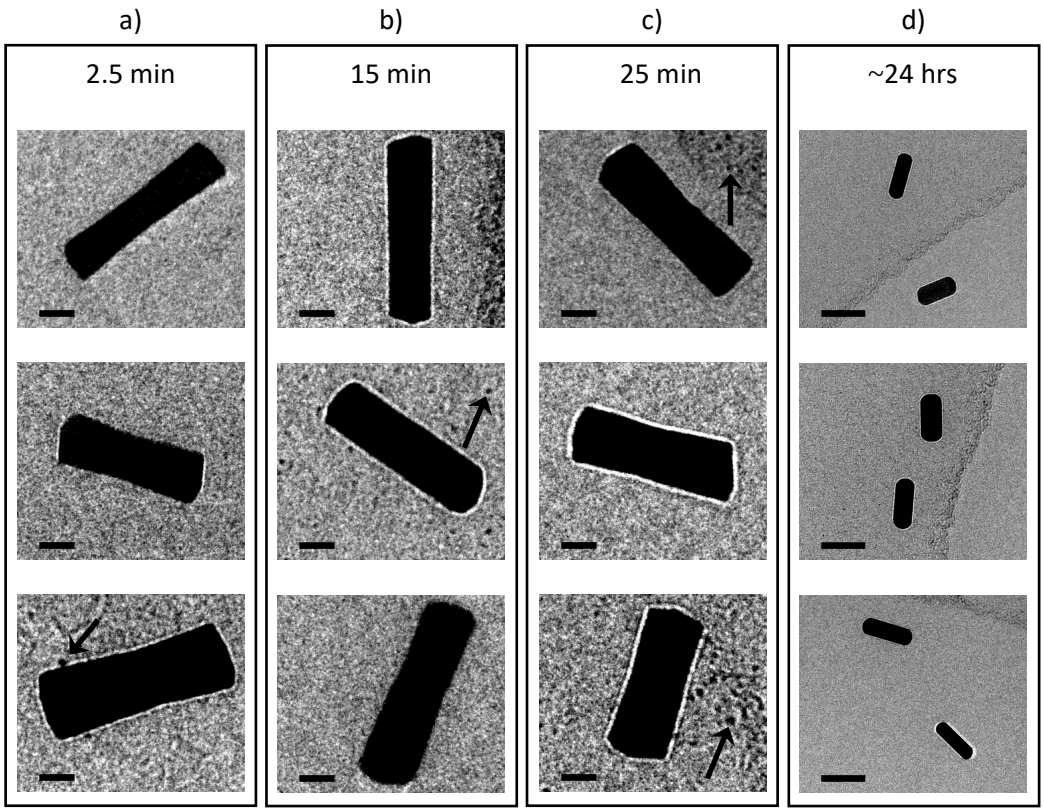

Figure 5-9 Cryo-TEM images of samples of a growing gold nanorod solution with 0.65 mM H_2A taken at a) 2.5 min, b) 15 min, c) 25 min and d) 24 hours. Scale bars for a) – c) are equal to 10 nm and d) is equal to 50 nm. Arrows indicate fine gold particles with dimensions expected of seed particles.

The nanorods in Figure 5-9 and Figure 5-10 do not show any appreciable difference in particle dimensions at different times in the reaction sequence. In addition to their size they also display very different fine structure to the spherically-capped cylinder that was expected. The nanorods appear to have a 'bow-tie' like structure where the diameter in the middle of the particle is smaller than that at the ends. This could be where the seed particle is located and the initiation of the nanorod geometry is directed along the longitudinal axis with $180°$ symmetry. The end-caps of these particles are also somewhat different with a mix of virtually flat and conical geometries. For the aged nanoparticles, Figure 5-9d, this flared structure has disappeared and the familiar spherically-capped geometry is attained. The straightening of the flanks of the nanorods is also shown in the images of the 0.60 mM $\mathrm{H_2A}$ sample taken at 38 minutes, Figure 5-10d. I will discuss the intermediate structures further with respect to their simulated optical properties and my new growth model in Section 5.1.5.

The arrow(s) in Figure 5-9 and Figure 5-10 indicate the presence of very small gold nanoparticles that have dimensions that I expect for the seed particles, ~ 2 nm. This is another strong indication of the possibility that seed particles do not grow concurrently.

It should be noted that similar particles were observed in the cryo-TEM images of the growth solution without seed, Figure 4-5. Regardless of this fact, if the fine gold particles are present they should behave as seeds at some point in the reaction. Fewer seed-like particles are indicated for the 0.60 mM H_2A sample as they were not as conveniently positioned near the nanorods. An example of a similar presence of seed-like particles for this sample is presented as Appendix E.

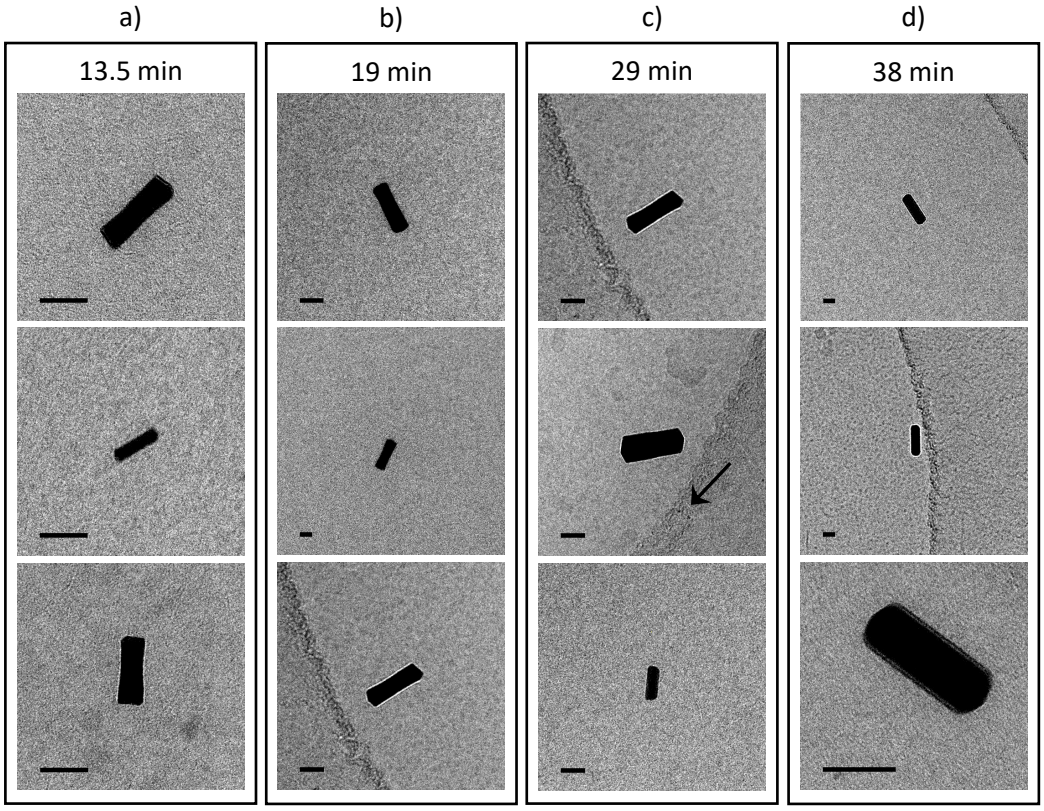

Figure 5-10 Cryo-TEM images of samples of a growing gold nanorod solution with 0.60 mM H_2A taken at a) 13.5 min, b) 19 min, c) 29 min and d) 38 min. Scale bars for a) – d) are equal to 20 nm. The arrow indicates fine gold particles with dimensions expected of seed particles.

These observed particle dimensions and the measured optical data are at variance with those produced by a model in which all the seeds grow concurrently. This is supported by the volume percent of gold (measured from the UV-Vis-NIR spectrum) where for the 0.65 mM H_2A sample and the $2.5 - 3$ minute mark (Figure 5-11) only about 1% of the gold has been reduced. However, the nanoparticles observed at this time in cryo-TEM images (Figure 5-9) have a volume that is already approximately $50 - 60\ \%$ that of the final nanorod. Similarly, for the 0.60 mM H_2A sample at 13.5 minutes the volume percent of Au_0 is still only 5% of the final value but the nanorods found already have similar particle volumes as for the 0.65 mM H_2A sample.

This notion has been previously suggested by Miranda *et al.*; "nucleation and growth are sequential within a micelle but parallel between micelles".[20] This statement was made in reference to the photochemical synthesis (with $AgNO_3$ and H_2A).

Zweifel and Wei reported particle dimensions that, at 15 minutes, were $\sim 30\%$ of the final particle volume.[103] If compared to my optical data for 0.60 mM H_2A then the volume of metallic gold at this point in the reaction is $\sim 6\%$ of the final amount expected. The actual gold percentage with respect to their sample is actually expected to be less as the concentration of H_2A used in their experiment was in a ratio of $1:1.1$ (~ 0.49 mM : ~ 0.54 mM, $AuBr_2^-$: H_2A).

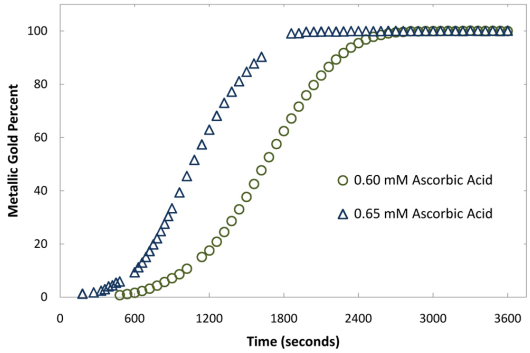

Figure 5-11 Percentage of metallic gold (with respect to the final concentration) during the growth of gold nanorods with 0.60 mM and 0.65 mM H_2A, respectively.

The initiation of the nanorod structure followed by expansion to such dimensions as in Figure 5-9 and Figure 5-10 must be an extremely rapid, burst-like growth event. A qualitative explanation of this event may be gained by considering the following form of Fick's first law:[349]

$$\mathrm{J} = -\mathrm{D}\frac{\mathrm{dc}}{\mathrm{d}x} \qquad 5.11$$

Where, J is the reactant flux, D is the diffusion coefficient and $\frac{\mathrm{dc}}{\mathrm{d}x}$ is the concentration gradient of the reactant. This states that the flux of a reactant species is proportional to the concentration gradient. The adsorption of a $AuBr_2^-$ molecule (or a few) on the surface of a seed particle could establish a concentration gradient. This could initiate a cascade effect where the $AuBr_2^-$ molecules in the surrounding solution are drawn in the direction of the sudden drop in solvated $AuBr_2^-$. This does not explain why the reaction halts. However, this may be a function of a localised equilibrium achieved by the build-up of $AuBr_4^-$, which is only removed by H_2A. Following on from this idea, the formation of dogbones could be a subsequent product of this buildup at the tips as the excess of ascorbic acid results in growth at these points.

From this surprising development I decided to try a simple experiment to confirm the presence of large volume nanoparticles in the early stages of the gold nanorod reaction. I prepared a growth solution with 0.60 mM H_2A according to GS method B and initiated the growth with 10 µL of freshly prepared gold nanoparticle seed B. I chose this concentration of H_2A to reduce the rate of the reaction. This was necessary to increase the efficacy of the following centrifugation steps (see Section 2.3.4 for details).

Figure 5-12 shows SEM images representative of the samples taken at $5-7$ minutes, $10-12$ minutes and $30-32$ minutes into the reaction. It should be noted that due to the centrifugation time it is possible that the reaction continued for some of this time. I have labelled the images with respect to this time range. It is also apparent that there are a significant population of spherical particles present (more than usual for these reaction conditions) and therefore the sample treatment process could also have affected the synthesis. The absorbance spectrum for the centrifuged sample at 60 minutes is shown as Appendix F which shows a relatively large intensity for the transverse resonance peak. Another indicator of this is that the nanoparticles do not show the same geometries observed in the cryo-TEM images, e.g. with flat ends and/or 'bow-tie' structure. Importantly, there are nanorods in the $5-7$ minute sample that have dimensions of ~ 40 nm long and ~ 10 nm wide. Again this is much bigger than can be described using the concurrent growth model. Also, there are very fine gold nanoparticles that have the approximate dimensions that are expected of the seed particles, indicated by the white arrow in Figure 5-12a.

The gold nanorods observed at 10 and 30 minutes appear to be quite well defined, with the 30 minutes sample showing a slight increase in the average volume of the nanorods.

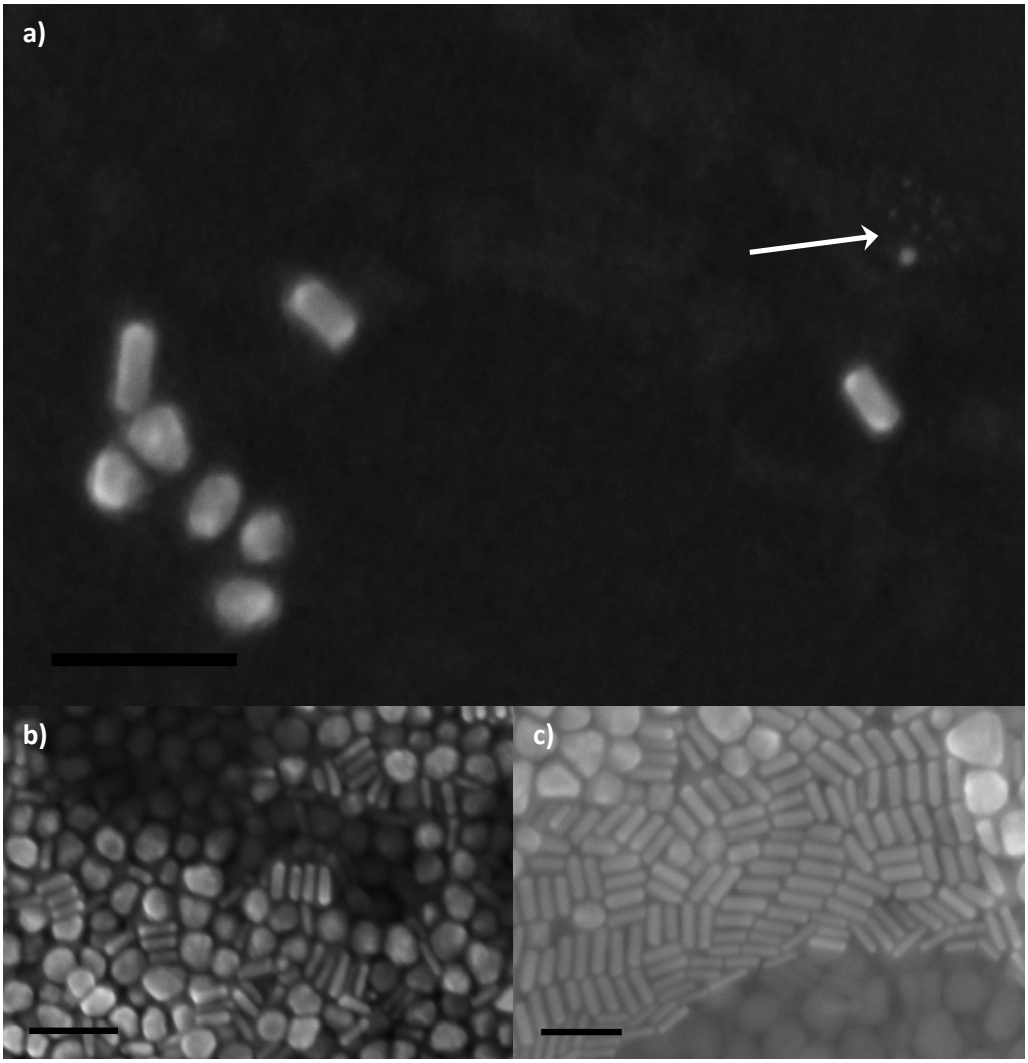

Figure 5-12 SEM images of samples of growing gold nanorods taken at a) 5-7 min, b) 10-12 min and c) 30-32 min. Scale bars = 100 nm. The arrow in a) indicates fine gold particles with dimensions expected of seed particles.

From these results I have concluded that the gradual growth model for gold nanorods, where all seed particles grow concurrently, is not accurate.

5.1.5 Simulated Optical Properties for New Growth Model

Previous models for the growth of nanorods have assumed that the final geometry is a hemi-spherically-capped right cylinder. However, as I have shown, this is not strictly correct. Furthermore, the actual shape of the nanorods in an ensemble is expected to exert a significant effect on its optical extinction[333] and therefore any conclusions drawn from the optical spectrum can suffer significantly. As I have shown in my cryo-TEM and SEM results it is now necessary to include sporadic, rapid growth events in the description of the gold nanorod reaction.

An immediate clue to the presence of intermediate particle geometries can be seen from the kinetics data towards the end of the primary reaction i.e. sans ageing, where a refinement of the transverse resonance peak is evident (Figure 5-13).

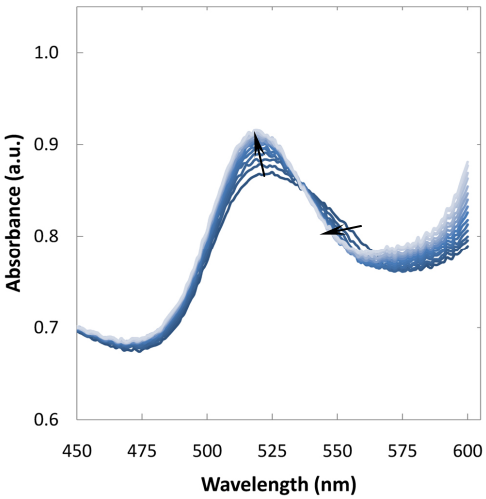

Figure 5-13 Refinement of the transverse resonance peak in the later stages of a growing gold nanorod solution. The arrows indicate increasing time.

This point indicates that the average geometry of the distribution is changing and as it corresponds with a blue shift in the longitudinal peak this geometry change is happening along the flanks of the nanorods. It is also likely that this indicates the smoothing of the flanks where the flared geometry e.g. Figure 5-14b, is beginning to approach the final, familiar spherically-capped-cylinder (Figure 5-14d). A nanoparticle with a flared structure (e.g. dog-bones) will display an additional resonance peak adjacent to the typical transverse peak,[333] Section 4.1.4.

I have incorporated the effect of intermediate nanorod shape into the model for growth. Intermediate nanoparticle geometries can be approximated from the silhouettes in Figure 5-9 and Figure 5-10 by assuming rotational symmetry about the longitudinal axis. Figure 5-14 illustrates the resulting computer models for prototypical examples of these intermediate geometries and the designations that I have assigned to them. The end product in the growth sequence is the familiar spherically-capped cylinder (SC).

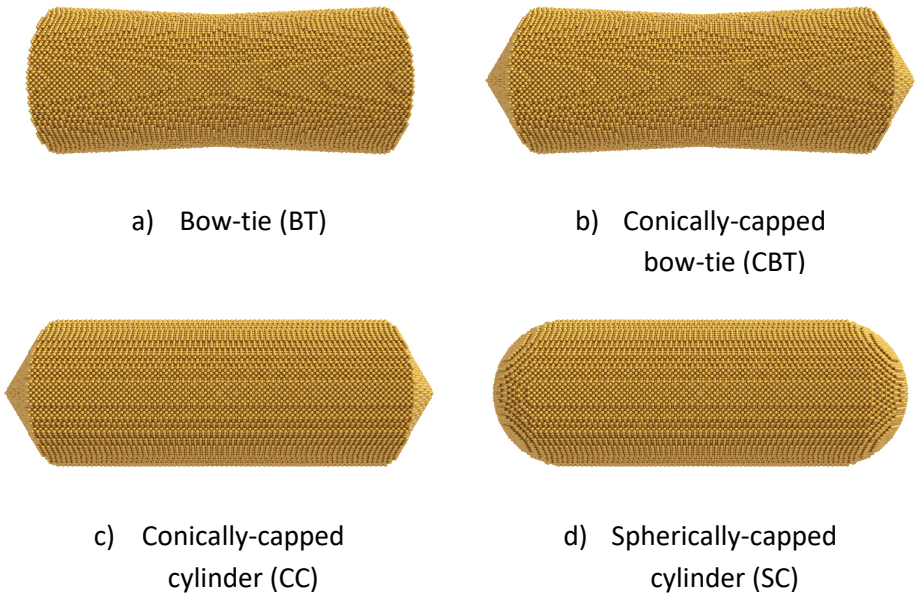

Figure 5-14 Nanoparticle geometries used for DDA simulations. a) – c) Intermediate nanoparticle geometries modelled from observations in cryo-TEM images. d) Final nanorod geometry.

Using these prototypical shapes (and size ranges observed in the cryo-TEM experiments) I then calculated their corresponding extinction spectra using DDSCAT, Figure 5-15. The shapes intermediate between the prototypes were generated by assuming a linear progression of the particle dimensions. The dimensions I have used for the calculations can be found in Section 2.4.1.1. An increase in volume has a known small red-shifting effect on the main extinction peak but it is clear that the shape assumed for the rod has an effect too. [333]

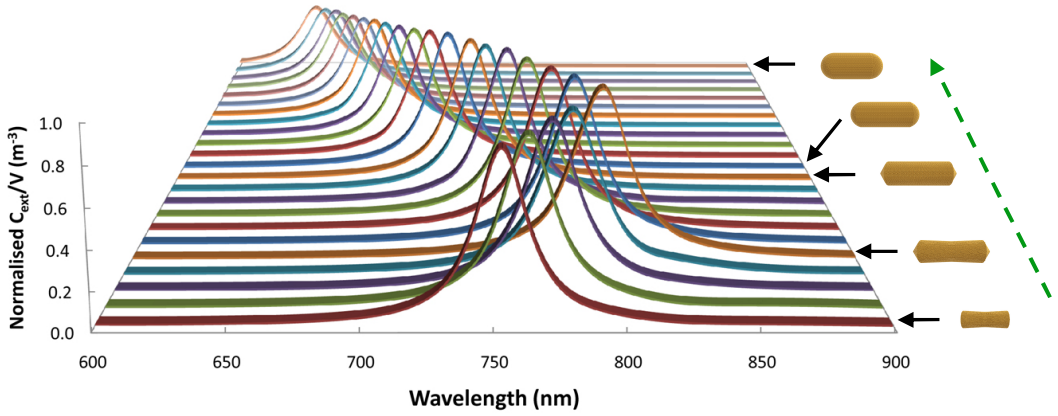

Figure 5-15 Volume-normalised, DDA simulated extinction spectra of intermediate nanoparticle geometries modelled on TEM observations. Green dashed arrow indicates growth direction. Black solid arrows link diagrams of nanoparticles with their corresponding extinction spectrum.

I have assumed that the BT particle geometry is the most primitive (resolvable in the absorbance spectrum) in the growth sequence and the progression thereafter in morphology is as indicated by the dashed arrow in Figure 5-15. For this assumed particle formation pathway it would be expected that the longitudinal peak should red shift at first, corresponding mainly to an increase in aspect ratio, and then blue shift when the waist of the particle begins to develop and/or the rod decreases in length and the end-caps change geometry (conical to semi-spherical). This sequence of peak movements is observed in the experimentally measured data.

If the following rules, drawn from observations of the experimental data, are applied to the simulated data in Figure 5-15, it is possible to achieve a representation of the experimental peak shift, Figure 5-16.

1. Each time is composed of a distribution of the calculated particles.
2. Subsequent times are constructed with respect to the previous.
    - Positive progression from $\mathrm{BT} \rightarrow \mathrm{SC}$ only i.e. once a particle is created it is considered for the following spectra
3. New particles are introduced up until gold percent $\sim 30\%$.
    - BT particle volume $= 30\%$ of the final particle (SC) volume.
4. Primary CBT intermediate is present in adequate proportion until 20 minutes.
    - The longitudinal peak edge remains red-shifted until this point despite blue shift in peak centre.
5. CC and SC represent the majority of the spectrum after 30 minutes.
    - Volume at $99 - 100\%$
6. Each simulated spectrum is normalised to the volume of gold for the corresponding spectrum from the measured experimental data

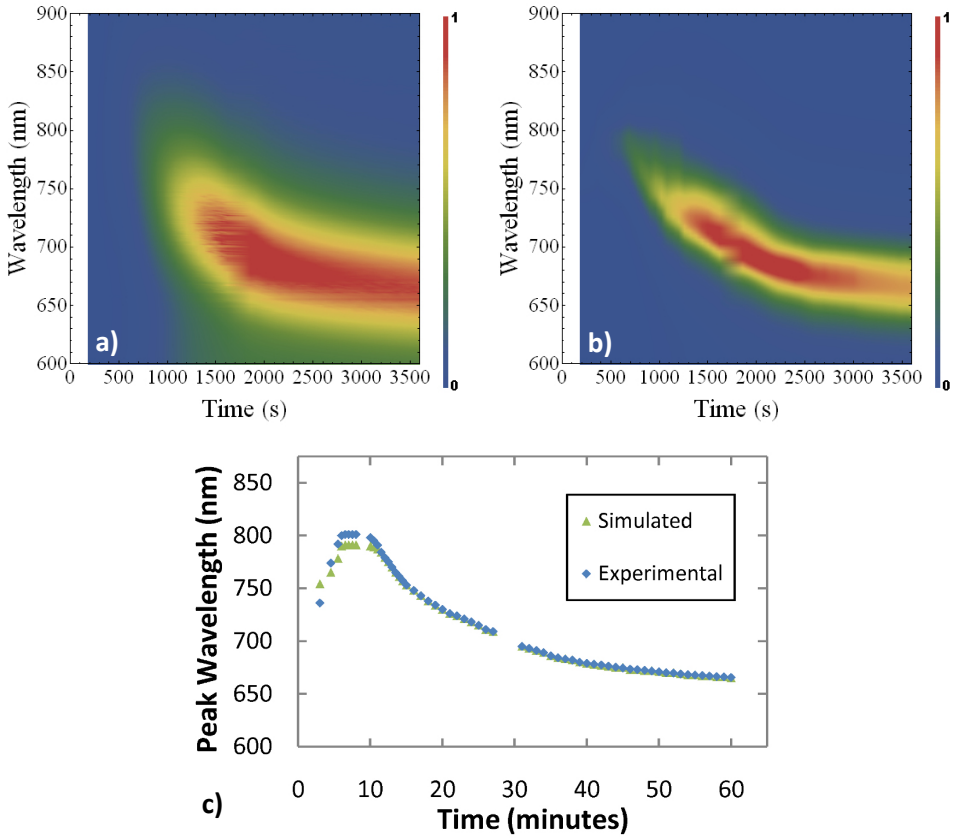

Figure 5-16 a) Experimentally measured absorbance spectrum of a growing gold nanorod solution with 0.65 mM H_2A in the growth solution. b) Distributions of simulated nanoparticle spectra combined according to several rules to mimic experimental spectra in a). c) Comparison of the peak positions for the experimental and simulated data in a) and b) respectively.

The experimental data has a broader peak shape than the simulated data. This is due to the fact that the experimental data represents a broader distribution of particle sizes where the simulated data represents the average for each distribution of particle sizes. In consideration of rule 4 above, the experimental peak width and shape fit well with the idea that the nanorods are at different stages of development, with respect to each other, during the reaction.

I have already established that the gold nanorod reaction is highly dependent on the concentration of H_2A in the growth solution, Section 4.1.4. If the data in Figure 4-9 and Figure 4-10 are again considered, it can be seen that the longitudinal peak also initially red-shifts with the increase of the $H_2A:Au^+$ ratio before blue shifting gradually. The shape of the peak during the blue shift can also show a fairly significant asymmetry. In the context of the current discussion it is possible that the progression of the distribution of nanoparticle geometries during the course of a nanorod reaction is fixed (with respect to all other reactants except H_2A). Therefore the endpoint that is achieved is controlled by the concentration of H_2A in the growth solution. This does not mean that there will always be BT or CBT particles if the sample is imaged, as the sample

treatment required for imaging results in geometry changes, as I have shown (Figure 5-12).

By using Equation 5.8 I have estimated the radius of gyration of the intermediate geometries that I have presented for the new growth model, Table 5-3.

Table 5-3 Estimated R_g values for intermediate nanoparticle geometries of the gold nanorod reaction

Shape	R_g (nm)
BT	9.64
CBT	15.45
CC	15.46
SC	12.36

The values in Table 5-3 do not follow the same trend as those determined by SAXS measurements i.e. gradually increasing (Table 5-1). However, this is expected as the result produced by SAXS measurements is a weighted average of the particles in a solution. In context of sporadic nanoparticle growth events, this means at early times the $\mathrm{R_g}$ will be greatly underestimated as the majority of particles are seeds. As the reaction continues the number of larger particles gradually increases which influences the $\mathrm{R_g}$ proportionately. The value for $\mathrm{R_g}$ measured at 45 minutes appears to indicate that the particle geometry represents the CC or something between the CC and SC particle geometries. This also correlates with the rules I have applied to the simulated spectra.

5.1.6 Summary

In this chapter I have provided a detailed analysis of the kinetics of gold nanorod formation. I have presented results from experiments performed using UV-Vis-NIR spectroscopy, cryo-TEM, SEM, SAXS and DDA simulations. I have also provided a novel analysis of a UV-Vis-NIR spectrum that produces realistic nanorod dimensions without the need for any imaging techniques.

I have combined the experimental results from the multiple techniques utilised to introduce a new model for the growth mechanism of gold nanorods synthesised by the well known wet chemistry procedure. This growth mechanism contradicts the broadly assumed notion that all seed particles grow as nanorods concurrently in the growth solution.

My growth model introduces the concept that the initiation of the nanorod geometry is extremely rapid and does not occur simultaneously for all seed particles. It follows that the nanorods in the solution can be at different stages of their development during the reaction. As the concentration of $\mathrm{H_2A}$ is depleted the growth of the nanorods approaches the endpoint of the reaction. If the concentration of $\mathrm{H_2A}$ is low enough the

endpoint can be within the stage of the reaction where there is a broad distribution of nanoparticles and this can manifest as an asymmetry in the longitudinal resonance peak.

I have also validated this new growth model by comparing the simulated optical properties of intermediate nanoparticle geometries observed in my TEM experiments with the measured UV-Vis-NIR spectra.

6 Conclusions

Plasmonically-active, precious metal nanoparticles have physical and chemical properties that make them uniquely suited for exploitation in diverse forms of nanotechnology. Gold is the most popular metal for the synthesis and application of plasmonically active nanoparticles. Applications of gold nanoparticles have been greatly strengthened by the advancement in synthetic procedures for control of their geometry. In particular, nanorods and nanoshells provide a simple yet effective means to exploit the features of nanoscale gold. The variations in physical dimensions and morphologies provide seemingly limitless options for exploitation of these effects. In general, it appears that synthesis of nanorods provides the simplest route to a reliable, monodisperse product.

Unfortunately, there is a very inefficient use of gold in the current synthetic procedures for producing gold nanorods. In this thesis I have addressed this problem, and found conditions for improving the amount of gold used in the nanorod synthesis. The revised methods of synthesis offer a means to increase the yield of useful product in the reaction. The dispersion of product sizes is not deleteriously effected and it remains possible to produce a range of desirable aspect ratios.

I have also produced evidence for the mechanism by which metallic gold is formed in the gold nanorod reaction. By introducing a co-reductant and changing the order of addition of reactants, I have shown that the formation of a significant quantity of nanorods requires an efficient 'weak' reductant.

I have provided a novel analysis of UV-Vis-NIR spectral data that produces realistic nanorod dimensions without the need for any imaging techniques.

Unfortunately, the mechanism by which a spherical seed particle converts to the nanorod geometry could not be determined. However, a significant advance in the understanding of the growth process was made using a new growth model in which the initiation of the nanorod geometry is extremely rapid and does not occur simultaneously for all seed particles. It follows that the nanorods in the solution can be at different stages of their development during the reaction. I have also validated this new growth model by comparing the simulated optical properties of intermediate nanoparticle geometries observed in my TEM experiments with the measured UV-Vis-NIR spectra. It is not clear why the longitudinal axis of the nanorod stops growing. If the disproportionation mechanism is considered with respect to the surface of the developing nanorod, then it is possible that the accumulation of AuBr_4^- at the ends of the rods establishes equilibrium where further growth is much slower. This could also provide an explanation for the effect observed at higher $\mathrm{H}_2\mathrm{A}$ concentrations where dog-bone particles form indicating a higher ionic gold presence or attraction at the ends.

Finally, some other types of nanoparticle with potential technological applications were also considered in this thesis. The synthesis of colloidal gold nanorings was explored and their useful optical properties demonstrated. The optical properties of gold nanorings can be considered a hybrid of gold nanorods and nanoshells. Due to their tuneable nature they could also be used in the same applications as nanorods and nanoshells. Some improvements in the synthesis of silver nanorods were found, but they do not show good stability anyway, which would be a concern for most applications. A synthesis method for platinum nanoparticles with a short-chain stabiliser was developed. This type of nanoparticle could conceivably be used in sinter inks for printable electronics.

Future Work

The question of the origin of the nanorod anisotropy still stands. Using the methods presented herein, it may be possible to capture this process if the concentrations of the growth solution are increased while maintaining the respective ratios. However, the efficacy of this is not guaranteed as, for instance, the ratio of Au^{3+}: $\mathrm{C}_{16}\mathrm{TABr}$ must be kept at $\sim 1:50$ to ensure that upon mixing the ensuing complex is solubilised.

Further evidence for the rapid particle formation event could be investigated using dark-field spectroscopy with increased time resolution. However, it will be difficult to separate diffusion based adsorption events to sudden growth events. A micro-fluidic cell with a seeded but static growth solution may be sufficient.

A further clue to the initial growth event may be present at the surface of the nascent seed particles. Time resolved SERS could be utilised to probe surface species during the nanorod reaction.

With some refinement, the wet chemical synthesis I have presented here could provide a route to producing large quantities of gold nanorings with well-controlled dimensions.

Characterisation of the sintering properties of platinum nanoparticles for use as sinterable inks is an attractive option particularly for microelectronic applications as fine structures can be deposited using, for example, inkjet printing. This provides a bottom up approach without significant waste, a major concern for such an expensive material.

References

1. Binnig, G.; Rohrer, Scanning tunneling microscopy - from birth to adolescence. In *Nobel Lectures in Physics*, 1981-1990 ed.; Ekspong, G., Ed. World Scientific Publishing Co.: 1986; pp 389 - 409.
2. http://nobelprize.org
3. Gates, B. D.; Xu, Q.; Stewart, M.; Ryan, D.; Willson, C. G.; Whitesides, G. M., New approached to nanofabrication: molding, printing, and other techniques. *Chem. Rev.* **2005,** 105, (4), 1171-1196.
4. Everett, D. H., Manual of symbols and terminology for physicochemical quantities and units, appendix II: Definitions, terminology and symbols in colloid and surface chemistry. *Pure Appl. Chem.* **1972,** 31, (4), 577-638.
5. Freestone, I.; Meeks, N.; Sax, M.; Higgitt, C., The Lycurgus Cup - A Roman nanotechnology. *Gold Bulletin* **2007,** 40, (4), 270-277.
6. Faraday, M., The Bakerian lecture: experimental relations of gold (and other metals) to light. *Philosophical Transactions of the Royal Society of London* **1857,** 147, 145-181.
7. Zsigmondy, R. A., Properties of colloids. In *Nobel lectures in chemistry*, 1922-1941 ed.; World Scientific Publishing Co.: 1925; Vol. 2, pp 45-57.
8. Hunt, L. B., The true story of purple of Cassius. *Gold Bulletin* **1976,** 9, (4), 134-139.
9. Wiesner, J.; Wokaun, A., Anisometric gold colloids - preparation, characterization, and optical-properties. *Chemical Physics Letters* **1989,** 157, (6), 569-575.
10. Zsigmondy, R. A., Amicroscopic gold germs. I. *Z. Physik. Chem.* **1906,** 56, (1), 65 - 76.
11. Jana, N. R.; Gearheart, L.; Murphy, C. J., Evidence for seed-mediated nucleation in the chemical reduction of gold salts to gold nanoparticles. *Chem. Mater.* **2001,** 13, (7), 2313-2322.
12. Jana, N. R.; Gearheart, L.; Murphy, C. J., Seeding growth for size control of 5-40 nm diameter gold nanoparticles. *Langmuir* **2001,** 17, (22), 6782-6786.
13. Jana, N. R.; Gearheart, L.; Murphy, C. J., Seed-mediated growth approach for shape controlled synthesis of spheroidal and rod-like gold nanoparticles using a surfactant template. *Adv. Mater.* **2001,** 13, (18), 1389 - 1393.
14. Turkevich, J.; Stevenson, P. C.; Hillier, J., A study of the nucleation and growth processes in the synthesis of colloidal gold. *Discuss. Faraday Soc.* **1951,** 11, 55-75.
15. Hauser, E. A.; Lynn, J. E., *Experiments in colloid chemistry*. McGraw-Hill: 1940.
16. Blaber, M. G.; Arnold, M. D.; Ford, M. J., A review of the optical properties of alloys and intermetallics for plasmonics. *J. Phys.: Condens. Matter* **2010,** 22, (14), 143201-1 - 15.
17. Harris, N.; Ford, M. J.; Mulvaney, P.; Cortie, M. B., Tunable infrared absorption by metal nanoparticles: The case for gold rods and shells. *Gold Bulletin* **2008,** 41, (1), 5-14.
18. Jain, P. K.; Lee, K. S.; El-Sayed, I. H.; El-Sayed, M. A., Calculated absorption and scattering properties of gold nanoparticles of different size, shape, and composition: applications in biological imaging and biomedicine. *J. Phys. Chem. B* **2006,** 110, (14), 7238 - 7248.
19. Jana, N. R., Gram-scale synthesis of soluble, near-monodisperse gold nanorods and other anisotropic nanoparticles. *Small* **2005,** 1, (8-9), 875-882.

20. Miranda, O. R.; Dollahon, N. R.; Ahmadi, T. S., Critical concentrations and role of ascorbic acid (vitamin C) in the crystallization of gold nanorods within hexadecyltrimethyl ammonium bromide (CTAB)/tetraoctyl ammonium bromide (TOAB) micelles. *Crystal Growth & Design* **2006,** 6, (12), 2747-2753.
21. Nikoobakht, B.; El-Sayed, M. A., Preparation and growth mechanism of gold nanorods using seed-mediated growth method. *Chem. Mater.* **2003,** 15, (10), 1957-1962.
22. Sau, T. K.; Murphy, C. J., Seeded high yield synthesis of short Au nanorods in aqueous solution. *Langmuir* **2004,** 20, (15), 6414-6420.
23. Kim, F.; Song, J. H.; Yang, P., Photochemical synthesis of gold nanorods. *J. Am. Chem. Soc* **2002,** 124, (48), 14316-14317.
24. Hubert, F.; Testard, F.; Spalla, O., Cetyltrimethylammonium bromide silver bromide complex as the capping agent of gold nanorods. *Langmuir* **2008,** 24, (17), 9219-9222.
25. Liu, M. Z.; Guyot-Sionnest, P., Mechanism of silver(I)-assisted growth of gold nanorods and bipyramids. *J. Phys. Chem. B* **2005,** 109, (47), 22192-22200.
26. Pérez-Juste, J.; Liz-Marzan, L. M.; Carnie, S.; Chan, D. Y. C.; Mulvaney, P., Electric-field-directed growth of gold nanorods in aqueous surfactant solutions. *Adv. Funct. Mater.* **2004,** 14, (6), 571-579.
27. Orendorff, C. J.; Murphy, C. J., Quantitation of metal content in the silver-assisted growth of gold nanorods. *J. Phys. Chem. B.* **2006,** 110, (9), 3990-3994.
28. Maier, S. A., *Plasmonics: Fundamentals and Applications*. Springer US: 2007; p 223.
29. Bohren, C. F.; Huffman, D. R., *Absorption and scattering of light by small particles*. John Wiley and Sons: 1983; p 530.
30. Etchegoin, P. G.; Le Ru, E. C.; Meyer, M., An analytic model for the optical properties of gold. *Journal of Chemical Physics* **2006,** 125, 164705-1 - 3.
31. Johnson, P. B.; Christy, R. W., Optical-constants of noble-metals
Phys. Rev. B **1972,** 6, (12), 4370-4379.
32. Weaver, J. H.; Frederikse, H. P. R., *Optical properties of selected elements*
CRC Press: Boca Raton, 2001.
33. Kreibig, U.; Vollmer, M., *Optical properties of metal clusters*. Springer: Berlin, 1995.
34. Arnold, M. D.; Blaber, M. G.; Ford, M. J.; Harris, N., Universal scaling of local plasmons in chains of metal spheres. *Optics Express* **2010,** 18, (7), 7528-7542.
35. Fuchs, R., Theory of optical-properties of ionic-crystal cubes
Physical Review B **1975,** 11, (4), 1732-1739.
36. Rodriguez-Fernandez, J.; Perez-Juste, J.; Mulvaney, P.; Liz-Marzan, L. M., Spatially-directed oxidation of gold nanoparticles by Au(III)-CTAB complexes. *J. Phys. Chem. B.* **2005,** 109, (30), 14257-14261.
37. Pérez-Juste, J.; Rodríguez-González, B.; Mulvaney, P.; Liz-Marzán, L. M., Optical control and patterning of gold-nanorod-poly(vinyl alcohol) nanocomposite films. *Adv. Funct. Mater.* **2005,** 15, 1065 - 1071.
38. van-der-Zande, B. M. I.; Pagès, L.; Hikmet, R. A. M.; van-Blaaderen, A., Optical properties of aligned rod-shaped gold particles dispersed in poly(vinyl alcohol) films. *J. Phys. Chem. B.* **1999,** 103, (28), 5761 - 5767.
39. Gluodenis, M.; Jr, C. A. F., The effect of mutual orientation on the spectra of metal nanoparticle rod-rod and rod-sphere pairs. *J. Phys. Chem. B* **2002,** 106, (37), 9484 - 9489.

40. Cortie, M. B.; Xu, X.; Ford, M. J., Effect of composition and packing configuration on the dichroic optical properties of coinage metal nanorods. *Phys. Chem. Chem. Phys.* **2006,** 8, (30), 3520 - 3527.
41. Funston, A. M.; Novo, C.; Davis, T. J.; Mulvaney, P., Plasmon coupling of gold nanorods at short distances and in different geometries. *Nano Letters* **2009,** 9, (4), 1651-1658.
42. Sandrock, M. L.; Foss, C. A., Synthesis and linear optical properties of nanoscopic gold particle pair structures. *J. Phys. Chem. B* **1999,** 103, (51), 11398 - 11406.
43. Slaughter, L. S.; Wu, Y. P.; Willingham, B. A.; Nordlander, P.; Link, S., Effects of symmetry breaking and conductive contact on the plasmon coupling in gold nanorod dimers. *ACS Nano* **2010,** 4, (8), 4657-4666.
44. Prodan, E.; Lee, A.; Nordlander, P., The effect of a dielectric core and embedding medium on the polarizability of metallic nanoshells. *Chemical Physics Letters* **2002,** 360, (3-4), 325-332.
45. Prodan, E.; Nordlander, P., Electronic structure and polarizability of metallic nanoshells. *Chemical Physics Letters* **2002,** 352, (3-4), 140-146.
46. Prodan, E.; Radloff, C.; Halas, N. J.; Nordlander, P., A hybridization model for the plasmon response of complex nanostructures. *Science* **2003,** 302, (5644), 419-422.
47. Blaber, M. G.; Arnold, M. D.; Ford, M. J., Search for the ideal plasmonic nanoshell: The effects of surface scattering and alternatives to gold and silver. *Journal of Physical Chemistry C* **2009,** 113, (8), 3041-3045.
48. Noguez, C.; Roman-Velazquez, C. E., Dispersive force between dissimilar materials: Geometrical effects. *Physical Review B* **2004,** 70.
49. Prodan, E.; Nordlander, P., Structural tunability of the plasmon resonances in metallic nanoshells. *Nano Letters* **2003,** 3, (4), 543-547.
50. Oldenburg, S. J.; Averitt, R. D.; Westcott, S. L.; Halas, N. J., Nanoengineering of optical resonances. *Chem. Phys. Lett.* **1998,** 288, 243 - 247.
51. Raschke, G.; Brogl, S.; Susha, A. S.; Rogach, A. L.; Klar, T. A.; Feldmann, J.; Fieres, B.; Petkov, N.; Bein, T.; Nichtl, A.; Kürzinger, K., Gold nanoshells improve single nanoparticle molecular sensors. *Nano Lett.* **2004,** 4, (10), 1853 - 1857.
52. Rasch, M. R.; Sokolov, K. V.; Korgel, B. A., Limitations on the optical tuneability of small diameter gold nanoshells. *Langmuir* **2009,** 25, (19), 11777 - 11785.
53. Alvarez, M. M.; Khoury, J. T.; Schaaff, T. G.; Shafigullin, M. N.; Vezmar, I.; Whetten, R. L., Optical absorption spectra of nanocrystal gold molecules. *Journal of Physical Chemistry B* **1997,** 101, (19), 3706-3712.
54. Palpant, B.; Prevel, B.; Lerme, J.; Cottancin, E.; Pellarin, M.; Treilleux, M.; Perez, A.; Vialle, J. L.; Broyer, M., Optical properties of gold clusters in the size range 2-4 nm. *Physical Review B* **1998,** 57, (3), 1963-1970.
55. Prodan, E.; Nordlander, P.; Halas, N. J., Effects of dielectric screening on the optical properties of metallic nanoshells. *Chemical Physics Letters* **2003,** 368, (1-2), 94-101.
56. Talley, C. E.; Jackson, J. B.; Oubre, C.; Grady, N. K.; Hollars, C. W.; Lane, S. M.; Huser, T. R.; Nordlander, P.; Halas, N. J., Surface-enhanced Raman scattering from individual Au nanoparticles and nanoparticle dimer substrates. *Nano Lett.* **2005,** 5, (8), 1569 - 1574.
57. Liu, J.; Cankurtaran, B.; McCredie, G.; Ford, M. J.; Wieczorek, L.; Cortie, M. B., Investigation of the optical properties of hollow aluminum 'nano-caps'. *Nanotechnology* **2005,** 16, 3023-3028.

58. Liu, J.; Cankurtaran, B.; Wieczorek, L.; Ford, M. J.; Cortie, M. B., Anisotropic optical properties of semitransparent coatings of gold nanocaps. *Adv. Funct. Mater.* **2006,** 16, (11), 1457 - 1461.
59. Mie, G., Beitrage zur Optik truber Medien speziell kolloidaler Metallosungen. *Ann. Phys.* **1908,** 25, 377 - 445.
60. Gans, R., Über die Form ultramikropischer Goldteilchen. *Ann. Phys. (Weinheim, Ger.)* **1912,** 37, 881-900.
61. Aden, A. L.; Kerker, M., Scattering of electromagnetic waves from 2 concentric spheres. *Journal of Applied Physics* **1951,** 22, (10), 1242-1246.
62. Xu, X. D.; Cortie, M. B., Shape change and color gamut in gold nanorods, dumbbells, and dog bones. *Adv. Funct. Mater.* **2006,** 16, (16), 2170-2176.
63. Prescott, S. W.; Mulvaney, P., Gold nanorod extinction spectra. *Journal of Applied Physics* **2006,** 99, (12).
64. Draine, B. T.; Flatau, P. J., Discrete-dipole approximation for scattering calculations. *J. Opt. Soc. Am.* **1994,** 11, (4), 1491 - 1499.
65. Draine, B. T.; Flatau, P. J. User guide to the discrete dipole approximation code DDSCAT 7.1. http://arXiv.org/abs/1002.1505v1
66. Draine, B. T.; Goodman, J., Beyond Clausius-Mossotti: wave propagation on a polarizable point lattice and the discrete dipole approximation. *Astrophys J* **1993,** 405, (2), 685 - 697.
67. Gutkowicz-Krusin, D.; Draine, B. T. Propagation of electromagnetic waves on a rectangular lattice of polarizable points. http://arxiv.org/abs/astro-ph/0403082v1
68. Brioude, A.; Jiang, X. C.; Pileni, M. P., Optical properties of gold nanorods: dda simulations supported by experiments. *J. Phys. Chem. B.* **2005,** 109, (27), 13138-13142.
69. Kealley, C. S.; Cortie, M. B., A computational exploration of the color gamut of nanoscale hollow scalene ellipsoids of Ag and Au. *Plasmonics* **2010,** 5, (1), 37-43.
70. ASTM Standard E308-08. **2008,** "Standard practice for computing the colors of objects by using the CIE system", ASTM International, West Conshohocken, PA, 2003, DOI: 10.1520/C0033-03, www.astm.org.
71. Diggle, J. W.; Downie, T. C.; Goulding, C. W., Anodic oxide films on aluminum. *Chemical Reviews* **1969,** 69, (3), 365-&.
72. Tierney, M. J.; Martin, C. R., Transparent metal microstructures. *J. Phys. Chem.* **1989,** 93, (8), 2878-2880.
73. Foss-Jr, C. A.; Tierney, M. J.; Martin, C. R., Template synthesis of infrared-transparent metal microcylinders: Comparison of optical properties with the predictions of effective medium theory. *J. Phys. Chem.* **1992,** 96, (22), 9001-9007.
74. van-der-Zande, B. M. I.; Böhmer, M. R.; Fokkink, L. G. J.; Schönenberger, C., Colloidal dispersions of gold rods: Synthesis and optical properties. *Langmuir* **2000,** 16, (2), 451-458.
75. Esumi, K.; Matsuhisa, K.; Torigoe, K., Preparation of rodlike gold particles by UV irradiation using cationic micelles as a template. *Langmuir* **1995,** 11, (9), 3285 - 3287.
76. Kurihara, K.; Kizling, J.; Stenius, P.; Fendler, J. H., Laser and pulse radiolytically induced colloidal gold formation in water and in water-in-oil microemulsions
Journal of the American Chemical Society **1983,** 105, (9), 2574-2579.
77. Kaneko, S.; Torigoe, K.; Esumi, K., Preparation of monodispersed concentrated gold hydrosols from gold tetrachloride(-)-cationic surfactant complexes. *J. Jpn. Soc. Colour Mater.* **1993,** 66, (1), 14-18.
78. Abdelmoti, L. G.; Zamborini, F. P., Potential-controlled electrochemical seed-mediated growth of gold nanorods directly on electrode surfaces. *Langmuir* **2010,** 26, (16), 13511-13521.

79. Miranda, O. R.; Ahmadi, T. S., Effects of intensity and energy of CW UV light on the growth of gold nanorods. *J. Phys. Chem. B* **2005,** 109, (33), 15724-15734.
80. Placido, T.; Comparelli, R.; Giannici, F.; Cozzoli, P. D.; Capitani, G.; Striccoli, M.; Agostiano, A.; Curri, M. L., Photochemical synthesis of water-soluble gold nanorods: The role of silver in assisting anisotropic growth. *Chem. Mater.* **2009,** 21, (18), 4192-4202.
81. Yu, Y. Y.; Chang, S. S.; Lee, C. L.; Chris-Wang, C. R., Gold nanorods: Electrochemical synthesis and optical properties. *J. Phys. Chem. B.* **1997,** 101, (34), 6661-6664.
82. Mohamed, M. B.; Ismail, K. Z.; Link, S.; El-Sayed, M. A., Thermal reshaping of gold nanorods in micelles. *J. Phys. Chem. B* **1998,** 102, (47), 9370-9374.
83. Niidome, Y.; Nishioka, K.; Kawasaki, H.; Yamada, S., Rapid synthesis of gold nanorods by the combination of chemical reduction and photoirradiation processes; morphological changes depending on the growing processes. *Chemical Communications* **2003**, (18), 2376-2377.
84. Nikoobakht, B.; Wang, Z. L.; El-Sayed, M. A., Self-assembly of gold nanorods. *J. Phys. Chem. B.* **2000,** 104, (36), 8635-8640.
85. Wang, Z. L.; Mohamed, M. B.; Link, S.; El-Sayed, M. A., Crystallographic facets and shapes of gold nanorods of different aspect ratios. *Surface Science* **1999,** 440, (1-2), L809-L814.
86. Wang, Z. L.; Gao, R. P.; Nikoobakht, B.; El-Sayed, M. A., Surface reconstruction of the unstable {110} surface in gold nanorods. *J. Phys. Chem. B.* **2000,** 104, (23), 5417-5420.
87. Carbó-Argibay, E.; Rodríguez-González, B.; Gómez-Graña, S.; Guerrero-Martínez, A.; Pastoriza-Santos, I.; Pérez-Juste, J.; Liz-Marzán, L. M., The crystalline structure of gold nanorods revisited: evidence for higer-index lateral facets. *Angew. Chem. Int. Edit.* **2010,** 49, (49), 9397-9400.
88. Guerrero-Martínez, A.; Pérez-Juste, J.; Carbó-Argibay, E.; Tardajos, G.; Liz-Marzán, L. M., Gemini-surfactant-directed self-assembly of monodisperse gold nanorods into standing superlattices. *Angew. Chem. Int. Edit.* **2009,** 48, (50), 9484-9488.
89. Johnson, C. J.; Dujardin, E.; Davis, S. A.; Murphy, C. J.; Mann, S., Growth and form of gold nanorods prepared by seed-mediated surfactant directed synthesis. *J. Mater. Chem.* **2002,** 12, 1765 - 1770.
90. Wei, Z. Q.; Zamborini, F. P., Directly monitoring the growth of gold nanoparticle seeds into gold nanorods. *Langmuir* **2004,** 20, (26), 11301-11304.
91. Jana, N. R.; Gearheart, L.; Murphy, C. J., Wet chemical synthesis of high aspect ratio cylindrical gold nanorods. *J. Phys. Chem. B.* **2001,** 105, (19), 4065-4067.
92. Garg, N.; Scholl, C.; Mohanty, A.; Jin, R., The role of bromide ions in seeding growth of Au nanorods. *Langmuir* **2010,** 26, (12), 10271 - 10276.
93. Chen, H. M.; Liu, R. S.; Asakura, K.; Jang, L. Y.; Lee, J. F., Controlling length of gold nanowires with large-scale: X-ray absorption spectroscopy approaches to the growth process. *J. Phys. Chem. C* **2007,** 111, (50), 18550-18557.
94. Nikoobakht, B.; Wang, J.; El-Sayed, M. A., Surface-Enhanced Raman Scattering of molecules adsorbed on gold nanorods: Off-surface plasmon resonance condition. *Chem. Phys. Lett.* **2002,** 366, 17-23.
95. Nikoobakht, B.; El-Sayed, M. A., Evidence for bilayer assembly of cationic surfactants on the surface of gold nanorods. *Langmuir* **2001,** 17, (20), 6368-6374.
96. Gao, J.; Bender, C. M.; Murphy, C. J., Dependence of the gold nanorod aspect ratio on the nature of the directing surfactant in aqueous solution. *Langmuir* **2003,** 19, (21), 9065-9070.

97. Iijima, S.; Ichihashi, T., Structural instability of ultrafine particles of metals. *Phys. Rev. Lett.* **1986,** 56, (6), 616 - 619.
98. Sau, T. K.; Murphy, C. J., Room temperature, high yield synthesis of multiple shapes of gold nanoparticles in aqueous solutions. *J. Am. Chem. Soc* **2004,** 126, (28), 8648 - 8649.
99. Kou, X.; Zhang, S.; Tsung, C.-K.; Yueng, M. H.; Shi, Q.; Stucky, G. D.; Sun, L.; Wang, J.; Yan, C., Growth of gold nanorods and bipyramids using CTEAB surfactant. *J. Phys. Chem. B.* **2006,** 110, (33), 16377 - 16383.
100. Gammons, C. H.; Yu, Y.; Williams-Jones, A. E., The disproportionation of gold (I) chloride complexes at 25 to 200oC. *Geochim. Cosmochim. Ac.* **1997,** 61, (10), 1971 - 1983.
101. Evans, D. H.; Lingane, J. J., Standard potentials of the couples involving AuBr4-,AuBr2- and Au in bromide media. *J. Electroanal. Chem.* **1963,** 6, (1), 1 - 10.
102. Zümreoglu-Karan, B., A rationale on the role of intermediate Au(III)-vitamin C complexation in the production of gold nanoparticles. *J. Nanopart. Res.* **2009,** 11, (5), 1099-1105.
103. Zweifel, D. A.; Wei, A., Sulfide-arrested growth of gold nanorods. *Chemistry of Materials* **2005,** 17, (16), 4256-4261.
104. Gou, L.; Murphy, C. J., Fine-tuning the shape of gold nanorods. *Chem. Mater.* **2005,** 17, (14), 3668 - 3672.
105. Keul, H. A.; Moller, M.; Bockstaller, M. R., Structural evolution of gold nanorods during controlled secondary growth. *Langmuir* **2007,** 23, (20), 10307-10315.
106. Sohn, K.; Kim, F.; Pradel, K. C.; Wu, J.; Peng, Y.; Zhou, F.; Huang, J., Construction of evolutionary tree for morphological engineering of nanoparticles. *ACS Nano* **2009,** 3, (8), 2191 - 2198.
107. Ratto, F.; Matteini, P.; Rossi, F.; Pini, R., Size and shape control in the overgrowth of gold nanorods. *J. Nanopart. Res.* **2010,** 12, (6), 2029-2036.
108. Sun, Y.; Mayers, B. T.; Xia, Y., Template-engaged replacement reaction: a one-step approach to the large-scale synthesis of metal nanostructures with hollow interiors. *Nano Letters* **2002,** 2, (5), 481 - 485.
109. Sun, Y. G.; Xia, Y. N., Shape-controlled synthesis of gold and silver nanoparticles. *Science* **2002,** 298, (5601), 2176-2179.
110. Jana, N. R.; Peng, X. G., Single-phase and gram-scale routes toward nearly monodisperse Au and other noble metal nanocrystals. *Journal of the American Chemical Society* **2003,** 125, (47), 14280-14281.
111. Zijlstra, P.; Bullen, C.; Chon, J. W. M.; Gu, M., High-temperature seedless synthesis of gold nanorods. *J. Phys. Chem. B.* **2006,** 110, (39), 19315 - 19318.
112. Boleininger, J.; Kurz, A.; Reuss, V.; Sonnichsen, C., Microfluidic continuous flow synthesis of rod-shaped gold and silver nanocrystals. *Physical Chemistry Chemical Physics* **2006,** 8, (33), 3824-3827.
113. Niidome, Y.; Nakamura, Y.; Honda, K.; Akiyama, Y.; Nishioka, K.; Kawasaki, H.; Nakashima, N., Characterization of silver ions adsorbed on gold nanorods: surface analysis by using surface-assisted laser desorption/ionization time-of-flight mass spectrometry. *Chemical Communications* **2009**, (13), 1754-1756.
114. Jiang, X. C.; Brioude, A.; Pileni, M. P., Gold nanorods: Limitations on their synthesis and optical properties. *Colloids and Surfaces A.* **2006,** 277, (2006), 201-206.
115. Jiang, X. C.; Pileni, M. P., Gold nanorods: Influence of various parameters as seeds, solvent, surfactant on shape control. *Colloids and Surfaces A.* **2007,** 295, (1-3), 228-232.

116. Smith, D. K.; Korgel, B. A., The importance of the CTAB surfactant on the colloidal seed-mediated synthesis of gold nanorods. *Langmuir* **2008,** 24, (3), 644-649.
117. Smith, D. K.; Miller, N. R.; Korgel, B. A., Iodide in CTAB prevents gold nanorod formation. *Langmuir* **2009,** 25, (16), 9518-9524.
118. Rayavarapu, R. G.; Ungureanu, C.; Krystek, P.; van Leeuwen, T. G.; Manohar, S., Iodide impurities in hexadecyltrimethyl ammonium bromide (CTAB) products: Lot-lot variations and influence on gold nanorod synthesis. *Langmuir* **2010,** 26, (7), 5050-5055.
119. Millstone, J. E.; Wei, W.; Jones, M. R.; Yoo, H. J.; Mirkin, C. A., Iodide ions control seed-mediated growth of anisotropic gold nanoparticles. *Nano Letters* **2008,** 8, (8), 2526-2529.
120. Gulati, A.; Liao, H.; Hafner, J. H., Monitoring gold nanorod synthesis by localised surface plasmon resonance. *J. Phys. Chem. B.* **2006,** 110, (45), 22323 - 22327.
121. Alekseeva, A. V.; Bogatyrev, V. A.; Dykman, L. A.; Khlebtsov, B. N.; Trachuk, L. A.; Melnikov, A. G.; Khlebtsov, N. G., Preparation and optical scattering characterization of gold nanorods and their application to a dot-immunogold assay. *Applied Optics* **2005,** 44, (29), 6285-6295.
122. Becker, J.; Schubert, O.; Sonnichsen, C., Gold nanoparticle growth monitored in situ using a novel fast optical single-particle spectroscopy method. *Nano Letters* **2007,** 7, (6), 1664-1669.
123. Takenaka, Y.; Kitahata, H., Analysis of the growth process of gold nanrods with time-resolved observation. *Phys. Rev. E.* **2009,** 80, (2), 020601 1 - 4.
124. Henkel, A.; Schubert, O.; Plech, A.; Sonnichsen, C., Growth kinetic of a rod-shaped metal nanocrystal. *J. Phys. Chem. C* **2009,** 113, (24), 10390-10394.
125. Morita, T.; Tanaka, E.; Inagaki, Y.; Hotta, H.; Shingai, R.; Hatakeyama, Y.; Nishikawa, K.; Murai, H.; Nakano, H.; Hino, K., Aspect-ratio dependence on formation process of gold nanorods studied by time-resolved distance distribution functions. *J. Phys. Chem. C* **2010,** 114, (9), 3804-3810.
126. Hubert, F.; Testard, F.; Rizza, G.; Spalla, O., Nanorods versus nanospheres: A bifurcation mechanism revealed by principal component TEM analysis. *Langmuir* **2010,** 26, (10), 6887-6891.
127. Kah, J. C. Y.; Phonthammachai, N.; Wan, R. C. Y.; Song, J.; White, T.; Mhaisalkar, S.; Ahmad, I.; Sheppard, C.; Olivo, M., Synthesis of gold nanoshells based on the deposition-precipitation process. *Gold Bulletin* **2008,** 41, (1), 23-36.
128. Phonthammachai, N.; Kah, J. C. Y.; Jun, G.; Sheppard, C. J. R.; Olivo, M. C.; Mhaisalkar, S. G.; White, T. J., Synthesis of contiguous silica-gold core-shell structures: Critical parameters and processes. *Langmuir* **2008,** 24, (9), 5109-5112.
129. West, J. L.; Halas, N. J.; Oldenburg, S. J.; Averitt, R. D. Metal nanoshells for biosensing applications. US 6699724, 2004.
130. Shi, W.; Sahoo, Y.; Swihart, M. T.; Prasad, P. N., Gold nanoshells on polystyrene cores for controls of surface plasmon resonance. *Langmuir* **2005,** 21, (4), 1610 - 1617.
131. Yong, K. T.; Sahoo, Y.; Swihart, M. T.; Prasad, P. N., Synthesis and plasmonic properties of silver and gold nanoshells on polystyrene cores of different size and of gold-silver core-shell nanostructures. *Colloids and Surfaces a-Physicochemical and Engineering Aspects* **2006,** 290, 89-105.
132. Zhou, H. S.; Honma, I.; Komiyama, H.; Haus, J. W., Controlled synthesis and quantum-size effect in gold-coated nanoparticles. *Phys. Rev. B* **1994,** 50, (16), 12052 - 12057.
133. Averitt, R. D.; Sarkar, D.; Halas, N. J., Plasmon resonance shifts of Au-coated Au_2S nanoshells: insight into multicomponent nanoparticle growth. *Phys. Rev. Lett.* **1997,** 78, (22), 4217 - 4220.

134. Norman, T. J.; Grant, C. D.; Magana, D.; Zhang, J. Z.; Liu, J.; Cao, D.; Bridges, F.; van-Buuren, A., Near infrared optical absorption of gold nanoparticle aggregates. *J. Phys. Chem. B.* **2002,** 106, (28), 7005 - 7012.
135. Raschke, G.; Brogl, S.; Susha, A. S.; Rogach, A. L.; Klar, T. A.; Feldmann, J.; Fieres, B.; Petkov, N.; Bein, T.; Nichtl, A.; Kürzinger, K., Reply to "comment on 'gold nanoshells improve single nanoparticle molecular sensors'". *Nano Letters* **2005,** 5, (4), 811 - 812.
136. Zhang, J. Z.; Schwartzberg, A. M.; Norman, T.; Grant, C. D.; Liu, J.; Bridges, F.; van-Buuren, T., Comment on "gold nanoshells improve single nanoparticle molecular sensors". *Nano Lett.* **2005,** 5, (4), 809 - 810.
137. Charnay, C.; Halas, N. J.; Bradley, R. K. Reduced symmetry nanoparticles. US 2003/0215638, 2003.
138. Halas, N. J.; Bradley, R. K. Partial coverage metal nanoshells and method of making same. US 6660381, 2003.
139. Liu, J.; Maaroof, A. I.; Wieczorek, L.; Cortie, M. B., Fabrication of hollow metal "nanocaps" and their red-shifted optical absorption spectra. *Adv. Mater.* **2005,** 17, (10), 1276 - 1281.
140. Sun, Y.; Xia, Y., Alloying and dealloying processes involved in the preparation of metal nanoshells through galvanic replacement reaction. *Nano Letters* **2003,** 3, (11), 1569 - 1572.
141. Sun, Y.; Xia, Y., Mechanistic study on the replacement reaction between silver nanostructures and chloroauric acid in aqueous medium. *J. Am. Chem. Soc.* **2004,** 126, (12), 3892 - 3901.
142. Schwartzberg, A. M.; Olson, T. Y.; Talley, C. E.; Zhang, J. Z., Synthesis, characterisation, and tuneable optical properties of hollow gold nanospheres. *J. Phys. Chem. B.* **2006,** 110, (40), 19935 - 19944.
143. Bao, Y. P.; Calderon, H.; Krishnan, K. M., Synthesis and characterization of magnetic-optical Co-Au core-shell nanoparticles. *Journal of Physical Chemistry C* **2007,** 111, (5), 1941-1944.
144. Edgar, J. A.; Zareie, H. M.; Blaber, M. G.; Dowd, A.; Cortie, M. B., Synthesis of hollow gold nanoparticles and rings using silver templates. *2008 International Conference on Nanoscience and Nanotechnology* **2008**, 36-39.
145. Au, L.; Lu, X.; Xia, Y., A comparative study of galvanic replacement reactions involving Ag nanocubes and AuCl2- or AuCl4-. *Adv. Mater.* **2008,** 20, (13), 2517 - 2522.
146. Daniel, M. C.; Astruc, D., Gold Nanoparticles: Assembly, Supramolecular Chemistry, Quantum-Size-Related Properties and Applications toward Biology, Catalysis and Nanotechnology. *Chem. Rev.* **2004,** 104, (1), 293-346.
147. Nakao, Y.; Kaeriyama, K., Dyeing of silk cloth with colloidal gold. *Journal of Applied Polymer Science* **1988,** 36, (2), 269-277.
148. Richardson, M. J.; Johnston, J. H., Sorption and binding of nanocrystalline gold by Merino wool fibres - An XPS study. *Journal of Colloid and Interface Science* **2007,** 310, (2), 425-430.
149. Gautier, C.; Cunningham, A.; Si-Ahmed, L.; Robert, G.; Burgi, T., Pigments based on silica-coated gold nanorods: Synthesis, colouring strength, functionalisation, extrusion, thermal stability and colour evolution. *Gold Bulletin* **2010,** 43, (2), 94-104.
150. Chowdhury, H.; Xu, X. D.; Huynh, P.; Cortie, M. B., Radiative heat transfer across glass coated with gold nano-particles. *Journal of Solar Energy Engineering-Transactions of the Asme* **2005,** 127, (1), 70-75.
151. Supansomboon, S.; Maaroof, A.; Cortie, M. B., "Purple glory": The optical properties and technology of AuAl2 coatings. *Gold Bulletin* **2008,** 41, (4), 296-304.

152. Xu, X.; Stevens, M.; Cortie, M. B., In situ precipitation of gold nanoparticles onto glass for potential architectural applications. *Chem. Mater.* **2004,** 16, (11), 2259 - 2266.
153. Xu, X.; Gibbons, T. H.; Cortie, M. B., Spectrally-selective gold nanorod coatings for window glass. *Gold Bulletin (London, United Kingdom)* **2006,** 39, (4), 156-165.
154. Cole, J. R.; Halas, N. J., Optimised plasmonic nanoparticle distributions for solar spectrum harvesting. *Appl. Phys. Lett.* **2006,** 89, (15), 153120/1 - 153120/3.
155. Vernon, K. C.; Funston, A. M.; Novo, C.; Gómez, D. E.; Mulvaney, P.; Davis, T. J., Influence of particle-substrate interaction on localized plasmon resonances. *Nano Letters* **2010,** 10, (6), 2080-2086.
156. Stokes, N. L.; Edgar, J. A.; McDonagh, A. M.; Cortie, M. B., Spectrally selective coatings of gold nanorods on architectural glass. *J. Nanopart. Res.* **2010,** 12, (8), 2821 - 2830.
157. Payne, J. D.; Jackson, J. B. Plasmon resonant based eye protection 2006.
158. Cortie, M. B.; McDonagh, A. M.; Mulvaney, P. Devices having a variable optical property and processes of making such devices. Australian Patent Application AU2005/201737, 2005.
159. Chon, J. W. M.; Bullen, C.; Zijlstra, P.; Gu, M., Spectral encoding on gold nanorods doped in a silica sol-gel matrix and its application to high-density optical data storage. *Adv. Funct. Mater.* **2007,** 17, (6), 875-880.
160. Zijlstra, P.; Chon, J. W. M.; Gu, M., Five-dimensional optical recording mediated by surface plasmons in gold nanorods. *Nature* **2009,** 459, (7245), 410-413.
161. Cang, H.; Wong, C. M.; Shan, C.; Rizvi, A. H.; Yang, H., Confocal three dimensional tracking of a single nanoparticle with concurrent spectroscopic readouts. *Appl. Phys. Lett.* **2006,** 88, (22), 223901/1-223901/3.
162. Kimura, S.; Wilson, T., Confocal scanning dark-field polarisation microscopy. *Appl. Optics* **1994,** 33, (7), 1274 - 1278.
163. Chang, S. S.; Shih, C. W.; Chen, C. D.; Lai, W. C.; Wang, C. R. C., The shape transition of gold nanorods. *Langmuir* **1999,** 15, (3), 701-709.
164. Pérez-Juste, J.; Mulvaney, P.; Liz-Marzán, L. M., Patterning and encryption using gold nanoparticles. *Int. J. Nanotechnol.* **2007,** 4, (3), 215 - 224.
165. Wan, D. H.; Chen, H. L.; Tseng, S. C.; Wang, L. A.; Chen, Y. P., One-shot deep-UV pulsed-laser-induced photomodification of hollow metal nanoparticles for high-density data storage on flexible substrates. *ACS Nano* **2010,** 4, (1), 165-173.
166. Haruta, M.; Kobayashi, T.; Sano, H.; Yamada, M., Novel gold catalysts for the oxidation of carbon-monoxide at a temperature far below 0-degrees-c. *Chem. Lett.* **1987**, 405 - 408.
167. Haruta, M.; Sano, H.; Kobayashi, T. Method for manufacture of catalyst composite having gold or mixture of gold catalytic metal oxide deposited on carrier. United States Patent 4698324, 1987.
168. Hutchings, G. J., Vapor phase hydrochlorination of acetylene: correlation of catalytic activity of supported metal chloride catalysts. *J. Catalysis* **1985,** 96, 292 - 295.
169. Thompson, D. T., Using gold nanoparticles for catalysis. *Nano Today* **2007,** 2, (4), 40-43.
170. Bond, G. C.; Thompson, D. T., Gold-catalysed oxidation of carbon monoxide. *Gold Bulletin* **2000,** 33, (2), 41-51.
171. Bai, X. T.; Gao, Y. A.; Liu, H. G.; Zheng, L. Q., Synthesis of Amphiphilic Ionic Liquids Terminated Gold Nanorods and Their Superior Catalytic Activity for the Reduction of Nitro Compounds. *Journal of Physical Chemistry C* **2009,** 113, (41), 17730-17736.

172. Kundu, S.; Lau, S.; Liang, H., Shape-controlled catalysis by cetyltrimethylammonium bromide terminated gold nanospheres, nanorods, and nanoprisms. *Journal of Physical Chemistry C* **2009,** 113, (13), 5150-5156.
173. Novo, C.; Funston, A. M.; Mulvaney, P., Direct observation of chemical reactions on single gold nanocrystals using surface plasmon spectroscopy. *Nature Nanotechnology* **2008,** 3, (10), 598-602.
174. Novo, C.; Funston, A. M.; Gooding, A. K.; Mulvaney, P., Electrochemical charging of single gold nanorods. *Journal of the American Chemical Society* **2009,** 131, (41), 14664-14666.
175. Heck, K. N.; Janesko, B. G.; Scuseria, G. E.; Halas, N. J.; Wong, M. S., Observing metal-catalyzed chemical reactions in situ using Surface-Enhanced Raman Spectroscopy on Pd-Au nanoshells. *J. Am. Chem. Soc.* **2008,** 130, (49), 16592-16600.
176. Katz, E.; Willner, I., Integrated nanoparticle-biomolecule hybrid systems: synthesis, properties, and applications. *Angew. Chem. Int. Ed.* **2004,** 43, (45), 6042-6108.
177. Shipway, A. N.; Katz, E.; Willner, I., Nanoparticle arrays on surfaces for electronic, optical and sensor applications. *ChemPhysChem* **2000,** 1, 18-52.
178. Wilson, R., The use of gold nanoparticles in diagnostics and detection. *Chemical Society Reviews* **2008,** 37, (9), 2028-2045.
179. Chen, C.-D.; Cheng, S.-F.; Chau, L.-K.; Wang, C. R. C., Sensing capability of the localised surface plasmon resonance of gold nanorods. *Biosens. Bioelectron.* **2007,** 22, (6), 926 - 932.
180. Sun, Y.; Xia, Y., Increased sensitivity of surface plasmon resonance of gold nanoshells compared to that of gold solid colloids in response to environmental changes. *Anal. Chem.* **2002,** 74, (20), 5297 - 5305.
181. Sönnichsen, C.; Alivisatos, A. P., Gold nanorods as novel nonbleaching plasmon-based orientation sensors for polarised single-particle microscopy. *Nano Lett.* **2005,** 5, (2), 301 - 304.
182. Chau, L. K.; Hsu, W. T.; Cheng, S. F. Surface plasmon resonance sensing system and method thereof. 2007.
183. Marinakos, S. M.; Chen, S.; Chilkoti, A., Plasmonic detection of a model analyte in serum by a gold nanorod sensor. *Anal. Chem.* **2007,** 79, (14), 5278 - 5283.
184. Mayer, K. M.; Lee, S.; Liao, H.; Rostro, B. C.; Fuentes, A.; Scully, P. T.; Nehl, C. L.; Hafner, J. H., A label-free immunoassay based upon localised surface plasmon resonance of gold nanorods. *ACS Nano* **2008,** 2, (4), 687 - 692.
185. Yu, C.; Irudayaraj, J., Multiplex biosensor using gold nanorods. *Anal. Chem.* **2007,** 79, (2), 572 - 579.
186. Li, C.-Z.; Male, K. B.; Hrapovic, S.; Luong, J. H. T., Fluorescence properties of gold nanorods and their application for DNA biosensing. *Chem. Commun.* **2005**, 3924 - 3926.
187. Bishnoi, S. W.; Rozell, C. J.; Levin, C. S.; Gheith, M. K.; Johnson, B. R.; Johnson, D. H.; Halas, N. J., All-optical nanoscale pH meter. *Nano Letters* **2006,** 6, (8), 1687 - 1692.
188. Halas, N. J.; Lal, S.; Nordlander, P.; Jackson, J. B.; Moran, C. E. Nanoparticle-based all-optical sensors. US 6778316, 2004.
189. Hirsch, L. R.; Jackson, J. B.; Lee, A.; Halas, N. J.; West, J. L., A whole blood immunoassay using gold nanoshells. *Anal. Chem.* **2003,** 75, (10), 2377 - 2381.
190. Nehl, C. L.; Grady, N. K.; Goodrich, G. P.; Tam, F.; Halas, N. J.; Hafner, J. H., Scattering spectra of single gold nanoshells. *Nano Lett.* **2004,** 4, (12), 2355 - 2359.
191. Novo, C.; Gomez, D.; Perez-Juste, J.; Zhang, Z.; Petrova, H.; Reismann, M.; Mulvaney, P.; Hartland, G. V., Contributions from radiation damping and surface scattering to the linewidth of the longitudinal plasmon band of gold nanorods: a single particle study. *Phys. Chem. Chem. Phys.* **2006,** 8, (30), 3540 - 3546.

192. Schultz, S.; Smith, D. R.; Mock, J. J.; Schultz, D. A., Single-target molecule detection with nonbleaching multicolour optical immunolabels. *Proc. Natl. Acad. Sci.* **2000,** 97, (3), 996 - 1001.
193. Sönnichsen, C.; Geier, S.; Hecker, N. E.; von-Plessen, G.; Feldmann, J.; Ditlbacher, H.; Lamprecht, B.; Krenn, J. R.; Aussenegg, F. R.; Chan, V. Z.-H.; Spatz, J. P.; Möller, M., Spectroscopy of single metallic nanoparticles using total internal reflection microscopy. *Appl. Phys. Lett.* **2000,** 77, (19), 2949 - 2951.
194. Frasch, W. D.; Chapsky, L. Polarization-enhanced detector with gold nanorods for detecting nanoscale rotational motion and method thereof. 2006.
195. Chang, W. S.; Ha, J. W.; Slaughter, L. S.; Link, S., Plasmonic nanorod absorbers as orientation sensors. *P. Natl. Acad. Sci. USA* **2010,** 107, (7), 2781-2786.
196. Nath, N.; Chilkoti, A., A colourimetric gold nanoparticle sensor to interrogate biomolecular interactions in real time on a surface. *Anal. Chem.* **2002,** 74, (3), 504 - 509.
197. Chen, H. J.; Kou, X. S.; Yang, Z.; Ni, W. H.; Wang, J. F., Shape- and size-dependent refractive index sensitivity of gold nanoparticles. *Langmuir* **2008,** 24, (10), 5233-5237.
198. Mayer, K. M.; Hao, F.; Lee, S.; Nordlander, P.; Hafner, J. H., A single molecule immunoassay by localized surface plasmon resonance. *Nanotechnology* **2010,** 21, (25).
199. Becker, J.; Trugler, A.; Jakab, A.; Hohenester, U.; Sonnichsen, C., The optimal aspect ratio of gold nanorods for plasmonic bio-sensing. *Plasmonics* **2010,** 5, (2), 161-167.
200. Yu, C.; Irudayaraj, J., Quantitative evaluation of sensitivity and selectivity of multiplex nanoSPR biosensor assays. *Biophys. J.* **2007,** 93, (10), 3684 - 3692.
201. Haynes, C. L.; McFarland, A. D.; Van Duyne, R. P., Surface-Enhanced Raman spectroscopy. *Anal. Chem.* **2005,** 77, (17), 338A-346A.
202. Kneipp, K.; Kneipp, H.; Kartha, V. B.; Manoharan, R.; Deinum, G.; Itzkan, I.; Dasari, R. R.; Feld, M. S., Detection and identification of a single DNA base molecule using surface-enhanced Raman scattering (SERS). *Phys. Rev. E* **1998,** 57, (6), R6281-R6284.
203. Fleischmann, M.; Hendra, P. J.; McQuillan, A. J., Raman spectra of pyridine adsorbed at a silver electrode. *Chem. Phys. Lett.* **1974,** 26, (2), 163 - 166.
204. Creighton, J. A.; Blatchford, C. G.; Albrecht, M. G., Plasma resonance enhancement of Raman scattering by pyridine adsorbed on silver or gold sol particles of size comparable to the excitation wavelength. *J. Chem. Soc. Faraday Trans.* **1979,** 75, (5), 790-798.
205. Wang, D. S.; Kerker, M., Enhanced Raman scattering by molecules adsorbed at the surface of colloidal spheroids. *Physical Review B: Condensed Matter and Materials Physics* **1981,** 24, (4), 1777-90.
206. Orendorff, C. J.; Gearheart, L.; Jana, N. R.; Murphy, C. J., Aspect ratio dependence on surface enhanced Raman scattering using silver and gold nanorod substrates. *Phys. Chem. Chem. Phys.* **2006,** 8, (1), 165 -170.
207. Oyelere, A. K.; Chen, P. C.; Huang, X.; El-Sayed, I. H.; El-Sayed, M. A., Peptide-conjugated gold nanorods for nuclear targeting. *Bioconjugate Chem.* **2007,** 18, (5), 1490 - 1497.
208. Oldenburg, S. J.; Westcott, S. L.; Averitt, R. D.; Halas, N. J., Surface enhanced Raman scattering in the near infrared using metal nanoshell substrates. *J. Chem. Phys* **1999,** 111, (10), 4729 - 4735.
209. Alvarez-Puebla, R. A.; Ross, D. J.; Nazri, G. A.; Aroca, R. F., Surface-enhanced Raman Scattering on nanoshells with tunable surface plasmon resonance. *Langmuir* **2005,** 21, (23), 10504-10508.

210. Talley, C. E.; Huser, T.; Hollars, C. W.; Jusinski, L.; Laurence, T.; Lane, S., Nanoparticle-based Surface-Enhanced Raman spectroscopy. *NATO Science Series, Series I: Life and Behavioural Sciences* **2005,** 369 (Advances in Biophotonics), 182 - 195.
211. Dieringer, J. A.; McFarland, A. D.; Shah, N. C.; Stuart, D. A.; Whitney, A. V.; Yonzon, C. R.; Young, M. A.; Zhang, X. Y.; Van Duyne, R. P., Surface enhanced Raman spectroscopy: new materials, concepts, characterization tools, and applications. *Faraday Discussions* **2006,** 132, 9-26.
212. Wokaun, A.; Gordon, J. P.; Liao, P. F., Radiation damping in surface-enhanced Raman scattering. *Phys. Rev. Lett.* **1982,** 48, (14), 957 - 960.
213. Oubre, C.; Nordlander, P., Finite-difference time-domain studies of the optical properties of nanoshell dimers. *J. Phys. Chem. B.* **2005,** 109, (20), 10042 - 10051.
214. Nikoobakht, B.; El-Sayed, M. A., Surface-enhanced Raman scattering studies on aggregated gold nanorods. *J. Phys. Chem. A.* **2003,** 107, (18), 3372 - 3378.
215. Weissleder, R., A clearer vision for in vivo imaging. *Nat. Biotechnol.* **2001,** 19, 316 - 317.
216. Faulk, W. P.; Taylor, G. M., Immunocolloid method for electron microscope *Immunochemistry* **1971,** 8, (11), 1081-&.
217. Harding, H. E., The recognition of metallic gold in tissue sections *Journal of Clinical Pathology* **1953,** 6, (2), 149-149.
218. Hayat, M. A., *Colloidal gold: Principles, methods and applications*. Academic Press: San Diego, CA, 1989.
219. Loo, C.; Lin, A.; Hirsch, L. R.; Lee, M. H.; Barton, J.; Halas, N.; West, J. L.; Drezek, R. A., Nanoshell-enabled photonics-based imaging and therapy of cancer. *Technol. Cancer. Res. T.* **2004,** 3, 33.
220. El-Sayed, I. H.; Huang, X. H.; El-Sayed, M. A., Surface plasmon resonance scattering and absorption of anti-EGFR antibody conjugated gold nanoparticles in cancer diagnostics: Applications in oral cancer. *Nano Letters* **2005,** 5, (5), 829-834.
221. Durr, N. J.; Larson, T.; Smith, D. K.; Korgel, B. A.; Sokolov, K.; Ben-Yakar, A., Two-photon luminescence imaging of cancer cells using molecularly targeted gold nanorods. *Nano Letters* **2007,** 7, (4), 941-945.
222. Wang, H.; Huff, T. B.; Zweifel, D. A.; He, W.; Low, P. S.; Wei, A.; Cheng, J.-X., In-vitro and In-vivo two photon luminescence imaging of single gold nanorods. *Proc. Natl. Acad. Sci.* **2005,** 102, (44), 15752 - 15756.
223. Boppart, S. A.; Wei, A. Multi-functional plasmon-resonant contrast agents for optical coherence tomography. US 2005/0171433.
224. Agarwal, A.; Huang, S. W.; O'Donnell, M.; Day, K. C.; Day, M.; Kotov, N.; Ashkenazi, S., Targeted gold nanorod contrast agent for prostate cancer detection by photoacoustic imaging. *J. App. Phys.* **2007,** 102, (6), 064701/1 - 064701/4.
225. Kim, K.; Huang, S.-W.; Ashkenazi, S.; O'Donnell, M.; Agarwal, A.; Kotov, N. A.; Denny, M. F.; Kaplan, M. J., Photoacoustic imaging of early inflammatory response using gold nanorods. *Appl. Phys. Lett.* **2007,** 90, (22), 223901.
226. Li, P. C.; Wei, C. W.; Liao, C. K.; Chen, C. D.; Pao, K. C.; Wang, C. R. C.; Wu, Y. N.; Shieh, D. B., Photoacoustic imaging of multiple targets using gold nanorods. *IEEE T. Ultrason. Ferr.* **2007,** 54, (8), 1642 - 1647.
227. Wang, Y.; Xie, X.; Wang, X.; Ku, G.; Gill, K. L.; O'Neal, D. P.; Stoica, G.; Wang, L. V., Photoacoustic tomography of a nanoshell contrast agent in the in vivo rat brain. *Nano Lett.* **2004,** 4, (9), 1689 - 1692.
228. Park, J.; Estrada, A.; Sharp, K.; Sang, K.; Schwartz, J. A.; Smith, D. K.; Coleman, C.; Payne, J. D.; Korgel, B. A.; Dunn, A. K.; Tunnell, J. W., Two-photon-induced

photoluminescence imaging of tumours using near-infrared excited gold nanoshells. *Opt. Express* **2008,** 16, (3), 1590 - 1599.
229. Gobin, A.; Lee, M.-H.; Halas, N. J.; James, W. D.; Drezek, R. A.; West, J. L., Near-infrared resonant nanoshells for combined optical imaging and photothermal cancer therapy. *Nano Lett.* **2007,** 7, (7), 1929 - 1934.
230. Masters, B. R.; So, P. T. C., Antecedents of two-photon excitation laser scanning microscopy. *Microscopy Research and Technique* **2004,** 63, 3 - 11.
231. Boyd, G. T.; Yu, Z. H.; Shen, Y. R., Photoinduced luminescence from the noble metals and its enhancement on roughened surfaces. *Phys. Rev. B: Condens. Matter.* **1986,** 33, (12, Pt. 1), 7923 - 7936.
232. Larson, D. R.; Zipfel, W. R.; Williams, R. M.; Clark, S. W.; Bruchez, M. P.; Wise, F. W.; Webb, W. W., Water-soluble quantum dots for multiphoton fluorescence imaging in vivo. *Science* **2003,** 300, 1434 - 1436.
233. Chithrani, B. D.; Ghazani, A. A.; Chan, W. C. W., Determining the size and shape dependence of gold nanoparticle uptake into mammalian cells. *Nano Letters* **2006,** 6, (4), 662-668.
234. Schmid, G.; Corain, B., Nanoparticulated gold: Syntheses, structures, electronics and reactivities. *Eur. J. Inorg. Chem.* **2003,** 2003, 3081 - 3098.
235. Ji, X.; Shao, R.; Elliott, A. M.; Stafford, R. J.; Esparza-Coss, E.; Bankson, J. A.; Liang, G.; Luo, Z.-P.; Park, K.; Markert, J. T.; Li, C., Bifunctional gold nanoshells with a superparamagnetic iron oxide-silica core suitable for both MR imaging and photothermal therapy. *Journal of Physical Chemistry C* **2007,** 111, (17), 6245-6251.
236. Gole, A.; Stone, J. W.; Gemmill, W. R.; zurLoye, H. C.; Murphy, C. J., Iron oxide coated gold nanorods: synthesis, characterisation, and magnetic manipulation. *Langmuir* **2008,** ACS ASAP.
237. Wang, Y.-X. J.; Hussain, S. M.; Krestin, G. P., Superparamagnetic iron oxide contrast agents: physicochemical characteristics and applications in MR imaging. *Eur. Radiol.* **2001,** 11, 2319 - 2331.
238. Hyeon, T.; Kim, J. Y.; Cho, M. H.; Kim, S. K.; Lee, J. Use of core-shell gold nanoparticle which contains magnetic nanoparticles for MRI T2 contrast agent, cancer diagnostic therapy. 2008.
239. Allen, T. J.; Beard, P. C., Dual wavelength laser diode excitation source for 2D photoacoustic imaging. *Proc. of SPIE* **2007,** 6437, 64371U/1 - 64371U/9.
240. Zemp, R. J.; Bitton, R.; Li, M.-L.; Shung, K. K.; Stoica, G.; Wang, L. V., Photoacoustic imaging of the microvasculature with a high-frequency ultrasound array transducer. *J. Biomed. Opt.* **2007,** 12, (1), 010501-1 - 010501-3.
241. Oraevsky, A. A.; Henrichs, P. M. High contrast optoacoustical imaging using nanoparticles. 2005.
242. Huang, D.; Swanson, E. A.; Lin, C. P.; Schuman, J. S.; Stinson, W. G.; Chang, W.; Hee, M. R.; Flotte, T.; Gregory, K.; Puliafito, C. A.; Fuijimoto, J. G., Optical Coherence Tomography. *Science* **1991,** 254, (5035), 1178 - 1181.
243. Drexler, W.; Morgner, U.; Ghanta, R. K.; Kärtner, F. X.; Schuman, J. S.; Fuijimoto, J. G., Ultrahigh-resolution ophthalmic optical coherence tomography. *Nature Medicine* **2001,** 7, (4), 502 - 507.
244. Cortesi, R.; Esposito, E.; Menegatti, E.; Gambari, R.; Nastruzzi, C., Effect of cationic liposome composition on in vitro cytotoxicity and protective effect on carried DNA. *Int. J. Pharm.* **1996,** 139, (1, 2), 69 - 78.
245. Connor, E. E.; Mwamuka, J.; Gole, A.; Murphy, C. J.; Wyatt, M. D., Gold nanoparticles are taken up by human cells but do not cause acute cytotoxicity. *Small* **2005,** 1, (3), 325-327.

246. Hauck, T. S.; Ghazani, A. A.; Chan, W. C. W., Assessing the effect of surface chemistry on gold nanorod uptake, toxicity, and gene expression in mammalian cells. *Small* **2008,** 4, (1), 153 - 159.
247. Pissuwan, D.; Valenzuela, S. M.; Killingsworth, M. C.; Xu, X., Targeted destruction of murine macrophage cells with bioconjugated gold nanorods. *J. Nanopart. Res.* **2007,** 9, (6), 1109 - 1124.
248. Pissuwan, D.; Valenzuela, S. M.; Miller, C. M.; Cortie, M. B., A golden bullet? Selective targeting of Toxoplasma gondii tachyzoites using antibody-functionalised gold nanorods. *Nano Lett.* **2007,** 7, (12), 3808 - 3812.
249. Alkilany, A. M.; Murphy, C. J., Toxicity and cellular uptake of gold nanoparticles: what we ahce learned so far? *J. Nanopart. Res.* **2010,** 12, (7), 2313 - 2333.
250. Alkilany, A. M.; Nagaria, P. K.; Wyatt, M. D.; Murphy, C. J., Cation exchange on the surface of gold nanorods with a polymerizable surfactan: polymerization, stability and toxicity evaluation. *Langmuir* **2010,** 26, (12), 9328 - 9333.
251. Bernardi, R. J.; Lowery, A. R.; Thompson, P. A.; Blaney, S. M.; West, J. L., Immunonanoshells for targeted photothermal ablation in medulloblastoma and glioma: an in vitro evaluation using human cells lines. *J. Neurooncol.* **2008,** 86, (2), 165 - 172.
252. Stern, J. M.; Stanfield, J.; Lotan, Y.; Park, S.; Hsieh, J. T.; Cadeddu, J. A., Efficacy of laser-activated gold nanoshells in ablating prostate cancer cells in vitro. *J. Endourol.* **2007,** 21, (8), 939 - 943.
253. Ferry, J. L.; Craig, P.; Hexel, C.; Sisco, P.; Frey, R.; Pennington, P. L.; Fulton, M. H.; Geoff-Scott, I.; Decho, A. W.; Kashiwada, S.; Murphy, C. J.; Shaw, T. J., Transfer of gold nanoparticles from the water column to the estuarine food web. *Nature Nanotechnology* **2009,** 4, (7), 441 - 444.
254. Pissuwan, D.; Valenzuela, S. M.; Killingsworth, M. C.; Cortie, M. B., Hyperthermal therapeutic treatment using gold nanoparticles. In *International Conference on Nanoscience and Nanotechnology (ICONN2008)*, Melbourne, Australia, 25th - 29th Feb. 2008.
255. Frederix, F.; Broek, B. V. d. Metal nanostructures and pharmaceutical compositions. 2007.
256. Huang, X.; El-Sayed, I. H.; Qian, W.; El-Sayed, M. A., Cancer cell imaging and photothermal therapy in the near-infrared region by using gold nanorods. *J. Am. Chem. Soc.* **2006,** 128, (6), 2115 - 2120.
257. Niidome, T.; Yamagata, M.; Okamoto, Y.; Akiyama, Y.; Takahashi, H.; Kawano, T.; Katayama, Y.; Niidome, Y., PEG-modified gold nanorods with a stealth character for in vivo applications. *Journal of Controlled Release* **2006,** 114, (3), 343-347.
258. Yu, C.; Varghese, L.; Irudayaraj, J., Surface modification of cetyltrimethylammonium bromide-capped gold nanorods to make molecular probes. *Langmuir* **2007,** 23, (17), 9114 - 9119.
259. Gobin, A. M.; O'Neal, D. P.; Watkins, D. M.; Halas, N. J.; Drezek, R. A.; West, J. L., Near infrared laser-tissue welding using nanoshells as an exogenous absorber. *Lasers in Surgery and Medicine* **2005,** 37, 123 - 129.
260. Hirsch, L. R.; Stafford, R. J.; Bankson, J. A.; Sershen, S. R.; Rivera, B.; Price, R. E.; Hazle, J. D.; Halas, N. J.; West, J. L., Nanoshell-mediated near-infrared thermal therapy of tumors under magnetic resonance guidance. *Proc. Natl. Acad. Sci.* **2003,** 100, (23), 13549-13554.
261. Loo, C.; Lowery, A.; Halas, N.; West, J.; Drezek, R., Immunotargeted nanoshells for integrated cancer imaging and therapy. *Nano Letters* **2005,** 5, (4), 709-711.

262. O'Neal, D. P.; Hirsch, L. R.; Halas, N. J.; Payne, J. D.; West, J. L., Photo-thermal tumour ablation in mice using near-infrared absorbing nanoparticles. *Cancer Letters* **2004,** 209, 171 - 176.
263. West, J. L.; Halas, N. J.; Hirsch, L. R. Optically-active nanoparticles for use in therapeutic and diagnostic methods. United States 6530944, 2003.
264. Wu, C.; Liang, X.; Jiang, H., Metal nanoshells as a contrast agent in near-infrared diffuse optical tomography. *Optics Communications* **2005,** 253, (1-3), 214-221.
265. Loo, C.; Lin, A.; Hirsch, L.; Lee, M.-H.; Barton, J.; Halas, N.; West, J.; Drezek, R., Diagnostic and therapeutic applications of metal nanoshells. *Nanofabrication towards Biomedical Applications* **2005**, 327-342.
266. van-Pieterson, L.; Hendriks, B. H. W.; Lucassen, G. W. System and method for interacting with a cell or tissue in a body. WO 2007/057838, 2007.
267. van-Pieterson, L.; Hendriks, B. H. W.; Lucassen, G. W. System and method for interacting with a cell or tissue in a body. United States 2008/0312532, 2008.
268. McCarthy, J. R.; Jaffer, F. A.; Weissleder, R., A macrophage-targeted theranostic nanoparticle for biomedical applications. *Small* **2006,** 2, (8-9), 983-987.
269. Link, S.; El-Sayed, M. A., Shape and size dependence of radiative, non-radiative and photothermal properties of gold nanocrystals. *Int. Rev. Phys. Chem.* **2000,** 19, (3), 409 - 453.
270. Ekici, O.; Harrison, R. K.; Durr, N. J.; Eversole, D. S.; Lee, M.; Ben-Yakar, A., Thermal analysis of gold nanorods heated with femtosecond laser pulses. *Journal of Physics D-Applied Physics* **2008,** 41, (18), -.
271. Harris, N.; Ford, M. J.; Cortie, M. B., Optimization of plasmonic heating by gold nanospheres and nanoshells. *Journal of Physical Chemistry B* **2006,** 110, (22), 10701-10707.
272. Angelides, K. Screening for cell-targeting ligands attached to metal nanoshells for use in target-cell killing. WO 2004/020973, 2004.
273. Gobin, A. M.; Watkins, E. M.; Quevedo, E.; Colvin, V. L.; West, J. L., Near-infrared-resonant gold/gold sulfide nanoparticles as a photothermal cancer therapeutic agent. *Small* **2010,** 6, (6), 745 - 752.
274. West, J. L.; Payne, J. D. Treatment of disease states characterized by excessive or inappropriate angiogenesis. WO/047633, 2003.
275. Norman, R. S.; Stone, J. W.; Gole, A.; Murphy, C. J.; Sabo-Attwood, T. L., Targeted photothermal lysis of the pathogenic bacteria, Pseudomonas aeruginosa, with gold nanorods. *Nano Letters* **2008,** 8, (1), 302-306.
276. Mauël, J., Macrophage-parasite interactions in Leishmania infections. *Journal of Leukocyte Biology* **1990,** 47, 187 - 193.
277. Shiotani, A.; Mori, T.; Niidome, T.; Niidome, Y.; Katayama, Y., Stable incorporation of gold nanorods into N-Isopropylacrylamide hydrogels and their rapid shrinkage induced by near-infrared laser irradiation. *Langmuir* **2007,** 23, (7), 4012 - 4018.
278. Bikram, M.; Gobin, A.; Whitmire, R. E.; West, J. L., Temperature-sensitive hydrogels with SiO_2-Au nanoshells for controlled drug delivery. *J. Control. Release* **2007,** 123, (3), 219 - 227.
279. Sershen, S. R.; Westcott, S. L.; Halas, N. J.; West, J. L., Temperature-sensitive polymer-nanoshell composites for photothermally modulated drug delivery. *J. Biomed. Mater. Res.* **2000,** 51, (3), 293 -298.
280. West, J. L.; Sershen, S. R.; Halas, N. J.; Oldenburg, S. J.; Averitt, R. D. Temperature-sensitive polymer/nanoshell composites for photothermally modulated drug delivery. United States 6645517, 2003.

281. West, J. L.; Sershen, S. R.; Halas, N. L.; Oldenburg, S. J.; Averitt, R. D. Temperature-sensitive polymer/nanoshell composites for photothermally modulated drug delivery. WO 01/05586, 2001.
282. Ludwig, F. N.; Pacetti, S. D.; Hossainy, S. F. A.; Davalian, D. Nanoshells on polymers. 2007.
283. Paciotti, G. F.; Kingston, D. G. I.; Tamarkin, L., Colloidal gold nanoparticles: A novel nanoparticle platform for developing multifunctional tumor-targeted drug delivery vectors. *Drug Development Research* **2006,** 67, (1), 47-54.
284. Chen, C. C.; Lin, Y. P.; Wang, C. W.; Tzeng, H. C.; Wu, C. H.; Chen, Y. C.; Chen, C. P.; Chen, L. C.; Wu, Y. C., DNA-gold nanorod conjugates for remote control of localized gene expression by near infrared irradiation. *Journal of the American Chemical Society* **2006,** 128, (11), 3709-3715.
285. Xie, H.; Gill-Sharp, K. L.; O'Neal, D. P., Quantitative estimation of gold nanoshell concentrations in whole blood using dynamic light scattering. *Nanomedicine* **2007,** 3, (1), 89 - 94.
286. Rodriguez-Fernández, J.; Pérez-Juste, J.; Liz-Marzán, L. M.; Lang, P. R., Dynamic light scattering of short Au rods with low aspect ratios. *J. Phys. Chem. C* **2007,** 111, (13), 5020 - 5025.
287. Dykman, L. A.; Sumaroka, M. V.; Staroverov, S. A.; Zaitseva, I. S.; Bogatyrev, V. A., Immunogenic properties of colloidal gold. *Biology Bulletin* **2004,** 31, (1), 75-79.
288. Breitinger, D. K.; Herrmann, W. A., *Synthetic methods of organometllic and inorganic chemistry*. George Thieme Verlag: 1999.
289. Jana, N. R.; Gearheart, L.; Murphy, C. J., Wet chemical synthesis of silver nanorods and nanowires of controllable aspect ratio. *Chem. Comm.* **2001**, (7), 617-618.
290. Brust, M.; Walker, M.; Bethell, D.; Schiffrin, D. J.; Whyman, R., Synthesis of thiol-derivatized gold nanoparticles in a 2-phase liquid-liquid system. *Journal of the Chemical Society-Chemical Communications* **1994**, (7), 801-802.
291. Ilavsky, J.; Jemian, P. R., Irena: tool suite for modeling and analysis of small-angle scattering. *J. Appl. Cryst.* **2009,** 42, 347-353.
292. Konarev, P. V.; Volkov, V. V.; Sokolova, A. V.; Koch, M. H. J.; Svergun, D. I., PRIMUS - a Windows-PC based system for small-angle scattering data analysis. *J. Appl. Cryst.* **2003,** 36, 1277 - 1282.
293. Konarev, P. V.; Petoukhov, M. V.; Volkov, V. V.; Svergun, D. I., ATSAS 2.1 - a program package for small-angle scattering data analysis. *J. Appl. Cryst.* **2006,** 39, 277-286.
294. Draine, B. T.; Flatau, P. J. User guide to the discrete dipole approximation code DDSCAT 6.1. http://arxiv.org/abs/astro-ph/0409262v2.
295. Lide, D. R., *CRC Handbook of Chemistry and Physics*. 85 ed.; CRC Press: Boca Raton, FL, 2004 - 2005; p 1281 - 1282.
296. Blaber, M. G.; Arnold, M. D.; Harris, N.; Ford, M. J.; Cortie, M. B., Plasmon absorption in nanospheres: A comparison of sodium, potassium, aluminium, silver and gold. *Physica B* **2007,** 394, (2), 184 -187.
297. Gasteiger, H. A.; Kocha, S. S.; Sompalli, B.; Wagner, F. T., Activity benchmarks and requirements for Pt, Pt-alloy, and non-Pt oxygen reduction catalysts for PEMFCs. *Appl. Catal. B-Environ.* **2005,** 56, (1-2), 9-35.
298. Narayanan, R.; El-Sayed, M. A., Catalysis with transition metal nanoparticles in colloidal solution: Nanoparticle shape dependence and stability. *J. Phys. Chem. B* **2005,** 109, (26), 12663 - 12676.

299. Coutts, M. J.; Cortie, M. B.; Ford, M. J.; McDonagh, A. M., Rapid and controllable sintering of gold nanoparticle inks at room temperature using a chemical agent. *J. Phys. Chem. C* **2009,** 113, (4), 1325 - 1328.
300. Kim, N.-S.; Han, K. N., Future direction of direct writing. *J. App. Phys.* **2010,** 108, (10), 102801-1 - 6.
301. Roy, S., Fabrication of micro- and nano-structured materials using mask-less processes. *J. Phys. D: Appl. Phys.* **2007,** 40, R413 - R426.
302. Jiang, L.-P.; Xu, S.; Zhu, J.-M.; Zhang, J.-R.; Zhu, J.-J.; Chen, H.-Y., Ultrasonic-assisted synthesis of monodisperse single-crystalline silver nanoplates and gold nanorings. *Inorg. Chem.* **2004,** 43, (19), 5877 - 5883.
303. Jiang, X.; Zeng, Q.; Yu, A., A self-seeding coreduction method for shape control of silver nanoplates. *Nanotechnology* **2006,** 17, (19), 4929 - 4935.
304. Aizpurua, J.; Hanarp, P.; Sutherland, D. S.; Käll, M.; Bryant, G. W.; García-de-Abajo, F. J., Optical properties of gold nanorings. *Phys. Rev. Lett.* **2003,** 90, (5), 057401 - 1, 057401 - 4.
305. Larsson, E. M.; Alegret, J.; Käll, M.; Sutherland, D. S., Sensing characteristics of NIR localized surface plasmon resonances in gold nanorings for applications as ultrasensitive biosensors. *Nano Lett.* **2007,** 7, (5), 1256 - 1263.
306. Ye, J.; Shioi, M.; Lodewijks, K.; Lagae, L.; Kawamura, T.; van-Dorpe, P., Tuning plasmonic interaction between gold nanorings and a gold film for surface enhanced Raman scattering. *Appl. Phys. Lett.* **2010,** 97, (16), 163106-1 - 3.
307. Kim, S.; Jung, J.-M.; Choi, D.-G.; Jung, H.-T.; Yang, S.-M., Patterned arrays of Au rings for localized surface plasmon resonance. *Langmuir* **2006,** 22, (17), 7109 - 7112.
308. Banaee, M. G.; Crozier, K. B., Gold nanorings as substrated for surface-enhanced Raman scattering. *Opt. Lett.* **2010,** 35, (5), 760 - 762.
309. Jiang, H.; Sabarinathan, J., Effects of coherent interactions on the sensing characteristics of near-infrared gold nanorings. *J. Phys. Chem. C* **2010,** 114, (36), 15243 - 15250.
310. Prevo, B. G.; Esakoff, S. A.; Mikhailovsky, A.; Zasadzinski, J. A., Scalable routes to gold nanoshells with tunable sizes and response to near-Infrared pulsed-laser irradiation. *Small* **2008,** 4, (8), 1183 - 1195.
311. Granqvist, C. G.; Hunderi, O., Optical absorption of ultrafine metal spheres with dielectric cores. *Zeitschrift fuer Physik* **1978,** 30, (1), 47 - 51.
312. Mulvaney, P., Surface plasmon spectroscopy of nanosized metal particles. *Langmuir* **1996,** 12, (3), 788 - 800.
313. Green, D. E., The potentials of ascorbic acid. *Biochem. J.* **1933,** 27, (4), 1044-1048.
314. Ruiz, J. J.; Aldaz, A.; Domínguez, M., Mechanism of L-ascorbic acid oxidation and dehydro-L-ascorbic acid reduction on a mercury electrode .1. Acid-medium. *Can. J. Chem* **1977,** 55, (15), 2799-2806.
315. Drachev, V. P.; Chettiar, U. K.; Kildishev, A. V.; Yuan, H.-K.; Cai, W.; Shalaev, V. M., The Ag dielectric function in plasmonic metamaterials. *Opt. Express* **2008,** 16, (2), 1186-1195.
316. West, P.; Ishii, S.; Naik, G.; Emani, N.; Shalaev, V. M.; Boltasseva, A. Searching for better plasmonic materials. http://arxiv.org/abs/0911.2737v4
317. Blaikie, R. J.; Melville, D. O. S.; Alkaisi, M. M., Super-resolution near-field lithography using planar silver lenses: a review of recent developments. *Microelectron. Eng.* **2006,** 83, (4 - 9), 723729.

318. Morones, J. R.; Elechiguerra, J. L.; Camacho, A.; Holt, K.; Kouri, J. B.; Ramírez, J. T.; Yacaman, M. J., The bactericidal effect of silver nanoparticles. *Nanotechnology* **2005,** 16, (10), 2346-2353.
319. Bar-Ilan, O.; Albrecht, R. M.; Fako, V. E.; Furgeson, D. Y., Toxicity assessments of multisized gold and silver nanoparticles in zebrafish embryos. *Small* **2009,** 5, (16), 1897-1910.
320. Chen, S. H.; Fan, Z. Y.; Carroll, D. L., Silver nanodisks: Synthesis, characterization, and self-assembly. *Journal of Physical Chemistry B* **2002,** 106, (42), 10777-10781.
321. Hunyadi, S. E.; Murphy, C. J., Tunable one-dimensional silver-silica nanopeapod architectures. *Journal of Physical Chemistry B* **2006,** 110, (14), 7226-7231.
322. Langhammer, C.; Yuan, Z.; Zorić, I.; Kasemo, B., Plasmonic properties of supported Pt and Pd nanostructures. *Nano Lett.* **2006,** 6, (4), 833-838.
323. Ren, J.; Tilley, R. D., Shape-controlled growth of platinum nanoparticles. *Small* **2007,** 3, 1508-1512.
324. Xia, Y.; Xiong, Y. J.; Lim, B.; Skrabalak, S. E., Shape-controlled synthesis of metal nanocrystals: Simple chemistry meets complex physics? *Angew. Chem. Int. Edit.* **2009,** 48, (1), 60-103.
325. van-Rheenen, P. R.; McKelvey, M. J.; Glausinger, W. S., *J. Solid State Chem.* **1967,** 67, 151.
326. Sastry, M.; Patil, V.; Mayya, K. S.; Paranjape, D. V.; Singh, P.; Sainkar, S. R., Organisation of polymer-capped platinum colloidal particles at the air-water interface. *Thin Solid Films* **1998,** 324, (1-2), 239-244.
327. Castro, E. G.; Salvatierra, R. V.; Schreiner, W. H.; Oliviera, M. M.; Zarbin, A. J. G., Dodecanethiol-stabilized platinum nanoparticles obtained by a two-phase method: synthesis, characterization, mechanism of formation, and electrocatalytic properties. *Chem. Mater.* **2010,** 22, (2), 360-370.
328. Kumar, A.; Joshi, H. M.; Mandale, A. B.; Srivastava, R.; Adyanthaya, S. D.; Pasricha, R.; Sastry, M., Phase transfer of platinum nanoparticles from aqueous to organic solutions using fatty amine molecules. *Journal of Chemical Sciences* **2004,** 116, (5), 293-300.
329. Li, N.; Liu, S.; Luo, H., A new method for the determination of the first and second cmc in CTAB solution by resonance Rayleigh scattering technology. *Anal. Lett.* **2002,** 35, (7), 1229 - 1238.
330. Fang, L.; Gan-Zuo, L.; Li-Min, Z.; Li-Qiang, Z.; Hong-Li, W., Fluorescence probe studies on the second critical micelle concentration of several kinds of surfactants. *J. Disper. Sci. Technol.* **1994,** 15, (6), 705-710.
331. Elding, L. I.; Groning, A. B., Kinetics, mechanism and equilibria for halide substitution processes of chloro bromo complexes of gold(III)
Acta Chemica Scandinavica Series a-Physical and Inorganic Chemistry **1978,** 32, (9), 867-877.
332. McBryde, W. A. E.; Yoe, J. H., Colorimetric determination of gold as bromoaurate - separation of small amounts of gold by solvents extraction
Analytical Chemistry **1948,** 20, (11), 1094-1099.
333. Xu, X.; Cortie, M. B., Shape change and colour gamut in gold nanorods, dumbells and dog bones. *Adv. Funct. Mater.* **2006,** 16, 2170 - 2176.
334. Jaiswal, P. V.; Ijeri, V. S.; Srivastava, A. K., Effect of surfactants on the dissociation constants of ascorbic and maleic acids. *Colloids and Surfaces B: Biointerfaces* **2005,** 46, (1), 45 - 51.
335. Bielski, B. H. J.; Allen, A. O.; Schwarz, H. A., Mechanism of disproportionation of ascorbate radicals. *J. Am. Chem. Soc.* **1981,** 103, (12), 3516-3518.

336. Aswal, V. K.; Goyal, P. S.; Thiyagarajan, P., Small-angle neutron-scattering and viscosity studies of CTAB/NaSal viscoelastic micellar solutions. *Journal of Physical Chemistry B* **1998,** 102, (14), 2469-2473.
337. Inoue, T.; Inoue, Y.; Watanabe, H., Nonlinear rheology of CTAB/NaSal aqueous solutions: Finite extensibility of a network of wormlike micelles. *Langmuir* **2005,** 21, (4), 1201-1208.
338. Wang, Z.; Friedrich, D. M.; Ainsworth, C. C.; Hemmer, S. L.; Joly, A. G.; Beversluis, M. R., Ground-state proton transfer tautomer of Al(III)-salicylate complexes in ethanol solution. *J. Phys. Chem. A.* **2001,** 105, (5), 942 - 950.
339. Friedrich, D. M.; Wang, Z.; Joly, A. G.; Peterson, K. A.; Callis, P. R., Ground-state proton-transfer tautomer of the salicylate anion. *J. Phys. Chem. A.* **1999,** 103, (48).
340. Atkins, P.; de-Paula, J., *Atkins' Physical Chemistry*. 7th ed.; Oxford University Press: 2002.
341. Kawamura, G.; Nogami, M., Application of a conproportionation reaction to a synthesis of shape-controlled gold nanoparticles. *Journal of Crystal Growth* **2009,** 311, (19), 4462-4466.
342. Khoury, C. G.; Vo-Dinh, T., Gold nanostars for surface-enhanced Raman scattering: synthesis, characterization and optimization. *J. Phys. Chem. C* **2008,** 112, (48), 18849-18859.
343. Nehl, C. L.; Liao, H.; Hafner, J. H., Optical Properties of Star Shaped Gold Nanoparticles. *Nano Letters* **2006,** 6, (4), 683 - 688.
344. Palik, E. D., *Handbook of optical constants of solids*. Academic Press: Boston MA, 1985.
345. Glatter, O.; Kratky, O., *Small Angle X-Ray Scattering*. Academic Press: London, 1982.
346. Kaya, H., Scattering from cylinders with globular end-caps. *Journal of Applied Crystallography* **2004,** 37, 223-230.
347. Kaya, H.; de Souza, N. R., Scattering from capped cylinders (vol 37, pg 223, 2004). *Journal of Applied Crystallography* **2004,** 37, 508-509.
348. Morita, T.; Hatakeyama, Y.; Nishikawa, K.; Tanaka, E.; Shingai, R.; Murai, H.; Nakano, H.; Hino, K., Multiple small-angle X-ray scattering analyses of the structure of gold nanorods with unique end caps. *Chemical Physics* **2009,** 364, (1-3), 14-18.
349. Atkins, P.; de-Paula, J., *Atkins' Physical Chemistry*. 8th ed.; Oxford University Press: 2006.
350. Connors, K. A., *Chemical Kinetics: The study of reaction rates in solution*. VCH Publishers: 1990.
351. Aswal, V. K.; Kohlbrecher, J.; Goyal, P. S.; Amenitsch, H.; Bernstorff, S., Counterion condensation on charged micelles in an aqueous electrolyte solution as studied with combined small-angle neutron scattering and small-angle X-ray scattering. *J. Phys.: Condens. Matter* **2006,** 18, (50), 11399-11410.
352. Joshi, J. V.; Aswal, V. K.; Goyal, P. S., Effect of sodium salicylate on the structure of micelles of different hydrocarbon chain lengths. *Physica B-Condensed Matter* **2007,** 391, (1), 65-71.
353. Ciccariello, S.; Goodisman, J.; Brumberger, H., On the Porod law. *Journal of Applied Crystallography* **1988,** 21, 117-128.
354. Semenyuk, A. V.; Svergun, D. I., GNOM - a program package for small-angle scattering data processing. *J. Appl. Cryst.* **1991,** 24, 537 - 540.
355. Nudelman, F.; de-With, G.; Summerdijk, N. A. J. M., Cryo-electron tomography: 3-dimensional imaging of soft matter. *Soft Matter* **2011,** 7, (17), 17-24.

356. González, Y. I.; Kaler, E. W., Cryo-TEM studies of worm-like micellar solutions. *Curr. Opin. Colloid In.* **2005,** 10, 256-260.
357. Ziserman, L.; Abezgauz, L.; Ramon, O.; Raghavan, S. R.; Danino, D., Origins of the Viscosity Peak in Wormlike Micellar Solutions. 1. Mixed Catanionic Surfactants. A Cryo-Transmission Electron Microscopy Study. *Langmuir* **2009,** 25, (18), 10483-10489.
358. Alfredsson, V., Cryo-TEM studies of DNA and DNA-lipid structures. *Curr. Opin. Colloid In.* **2005,** 10, 269-273.
359. Matias, V. R. F.; Beveridge, T. J., Native cell wall organization shown by cryo-electron microscopy confirms the existence of periplasmic space in Staphylococcus aureus. *J. Bacteriol.* **2006,** 188, (3), 1011-1021.
360. Krichevski, O.; Levi-Kalisman, Y.; Szwarcman, D.; Lereah, Y.; Markovich, G., Growth of Au/Ag nanowires in thin surfactant solution films: An electron microscopy study. *Journal of Colloid and Interface Science* **2007,** 314, (1), 304-309.

Appendices

Appendix A

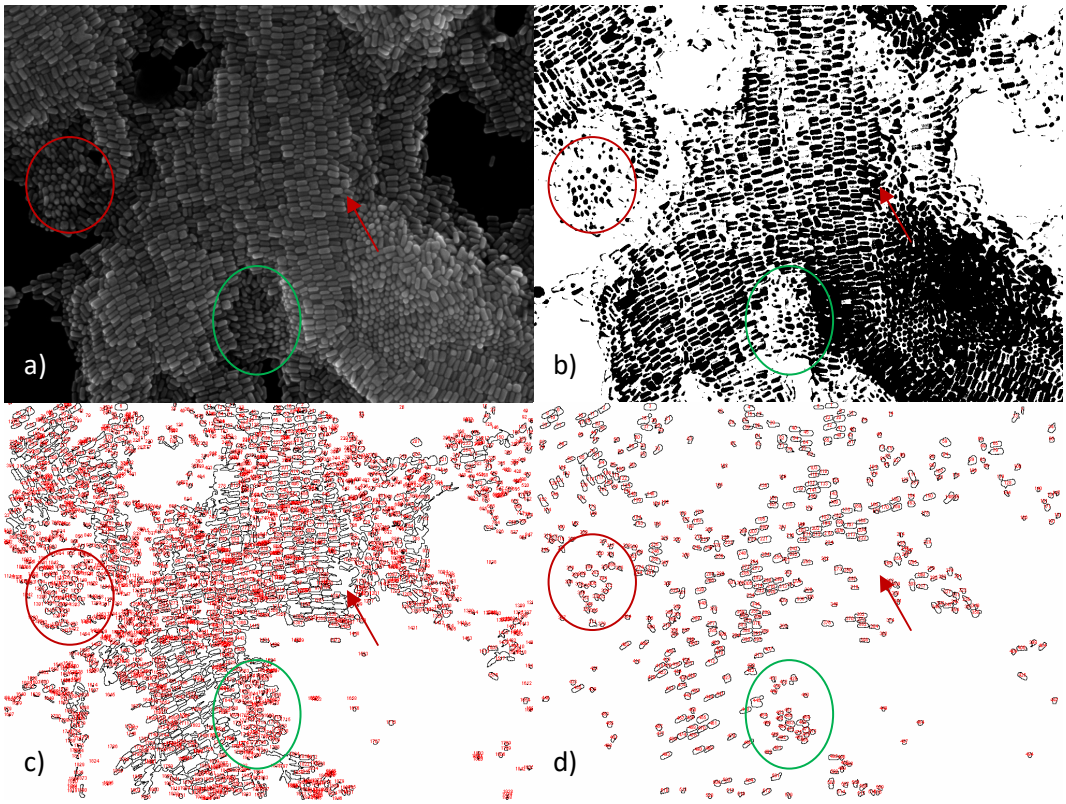

Figure A Analysis of an SEM image of gold nanorods with ImageJ software and particle analysis plug-in by Dougherty (http://www.optinav.com/Measure-Roi.htm), arrows indicate an example of insufficient greyscale difference from the original image and circled regions indicate regions where nanorods are oriented at an angle other than parallel to the substrate with respect to the longitudinal axis. a) Original image b) image threshold where greyscale values below the threshold are set to 0 and those above set to 1 c) particle analysis with default parameters d) particle analysis with area constraints applied to remove unseparated particles and suspect particles (low areas)

Figure A shows the analysis of an SEM image using ImageJ software. The regions indicated in the figure represent the same region after each treatment. An immediate problem for the determination of particle sizes from SEM images is the orientation of the nanorods on the substrate. If the particles are oriented at any angle other than parallel to the substrate (with respect to the longitudinal axis) then the algorithm will return false particle dimensions.

The sample in Figure A was prepared by a drop-cast/desiccation method. Using this method most nanoparticles end up in a ring at the perimeter of the original droplet. This ring is probably a few hundred nanometres thick. In many cases the nanorods will self assemble (as in Figure Aa) to give ordered layers. However, due to the thickness of the layer it is also possible for the nanorods to align perpendicular to the substrate. A quick resolution to this problem is to analyse the particles anywhere within the perimeter of the ring. This method could give a false representation of the particle distribution as it is

undetermined if the capillary forces endured during desiccation deposit different geometries or volumes at different regions of the drop.

Another problem with the use of SEM for automated particle analysis is lower resolution (with respect to TEM) which results in a less defined particle profile and potentially "over"-thresholding to separate the particles. The effect of "over"-thresholding is most apparent for nanoparticles in very close proximity where applying a threshold value to separate the particles can result in the loss of relevant data. The resolution in the SEM images is good enough to define particles by sight but the greyscale is too close to apply a threshold on a global scale (with respect to the total image).

Reducing the concentration of particles in the drop applied to the substrate could prevent these issues by increasing the instance of isolated particles. However, this would reduce the number of particles in the field-of-view as even at low concentrations the nanoparticles tend to coalesce.

Appendix B

The following images show the Mathematica script that I have written to extract the dimensions of gold nanorods from their UV-Vis spectrum. I have included comments in the script to describe the role of each step and how it is achieved.

```
In[1]:= "In this step I clear the variables to be used for the input and calculation of the data.
    Also I create an array for the parameters and some lists for the output of the
    particle dimensions in graphical form. The input is constructed as a list of the
    form {time,aspect ratio, volume,...}. The input array uses 0's as placeholders as
    this array is also used to display the results";
  Clear[V, r, hc, ARLSP, L, NRPARAMETERS, Results, NanorodGrow]
  NRPARAMETERS = {{480, 3.3599, 103.08, 0, 0, 0}, {540, 3.4103, 132.37, 0, 0, 0},
    {600, 3.4943, 173.59, 0, 0, 0}, {660, 3.6539, 224.78, 0, 0, 0}, {720, 3.7127, 294.24, 0, 0, 0},
    {780, 3.7715, 378.04, 0, 0, 0}, {840, 3.8387, 476.66, 0, 0, 0}, {900, 3.8639, 589.55, 0, 0, 0},
    {960, 3.8723, 712.63, 0, 0, 0}, {1020, 3.8807, 870.14, 0, 0, 0}, {1140, 3.8891, 1202.1, 0, 0, 0},
    {1200, 3.8891, 1394.06, 0, 0, 0}, {1260, 3.8555, 1646.03, 0, 0, 0}, {1320, 3.8051, 1932.04, 0, 0, 0},
    {1380, 3.7547, 2244.77, 0, 0, 0}, {1440, 3.7127, 2577.63, 0, 0, 0}, {1500, 3.6455, 2932.95, 0, 0, 0},
    {1560, 3.6035, 3303.03, 0, 0, 0}, {1620, 3.5531, 3684.21, 0, 0, 0}, {1680, 3.4943, 4058.67, 0, 0, 0},
    {1740, 3.4439, 4429.08, 0, 0, 0}, {1800, 3.4187, 4794.68, 0, 0, 0}, {1860, 3.3599, 5143.06, 0, 0, 0},
    {1920, 3.3263, 5479.96, 0, 0, 0}, {1980, 3.2927, 5792.8, 0, 0, 0}, {2040, 3.2591, 6078.05, 0, 0, 0},
    {2100, 3.2087, 6338.06, 0, 0, 0}, {2160, 3.1751, 6567.66, 0, 0, 0}, {2220, 3.1331, 6773.14, 0, 0, 0},
    {2280, 3.0995, 6944.89, 0, 0, 0}, {2340, 3.0575, 7087.34, 0, 0, 0}, {2400, 3.0407, 7207.43, 0, 0, 0},
    {2460, 3.0239, 7297.25, 0, 0, 0}, {2520, 2.9903, 7368.19, 0, 0, 0}, {2580, 2.9735, 7411.43, 0, 0, 0},
    {2640, 2.9651, 7451.77, 0, 0, 0}, {2700, 2.9567, 7476.2, 0, 0, 0}, {2760, 2.9399, 7483.53, 0, 0, 0},
    {2820, 2.9315, 7495.62, 0, 0, 0}, {2880, 2.9231, 7498.33, 0, 0, 0}, {2940, 2.9147, 7493.84, 0, 0, 0},
    {3000, 2.9063, 7494.01, 0, 0, 0}, {3060, 2.8895, 7492.85, 0, 0, 0}, {3120, 2.8727, 7490.81, 0, 0, 0},
    {3180, 2.8643, 7486.25, 0, 0, 0}, {3240, 2.8643, 7487.84, 0, 0, 0}, {3300, 2.8559, 7484.11, 0, 0, 0},
    {3360, 2.8559, 7486.16, 0, 0, 0}, {3420, 2.8475, 7482.21, 0, 0, 0}, {3480, 2.8475, 7487.28, 0, 0, 0},
    {3540, 2.8475, 7483.7, 0, 0, 0}, {3600, 2.8391, 7476.21, 0, 0, 0}};

  Diagrams = List[0, 0, 0, 0, 0, 0, 0, 0, 0, 0, 0, 0, 0, 0, 0, 0, 0, 0, 0, 0, 0, 0, 0, 0, 0, 0,
    0, 0, 0, 0, 0, 0, 0, 0, 0, 0, 0, 0, 0, 0, 0, 0, 0, 0, 0, 0, 0, 0, 0, 0, 0, 0, 0, 0, 0, 0];
  CrossSections = List[0, 0, 0, 0, 0, 0, 0, 0, 0, 0, 0, 0, 0, 0, 0, 0, 0, 0, 0, 0, 0, 0, 0, 0, 0,
    0, 0, 0, 0, 0, 0, 0, 0, 0, 0, 0, 0, 0, 0, 0, 0, 0, 0, 0, 0, 0, 0, 0, 0, 0, 0, 0, 0, 0, 0, 0];

In[6]:= "In this step I arrange the input parameters into a table";
  TableForm[NRPARAMETERS,
    TableHeadings → {None, {"Time (s)", ARLSP, "Volume (nm3)", +"radius", "hc (nm)", "Length (nm)"}}];
```

In[8]:=
```
"Here I calculate the particle dimensions for each time step (time can be replaced by a
  position holder, i.e. time is not included in any calculation). The calculation is
  looped over the number of elements in the input array. The respective variables for
  each time are called by using the value i (the loop number) as the position in the
  input array and the position of the variable in that element. I calculate the radius
  of the nanorod by solving the volume equation V[r_] for r. Mathematica also returns
  the complex roots of the volume equation and so I store the results in a list and
  check which position the real answer is stored to call this value for the subsequent
  calculations. I then place the result in the first empty position of the input list
  for the respective element. I calculate the length, L, and the parameter hc (height
  of the cylinder in the geometric model) using the aspect ratio equation and geometric
  relationship of the hemi-spherically capped cylinder, respectively. I place these
  parameters in the second and third empty positions in the input list. This completes
  the evaluation of the particle parameters. Using the calculated parameters I create
  2D and 3D diagrams of the nanorod and store the result in the Crosssections and
  Diagrams lists respectively.";

Do[
 T = NRPARAMETERS[[i, 1]];
 ARLSP = NRPARAMETERS[[i, 2]];

 L[r_] := ARLSP * 2 * r;
 hc[r_] := L[r] - 2 r;

 V[r_] := 2 * π * (r^3) * (ARLSP - (1 / 3));

 Results = Solve[V[r] == NRPARAMETERS[[i, 3]]]; (*Check position of real solution*)


 NRPARAMETERS[[i, 4]] = r /. Results[[3, 1]];
 NRPARAMETERS[[i, 5]] = hc[r /. Results[[3, 1]]];
 NRPARAMETERS[[i, 6]] = L[r /. Results[[3, 1]]];


 Diagrams[[i]] =
  Graphics3D[{EdgeForm[], Blend[{Yellow, Brown}, 1 / 2],
    Cylinder[{{((-hc[(NRPARAMETERS[[i, 4]])]) / 2), 0, 0}, {((hc[(NRPARAMETERS[[i, 4]])]) / 2), 0, 0}},
     (NRPARAMETERS[[i, 4]])], EdgeForm[], Blend[{Yellow, Brown}, 1 / 2],
    Sphere[{((-hc[(NRPARAMETERS[[i, 4]])]) / 2), 0, 0}, (NRPARAMETERS[[i, 4]])], EdgeForm[],
    Blend[{Yellow, Brown}, 1 / 2], Sphere[{((hc[(NRPARAMETERS[[i, 4]])]) / 2), 0, 0},
     (NRPARAMETERS[[i, 4]])]}, Lighting → {{"Directional", White, {{1, -1, 1}, {0, 0, 0}}}},
   PlotRange → {{-30, 30}, {-20, 15}, {-20, 20}}, ImageSize → Small];

 CrossSections[[i]] =
  Graphics[{EdgeForm[{Thick, RGBColor[0.8`, 0.7`, 0.1`]}], Blend[{Yellow, Brown}, 1 / 2],
    Rectangle[{-(NRPARAMETERS[[i, 6]] / 2), -NRPARAMETERS[[i, 4]]},
     {(NRPARAMETERS[[i, 6]] / 2), NRPARAMETERS[[i, 4]]}], EdgeForm[{Thin, RGBColor[0.8`, 0.7`, 0.1`]}],
    Blend[{Yellow, Brown}, 1 / 2], Disk[{-(NRPARAMETERS[[i, 6]] / 2), 0}, NRPARAMETERS[[i, 4]],
     {Pi / 2, 3 Pi / 2}], EdgeForm[{Thin, RGBColor[0.8`, 0.7`, 0.1`]}], Blend[{Yellow, Brown}, 1 / 2],
    Disk[{(NRPARAMETERS[[i, 6]] / 2), 0}, NRPARAMETERS[[i, 4]], {-Pi / 2, Pi / 2}]},
   PlotRange → {{-40, 40}, {-30, 30}}, ImageSize → 60]


 , {i, 1, 52}]
```

In[10]:=
```
"I display the Results list to check the position of the real value of r";
Results
```

Out[11]=
```
{{r → -3.90083 - 6.75644 i}, {r → -3.90083 + 6.75644 i}, {r → 7.80166}}
```

In[12]:=
```
"Now that all of the parameters are evaluated I can display the results in a table";
TableForm[NRPARAMETERS,
 TableHeadings → {None, {"Time (s)", "ARLSP", "Volume (nm3)", "radius (nm)", "h_c (nm)", "Length (nm)"}}]
```

Out[13]//TableForm=

Time (s)	ARLSP	Volume (nm3)	radius (nm)	h_c (nm)	Length (nm)
480	3.3599	103.08	1.75663	8.29096	11.8042
540	3.4103	132.37	1.89887	9.1537	12.9514
600	3.4943	173.59	2.05988	10.2759	14.3957
660	3.6539	224.78	2.20862	11.7229	16.1402
720	3.7127	294.24	2.40194	13.0315	17.8354
780	3.7715	378.04	2.59623	14.3909	19.5834
840	3.8387	476.66	2.78675	15.8215	21.395
900	3.8639	589.55	2.98423	17.0931	23.0615
960	3.8723	712.63	3.17641	18.2472	24.6
1020	3.8807	870.14	3.39235	19.5447	26.3294
1140	3.8891	1202.1	3.77522	21.814	29.3644
1200	3.8891	1394.06	3.96634	22.9183	30.851
1260	3.8555	1646.03	4.20548	24.0175	32.4285
1320	3.8051	1932.04	4.45754	25.0077	33.9228
1380	3.7547	2244.77	4.70902	25.9439	35.3619
1440	3.7127	2577.63	4.95148	26.8638	36.7667
1500	3.6455	2932.95	5.204	27.5344	37.9424
1560	3.6035	3303.03	5.43735	28.3123	39.187
1620	3.5531	3684.21	5.66822	28.9431	40.2795
1680	3.4943	4058.67	5.89017	29.3837	41.1641
1740	3.4439	4429.08	6.09675	29.7997	41.9932
1800	3.4187	4794.68	6.27708	30.3647	42.9189
1860	3.3599	5143.06	6.46692	30.5225	43.4564
1920	3.3263	5479.96	6.62977	30.8457	44.1052
1980	3.2927	5792.8	6.77907	31.0847	44.6429
2040	3.2591	6078.05	6.91483	31.2426	45.0723
2100	3.2087	6338.06	7.05279	31.155	45.2606
2160	3.1751	6567.66	7.16497	31.169	45.499
2220	3.1331	6773.14	7.27494	31.0364	45.5862
2280	3.0995	6944.89	7.3655	30.9277	45.6588
2340	3.0575	7087.34	7.45344	30.6709	45.5778
2400	3.0407	7207.43	7.51077	30.6545	45.676
2460	3.0239	7297.25	7.55751	30.5913	45.7063
2520	2.9903	7368.19	7.61374	30.3073	45.5348
2580	2.9735	7411.43	7.64476	30.1738	45.4634
2640	2.9651	7451.77	7.66674	30.1318	45.4653
2700	2.9567	7476.2	7.68329	30.0678	45.4344
2760	2.9399	7483.53	7.70228	29.8833	45.2879
2820	2.9315	7495.62	7.71472	29.802	45.2314
2880	2.9231	7498.33	7.72398	29.708	45.156
2940	2.9147	7493.84	7.73081	29.6044	45.066
3000	2.9063	7494.01	7.73927	29.5067	44.9853
3060	2.8895	7492.85	7.75579	29.3091	44.8207
3120	2.8727	7490.81	7.77215	29.1098	44.6541
3180	2.8643	7486.25	7.77916	29.0054	44.5637
3240	2.8643	7487.84	7.77971	29.0074	44.5668
3300	2.8559	7484.11	7.78704	28.9039	44.478
3360	2.8559	7486.16	7.78775	28.9066	44.4821
3420	2.8475	7482.21	7.79505	28.8027	44.3928
3480	2.8475	7487.28	7.79681	28.8092	44.4028
3540	2.8475	7483.7	7.79556	28.8046	44.3957
3600	2.8391	7476.21	7.80166	28.6961	44.2994

In[14]:=
```
"I can use the various features of Mathematica to display the diagrams produced by the
   evaluation loop";
ListAnimate[Diagrams, 4, AnimationDirection → Forward, AnimationRate → 1, AnimationRepetitions → 1]
```

Out[15]=

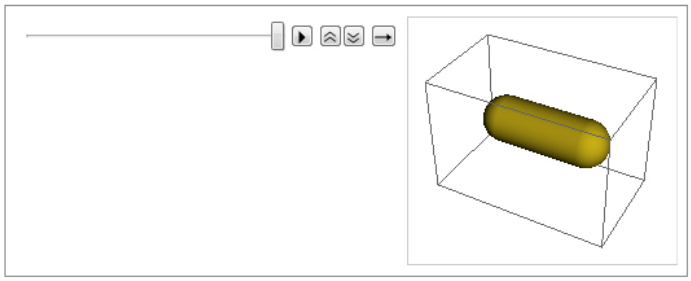

In[16]:=
```
"I can create a table of the diagrams";
Clear[Diagramstable]
Diagramstable = List[{Diagrams[[1]], Diagrams[[2]], Diagrams[[3]], Diagrams[[4]], Diagrams[[5]]},
   {Diagrams[[6]], Diagrams[[7]], Diagrams[[8]], Diagrams[[9]], Diagrams[[10]]},
   {Diagrams[[11]], Diagrams[[12]], Diagrams[[13]], Diagrams[[14]], Diagrams[[15]]},
   {Diagrams[[16]], Diagrams[[17]], Diagrams[[18]], Diagrams[[19]], Diagrams[[20]]},
   {Diagrams[[21]], Diagrams[[22]], Diagrams[[23]], Diagrams[[24]], Diagrams[[25]]},
   {Diagrams[[26]], Diagrams[[27]], Diagrams[[28]], Diagrams[[29]], Diagrams[[30]]},
   {Diagrams[[31]], Diagrams[[32]], Diagrams[[33]], Diagrams[[34]], Diagrams[[35]]},
   {Diagrams[[36]], Diagrams[[37]], Diagrams[[38]], Diagrams[[39]], Diagrams[[40]]},
   {Diagrams[[41]], Diagrams[[42]], Diagrams[[43]], Diagrams[[44]], Diagrams[[45]]},
   {Diagrams[[46]], Diagrams[[47]], Diagrams[[48]], Diagrams[[49]], Diagrams[[50]]},
   {Diagrams[[51]], Diagrams[[52]]}];

"I have suppressed the output of the diagrams table to save space, it can be displayed
   by deleting the semi-colon above or evaluating this step. The result will be a table
   of diagrams at each time step similar to that in the animations step but with the
   dimensions of each respective time step.";
TableForm[Diagramstable]
```

In[19]:=
```
"As above";
ListAnimate[CrossSections, 4, AnimationDirection → Forward, AnimationRepetitions → 1]
```

Out[20]=

In[21]:=
```
"This table displays the cross-section of the nanorods calculated";
CrossSectionsTable =
  List[{CrossSections[[1]], CrossSections[[2]], CrossSections[[3]], CrossSections[[4]],
    CrossSections[[5]]}, {CrossSections[[6]], CrossSections[[7]], CrossSections[[8]],
    CrossSections[[9]], CrossSections[[10]]},
   {CrossSections[[11]], CrossSections[[12]], CrossSections[[13]], CrossSections[[14]],
    CrossSections[[15]]}, {CrossSections[[16]], CrossSections[[17]], CrossSections[[18]],
    CrossSections[[19]], CrossSections[[20]]},
   {CrossSections[[21]], CrossSections[[22]], CrossSections[[23]], CrossSections[[24]],
    CrossSections[[25]]}, {CrossSections[[26]], CrossSections[[27]], CrossSections[[28]],
    CrossSections[[29]], CrossSections[[30]]},
   {CrossSections[[31]], CrossSections[[32]], CrossSections[[33]], CrossSections[[34]],
    CrossSections[[35]]}, {CrossSections[[36]], CrossSections[[37]], CrossSections[[38]],
    CrossSections[[39]], CrossSections[[40]]},
   {CrossSections[[41]], CrossSections[[42]], CrossSections[[43]], CrossSections[[44]],
    CrossSections[[45]]}, {CrossSections[[46]], CrossSections[[47]], CrossSections[[48]],
    CrossSections[[49]], CrossSections[[50]]}, {CrossSections[[51]], CrossSections[[52]]}];

"As above";
TableForm[CrossSectionsTable]
```

In[23]:=
```
"I have included this step to summarise the progression of the nanorods growth in the
   assumption that all nanorods grow concurrently";
ARROW = Graphics[{Arrowheads[0.5], Arrow[{{-0.5, 0}, {1, 0}}]}, ImageSize → 20];
GraphicsRow[{CrossSections[[1]], ARROW, CrossSections[[6]], ARROW, CrossSections[[11]],
  ARROW, CrossSections[[16]], ARROW, CrossSections[[21]], ARROW, CrossSections[[26]],
  ARROW, CrossSections[[31]], ARROW, CrossSections[[36]], ARROW, CrossSections[[41]],
  ARROW, CrossSections[[46]], ARROW, CrossSections[[51]]}, -28]
```

Out[25]=

Appendix C

Below I have included the variables and components of my POV-Ray scene for drawing gold nanoparticles of a desired shape/structure.

```
#include "colors.inc"
#include "golds.inc"
#include "math.inc"
#include "glass.inc"

camera {

    perspective

    location <120,80,50>

    look_at <0,0,0>

    sky   <0,0,1>


}

background {White}

#declare AUROD =
                object {
                        union {


#declare RADIUS = (sqrt(2)/4);
#declare D1 = 10;
#declare D2 = 10;
#declare AR = 3;
#declare L = AR*D1;
#declare ENDX = D1/(2+sqrt(2)); // end cap "radius"
#declare H = L - 2*ENDX; // Length minus end caps
#declare ENDFACE = (2*(ENDX)*sqrt(2))/(2*(2+sqrt(2)));

#declare xincrement = 1;
#declare yincrement = 0.5;
#declare zincrement = 0.5;
#declare xoffset = 0.5;
#declare yoffset = 0.5;
#declare zoffset = 0.5;


#declare xstartpos = -(H/2)-(ENDX);  //Min. x coordinate
#declare ystartpos = (-D1/2) - 1;  //Min. y coordinate
#declare zstartpos = (-D1/2) - 1;  //Min. z coordinate

#declare xnum = L;  // x length of bounding shape
#declare ynum = (2*D1) + 2;  // y length of bounding shape
#declare znum = (2*D1) + 2;  // z length of bounding shape

#declare zIndex = 0;

#declare zpos = zstartpos;
```

The #IF statements below produce the current structure published for gold nanorods by the group of Liz-Marzán (reference [87]).

```
(zIndex <= znum)
 #declare yIndex = 0;

 #if (mod(abs(zIndex),2) = 0)

 #declare ypos = ystartpos + yoffset;

 #else

 #declare ypos = ystartpos;

 #end

 #while (yIndex <= ynum)

         #declare xIndex = 1;

         #if (mod(abs(yIndex),2) = 0)

         #declare xpos = xstartpos + xoffset;

         #else


         #declare xpos = xstartpos;

         #end

                 #while (xIndex <= xnum)


                         #declare FACTOR025052   = (D1/2);
                         #declare FACTOR110 = ((9.5*D1)/(10*sqrt(2)));
```

```
#if ( xpos < 0 )
#if ( ypos >= ystartpos + 1 )
#if ( zpos >= zstartpos + 1 )
#if ( ypos <= D1/2 )
#if ( zpos <= D1/2 )
#if ( (ypos)+(zpos)<=FACTOR110)   //Rounded Rod
#if ( (ypos)+(-zpos)<=FACTOR110)   //Rounded Rod
#if ( (-ypos)+(zpos)<=FACTOR110)   //Rounded Rod
#if ( (-ypos)+(-zpos)<=FACTOR110)   //Rounded Rod
#if ( ((2/5)*ypos)+(zpos)<=FACTOR025052)
#if ( ((2/5)*ypos)+(-zpos)<=FACTOR025052)
#if ( ((2/5)*-ypos)+(zpos)<=FACTOR025052)
#if ( ((2/5)*-ypos)+(-zpos)<=FACTOR025052)
#if ( (ypos)+((2/5)*zpos)<=FACTOR025052)
#if ( (ypos)+((2/5)*-zpos)<=FACTOR025052)
#if ( (-ypos)+((2/5)*zpos)<=FACTOR025052)
#if ( (-ypos)+((2/5)*-zpos)<=FACTOR025052)

#if ( (-xpos)+(-zpos)<=((H/2)+(D1/2)))
#if ( (-xpos)+(zpos)<=((H/2)+(D1/2)))
#if ( (-xpos)+(-ypos)<=((H/2)+(D1/2)))
#if ( (-xpos)+(ypos)<=((H/2)+(D1/2)))
#if ( (-xpos)+(ypos)+(zpos)<=((H/2)+(D1/2)+ENDFACE))
#if ( (-xpos)+(-ypos)+(zpos)<=((H/2)+(D1/2)+ENDFACE))
#if ( (-xpos)+(ypos)+(-zpos)<=((H/2)+(D1/2)+ENDFACE))
#if ( (-xpos)+(-ypos)+(-zpos)<=((H/2)+(D1/2)+ENDFACE))

     sphere { < xpos, ypos, zpos >, RADIUS
              pigment { P_Gold4}
              finish {F_MetalA}
            }
```

The nested while loops for placing the gold atoms in the desired geometry are shown below. In this example a sphere of radius 20 units will be drawn (radius ≈ 8 nm). To

draw a facetted nanoparticle the Cartesian equation for the sphere is replaced with multiple statements (such as those above) for all of the desired facets. It should be noted that in the example given above that not all of the facets required for a nanorod model are given. This set of statements is only for the negative half (the rod is centre at (0,0,0)) of a nanorod. I have split the particle into two halves in the scene to include the option of producing bow-tie shaped nanoparticles.

```
#while (zIndex <= znum)
        #declare yIndex = 0;
        #if (mod(abs(zIndex),2) = 0)
        #declare ypos = ystartpos + yoffset;
        #else
        #declare ypos = ystartpos;
        #end
        #while (yIndex <= ynum)
                #declare xIndex = 1;
                #if (mod(abs(yIndex),2) = 0)
                #declare xpos = xstartpos + xoffset;
                #else

                #declare xpos = xstartpos;
                #end
                        #while (xIndex <= xnum)


                                #if ( (xpos*xpos)+(ypos*ypos)+(zpos*zpos) <= 400)

                                     sphere { < xpos, ypos, zpos >, RADIUS
                                                pigment { P_Gold4}
                                                finish {F_MetalA}
                                              }

                                #else
                                #end


                                #declare xIndex = xIndex + 1;
                                #declare xpos = xpos + xincrement;
                                #end
                #declare yIndex = yIndex + 1;
                #declare ypos = ypos + yincrement;
        #end
        #declare zIndex = zIndex + 1;
        #declare zpos = zpos + zincrement;
#end

        }
       };
AUROD

  light_source {
    <100,100,100>, rgb <1.4,1.4,1.4>
                shadowless
                }
```

Appendix D

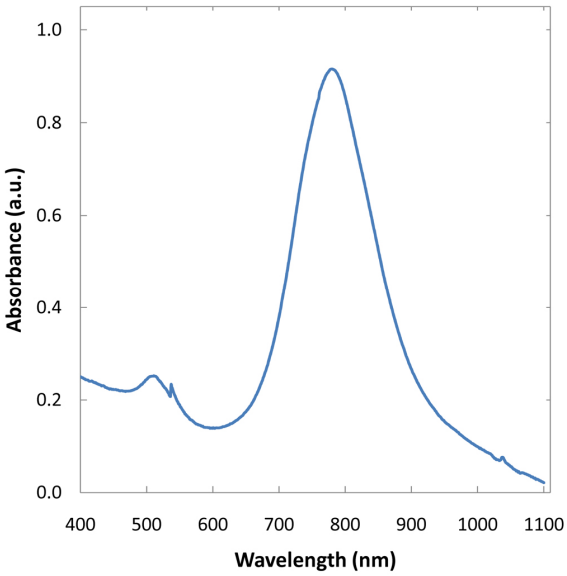

Figure D1 Nanorod spectrum for sample prepared with ascorbic acid to gold (III) concentration below 1:1, with supplemental sodium salicylate

Appendix E

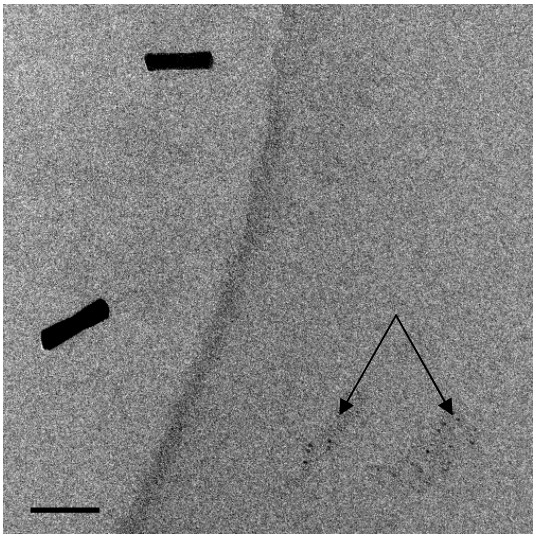

Figure E Cryo-TEM image of sample 0.60 mM H_2A with seed-like particles indicated by the arrows.

Appendix F

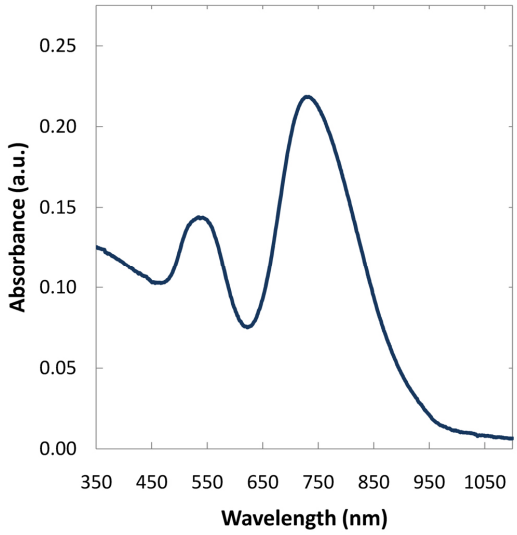

Figure F Absorbance spectrum for gold nanorods sample after centrifugation during growth process.